Catalysts for sustainable hydrogen production via bioethanol reforming in a fluidized bed membrane reactor

Concetta Ruocco

a Carmine e a Clara

UNIVERSITY OF SALERNO

DEPARTMENT OF INDUSTRIAL ENGINEERING

Ph.D. Course in Industrial Engineering
Curriculum in Chemical Engineering - XXXIII Cycle

Catalysts for sustainable hydrogen production via bioethanol reforming in a fluidized bed membrane reactor

Supervisor	**Ph.D. student**
Prof. Vincenzo Palma	*Concetta Ruocco*

Scientific Referees
Prof. Vincenzo Palma
Prof. Vincenzo Vaiano

Ph.D. Course Coordinator
Prof. Francesco Donsì

Acknowledgments

Il mio primo ringraziamento va al Prof. Vincenzo Palma per avermi guidato in questo importante percorso, incoraggiandomi e trasmettendomi la sua grande passione per la ricerca.

Ringrazio i miei colleghi dei lab. T1 e T3: Daniela, Eugenio, Giusy, Marco, Marta e Simona, con cui ho condiviso tante esperienze indimenticabili e che mi hanno supportato in questi anni, rendendo più leggere le lunghe giornate in laboratorio. Un ringraziamento speciale va al Prof. Vincenzo Vaiano, per l'aiuto che ha saputo darmi e per la sua capacità di stemperare le mie ansie.

Ringrazio le mie compagne di avventura, Livia, Paola, Ida e Antonella, per le confidenze, l'aiuto reciproco e i tanti momenti trascorsi insieme. Ringrazio Olga, per aver condiviso con me un pezzo importante di questo percorso.

Ringrazio Antonio, che mi ha spronato ad intraprendere il dottorato, nonostante i miei mille dubbi, per l'attenzione che ha sempre prestato alle mie richieste e per tutto il tempo che ha saputo dedicarmi, anche da "remoto".

Un grande ringraziamento va ai miei genitori e ad Alfonso e Michele, per aver sempre creduto in me e per avermi incoraggiato durante gli anni trascorsi in laboratorio (pur non capendo del tutto qual è il mio "lavoro"), alleggerendo le mie giornate e rendendo meno faticoso questo percorso. Ringrazio Laura, la seconda parte di me, il mio sostegno in ogni momento. Un ringraziamento speciale va a mio cognato Carmine, per il supporto tecnologico che non mi ha mai fatto mancare e per avermi spronato a dare sempre il meglio.

Ringrazio le mie amiche di sempre, Alfonsina, Angela, Chiara, Imma, Maria e Sara, per la loro presenza silenziosa e mai invadente, per la carica che mi hanno dato le tante esperienze vissute insieme e per il bene profondo che hanno sempre saputo trasmettermi. Ringrazio i miei amici del gruppo di "fuoco", per i momenti indimenticabili che mi hanno regalato e per il senso di tranquillità che sanno trasmettermi, allontanando i cattivi pensieri.

Un ringraziamento speciale va a Maria, la mia amichetta "monzese", che non ha mai smesso di farmi sentire la sua vicinanza in questi anni e che occupa un posto importante nel mio cuore. Ringrazio Antonella, per la sua presenza dolce e per i consigli importanti che ha sempre saputo darmi. Ringrazio la mia SuperMary, che mi ha sempre trasmesso leggerezza e spensieratezza, rendendo meno pesante questo percorso.

Ringrazio Virginia, per i consigli che ha sempre saputo darmi e per la voglia di diventare ingegnere che mi ha trasmesso. Ringrazio la mia famiglia allargata e i miei nipotini, per la tenerezza con cui hanno rallegrato le mie giornate e la gioia che hanno saputo darmi.

Ringrazio infine Carmine, per avermi sostenuto in questi lunghi anni che ho trascorso in laboratorio, gioendo dei miei tanti traguardi e mostrandomi la strada più semplice per superare gli ostacoli che ho incontrato in questo percorso. Lo ringrazio per l'amore che mi trasmette ogni giorno e soprattutto per avermi regalato la cosa più preziosa che ho.

Publication list

Palma, V., Ruocco, C., Ricca, A. (2018) Oxidative steam reforming of ethanol in a fluidized bed over CeO_2-SiO_2 supported catalysts: effect of catalytic formulation, *Renew. Energy*, **125**, 356-364.
DOI 10.1016/j.renene.2018.02.118

Palma, V., Ruocco, C., Ricca, A. (2018) Renewable H_2 Production via Oxidative Reforming on Ni Catalysts: an Experimental and Kinetic Study, *Chem. Eng. Trans*., **70,** 1321-1326.
DOI 10.3303/CET1870221

Palma, V., Meloni, E., Ruocco, C., Martino, M., Ricca, A. (2018) State of the Art of Conventional Reactors for Methanol Production, In *Methanol Science and Engineering* (A. Basile and F. Dalena Eds), Elsevier, Amsterdam, Chapter 2.
DOI 10.1016/B978-0-444-63903-5.00002-9

Palma, V., Ruocco, C., Ricca, A., Oxidative steam reforming of ethanol in a fluidized bed over CeO_2-SiO_2 supported catalysts, Proc. of the 7th *Conference "European Fuel Cell Technology & Applications Piero Lunghi Conference & Exhibition"*, December 12-15, 2017, Naples (ITALY), p.77-78.
ISBN 978-88-8286-356-2

Viviente, J.L., Meléndez, J., Pacheco Tanaka, D.A., Spallina, V., Gallucci, F., Escribano, S., Manzolini, G., Foresti, S., Palma, V., Ruocco, C., Boaventura, M., Tregambe, C., Roses, L., Magaud, V., Guinard, C., Advanced m-CHP fuel cell system based on a novel bio-ethanol fluidized bed membrane reformer, Proc. of the *Conference on European Hydrogen Energy*, March 14-16, 2018, Malaga (SPAIN), p.196-197.
ISBN: 978-84-09-01620-4

Palma, V., Ruocco, C., Ricca, A., Hydrogen production by oxidative reforming of ethanol in a fluidized bed reactor using a Pt-Ni/CeO_2-SiO_2 catalyst, Proc. of the *Conference on European Hydrogen Energy*, March 14-16, 2018, Malaga (SPAIN), p. 239-240.
ISBN: 978-84-09-01620-4

Ruocco, C., Palma, V., Ricca, A., Kinetics of oxidative steam reforming of ethanol over Pt-Co and Ni-Co/CeO_2-SiO_2 catalysts, Proc. of *the 4th International Symposium on Catalysis for Clean Energy and Sustainable Chemistry*, July 9-11, 2018, Bilbao (SPAIN) p.40-41.

Ruocco, C., Palma, V., Ricca, A., Structured catalysts for bio-hydrogen production, Promeca Workshop on *Energy Analysis and modelling of Membrane reactors*, 16 November, 2017, Chieti (ITALY).

Palma, V., Ruocco, C., Ricca, A., Experimental study of hydrogen production from ethanol reforming in a fluidized bed reactor, Summer School on *Advanced chemical reactors and Circular economy concepts in process engineering*, May 16-19, 2018, Pisa (ITALY).

Palma, V., Ruocco, C., Ricca, A., Experimental study of hydrogen production from ethanol reforming in a fluidized bed reactor, *25th International Conference on Chemical Reaction Engineering*, May 20-23, 2018, Firenze (ITALY).

Ruocco, C., Palma, V., Ricca, A. (2019) Experimental and kinetic study of oxidative steam reforming of ethanol over fresh and spent bimetallic catalysts, *Chem. Eng. J.*, **377**, 119778.
DOI 10.1016/j.cej.2018.08.164

Palma, V., Ruocco, C., Ricca, A. (2019) Hydrogen production by oxidative reforming of ethanol in a fluidized bed reactor using a Pt-Ni/ CeO_2-SiO_2 catalyst, *Int. J. Hydrogen Energ.*, **44**, 12661-12670.
DOI doi.org/10.1016/j.ijhydene.2018.12.154

Ruocco, C., de Caprariis, B., Palma, V., Petrullo, A., Ricca, A., Scarsella, M., De Filippis, P. (2019) Methane dry reforming on Ru perovskites, $AZrRuO_3$: Influence of preparation method and substitution of A cation with alkaline earth metals, *J. CO_2 Util.*, **30**, 222-231.
DOI doi.org/10.1016/j.jcou.2019.02.009

Ruocco, C., Palma, V., Ricca, A. (2019) Kinetics of Oxidative Steam Reforming of Ethanol Over Bimetallic Catalysts Supported on CeO_2–SiO_2: A Comparative Study, *Top. Catal.*, **62**, 467-478.
DOI doi.org/10.1007/s11244-019-01173-2

Palma, V., Ruocco, C., Ricca, A. (2019) H_2 Generation via Ethanol Reforming over CeO_2-SiO_2 Based Catalysts, *Chem. Eng. Trans.*, **73**, 133-138.
DOI doi.org/10.3303/CET1973023

Palma, V., Ruocco, C., Martino, M., Ricca, A. (2019) H_2 Production over Pt-Ni/CeO_2-SiO_2 via Ethanol Reforming in a Fluidized Bed, *Chem. Eng. Trans.*, **74**, 505-510.
DOI: doi.org/10.3303/CET1974085

Palma, V., Ruocco, C., Cortese, M., Martino M. (2019) Recent Advances in Structured Catalysts Preparation and Use in Water-Gas Shift Reaction (Review), *Catalysts,* **9**, 991-1014.
DOI: https://doi.org/10.3390/catal9120991

Palma, V., Martino, M., Ruocco, C., Ceria-coated aluminum foams as promising catalysts for the water gas shift process, *Proc. of the Chemistry meets Industry and Society A creative showcase conference* (CIS 2019), August 28-31 2019, Salerno (ITALY).

Palma, V., Barba, D., Meloni, E., Renda, S., Ruocco, C., Ultracompact biofuels catalytic reforming processes for distributed renewable hydrogen production, In *Studies in Surface Science and Catalysis* (A. Basile, G. Centi, M. De Falco, G. Iaquaniello Eds) Elsevier, Amsterdam, Chapter 17.
DOI: doi.org/10.1016/B978-0-444-64337-7.00017-3

Palma, V., Ruocco, C., Martino, M., Efficient catalysts for hydrogen production via ethanol reforming in a fluidized bed reactor, Proc. of the 8th *Conference "European Fuel Cell Technology & Applications Piero Lunghi Conference & Exhibition"*, December 9-11, 2019, Naples (ITALY), p.99-100.
ISBN 978-88-8286-386-9

Palma, V., Barba, D., Meloni, E., Ruocco, C., Martino, M. (2020) Membrane reactors for H_2 and energy production, In *Current Trends and Future Developments on (Bio-) Membranes in Environmental Applications* (A. Iulianelli and A. Basile Eds), Elsevier, Amsterdam, Chapter 2.
DOI: doi.org/10.1016/B978-0-12-817110-3.00002-3

Palma, V., Ruocco ,C., Meloni, E., Martino, M., Barba, D. (2020) Membrane reactor technology and catalysis for intensified hydrogen production, In *Current Trends and Future Developments on (Bio-) Membranes in Environmental Applications*, (A. Iulianelli and A. Basile Eds), Elsevier, Amsterdam, Chapter 6.
DOI: doi.org/10.1016/B978-0-12-817384-8.00006-6

Palma, V., Ruocco, C., Martino, M., Barba, D., Meloni, E. (2020) General catalyst-related issues, *In Current Trends and Future Developments on (Bio-) Membranes in Environmental Applications* (A. Iulianelli and A. Basile Eds), Elsevier, Amsterdam, Chapter 14.
DOI: doi.org/10.1016/B978-0-12-816778-6.00014-X

Palma, V., Goodall, R., Thompson, A., Ruocco, C., Renda S., Leach, R., Martino, M. (2021), Ceria-coated replicated aluminium sponges as catalysts

for the CO-water gas shift process, *Int. J. Hydrogen Energy*, **46**, 12158-12168.
DOI: doi.org/10.1016/j.ijhydene.2020.04.065

Palma, V., Gallucci, F., Pullumbi, P., Ruocco, C., Meloni, E., Martino, M. (2020) Pt/Re/CeO_2 Based Catalysts for CO-Water–Gas Shift Reaction: From Powders to Structured Catalyst, *Catalysts*, **10**, 564-580.
DOI: doi.org/10.3390/catal10050564

Palma, V., Ruocco, C., Cortese, M., Renda, S., Meloni, E., Festa, G., Martino, M. (2020) Platinum Based Catalysts in the Water Gas Shift Reaction: Recent Advances, *Metals*, **10**, 866-933.
DOI: doi.org/10.3390/met10070866

Palma, V., Cortese, M., Renda, S., Ruocco, C., Martino, M., Meloni, E. (2020) A Review about the Recent Advances in Selected NonThermal Plasma Assisted Solid–Gas Phase Chemical Processes, *Nanomaterials*, **10**, 1596-1652.
DOI: doi.org/10.3390/nano10081596

Palma, V., Ruocco, C., Cortese, M., Martino, M. (2020) Bioalcohol Reforming: An Overview of the Recent Advances for the Enhancement of Catalyst Stability, *Catalysts*, **10**, 665-735.
DOI: doi.org/10.3390/catal10060665

Palma, V., Ruocco, C., Cortese, M., Martino, M.(2020) Noble Metals-Based Catalysts for Hydrogen Production via Bioethanol Reforming in a Fluidized Bed Reactor, *Chemistry Proc.*, **2**, 1-5.
DOI: doi.org/10.3390/ECCS2020-07543

Megía, J. P., Cortese, M., Ruocco, C., Vizcaíno, A.J., Calles, J. A., Carrero, A., Palma, V. (2020) Catalytic Behavior of Co-Based Catalysts in the Kinetic Study of Acetic Acid Steam Reforming, *Ind. Eng. Chem. Res.*, 59, 19531-19538.
DOI: doi.org/10.1021/acs.iecr.0c03599

Cortese, M., Ruocco, C., Palma, V., Megía P.J., Carrero, A., Calles J.A: (2021) On the Support Effect and the Cr Promotion of Co Based Catalysts for the Acetic Acid Steam Reforming, *Catalysts*, 11, 133-149.
DOI: doi.org/10.3390/catal11010133

Pio, G., Ruocco, C., Palma, V., Salzano, E. (2021) Detailed kinetic mechanism for the hydrogen production via the oxidative reforming of ethanol, *Chem. Eng. Sci.*, 237, 116591.
DOI: doi.org/10.1016/j.ces.2021.116591

Martino, M., Ruocco, C., Meloni, M., Pullumbi, P., Palma, V. (2021) Main Hydrogen Production Processes: an Overview, *Catalysts*, 11, 547.
DOI:doi.org/10.3390/catal11050547

Summary

Index of Figures

Index of Tables

ABSTRACT

Hydrogen, widely regarded as the next generation fuel for transportation as well as stationary applications, can be produced from renewable sources. Bioethanol is a prosperous sustainable energy carrier mainly obtained via biomass fermentation and bioethanol reforming provides a promising method for hydrogen generation from renewables. Bioethanol (i.e. ethanol produced from biomass) mainly contains water and ethanol; however, different types of organic as well as inorganic impurities are present, which may have a significant effect on the reforming reaction and play a crucial rule on catalyst deactivation. In this regard, as impurities removal is a highly energetic demanding process, the use of crude bioethanol is of major importance for a cost effective industrial application of bioethanol reforming.

Ethanol steam reforming (ESR) is and endothermic reaction which, according to the thermodynamics, allows producing six hydrogen moles for every mole of converted ethanol. However, the reaction mechanism is very complex and the formation of various by-products (including coke) can reduce hydrogen selectivity. Under a thermal point of view, oxygen addition to the reacting system, due to contribution of oxidation reactions, can provide the heat necessary to carry out the reaction allowing, at the same time, an easier removal of carbonaceous species eventually deposited on catalyst surface. The role of the reactor configuration on the process efficiency is also crucial: fluidised bed reactors, due to the enhanced contact between gas and solid phases, can improve coke gasification; moreover, the excellent catalyst mixing helps avoiding hot or cold-spots phenomena, thus enhancing catalyst lifetime. In addition, the choice of fluidized bed membrane reactors can lead to a high degree of process intensification, assuring the selective separation of a reaction product (i.e. hydrogen) with a consequent increase of fuel conversion beyond the thermodynamic limitations as well as the direct product separation.

Several catalytic formulations have been investigated for ethanol reforming; however, the issue of catalyst durability (hundreds of hours of operation), especially in the case of raw bioethanol, was poorly investigated in the recent literature.

The main objective of this work is to develop highly active and stable catalytic formulations for the oxidative steam reforming of biomass-derived ethanol in a fluidized bed membrane reactor. A previously developed Pt-Ni/CeO_2-SiO_2 catalyst, tested in a fixed bed mode, was the starting point of this research activity. The bimetallic catalyst was tested in a fluidized bed

reactor at 500°C and a preliminary screening was performed in the presence of a simulated bioethanol stream (i.e. pure water and ethanol). Its performance were compared with several catalytic formulations, developed in the attempt of improving the stability and reducing the carbon formation rate of the first generation catalyst. In this regard, alkali metals were added and Ni was substituted by Co obtaining, however, a worse activity and stability compared to the Pt-Ni/CeO_2-SiO_2 catalyst. Thus, for the latter sample, the influence of cerium salt precursor (nitrate, ammonium nitrate and acetylacetonate) on catalyst durability was investigated, finding that the organic salt can assure a better active species dispersion and a consequent improvement of sample stability.

The influence of the water/ethanol ratio, oxygen/ethanol ratio and temperature on the activity and stability of the 3Pt-10Ni/CeO_2-SiO_2 catalyst prepared from acetylacetonate was studied in order to select the operative conditions minimising carbon formation rate (i.e. 4, 0.5 and 500°C, respectively), which were fixed for the further tests.

In view of mitigating the costs of the final catalyst, the chance of reducing Pt loading as well as substituting platinum by cheaper metals (i.e. silver or ruthenium) was also investigated. Silver substitution was detrimental in terms of catalyst activity while ruthenium appeared a promising metal for oxidative steam reforming of ethanol. The highest activity was recorded over the 0.5Pt-10Ni/CeO_2-SiO_2 and 0.5Ru-10Ni/CeO_2-SiO_2 catalysts which, together with the monometallic Ni/CeO_2-SiO_2 sample, were selected for the development of a kinetic model able to predict the products gas distribution as a function of reaction temperature. The model involves four reactions (ethanol decomposition, methane oxidation, methane steam reforming, water gas shift) and assures a fairly good agreement with experimental data.

However, looking at the stability performance of the catalysts prepared at different loadings of the noble metals, it was clear that a content of 2 wt% was required to minimize the carbon formation rate for both the Pt and Ru series; in addition, the highest durability was recorded over the 2Pt-10Ni/CeO_2-SiO_2, which was selected for the tests under fuel grade bioethanol, provided by Eldor corporation S.p.a.

The sample was tested for several hours at 500°C, H_2O/C_2H_5OH ratio of 4 and O_2/C_2H_5OH ratio of 0.5; the contact time was fixed to 250 ms and two kinds of experiments were performed: catalyst alone and catalyst mixed with the bare CeO_2-SiO_2 in a volumetric ratio of 1 to 4. The results demonstrated that the presence of the filler is detrimental in terms of stability, due to its higher acidity compared to the final catalyst. On the contrary, the 2Pt-10Ni catalyst assured complete conversion and a stable hydrogen yield (around 45%) for more than 200 hours; thereafter, a gradual deactivation was observed. However, after 450 hours, a new stationary condition was reached, with no more activity loss observed for further 50 hours. The carbon formation rate measured at the end of the test is considerably lower than the values reported over other catalysts; anyway, to the best of our knowledge, no tests performed under raw bioethanol in a fluidized bed reactor for more than 200 hours are available in the literature, which helps to conclude that the 2Pt-10Ni/CeO_2-SiO_2 catalyst is a very promising candidate for oxidative reforming of commercial Fuel grade bioethanol.

Finally, the formulation developed in this work was preliminary tested in a fluidized bed catalytic integrated membrane reactor (in collaboration with TUe University of Eindhoven), working in the Oxidative ESR reaction, finding an hydrogen recovery factor of 35% at 500°C and 4 bar, which is similar or higher than the values reported by other authors applying the same pressure difference (almost 400 kPa).

INTRODUCTION

The search for clean technology approaches able to assure safe and sustainable energy production is increasingly gaining ground due to the heavy impacts of fossil fuels on the world economy (oil price fluctuation), on the global warming and on the human health. An effective solution proposed to reduce the consumption of conventional feedstocks involves the use of hydrogen as an energetic vector, which leads to no or very low carbon emissions, thus limiting the release of atmospheric pollutants. Nowadays, steam reforming of natural gas is the most widespread technology for hydrogen production and applying the same technology to new-generation (biomass-derived) fuels could offer significant advantages under both an energetic and an environmental point of view. Biomass is abundantly available in different forms. Moreover, the use of biomass for energy generation results in a neutral carbon balance; only trace amounts of sulphur and heavy metals are present in biomass compared to fossil fuels, thus limiting the formation of harmful substances. Among the available fuels produced from biomass, bioalcohols are emerging as competitive sources for hydrogen production via reforming. Bioalcohols (i.e., alcohols generated from biomass or biological routes) can be produced from different feedstocks, including crops, agricultural as well as forestry wastes, and food wastes: for example, bioethanol is mainly obtained via fermentation of sugar cane or starches.

Bioethanol conversion to hydrogen can follow different routes, including catalytic steam reforming and oxidative steam reforming. According to the stoichiometry of the reaction, steam reforming gives the highest hydrogen yields. However, several side reactions may occur during reforming which, besides affecting the H_2 selectivity, may also be responsible for carbon formation and catalyst deactivation. In this regard, the addition of oxygen via the oxidative process has been investigated as a viable route to mitigate carbon deposition. The main pathways favouring coke formation during reforming include the Boudouard reaction, decomposition of carbon-containing intermediates (i.e., CH_4), dehydration, and subsequent polymerization reactions. The same intermediates participating in the main reactions, in fact, may also be involved in coking pathways, while the contribution of side reactions depends on the operating conditions and the nature of both the active metal and the selected support. Due to the complexity of the reaction systems, most of the studies focused on ethanol reforming have been carried out under simulated feedings (pure ethanol and water); in fact, the impurities found in crude bioethanol mixtures can act as coke precursors, leading to a more pronounced carbon formation. Thus, the proper selection of the catalytic formulation is crucial to achieve the desired

H_2 yield during bioethanol reforming. In addition, the reactor configuration was shown to affect the coke selectivity of the catalyst, with fluidized bed reactors facilitating the separation of coke from catalytic particles and promoting the oxidation of carbonaceous deposits.

The integration of the reactor with H_2-selective (specifically palladium-based) membranes can help in modulating by-products formation: hydrogen separation may shift the product distribution in the desired direction, (i.e., toward the reactions that mainly produce hydrogen).

Chapter I

I H_2 production and ethanol reforming

I.1 Hydrogen as a clean energy source

The growth in global population, industrialization and urbanization is the direct cause of fossil fuels depletion and environmental deterioration. In the 2017, 81% of total primary energy supply and 66% of electricity production came from coal, natural gas and oil utilization (Baykara, 2018), with a heavy increase of CO_2 emissions (of almost 2 ppm·year^{-1} (Asumadu-Sarkodie and Owusu, 2016)): in the past 10 years, the energy sector has been the primary source of GHG emissions (Gao et al., 2018). However, besides the environmental concerns, based on the actual consumption rates, world's proven coal, oil and natural gas reserves are expected to run out quickly (within approximately 200, 40 and 60 years, respectively). As a result, the interest towards the employment of H_2 as a clean energy carrier is increasing more and more: the high versatility, efficiency and sustainability of hydrogen makes this source a potential substitute of fossil fuels in the long term both for stationary applications and for the mobility (Guandalini et al., 2016).

Hydrogen, although being the lightest element in the nature, has the highest energy content for unit mass among all the fuels. In fact, the main advantage of H_2 as fuel is related to its high net calorific value compared to other fuels (Table I. 1 (Łukajtis et al., 2018)). For example, one kilogram of H_2 is equivalent to 2.75 kg of gasoline and 6 kg of methanol with respect to its net calorific value. Moreover, the high efficiency of H_2 makes this fuel competitive with other renewable energy systems, including solar and wind energies.

In an energetic framework, hydrogen can produce electricity using fuel cells, which have virtually no pollutant emissions and only generate water as by-product (Khetkorn et al., 2017).

Hydrogen is scarce on Earth's surface (0.14%) and it is found only in trace amounts (0.07%) in the atmosphere. Thus, in order to produce hydrogen, it is necessary to convert chemical compounds in which H_2 is present. In the following paragraph, the main technologies for hydrogen production are described and compared.

Table I. 1 *Properties of various fuels (Łukajtis et al., 2018).*

Fuel	**Relative amount needed to match H_2 weight composition (Heat of combustion·(heat of combustion of H_2)$^{-1}$)**	**Hydrogen density in fuel (g·dm^{-3})**	**Net calorific value (kJ·g^{-1})**
Hydrogen	1	70.5	120.0
Methane	2.4	104.1	50.0
Methanol	6.0	113.7	20.1
Ethanol	4.4	104.1	26.8
Gasoline	2.7	112.1	46.7

I.2 Hydrogen production methods

The available methods for hydrogen production are based on the conversion of both fossil fuels and renewable sources. The processes of steam reforming, partial oxidation, auto thermal reforming and gasification mainly involve the usage of fossil materials while, in the field of sustainable sources, biomass gasification/pyrolysis and water splitting offer a cleaner route for hydrogen generation (Abdalla et al., 2018). The technologies based on fossil fuels usage involve commercialized methods able to assure high efficiency (ranging from 70 to 85% in the case of methane steam reforming and from 60 to 75% for partial oxidation) and low production costs. Coal gasification is another well-established technology, capable of producing up to 97% of pure hydrogen.

Hydrogen production via pyrolysis/gasification of biomass is based on a process similar to coal gasification; however, due to the lower calorific value of biomass compared to coal, larger size plants are required (Ibrahim et al., 2014). H_2 can be released from water via electrolysis, direct thermal decomposition or thermolysis, thermochemical processes and photolysis. For example, water electrolysis is a well-developed technology, which exploits electricity from the grid and assures efficiencies ranging from 70 to 90%

(Baykara, 2018); however, it suffers from the considerable electricity costs (Jha et al., 2017).

Among the sustainable technologies for H_2 production, biomass conversion is one of the most relevant route. Various biomass materials (including energy crops, agricultural residues and waste, forestry waste, industrial and community waste (Demirbaş, 2001)) can be used as hydrogen source. The technologies based on biomass conversion involves thermochemical and biological methods, which can allow the production of solid, liquid and gaseous fuels (H_2-rich). Thermochemical processes involve combustion, pyrolysis and gasification. The main challenges for biomass gasification (abovementioned) is related to the low thermal efficiency due to the moisture content. In fact, the gasification process can only be used for biomass with moisture content less than 35% (Demirbaş, 2002). The gasification may also be accompanied by the formation of tar aerosols and ash (Arvelakis and Koukios, 2002). Biological processes involve biophotolysis, photo-fermentation and dark fermentation (Levin et al., 2004). All the biological processes are well controlled though H_2 producing enzymes (i.e. hydrogenase and nitrogenase). The dark fermentation has several advantages compared to other biological methods, which includes high H_2 flow-rates, simplicity of the technique, low energy input and use of low-values materials as feedstock (Ni et al., 2006). Table I. 2 compares the main technologies for H_2 production in terms of process efficiency and advancement of technology.

Table I. 2 *Efficiency and advancement of the main technologies for H_2 production (Abdalla et al., 2018).*

Process	**Efficiency (%)**	**Maturity**
Steam reforming	70-85	Commercial
Partial oxidation	60-75	Commercial
Auto thermal reforming	60-75	Near-Term
Biomass pyrolysis	35-50	No data
Biomass gasification	35-50	Commercial
Biophotolysis	0.5	Long-term
Dark fermentation	60-80	Long-term
Photo-fermentation	0.1	Long-term
Photo-electrolysis	0.06	No data

Of special interest are also the methods in which biomass is converted to intermediate liquid biofuels which, thanks to their high energy density and the ease of handling, can be used as petrol and diesel substitutes in internal combustion engines (thus overcoming the energy vulnerability in the transportation sector (Lee et al., 2017)) as well as for the on-demand production of H_2 in fuel cells devices (Fatsikostas et al., 2002). In the latter case, the implementation of a relatively mature technology such as reforming on non-fossil substrates offers a ready opportunity to produce H_2 from renewables. In particular, among the various alcoholic feedstocks, bioethanol is used extensively as an efficient source of hydrogen due to its high H/C ratio, low volatility and toxicity, high safety and easy handling (Saidi and Jahangiri, 2018).

In the following sections, a brief description of the bioethanol production, the main technologies for H_2 production form bioethanol and the fuel cells operation will be reported.

I.3 Bioethanol production and properties

Bioethanol is the most popular alcoholic biofuel and can be produced from various renewable sources rich in carbohydrates. In fact, the sources used for bioethanol production include sugars, starch, lignocellulosic biomass and algae. When sugars and starch are used as feedstock, the corresponding bioethanol is referred as first generation bioethanol, while lignocellulosic biomass and algae produce second and third generation bioethanol, respectively. The process involving the conversion of algae to bioethanol is still in an immature stage and confined to the laboratory research (Zabed et al., 2017), while other types of biomass have shown potential as bioethanol feedstocks on commercial scale. For the first and second generation case, based on the feedstock, the bioethanol production processes differ significantly. In fact, sugar based raw materials require only an extraction process to get fermentable sugars, while starchy crops need to undergo hydrolysis to convert starch into glucose. On the other hand, lignocellulosic biomass has to be pre-treated before hydrolysis in order to alter cellulose structures for enzyme accessibility.

Figure I. 1 provides a schematic representation of the main steps involved in bioethanol production, based on the available raw material. Once the biomass reaches the ethanol plant, it is stored in a warehouse where it is conditioned to prevent early fermentation and bacterial contamination. Through the pre-treatment, carbohydrates are extracted or made more accessible to the further extraction. The hydrolysate, yeasts, nutrients and other ingredients are added to the fermentation at the beginning of the operation. The fermentation reactions occur at temperatures between 25 °C and 30 °C and last between 6 h and 72 h depending on the composition of the hydrolysate, physiological activity and yeast species (Vohra et al., 2014). The broth typically contains 8–14% of ethanol on a volume basis. Above this latter concentration, inhibition of yeasts may occur that reduces their activity. The distillation step yields an azeotropic mixture made up of 95.5% alcohol and 4.5% water that is the ‘‘hydrous’’ or ‘‘hydrated’’ ethanol which is then dehydrated to obtain an ‘‘anhydrous’’ ethanol containing up to 99.6% alcohol and 0.4% water (Pandey, 2008). The oil, protein and fibres in the

raw material are recovered after fermentation as animal feed (DDGS) while corn gluten meal (CGM) and corn gluten feed (CGF) have a value for food.
Currently, sugarcane and corn together produce almost all the bioethanol on the commercial scale. However, these two feedstocks are not enough to meet the rising demand of the bioethanol as well as replace huge amounts of conventional fuels currently consumed. For this reason, recent research efforts have focused on the searching for potential ethanol sources, with a particular attention on the lignocellulosic biomass, interesting because of being based on non-food crops.
Bioethanol is an aqueous diluted solution containing 12–15 wt% of ethanol and some by-products depending upon the raw material used (Wang and Wang, 2010). Lignocellulosic ethanol generally contains higher concentrations and a great variety of organic compounds (especially methanol, acetaldehyde and acetic acid) compared to sugar- or starch-derived bioethanol (Habe et al., 2013). Only organosulfur compounds were found in bioethanol produced from sugar and starch while furan-related compounds were detected for bioethanol mixtures produced form lignocellulose. Catalyst deactivation by impurities can be a serious problem in the direct use of bioethanol for hydrogen production (i.e. reforming technology) and it is necessary to take into account their effect on catalytic properties.

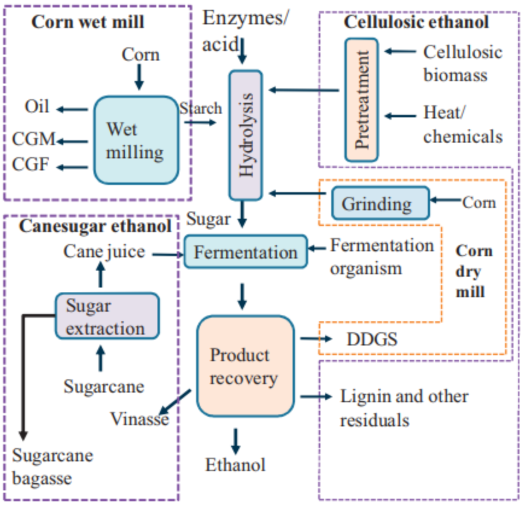

Figure I. 1 *Schematic representation of ethanol production from different raw-materials (Wyman, 2004).*

I.3.1 H_2 production from bioethanol

Hydrogen may be generated from ethanol by different technologies, including steam reforming (SR), partial oxidation (POX) and oxidative steam reforming (OSR). Steam reforming of ethanol (ESR) is one of the most attractive way of hydrogen production form biomass (Sarkar et al., 2012, Gac et al., 2018). In fact, it avoids the high costs required for feedstock dehydration (estimated at 50% of the total product cost), which are necessary when bioethanol is valorised as a fuel (dehydrated ethanol)(Montero et al., 2018). Ethanol can produce 6 moles of H_2 (in spite of the 3 moles of methane) by reacting with steam (eq. (I. 1)). However, the reaction system turns to be more complicated due to the C-C in the ethanol and the endothermic properties of the reaction. In fact, ESR comprises a series of step that involve multiple reactions and is often accompanied by parallel side reactions, which may produce undesirable products, including CO, acetaldehyde, methane, ethylene and coke (Li et al., 2018).

As a result, coke formation and catalyst stability is one of the main issues in the production of hydrogen from steam reforming of bioethanol (Zhang et al., 2006). Moreover, the by-products obtained during the reaction can be responsible for decreased H_2 yield, through reactions such as methanation of CO and CO_2. In particular, high-temperature ESR shifts the equilibrium of the WGS reaction toward the formation of CO, requiring further costly purification steps to remove this by-product in order to obtain fuel-cell-grade H_2. In fact, the remaining concentrations of CO (although being low) may poison the fuel cell catalyst.

Thus, many researchers hope to efficiently reform ethanol at lower temperatures, and ESR has been carried out at relatively low temperatures (in the range of 300-400 °C) in some studies (Lee et al., 2012). Ethanol may decompose to H_2, CH_4, and CO (eq. (I. 2)), and, instead of methane steam reforming (eq.(I. 3)), the CO-WGS reaction (eq.(I. 4)) is more favoured in the above temperature range, contributing to the production of H_2 (Palma et al., 2015a). As an example, Figure I. 2 shows the reaction mechanism of ethanol steam reforming over a Ni-based catalyst between 300 and 700°C. This scheme includes ethanol decomposition (eq. (I. 2)), dehydrogenation to acetaldehyde (eq. (I. 5)) followed by its decomposition to CO and CH_4, together with the subsequent reactions of products decomposition (WGS reaction and CH_4 reforming (MSR)/methanation (eq. (I. 3)))(de Lima et al., 2010); dehydration to ethylene (eq. (I. 6)) and its subsequent polymerization to coke (eq. (I. 7)) may also occur. The relative weight of each individual reaction changes with temperature: at high temperatures, direct reforming is favoured and the equilibriums of the WGS and methanation reactions are inverted. The scheme also involve the possible pathways of coke formation: from intermediate compounds (acetaldehyde, acetone and ethylene), whose concentration in the reaction medium is only significant at 300 °C, which generate the encapsulating coke responsible for the fast deactivation observed at this temperature; from ethanol, due to the capacity of ethanol molecules (adsorbed as ethoxy ions) to yield encapsulated coke by means of condensation and dehydration (eq. (I. 6)) mechanisms (Tripodi et al., 2016);

by CH_4 decomposition (Muroyama et al., 2010) (eq. (I. 8)), which also generates filamentous coke; from CO, by Boudouard reaction (Ni et al., 2007) (eq.(I. 9)), which generates filamentous coke. In particular, the increase in the reaction temperature favours the routes of filamentous coke formation and its condensation (Vicente et al., 2014a).

Thus, the efficiency of this complicated process depends on various parameters like process conditions, catalyst choice and reactor configuration (Dehkordi et al., 2016, Sun et al., 2018).

ESR is a highly endothermic reaction, requiring large amount of energy, which becomes a serious drawback in terms of cost and practicality of hydrogen production, especially for on-board applications. Partial oxidation (POX) (eq. (I. 10)) is exothermic and fast, making it suitable for coping with rapid load variations, such as those required for on-board reformers. However, H_2 yield is much lower than that from SR and POX can be characterized by difficulties in thermal management, due to hot-spot formation (Palma et al., 2017b). Oxidative steam reforming of ethanol (eq. (I. 11)), which combines SR and POX, is a reasonable compromise between energy efficiency increasing and hydrogen productivity lowering (de Lima et al., 2008). In fact, by properly selecting the composition of the mixture of ethanol, water, and oxygen, the exothermic partial oxidation can provide the heat necessary for the endothermic steam reforming. Moreover, the presence of oxygen in the reaction mixture also promotes the efficient removal of carbon species formed during the course of reaction. However, oxygen co-feeding can make the reaction pathway more complex, due to the evolution of other (oxidation) reactions (eq. (I. 10)-(I. 14)))(Mondal et al., 2015a), which are expected to reduce H_2 yield. In this respect, the choice of highly selective catalyst is crucial to achieve the desired performance. Moreover, despite the less favoured coke formation during oxidative steam reforming, the catalyst stability still remains an open issue for practical applications during oxidative steam reforming of ethanol (Cai et al., 2008).

$$C_2H_5OH + 2H_2O \leftrightarrow 2CO_2 + 6H_2O \quad \Delta H^{\circ}_{298K} = 173.2 kJ \cdot mol^{-1} \tag{I. 1}$$

$$C_2H_5OH \leftrightarrow H_2 + CO + CH_4 \; \Delta H^{\circ}_{298K} = 49 kJ \cdot mol^{-1} \tag{I. 2}$$

$$CH_4 + 2H_2O \leftrightarrow 4H_2 + CO_2 \; \Delta H^{\circ}_{298K} = 165 kJ \cdot mol^{-1} \tag{I. 3}$$

$$CO + H_2O \leftrightarrow H_2 + CO_2 \; \Delta H^{\circ}_{298K} = -41 kJ \cdot mol^{-1} \tag{I. 4}$$

$$C_2H_5OH \leftrightarrow H_2 + C_2H_4O \; \Delta H^{\circ}_{298K} = 68 kJ \cdot mol^{-1} \tag{I. 5}$$

$$C_2H_5OH \leftrightarrow H_2O + C_2H_4 \; \Delta H^{\circ}_{298K} = 45 kJ \cdot mol^{-1} \tag{I. 6}$$

$$C_2H_4 \rightarrow polymers \rightarrow coke \tag{I. 7}$$

$$CH_4 \rightarrow C_{(s)} + 2H_2 \; \Delta H^{\circ}_{298K} = 75kJ \cdot mol^{-1} \tag{I. 8}$$

$$2CO \rightarrow C_{(s)} + CO_2 \; \Delta H^{\circ}_{298K} = -171kJ \cdot mol^{-1} \tag{I. 9}$$

$$C_2H_5OH + 0.5O_2 \rightarrow 2CO_2 + 3H_2 \quad \Delta H^{\circ}_{298K} = -554kJ \cdot mol^{-1} \tag{I. 10}$$

$$C_2H_5OH + 2H_2O + 0.5O_2 \rightarrow 2CO_2 + 5H_2 \quad \Delta H^{\circ}_{298K} = 4.4kJ \cdot mol^{-1} \tag{I. 11}$$

$$H_2 + 0.5O_2 \rightarrow H_2O \; \Delta H^{\circ}_{298K} = 241.8kJ \cdot mol^{-1} \tag{I. 12}$$

$$CO + 0.5O_2 \rightarrow CO_2 \; \Delta H^{\circ}_{298K} = -283kJ \cdot mol^{-1} \tag{I. 13}$$

$$CH_4 + 2O_2 \rightarrow CO_2 + H_2O \quad \Delta H^{\circ}_{298K} = -802.2kJ \cdot mol^{-1} \tag{I. 14}$$

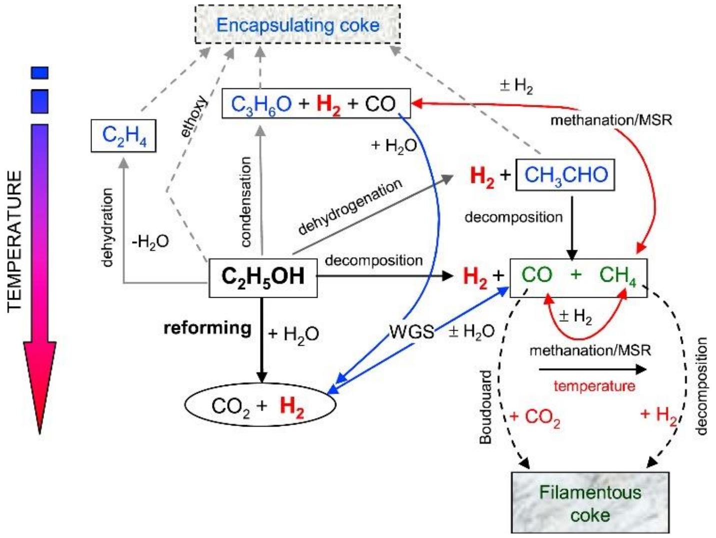

Figure I. 2 *Kinetic scheme for ethanol steam reforming over a Ni-based catalyst in the temperature interval 300-700°C (Vicente et al., 2014a).*

Due to the already complicated reaction mechanism during ethanol reforming, only few studies carried out in the presence of raw bioethanol mixtures (whose impurities may interfere in the reaction pathway) are available in the recent literature (Iulianelli et al., 2016a, Rass-Hansen et al., 2008, Bilal and Jackson, 2017).

I.4 Hydrogen conversion in fuel cells

Hydrogen can be converted to electrical energy by means of a fluid cell device. Using pure hydrogen, fuel cells only produces water, thus eliminating all the emissions otherwise caused by electricity production. Fuel cells, in fact, are regarded as low carbon technologies because of their high efficiency, low noise and clean operation. The produced electricity can be used for power requirements that range from driving cars to heating houses.

The basic structure of all fuel cells is similar: the cell consists of two electrodes which are separated by the electrolyte and connected in an external circuit. In the case of fuel cells with a proton conducting electrolyte (PEMFC, proton exchange membrane fuel cell), H_2 is oxidized at the anode ($H_2 \rightarrow 2H^+ + 2e^-$) while protons enter the electrolyte and are transported to the cathode; at the cathode, the supplied oxygen reacts ($O_2 + 4e^- \rightarrow 2O^{2-}$). Electrons flow in the external circuit during these reactions and the oxygen ions recombine with protons to form water ($O_2 + 2H^+ \rightarrow H_2O$). A schematic representation of fuel cell operation is reported in Figure I. 3.

Fuel cells are usually classified based on the electrolyte employed in the cell. Moreover, they are divided in low- and high-temperature fuel cells. The PEMFC fed by H_2 operates between 60 and 80°C, assuring a mean theoretical electrical efficiency of 83% (Badwal et al., 2014). Together with the alkaline fuel cells (AFC), operating in the range 90-100°C, the PEMFC are quite popular.

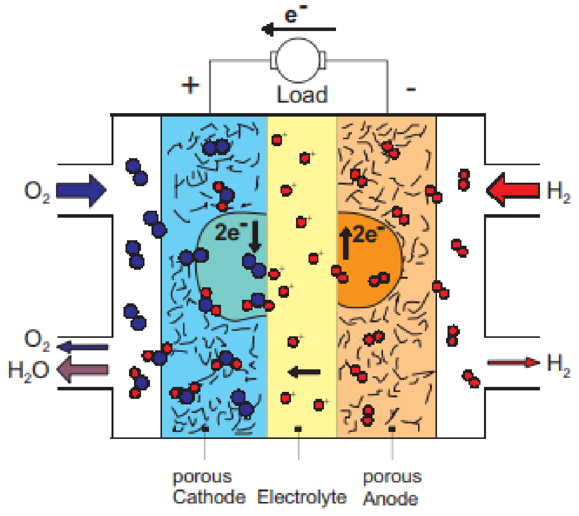

Figure I. 3 *H_2/O_2 fuel cell with a proton exchange membrane (Carrette et al., 2001).*

On the other hand, solid oxide fuel cells, which use ceramic materials as electrolytes, can be employed at temperatures between 700 and 1000°C (Ejikeme et al., 2016). The above fuel cells also differ for the catalytic material employed for anode and cathode layers.

Fuel cells can produce a wide range of power from 1 to 10 MW. Generally higher output power can be achieved at higher operative temperatures. PEMFC and AFC assure comparable high electrical efficiency while the highest performance in combined Heat & Power unit are assured by solid oxide fuel cells (Mekhilef et al., 2012).

Nowadays, the two greatest barriers for fuel cell technology to take off are related to the issue of durability and cost (Colpan et al., 2018). Hence, the main research topic for fuel cells is finding new materials, designs, and manufacturing techniques to decrease their cost and increase their durability while not causing any performance losses.

I.5 Bioethanol reforming: main parameters affecting the process efficiency

I.5.1 Effect of the operative conditions

Ethanol reforming is a reaction which proceed with increasing moles number; thus, the reaction is favoured at low pressures. Hence, the majority of the ethanol reforming studies are carried at ambient pressure (Md Zin et al., 2015, Llorca et al., 2002, Peela and Kunzru, 2011, Mondal et al., 2015a). Therefore, the reaction conditions affecting process efficiency are temperature, feeding conditions and space velocity. According to thermodynamic predictions, an increase in temperature leads to a growth in the H_2 and CO concentrations, with a decrease in CH_4 yield at equilibrium (Wenju and Q., 2008). According to these predictions, the beneficial effect of an increase in the reaction temperature on H_2 production during ethanol reforming was reported for several catalytic systems (Wu and Williams, 2012, Yang et al., 2006, Fierro et al., 2005, Greluk et al., 2016a). Moreover, the most favourable conditions for coke formation and catalyst deactivation are at lower temperatures, where the reactions rates leading to coke formation are much higher than those of carbon gasification reactions (Coll et al., 2001, Palma et al., 2017c). Similarly, by increasing the water to ethanol ratio, improved H_2 yield were observed, according to thermodynamics which predicts a promotion of steam reforming and water gas shift reactions (Palma et al., 2016). Moreover, water/ethanol ratios higher than the stoichiometric value of 3 can minimize carbon formation rate due to the grown extent of coke gasification reactions. In fact, as previously observed (Comas et al., 2004, Fishtik et al., 2000, Srivastava and Pant, 2013), under both steam and oxidative steam reforming conditions, the increase of water/ethanol ratio may be beneficial for reforming reactions, resulting in a visible gain in terms of H_2 selectivity, and for the suppression of carbonaceous deposits on catalyst surface. On the other hand, for higher oxygen contents in the reacting mixture, the majority of the authors observed a worsening in terms of hydrogen production, due to the promotion of oxidation reactions (Mondal et al., 2015a, Cih-Ying and Jeng-Han, 2013).

Concerning the effect of contact time, it was observed that a lower space velocity tends to increase selectivity of H_2 and CO_2, and decrease the selectivity of undesired gases such as CO and CH_4. This is because of ethanol decomposition which is more favoured than steam reforming reaction at lower contact time (Sahoo et al., 2007). In addition, by increasing the total flow-rate with respect to the catalytic volume, a negative impact in terms of carbon formation rate has also been reported (Palma et al., 2016): an increase in the contact time, in fact, can slow down the coke gasification reactions, which, being heterogeneous, are intrinsically less fast than the reactions in gaseous phase.

Even if high temperatures and high steam to ethanol ratios promote the formation of hydrogen, they can negatively affect system efficiency due to the higher heat losses and materials as well as operative costs. Similarly, lower contact time can assure a reduced catalytic volume, but the negative effect on the catalytic performance in terms of both selectivity and stability are not negligible.

As a result, the low-temperature ethanol reforming appears a promising alternative to improve the thermal efficiency of the process, keeping low the plant costs. On the other hand, a satisfactory performance in terms of hydrogen production and catalyst resistance towards deactivation was recorded under stoichiometric feed conditions or slightly higher (Hou et al., 2015a, Palma et al., 2013, Hou et al., 2015b).

I.5.2 Effect of the catalyst choice

In the past few years, plenty of research has been focused on developing highly efficient catalysts for ethanol reforming including Pt, Rh, Ru, Co, Ni, Cu and Fe-based catalysts (Wu et al., 2017, Bilal and Jackson, 2017, Pinton et al., 2017, Chen et al., 2010, Han et al., 2016). The use of noble metals assures a good catalytic performance with high selectivity to hydrogen and a limited amount of carbonaceous deposits on catalyst surface. However, their high price and poor availability moves towards the use of cheaper alternatives, especially nickel, but also cobalt. Ni-based catalysts are recognized as good candidates due to their low cost, wide availability and high activity towards C-C and C-H bond breaking (Gong et al., 2010). As a result, the formation of H_2 is facilitated. However, the main challenges related to the employment of Ni catalysts for ethanol reforming are linked to their poor stability caused by carbon deposition and/or aggregation of Ni particles. Co catalysts are also attractive materials for ethanol reforming, displaying high ethanol conversion in the low-temperature range (350-550°C) due to the cobalt capacity in promoting C-C, C-H and O-H bond cleavage (Tuti and Pepe, 2008). However, also Co catalysts suffer for a faster deactivation compared to noble metals based catalysts; in particular, the deactivation rate of Ni as well as Co-based catalysts was related to the dimension of the particle sizes: smaller Co and Ni particles assured a significantly less carbon deposition (Song et al., 2012, Palma et al., 2017d).

Bimetallic catalysts have also attracted the research interest for ethanol reforming, with the aim of creating a synergy of positive effects of the two metals (Zhao and Lu, 2016). In some cases, bimetallic formulations were developed by adding small amounts of noble metals to the monometallic sample, in order to improve the performance of the final catalyst without having a strong effect on the catalyst price (Palma et al., 2015b, Kugai et al., 2006). It was also shown that adding promoters to Ni-based catalysts is an effective method to prevent carbon deposition. In fact, alkali metals (K, Cs, Na, Mg, Ca), being electron donators, display excess mobile electrons, which enhances catalyst reducibility, thus improving the gasification of the coke deposited on catalyst surface (Palma et al., 2017c, Carrero et al., 2010).

The key role of support in determining the activity, selectivity and stability of the final formulation was also described in depth. Acidic solids like Al_2O_3 are rarely used alone for ethanol reforming, due to the favoured pathways of ethylene dehydration, which is a well-known coke precursor (Fatsikostas and Verykios, 2004). Conversely, the addition of basic oxides (MgO, CaO) was beneficial to assure higher resistance towards deactivation, due to their capability of generating more oxygenated compounds (Freni et al., 2003). On the other hand, rare earth based oxides like CeO_2 assure enhanced thermal stability to the metallic phases and are characterized by high oxygen storage capacity and high oxygen mobility, which assures considerable activity towards the water gas shift reaction and the oxidation of coke precursors (Contreras et al., 2014, Muñoz et al., 2016).

I.5.3 Effect of the reactor type

The ethanol reforming reaction has been widely studied in traditional reactors (i.e. packed beds, PBR), as reported in the literature (Nieto-Márquez et al., 2013, Weng et al., 2017, Ma et al., 2016). However, in a process intensification view, the choice of fluidized reactors (FBR) helps to overcome typical drawbacks of fixed bed systems, particularly relevant at an industrial scale: low mass and heat transfer rates, non-optimized gas-solid contact, cold or hot spots, diffusion resistance, catalyst sintering, reactor plugging and catalyst deactivation due to coke formation (Barbarias et al., 2016, Leal et al., 2016, Shi et al., 2013). Concerning reforming processes, one of the main advantages of fluidized beds lies in the easy separation of external filamentous coke from catalyst surface, which minimizes pore blocking and extends catalyst lifetime. Therefore, activity losses are not expected because regeneration take place simultaneously with the reaction. In addition, an easier temperature control (absence of radial and axial temperature gradients) can be achieved, thus improving the global heat management (Psara et al., 2015, García-Lario et al., 2015). It is also interesting to observe that, in a FB reactor, catalysts, also during oxidative reforming operations, maintain a high reducibility level that enhances reactants conversion (Jing et al., 2009). Moreover, in view of industrial applications, the fluidized bed reactor assures an easier plant scale-up because of its ability to work with catalyst circulation in a reactor-regenerator system. However, the chosen catalytic support has to display good mechanical properties: in particular, a proper resistance to attrition is required, which is critical for catalyst use in a fluidized bed reactor.

When a fixed bed is employed, the pressure drops through the bed increase linearly with the gas velocity until balancing with the weight of the particles. The velocity corresponding to this balance is denoted as minimum fluidization velocity (u_{mf} and the corresponding height of the catalytic bed is indicated as H_{mf}). Once reached the bubbling regime, the pressure drops remain unchanged, independently from the gas velocity. Only if the gas velocity is above the terminal velocity of the particles (u_t), pressure drops decrease with the gas velocity and the pneumatic transport occurs (Yang, 2003).

In a fluidized bed, the required fluidization regime can be set by properly selecting the gas velocity. In the case of the fixed bed, gas velocity is low and the bed is static. When the fluidization starts (Figure I. 4), the minimum fluidization regime is achieved. When the gas velocity exceeds u_{mf}, fluidization regime is achieved, thus generating instability in the flow. If the gas velocity is greater than the terminal velocity, the regime is called pneumatic transport and the circulating fluidized bed condition is reached.

The behaviour of particles in a fluidized bed depends on the particles properties (size and density). Geldart classified the particles behaviour during fluidization into four groups (Geldart, 1973) (Figure I. 5), as follows:

- Group A: Small particles (30–150 µm), and low density (<1.4 $g\cdot cm^{-3}$). The fluidization is easy, smooth and homogeneous. It makes possible operating with low gas flows and controlling the growth and the speed of the bubbles.
- Group B: Particles with medium diameter (40–500 µm) and density between 1.4 and 4 $g\cdot cm^{-3}$. The fluidization is good for high gas flow rates. The bubbles tend to grow a lot and appear at the beginning of fluidization ($u_{mf} \approx u_{mb}$ that is the mean bubble velocity).
- Group C: Very small particles (d < 30 µm). Fluidization is difficult.
- Group D: Dense and large particles (d > 500 µm). Fluidization is difficult and non-uniform, ideal for spouted beds.

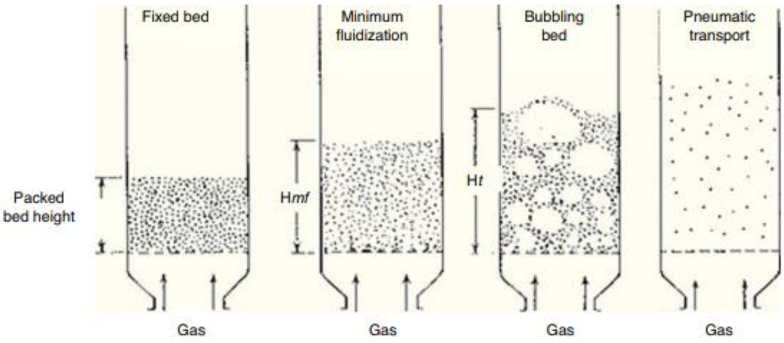

Figure I. 4 *Hydrodynamic behaviour of fluidized beds (Kunii and Levenspiel, 2013) (H_{mf} is the height corresponding to the minimum fluidization velocity while H_t is the height corresponding to the terminal velocity).*

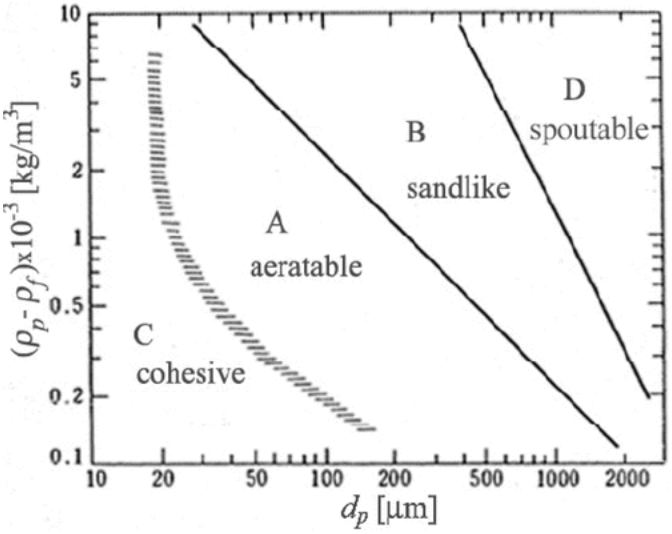

Figure I. 5 *Powder classification diagram for fluidization by air (de Vasconcelos and Mesquita, 2011).*

I.5.4 Effect of the choice of the H_2 separation system

One of the main disadvantages of conventional reforming reactors is that the reactions are equilibrium limited (even when completed ethanol conversion is observed), thus yielding an H_2-rich stream also containing carbon oxides and other by-products. Therefore, in order to produce pure hydrogen, the reforming process involves other reaction units (Figure I. 6, high HT and LT low temperature water gas shift reactors) followed by separation units (mostly pressure swing adsorption) (de Nooijer et al., 2018). However, this configuration decreases the system efficiency and makes scale-down uneconomical. Conversely, by combining reaction and separation in the same unit, an high degree of process intensification can be reached: higher conversions at the same temperatures or the same conversion at lower temperatures compared with conventional packed bed reactors are observed, due to the shift of equilibrium driven by the Le Chatelier's principle (Lee et al., 2016). By operating at milder temperatures with respect to those conventionally selected for reforming process, the costs of materials can be reduced and all these advantages make more attracting the hydrogen production on a smaller scale.

Thus, the application of membrane reactors (schematized in Figure I. 7) in the reforming process has recently drawn particular attention. The choice of palladium-based membranes (inorganic membranes in which H_2 permeates selectively from the feed/retentate to the permeate side) assures high efficiency and high purity in terms of the produced hydrogen, thus making its application particularly suitable for integrated PEM fuels cells in domestic units (Jian et al., 2015).

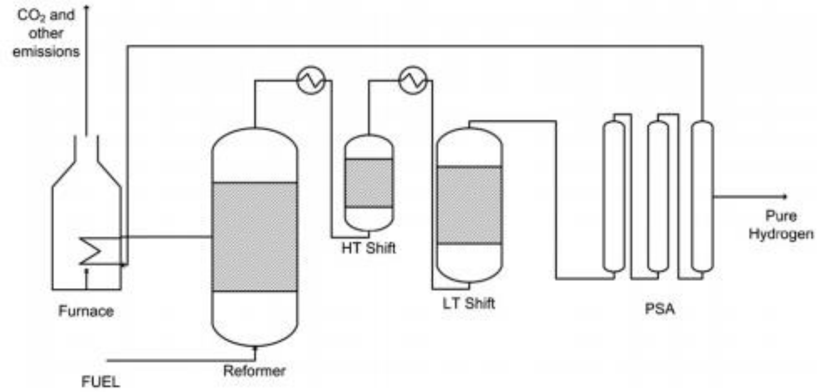

Figure I. 6 *Conventional scheme for steam reforming process (Gallucci et al., 2013).*

Nevertheless, the commercialization of pure palladium membranes is still limited by several factors: pure palladium membranes undergo the embrittlement phenomenon when exposed to pure hydrogen at temperatures below 300 °C, are subject to deactivation by carbon compounds at temperature above 450 °C, suffer for irreversible poisoning by sulphur compounds, the cost of palladium is high. In order to reduce the aforementioned drawbacks, palladium can be alloyed with a variety of other metals (Cu, Ag, Au, etc.), able to increase the hydrogen permeability shown by the pure palladium membranes (Basile et al., 2011). In this context, Pd-based composite membranes, i.e. thin Pd or Pd/alloy layer supported on porous materials such as ceramics, stainless steel, or vycor glass have been considered due to their lower cost (thinner Pd-layers) and higher mechanical strength (porous support) compared to dense unsupported Pd-based membranes (Anzelmo et al., 2018).

The hydrogen molecular transport in the palladium membranes occurs through a solution/diffusion mechanism, which follows six different activated steps: (I) dissociation of molecular H_2 at the gas/metal interface; (II) adsorption of the atomic hydrogen on membrane surface; (III) dissolution of atomic hydrogen into the palladium matrix; (IV) diffusion of atomic hydrogen through the membrane; (V) re-combination of atomic hydrogen to form H_2 molecules at the gas/metal interface; (VI) desorption of H_2 molecules (Koros and Fleming, 1993). Depending on temperature, pressure, gas mixture composition and thickness of the membrane, each one of these steps may control hydrogen permeation through the dense film (Basile, 2008). As a result, the hydrogen permeating flux can be expressed by means of the eq. (I. 15):

$$J_{H2} = (P_{eH2} \cdot \delta^{-1}) \cdot (P^{n}_{H2,ret} - P^{n}_{H2,perm}) \qquad \text{(I. 15)}$$

$$P_{eH2} = (P^{0}_{eH2} \cdot \delta^{-1}) \cdot ezp(-E_a \cdot R^{-1} \cdot T^{-1}) \qquad \text{(I. 16)}$$

where n (variable in the range 0.5–1) is the dependence factor of the hydrogen flux to the hydrogen partial pressure, J_{H2} the hydrogen flux permeating through the membrane, P_e the hydrogen permeability, δ the membrane thickness, $P_{H2, ret}$ and $P_{H2;perm}$ the hydrogen partial pressures in the retentate (the reaction side) and permeate sides (the volume in which the hydrogen permeating through the membrane is collected), respectively. When the pressure is relatively low, the diffusion is assumed to be the rate-limiting step and the factor n is equal to 0.5. In this case, eq. (I. 15) becomes the Sieverts–Fick law (Dolan et al., 2006). The relationship between hydrogen permeability and temperature follows an Arrhenius behaviour (eq. (I. 16), where P_e^0 is the pre-exponential factor, E_a the apparent activation energy, R the universal gas constant and T the absolute temperature), while n generally does not depend on the temperature.

A considerable issue of membrane reactor is that a faster coking of the catalyst is often observed in comparison with the classical fixed-bed reactor without H_2 removal (Schäfer et al., 2003). H_2 separation, in fact, results in a decline of the H/C ratio of the process gas. The increase of the concentration of C-containing products may promote unwanted pathways (i.e. CH_4 decomposition) responsible for an easier coke deposition on catalyst surface. Therefore, the selection of membrane reactors may induce severe operative conditions for the catalytic system, which is required to be more efficient in terms of resistance towards deactivation by coking.

Despite the reported advantages of membrane reactors, the choice of packed bed membrane systems, especially in the case of high hydrogen fluxes and in the presence of active catalysts, can lead, as a drawback, to external mass transfer limitations from the catalyst bed to the membrane (known as concentration polarization), thus limiting the H_2 production capacity and increasing the required membrane area. A possible solution to the above drawback can be reached by employing micro-reactors or fluidized bed reactors. Despite micro-reactors have the potential of reducing heat and mass transfer limitations, the required amount of catalyst to avoid inappropriate growth in pressure drops is very low; in addition, manifolding and gas distribution in membrane micro-reactors is quite hard (Ruocco et al., 2016). Conversely, fluidized bed membrane reactors (FBMR) offer a promising alternative to face the issues related to mass transfer and pressure drops.

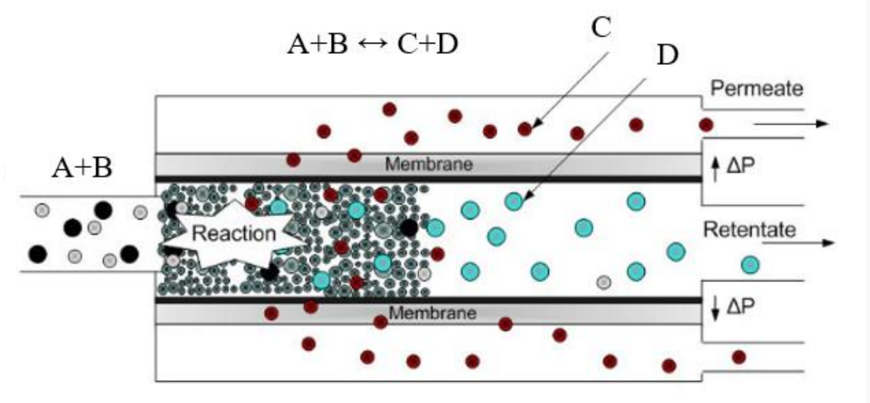

Figure I. 7 *Schematic o f a tubular packed bed membrane reactor.*

In a FBMR, the permeable membranes are integrated in a fluidized reaction bed to intensify the process. Such integration exploits the advantages of both membrane and fluidized bed resulting, at the same time, in a synergistic effect between them. Fluidized bed membrane reactors (Figure I. 8) are characterized by a remarkable temperature uniformity, due to the intense solid mixing induced by the rising bubbles; pressure drops through the bed as well as heat and mass transfer limitations are negligible. In addition, due to the presence of the inserts and gas permeation though the membrane, a reduced axial gas back-mixing and enhanced bubble breakage is observed: lower bubble sizes increase bubble-to-emulsion mass transfer and membrane permeation (Deshmukh et al., 2007). As a drawback, difficulties in reactor construction and membrane sealing at the wall together with the erosion of reactor internals and catalysts attrition phenomena can be observed.

Nevertheless, the employment of fluidized bed membrane reactors is one of the most promising solution for pure H_2 production devoted to fuel cells applications. However, the main barrier to the commercial development of FMBRs is related to their limited long-term stability above 400°C: defects can appear due to the mobility of the atoms present in the selective layer or as consequence of the attrition by the fluidized particles (Arratibel et al., 2018).

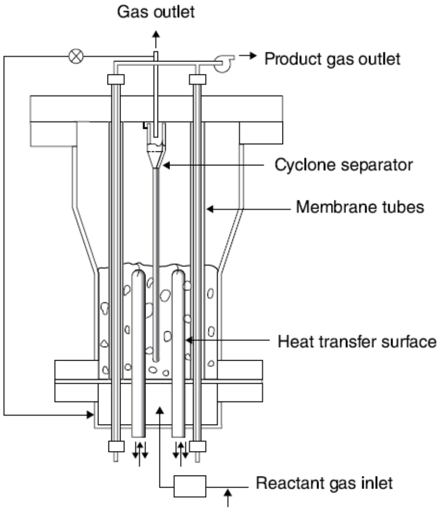

Figure I. 8 *Typical structure of a FBMR for the selective removal of a product (Adris et al., 1994).*

Recently, Iulianelli et al. (Iulianelli et al., 2018) compared the performance of different membranes employed for ethanol reforming. The analysis of the results revealed the high performance of the dense self-supported Pd-based membranes. However, the amount of palladium is quite high, making these membranes not a competitive solution for the scaling-up of ethanol reforming process at industrial level. On the other hand, among the low-Pd content composite membranes, interesting results were found over a Pd/Al_2O_3 membrane (Murmura et al., 2015).

Due to the complexity of the reforming reaction system in the presence of real bioethanol mixtures, only few studies investigated the interaction of membranes with ethanol impurities: a considerably higher coke formation on the catalyst surface is observed as a consequence of the carbonaceous intermediates reactions (Seelam et al., 2012). For example, in the presence of a composite Pd/Al_2O_3 membrane during raw bioethanol steam reforming in a fixed bed reactor, despite the high purity of the produced H_2, the recovery did not exceed the 70% and quite low values of ethanol conversion were recoded (Iulianelli et al., 2018).

I.6 Aim of the work

Oxidative steam reforming of ethanol is a promising route for hydrogen production. However, due to the high impact of the feedstock costs on the price of the produced hydrogen, it should be very useful to directly employ ethanol form biomass (i.e. bioethanol) for H_2 generation. Moreover, in a process intensification view, the choice of fluidized bed membrane reactors is auspicious to improve on one hand, the H_2 yield, and, on the other hand, the plant compactness.

In this regard, the main objective of this research study is the development of selective and highly stable catalysts for hydrogen production via oxidative reforming of biomass-derived ethanol in a fluidized bed membrane reactor.

Starting from a 3Pt-10Ni/CeO_2-SiO_2 catalyst (prepared by sequential wet impregnation) previously developed in the Proceed labs of UNISA and tested in a fixed bed reactor, its behaviour in a fluidized bed reactor will be studied. Several strategies will be followed in order to improve its resistance towards deactivation, including the study of the effect of alkali addition, Ni substitution by Co, Pt substitution by Ag or Ru. Moreover, the influence of cerium salt precursor on the activity and stability of the developed catalyst will be investigated.

In particular, in the attempt of reducing the final cost of the catalyst, the effect of Pt loading as well as the effect of Pt substitution by cheaper metals (i.e. silver and ruthenium) on the performance of the catalyst for oxidative reforming of a simulated bioethanol (i.e. pure ethanol and water) will be investigated. Once selected the most active sample, a kinetic model will be developed to evaluate the dependence of products gas distribution on reaction temperature. Moreover, the best formulation (in terms of durability and reduced carbon formation rate) will be tested in the presence of fuel grade bioethanol in the fluidized bed reactor for several hours. Finally, the activity of the most promising formulation will be also evaluated in a fluidised bed membrane reactor.

Chapter II

II State of the Art

II.1 Ethanol reforming and catalysts stability

During ethanol steam reforming, the main pathways responsible for coke formation are ethanol cracking, dehydration reaction to ethylene and its polymerization, aldol condensation of acetone, followed by dehydration and oligomerization of mesityl oxide, CO disproportion (Boudouard reaction) and methane dehydrogenation; ethane can also be formed and subsequently dehydrogenated (Mondal et al., 2015a, Li and Wang, 2018, Grewal and Roy, 2016). Based on the involved mechanism, different types of carbon can be formed (monoatomic adsorbed carbon, amorphous polymeric films, vermicular filaments and graphitic crystalline platelets): while the monoatomic adsorbed carbon and polymeric coke derive from the thermal decomposition of hydrocarbons, metallic sites are directly involved in the formation of filamentous and graphitic coke (Argyle and Bartholomew, 2015). The crystallization of carbon coming from ethylene polymerization is favoured at high temperatures while carbide species mainly derive from CH_4 decomposition, which can polymerize and form amorphous carbon or carbon whiskers; finally, carbon growth during Boudouard reaction may involve islands formation (Trevisanut et al., 2015, Sharma et al., 2017). For several transition metals (including Ni, Co, Rh, Ru, Pd, Pt)(Li et al., 2016), it was observed that that, before C-C bond breaking, an intermediate CH-CO is formed which, based on the reaction conditions and the nature of the metal surface, during the C-C rupture, can either dehydrogenate to form solid carbon or be hydrogenated to CH_4. For example, in the case of Ni, it was shown that elevated temperatures favour intermediate decomposition over their hydrogenation.

Ethanol reforming has been widely investigated under simulated bioethanol feeding (only containing water and ethanol); some studies were also performed under crude bioethanol feedings or model mixtures containing typical impurities. However, in the latter case, a faster catalyst deactivation was described: glycerol and acetic acid are known as the major coke precursors; moreover, higher alcohols are not easily reformed but can be dehydrated to the corresponding olefins (Lazar et al., 2019).

Liu et al.(Liu et al., 2015a) described the mechanism of carbon formation on Ni/CeO_2 catalysts and the role of the hydroxyls groups in suppressing carbon formation (Figure II. 1). During ethanol steam reforming on the above catalysts, coke formation was mainly due to the dehydrogenation of the surface methyl groups. Ni^0, in fact, was the active phase leading to both the C-C and C-H cleavage of ethanol. In general, such methyl groups are not stable on the Ni(111) surface and are mostly dehydrogenated to surface carbon and hydrogen. However, in this study, surface carbon was formed through the generation of nickel carbides, which can also be originated from small amounts of ethoxy species decomposing on the Ni sites to form Ni_3C. Water can easily dissociate on the $Ni\text{-}CeO_x$ to form hydroxyls groups which, together with the lattice oxygen on the surface, promote the oxidation of deposited carbon. However, the oxygen transfer from ceria lattice to Ni particles is an endothermic reaction and only occurs above 470°C. Thus, two competitive processes were described on the surface (carbon deposition and its oxidation by hydroxyls); the redox nature of the support as well as the Ni-ceria interactions are crucial to improve the oxygen transport and coke removal.

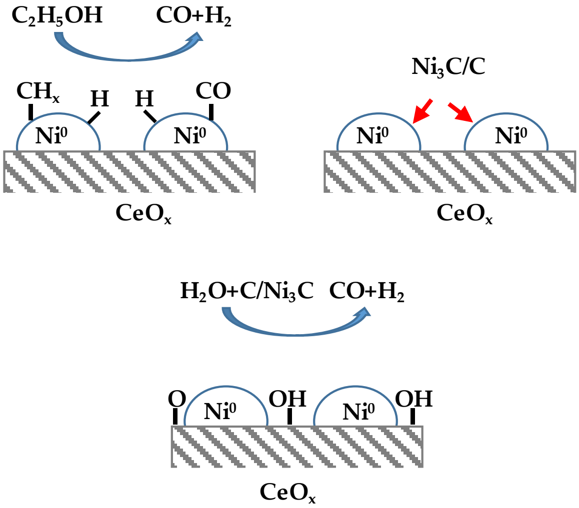

Figure II. 1 *Mechanism of ethanol formation and removal on a* Ni/CeO_x *catalyst during ethanol steam reforming (Liu et al., 2015a).*

The rate of ethylene formation throughout ESR is related to the support acidity and the amount of acidic sites on the catalyst surface. Figure II. 2 displays the positive effect of acidic surface tailoring by Ti addition for a nanostructured Ni-Al catalyst (Gonçalves et al., 2017). Ti doping resulted in an expansion of pore sizes, thus improving the mass transfer and the contact between catalytic sites and reactants; moreover, the redox properties of the Ti^{4+}/Ti^{3+} couple strongly influenced catalyst selectivity. In fact, due to titania effect on the surface basicity, the ethylene formed via ethanol dehydration is more stable and coke generated from C_2H_4 by polymerization and carbonization was thermodynamically less favoured and easier to decompose compared to the Ni sample only containing alumina.

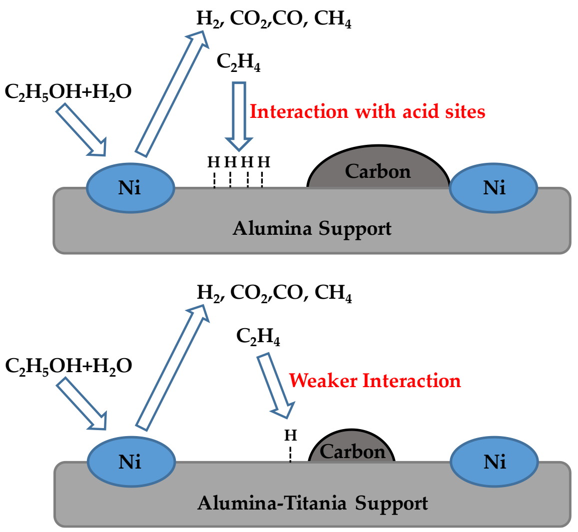

Figure II. 2 *Mechanism of carbon formation of Ni-Al and Ni-Al-Ti catalysts during ethanol steam reforming (Gonçalves et al., 2017).*

For alumina-based catalysts, the beneficial effects of support modification by the addition of CeO_2 or La_2O_3 was shown also in the case of noble metals as active species (i.e. rhodium) (Osorio-Vargas et al., 2016). The presence of low ceria loadings adds a Lewis acidity of a medium strength to the CeO_2-Al_2O_3 mixed oxide and the reduced carbon deposition on this support is related to the oxygen storage capacity and mobility of ceria. In fact, the reversible release of oxygen makes available O_x (lattice oxygen) on the oxide surface. Carbon monoxide adsorbs on the surface, reacting with O_x and producing CO_2. Moreover, the growth of carbon fibres is hindered by CeO_2 which provides extra oxygen for their gasification: solid carbon can react with oxygen lattices, further improving the yield to carbon oxides. Because CO is consumed to generate CO_2, less carbon monoxide is available to be convert to coke via the Boudouard reaction. A different mechanism of carbon build-up preventing was reported for La_2O_3. In the presence of lantania, carbon dioxide is subtracted to the equilibrium via the formation of $La_2O_3CO_3$, which can react with the carbon metal species in its vicinity and generate CO.

The origin and nature of coke formed over Ni/La_2O_3-αAl_2O_3 catalysts in ethanol steam reforming was reported in a work by Montero et al.(Montero et al., 2019). Acetaldehyde, ethylene and non-reacted ethanol were identified as the main coke precursors, responsible for the deposition of encapsulating coke via cracking and polymerization, while filamentous and partially graphitic coke derived from CH_4 and CO by decomposition and Boudouard reaction. As filamentous coke is located far from the metallic sites, its influence on catalyst deactivation is reduced and the main impact on catalyst deactivation comes from the encapsulation of metal active sites (Figure II. 3). The first mechanism is predominant at high temperatures and low space velocities while the second one is favoured at intermediates contact times, at which methane and carbon monoxide concentration reach a maximum; the increase of temperature and steam to ethanol ratio enhanced carbon gasification, reducing the concentration of coke precursors on the surface.

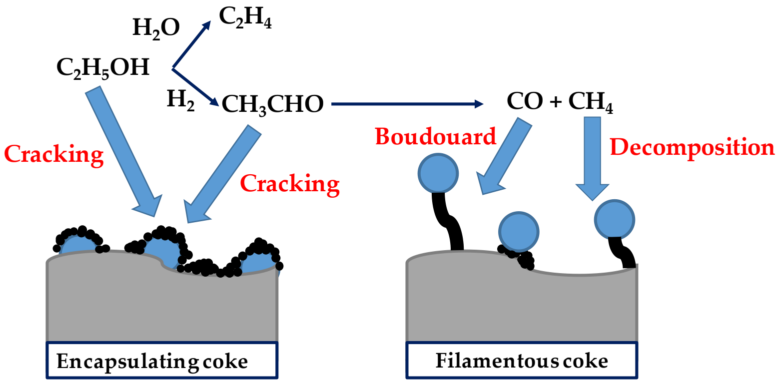

Figure II. 3 *Mechanism and nature of coke formed over Ni/ La_2O_3-αAl_2O_3 (Montero et al., 2019).*

For nickel core-shell structured catalysts, it was found that, during ESR reaction, ethanol molecule is firstly dehydrogenated to acetaldehyde, which decomposes to CH_4 and CO, with a subsequent formation of carbon lumps. Conversely, if the ethanol dehydration occurs, ethylene is formed as intermediate, which can easily polymerise to form carbon nanotubes (Jo et al., 2016) .

Co@CoO_x core-shell structured catalysts, exposed to mild oxidants (i.e. H_2O and CO_2) during ESR reaction, suffer for stressing and collapsing of the structure, with an oxidation of the CoO_x core by means of the oxygen-free radical species which, therefore, are no more available for coke gasification (the carbon is mainly formed via dehydrogenation or condensation reactions) (Chen et al., 2019). Thus, sintering and formation of amorphous carbon occurred. The promoting effect of ceria, related to the redox cycle Ce^{3+}/Ce^{4+}, assured an easier mobility of active oxygen species, preventing re-oxidation of metallic Co particles, and allowing, at the same time, a rapid consumption of carbonaceous species. For sol-gel alumina supported cobalt catalysts, it was reported that the catalytic decomposition of ethylene on the Co sites was responsible for the formation of graphitic carbon, while amorphous coke derived from the polymerization of carbon coming from methane decomposition. In addition, the influence of the CoO/Co^0 ratio on the carbon growth on the surface of the active sites was discussed. This ratio ruled the contribution of ethanol molecule activation and oxidation of adsorbed coke, with an optimal value of 1/3 selected to assure adequate activity and stability to the final catalyst (Passos et al., 2017).

Oxidative steam reforming of ethanol (OSR) has also received considerable attention, due to the role of gas phase oxygen species, together with those eventually presented as mobile lattice oxygen, in the oxidation of carbon deposited on the catalyst surface (Muñoz et al., 2017).

For Ni-Cu bimetallic catalysts derived from hydrotalcite-like compounds, the effect of oxygen co-feeding during ethanol steam reforming was investigated at 500°C under a molar ratio of water/ethanol/oxygen equal to 6/1/0.3. As depicted in Figure II. 4, O_2 addition mitigated the formation of filamentous-like coke deposits: oxygen promoted water production limiting, at the same time, the adsorption of hydrogen (thus hindering the reduction of NiO) and CO or CH_4 products on nickel active sites (which are converted to CO_2 and CO). Moreover, the dissolution of gasified carbon in nickel particles with its further diffusion though the metal was mitigated, thus hampering the growth of filamentous coke (Passos et al., 2019).

The Pt-Ni/CeO_2-SiO_2 catalysts, tested under a reacting stream of $C_2H_5OH/H_2O/O_2=1/4/0.5$ at 500°C, displayed a better stability compared to the ESR measurements: oxygen co-feeding improved coke gasification, thus resulting in a diminished accumulation of carbon on catalyst surface; moreover, oxygen addition in the presence of a catalytic support having a remarkable ionic conductivity encourages the oxidation of carbon-containing species, without affecting hydrogen production rate, which was almost the same for ESR and OSR tests (Palma et al., 2017d).

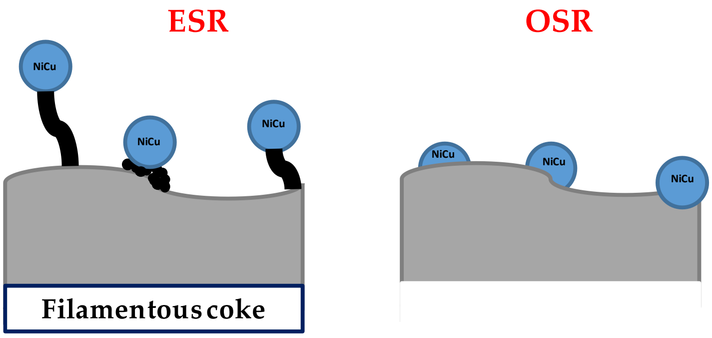

Figure II. 4 *Effect of oxygen addition on carbon formation during ESR over Ni-Cu catalysts derived from hydrotalcite-like compounds (Passos et al., 2019).*

Accordingly, in order to minimize the issue of carbon deposition, different strategies have been proposed in the literature, including the control of the metal particle sizes and the addition of a second metal or promoters able to change the electronic properties of the active species and modify its interactions with the support (Mulewa et al., 2017, Nejat et al., 2019, Di Michele et al., 2019). In the following paragraphs, bioethanol reforming with focus on carbon formation will be discussed based on the nature of the active phase (Par. II.1.1), the chosen supports (Par. II.1.2) and the effect of promoters/additives (Par. II.1.3). Due to the large number of papers focused on bioethanol reforming, in the present chapter, the discussion was focused on the most recent papers (published in the last 5 years).

II.1.1 The influence of the active phase

Ethanol reforming has been investigated over several noble and non-noble metals based catalysts. Nickel is the most widely selected metal for ethanol reforming followed by cobalt. Moreover, among the noble metals, platinum and rhodium are most commonly selected.

In the following paragraph, the role of active species selection on catalyst stability for bioethanol reforming are discussed. In particular, different examples related to cobalt and nickel-based catalysts are reported for the various investigated processes, followed by the description of the performance of noble metals-containing catalysts as well as copper-based catalysts.

At 500°C and under stoichiometric feeding conditions, CH_4 decomposition and Boudouard reaction were shown to be responsible for the formation of filamentous coke over Co_3O_4/CeO_2 catalysts during ESR (Carvalho et al., 2016): carbon dissolves and subsequently precipitates at the rear of the metal, warding off the Co^0 active sites from the support and leading to a loss of the Co^0 active centres. However, by modulating the cobalt loading and particles dispersion, it is possible to vary the thickness of the filamentous coke, thus resulting in a good catalytic stability. In fact, active species dispersion and metal-support interactions are key factors affecting catalyst resistance towards deactivation. Thus, the improved stability of Co/CeO_2 catalysts during ESR at different temperatures (400, 600, 800°C) under a steam to carbon ratio of 3, compared to Ni, Fe and Cu based samples, was ascribed to the strong metal-support interactions, which contributed to maintain the Co species in an oxidized state; moreover, the gas-solid reactions between the hydrocarbon species adsorbed on the surface and the oxygen groups assured an easier gasification of such species, preventing their decomposition to coke (Konsolakis et al., 2016). For $PtKCo/CeO_2$ catalysts tested during oxidative steam reforming of ethanol, only a partial activity loss was observed and the reduced catalyst performance was ascribed both to carbon deposition and oxidation of cobalt metallic sites (Greluk et al., 2016b). Carbon filaments are bonded to the support and contain cobalt particles at the top with the unblocked surface, thus not necessarily causing catalyst deactivation, while only few metallic particles are encapsulated by carbon and can no longer participate to the reaction. In addition, non-filamentous coke (formed as a result of condensation and graphitization of carbon-containing species chemisorbed on the catalyst surface) covered only the external surface of the active particles while the middle part was still accessible to the reactants. Pt addition had a negligible effect on carbon deposition and it was also shown that the oxygen from the feeding can oxidize the surface atoms of cobalt particles, with a rate that increases in the case of small particle sizes (lower than 4 nm).

The effect of the preparation method (mechanical mixing or sonication) on the stability performance of Co nanoparticles mixed with α-Al_2O_3 was reported by Riani et al.(Riani et al., 2019): well-dispersed Co nanoparticles displaying a good interaction with alumina were observed in the sonicated sample while for the mechanically mixed catalyst only aggregate nanoparticles were detected. The results of stability tests, carried out at 500°C and under a steam to ethanol ratio of 6, proved that Co aggregates produced long carbon nanotubes, which embedded the active particles, while the tendency to form graphitic carbon is very low for the nanoparticles interacting with alumina.

For NiCo-MgAl catalysts prepared by microwave/sonication assisted coprecititation, it was found that the pre-reduction of the catalyst is crucial to assure proper acid-base properties to the material, which affected catalyst stability during OSR. For the un-reduced sample, in fact, a high basicity was observed, which favoured some unwanted pathways (including acetone generation), with the formation of coke precursors (Muñoz et al., 2017).

The preparation method was also shown to affect the durability of Ni/SiO_2 catalysts for ESR (Mhadmhan et al., 2018). Compared to the impregnated samples and those prepared by deposition-precipitation, the catalysts synthetized via strong electrostatic adsorption displayed improved interactions between the active phase and the support, assuring a good control of Ni particle size, which helped reducing carbon deposition at 600°C under a H_2O/C_2H_5OH ratio of 9. The same authors demonstrated the benefits of employing silica fibers instead of the commonly used porous SiO_2. For porous catalysts, coke accumulates inside the pores and its gasification via the reaction with water is more difficult; conversely, carbon is deposited on the external surface of the fibers and its removal via gasification becomes easier.

The ultrasound assisted synthesis of $Ni/MgAl_2O_4$ catalysts allowed obtaining sufficiently dispersed Ni particles even at high Ni loading (Di Michele et al., 2019); the limited surface acidity, mainly due to the presence of Ni, promoted ethanol dehydration to ethylene which, however, for a Ni loading as high as 10% was further subjected to reforming, with very limited coking phenomena. $Ni/Ce_{0.9}Sm_{0.1}O_{2-\delta}$ nanowires were prepared via a simple two-step hydrothermal method followed by Ni deposition via wet impregnation. Such catalysts displayed high concentration of oxygen vacancies at surface and very low dimensions for Ni crystallites, thus assuring enhanced metallic surface area compared to their analogue catalysts prepared from commercial doped-ceria. Due to such improved properties, the $Ni/Ce_{0.9}Sm_{0.1}O_{2-\delta}$ sample displayed an exceptional stability with no loss of activity after 192 h of reaction at 550 °C under stoichiometric feeding conditions (no carbon deposits or filaments were detected over the spent catalyst) during ESR (Rodrigues et al., 2019).

For Co/CeO_2 catalysts, the use of nitrates as inorganic salt precursors was shown to increase acetaldehyde as well as ethylene selectivity, with a severe carbon deposition (Sohn and Ozkan, 2016); conversely, the choice of cobalt acetyl acetonate strongly enhanced catalyst stability during ESR at 450°C under a steam to ethanol ratio of 10: the organic ligands linked to the metal sites decreased cobalt particles size, improving their dispersion, and assured them a sort of imprinting effect, increasing the sites accessibility to ethanol and water. Similarly, He et al.(He et al., 2017) prepared Ni/SBA-15 starting from two different nickel precursors (nitrate and citrate) and tested them for ethanol reforming at 500°C and H_2O/C_2H_5OH ratio of 3: in the first case, NiC_x species were detected, which can be easily removed from catalyst surface. On the contrary, the choice of Ni nitrate as precursor lead to the formation of carbon nanofibers having regular graphite-structure, which covered the Ni active sites and are more difficult to be removed.

Ni catalysts prepared by using smectite-derived material as starting precursor compared to conventionally impregnated samples displayed reduced crystallite sizes of Ni and a consequent higher resistance towards carbon formation (Yoshida et al., 2015). In fact, during the synthesis, Ni species migrate in the framework of smectite and, despite moving towards the surface during the reaction, a strong interaction with the framework is maintained, which inhibits sintering. Since such interaction contributed to limit particles size growth, considerable nickel contents (up to 35 wt%) can be reached, thus resulting in high catalytic performance for ESR.

Noble metals-based catalysts displays lower coke formation and enhanced stability with time-on-stream compared to Ni or Co (Ogo and Sekine, 2020, Hou et al., 2015a). Moraes et al. (Moraes et al., 2015) investigated the effect on carbon build-up of Pt addition to a Ni/CeO_2-nanocube catalyst for ethanol steam reforming at 300°C and a steam to ethanol ratio of 3. The formation of a nickel carbide phase (solid solution of carbon in Ni), catalytically inactive, was observed over the monometallic sample which, together with the accumulation of adsorbed acetates on the surface, led to a significant catalyst deactivation. A depicted in Figure II. 5, Pt inhibited the formation of NiC_x species, enhancing the hydrogenation rate of carbonaceous species; moreover, due to the slower kinetics for carbon diffusion of the noble metal, a decrease of the carbon diffusion rate throughout Ni lattice was assured by platinum particles (Ni carburization during reaction was mitigated by a discontinuous Pt surface outer shell) (Moraes et al., 2016). As a result, carbon formation rate during 28 hours of TOS was reduced of 4 times.

For noble-metals based catalysts, in fact, due to the reduced solubility of carbon on the surface, it was shown that carbon nucleation is energetically unfavourable: noble metal lattice is too large compared to graphene lattice, thus inhibiting its formation. As a consequence, the formation of superficial carbon instead of more structured deposits is favoured in the presence of supported noble metal catalysts (the solubility of carbon in the latter materials is very low) (Cifuentes et al., 2015).

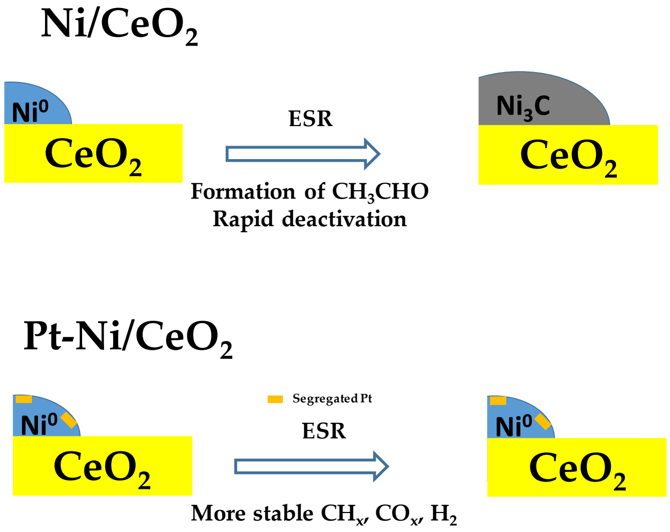

Figure II. 5 *Effect of Pt addition on carbon formation over Pt/CeO_2 catalysts (Moraes et al., 2016).*

Similar results were also reported by Palma et al. (Palma et al., 2017e).

The addition of Rh of Ni/CeO_2-La_2O_3 enhanced the catalyst stability due to multiple effects, involving the reduced accumulation of acetate as well as the higher capacity to gasify the methyl groups produced via decomposition of intermediates. Acetates, deriving from acetaldehyde dehydrogenation and subsequent oxidation, can be converted to CH_x species or may accumulate on the surface of the Rh-free catalyst, leading to acetone formation and subsequent carbon deposition. As a result, the Rh-Ni catalyst displayed almost no carbon formation for 24 h of reaction at 500°C under a steam to ethanol ratio of 3 (Campos et al., 2019). The excellent stability of Rh-Pt/CeO_2 catalysts during ESR under stoichiometric feeding conditions at 700°C was ascribed to the formation of a Rh-Pt alloy containing both Rh and Pt oxidized species, which also lead to small metal particles (almost 5 nm). The control of carbon accumulation was related to the availability of surface oxygen, which travels from the support, crossing the active metals and reaching the CH_x coke precursors (Cifuentes et al., 2015).

The basic properties of the $Rh_{0.4}Pt_{0.4}/CeO_2$ assured stable performance during steam reforming of a bioethanol feed (having a steam to ethanol ratio of 3 and containing ethyl acetate 0.5 mol%, 1,1-diethoxyethane 0.2 mol%, trace constituents: propanol, 2-methyl-1-propanol, 3-methyl-1-butanol, and 2-methyl-1-butanol) at 700°C: alcohol dehydration is disadvantaged, as well as olefin production and further carbonaceous deposition on the catalyst surface (Sanchez et al., 2016).

Due to their different affinity for carbon deposits formation (different adsorption energies of the C-containing intermediate species were reported), Pt/Al_2O_3 and Rh/Al_2O_3 catalysts displayed dissimilar behaviour during steam reforming of crude bioethanol at 500°C under a steam to ethanol ratio of 5 and 1% of impurities (Bilal and Jackson, 2017). Carbon formation rate on the platinum-based catalyst was affected by the type of impurity selected and decreased in the order IPA>1-propanol>pure ethanol>propanal> propylamine > acetone while the Rh/ Al_2O_3 showed a higher durability, with a negligible trend related to the contaminants. A Pt-Co/CeO_2-ZrO_2-Al_2O_3 catalyst was successfully employed for the steam reforming of a real bioethanol feed coming from the industry (having a steam to ethanol ratio approximately of 6 and containing also sulphur/phosphorous compounds): during stability measurements at 400°C, coke deposition did not occur (Iulianelli et al., 2018).

In some cases, the addition of a second non-noble metal (i.e. Co or Cu) displayed a mitigating effect in term of carbon deposition (Shahed Gharahshiran et al., 2020, Nichele et al., 2015). The improved stability of Ni-Co/SBA-15 catalysts upon cobalt deposition was ascribed to the formation of a carbide phase (thermodynamically stable against decomposition to metallic Co and graphitic carbon), which assures a decrease in cobalt particles sizes (Rodriguez-Gomez and Caballero, 2018). A reduced C_2H_4 formation was observed during ESR over NiCu ex-hydrotalcite catalysts compared to the copper-free sample, which limited the deposition of graphitic carbon as well as the formation of carbon filaments having small metallic particles at their growing tips.

For copper-nickel oxide catalysts (Chen et al., 2015), it was also reported that the metal-oxide interface facilitate the transformation of CH_x adsorbed species coming from acetaldehyde decomposition into methoxy-like adsorbed species, which are readily reformed to produce H_2 instead of being decomposed to solid carbon.

Braga et al. (Braga et al., 2018) investigated the effect of Co addition to $Ni/MgAl_2O_4$ on their stability during OSR of ethanol at 500°C under $H_2O/EtOH/O_2 = 3/1/0.5$. Filamentous carbon was deposited on bimetallic Ni-Cu samples and the rate of carbon deposition increased for lower Co contents. The carbon gasification rate depends on the presence of surface oxygen for the oxidation of the *C species: the small dimension of cobalt particles (lower than 5 nm) interacting with Ni contributed to enhance the fraction of oxidized Co available to oxidize the carbon species on metal sites. Thus, cobalt deposition on $Ni/MgAl_2O_4$ effectively mitigate coke accumulation, with the best results recorded over the 4Co-4Ni catalyst.

II.1.2 The role of the support

The present paragraph describes the crucial role played by the catalytic support in preventing coking phenomena, mainly linked to its acid/basic features as well as structural properties. Thus, the identification of the acid/basic sites of the support is fundamental for the understanding of coke formation mechanisms.

For Rh/CeO_2 catalysts tested during ESR (Baruah et al., 2017), characterization measurements indicate the presence of strong basic sites; however, a slightly acid behaviour was also observed. A different path for the ethanol molecule activation is observed based on the site feature: acidic sites favour dehydration reactions and ethylene formation, which is a well-known coke precursor, while dehydrogenation pathway is promoted over basic sites, leading to the formation of $C_2H_5O^*$ intermediates, which can decompose to CH_x species and further be oxidized to CO and CO_2.

$La_2Ce_{2-x}Ni_xO_{7-\delta}$ catalysts displayed a very stable behaviour during oxidative steam reforming of ethanol: Ni incorporation into the pyrochlore structure as well as the synergistic effect of nickel and cerium ions induced the formation of Ce^{3+} ions, thus creating oxygen vacancies. This effect, together with the good dispersion of Ni particles and the presence of NiO as impurity (sintered nickel oxides promote coke accumulation) mitigate coke deposition (Weng et al., 2017). The same authors synthesized pyrochlore catalysts substituted by Li and Ru in A and B sites and supported them on Al_2O_3 or $La_2Zr_2O_7$. Substitution of La^{3+} by Li^+ metal cations modified the relative compositions of active metal ions Ru^{n+}/Ru^{4+} and Ce^{4+}/Ce^{3+}, thus enhancing formation of vacancies and increasing carbon oxidation rate. Moreover, during tests performed at 350°C under stoichiometric feeding conditions, disordered carbonaceous and ordered graphitic species were formed over the alumina-supported catalyst while no coke accumulation was observed for the $La_2Zr_2O_7$-based sample. The basic properties of this support, in fact, suppressed ethylene formation and its successive polymerization (Hsieh et al., 2019a).

The metal particles size and the dispersion of the active phase is also affected by the structure of the support. Da Costa-Serra & Chica (Da Costa-Serra and Chica, 2018) studied ethanol steam reforming over two Co-based catalysts supported on structured manganese oxides (Birnessite and Todorokite). In the latter case, the special microporous structure of the support provided high-quality positions for the stabilization of the cobalt particles during the preparation, thus leading to smaller metal particles compared to the birnessite-based sample (6 vs 12 nm). As a result, carbon accumulated during a 24 hours ESR test at 500°C under a H_2O/C_2H_5OH ratio of 13 was almost one half over the todorokite-supported Co catalyst.

The superior stability of a Ni/KIT-6 catalyst (ordered silica) for ethanol steam reforming at 550°C under a C_2H_5OH/CO_2 ratio of 1, compared to a nickel sample supported on mesoporous silica, was ascribed to the stabilization of the Ni species via the formation of Si-O-Ni-O-Si bonds, with a consequent confinement within the pores of the ordered structure; such confinement resulted in a stronger metal-support interaction and smaller Ni particles, compared to the Ni/SiO_2 catalyst, which enhanced the resistance towards coke formation (Wei et al., 2020). By depositing a $Pt\text{-}Ni/CeO_2$ catalyst on high surface area mesoporous silica, a better dispersion of both metal as well as ceria particles was observed compared to the silica-free sample, thus enhancing the catalyst stability during ESR. The bimetallic catalysts were also prepared at different CeO_2/SiO_2 ratios (25, 30 and 40%) and the relationship between the carbon formation rate and the average Ni crystallites calculated for the spent catalysts was investigated. The smallest crystallite size, linked to the minimum coke selectivity, was recorded for a ratio of 30% (Palma et al., 2017d).

Catalyst deposition on specific structured carriers may also affect their stability performance for ethanol reforming. The enhanced mass transfer rate and the improved gas-solid contact of the structured carriers (i.e. foams, honeycombs and monoliths) is expected to increase the contribution of coke gasification reactions, with a consequent mitigation in the deactivation of the catalytic formulation (Palma et al., 2015a, Chai et al., 2015). $Rh/CeSiO_2$ catalysts supported on a ceramic monolith was subjected to a water/ethanol mixture of 3.5 at 755 °C and no coke formation was observed during 96 hours of operation (Moraes et al., 2018). Cobalt deposition on a Y_2O_3-doped ZrO_2 monolith eliminated the formation of undesired by-products (C_2H_2 and

C_2H_4O), whose formation in the presence of the corresponding powder material was responsible for carbon deposition. Moreover, the stability of such structured catalysts was enhanced by infiltrating La into the monolith structure (Gaudillere et al., 2017).

For the steam reforming of a simulated bioethanol feed (containing 1 mol% of the following impurities acetaldehyde, isopropyl alcohol, isobutyl alcohol, isoamyl alcohol) over a Pt-Ni/CeO_2-ZrO_2 catalyst supported on a SiC foam, it was observed that the binder employed during the deposition of the catalytic washcoat on the structured carrier may affect catalyst stability (Palma et al., 2016). The choice of boehmite as binder reduced carbon formation rate during tests at 450°C ad for a steam to ethanol of 3, compared both to the corresponding powder sample as well as to the structured carrier containing silica as ligand. In the latter case, in fact, a very fast deactivation (Figure II. 6) was observed which was described as follows: during reforming reactions, steam can attack Si atoms of silica structure, with consequent structural changes for silica. Thus, active species particles can be wrapped and/ or buried within the structure, losing their activity. Anyway, both the structured catalysts, tested again a power sample, displayed a clear improvement in terms of activity and stability.

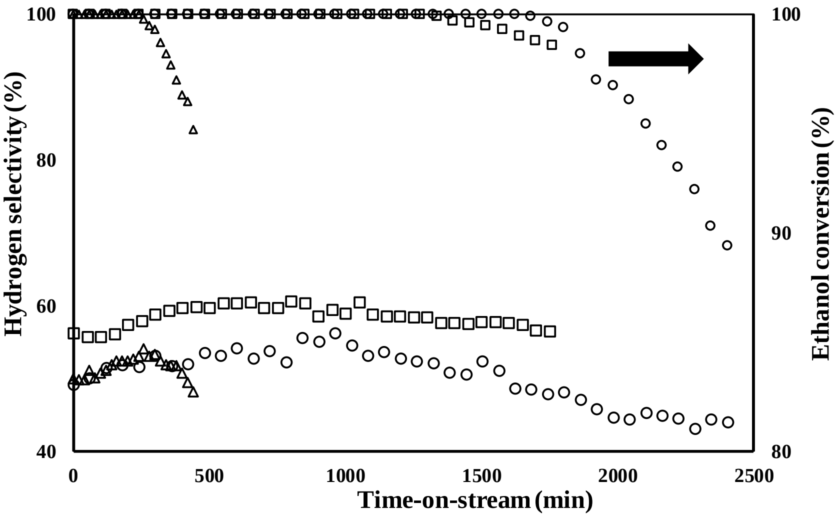

Figure II. 6 *Ethanol conversion and hydrogen selectivity as a function of time-on-stream for powder catalyst (square), SiO_2-foam (triangle) and AlOOH-foam (circle), r.a.= 6 and 1 mol % of C_2H_4O, C_2H_7OH, C_3H_9OH and $C_5H_{11}OH$; GHSV=15000 h^{-1}, T=450°C.*

II.1.3 The effect of promoters addition

The addition of promoters is a common strategy to mitigate carbon deposition on catalyst surface during ethanol reforming and, in the following paragraph, the influence of various promoters (mainly alkali metals and rare earths elements) on catalyst stability for bioethanol reforming is discussed.

For Co/CeO_2 catalysts tested during ESR, it was reported that Co particle size influence the type of carbonaceous deposits: large cobalt particles caused the formation of carbon filaments with encapsulated cobalt (carbon diffuses inside the crystallites destroying them and causing growth of nanofibers) while few atomic layers of carbon, mainly located at the boundary of the Co and CeO_2 particles, were detected over small cobalt particles. The same authors found that the concentration of hydroxyls groups (which depends on the steam to ethanol ratio) on the catalyst surface is crucial to modulate coke selectivity. In this regard, upon potassium addition, an higher concentration of OH species and K-O sites was assured, able to favour the conversion of coke precursors to CH_x instead of fully dehydrogenated C=C species (mainly graphitic whiskers and layers)(Turczyniak et al., 2017). Moreover, the formation of carbonaceous deposits was also prevented over Co/ZrO_2 catalysts promoted by potassium, mainly due to the decreased contribution of CO disproportion reaction (Greluk et al., 2015). La_2O_3 promotion improved the active species dispersion and the metal-support interactions for Co/CeO_2 (and Ni/CeO_2) catalysts: the lower carbon formation was attributed to the formation of $La_2O_2CO_3$ as intermediate phase, which contributes to eliminate carbon deposits leading to the formation of carbon monoxide (Greluk et al., 2020). Cerdà-Moreno et al. investigated the effect of La addition as promoter on the stability of Zn-hydrotalcites containing Co as active phase at 600°C for the steam reforming of a raw bioethanol stream containing several impurities (acetaldeyde, methanol, propanol and SO_2) and having a steam to ethanol ratio of 10: the improved performance of the lanthanum containing catalyst are mainly related to the reduced C_2H_4 selectivity (Cerdá-Moreno et al., 2019).

For Ni/SBA-15 catalysts, Mn introduction as promoter and the subsequent change in the redox properties of the catalyst favoured the formation of a lower amount of coke lumps (carbon donuts surrounding Ni particles), with a less activity loss compared to the Mn-free catalysts during ESR (Jo et al., 2016). A similar reduction in the extent of deactivation and the same difference in the type of formed coke was observed by adding Mo to Ni/SBA-15 catalysts (Kim et al., 2015) and Mn to Co/SBA-15 catalysts (Kwak et al., 2015). The synthesis of a Ni-Ce-W oxide catalyst via reverse microemulsion allowed W and part of the Ni to be incorporated into the ceria lattice, while the remaining Ni formed highly dispersed nano-NiO (almost 2 nm) outside the Ni-W-Ce oxide structure. Due to the synergy between Ni and W inside the ceria lattice, an increase of the oxygen vacancies with respect to the W-free sample was observed, which assured higher resistance towards coke formation during ESR (Liu et al., 2015b).

Compared to the ceria-free samples, CeO_2-promoted Ni/SBA-15 catalysts displayed well-dispersed nickel particles confined in the mesoporous channels of SBA-15 (Li et al., 2015): the metal-support interactions lead to a homogeneous distribution of Ni and Ce with a large Ni-CeO_2 interface, which contributed to control the size of Ni particles. Ni ability to break C-O bonds, responsible for CO disproportion and carbon deposits formation, was mitigated due to the strong electronic perturbation induced by ceria. In addition, the OH groups present on ceria surface and deriving from steam can easily react with methyl groups to generate CO, CO_2 and H_2: due to the high oxygen mobility in ceria lattice, an enhanced carbon gasification rate is observed, along with a lower rate of carbon deposition. Thus, ceria can effectively minimize sintering and coking over Ni/SBA-15 catalysts during ethanol steam reforming at 700°C and H_2O/C_2H5OH ratio of 4, reducing the accumulated amount of coke deposition of almost 70%.

In the attempt of improving the stability of NiMgAl catalysts, Du et al. (Du et al., 2017) investigated the addition of various promoters, which differently modulated the electronic properties of the final catalyst: NiCoMgAl catalysts compared to the Mn- or Zr-promoted samples displayed higher durability, ascribable to the good metal dispersion and small metal size, which hindered carbon deposition and sintering (small particles of metals such as Ni have been found to block the mechanism of growth of the carbon filaments, thus decreasing carbon accumulation). Conversely, an enhanced rate of carbon formation (mainly in a filamentous form) was observed over the NiMnMgAl and NiZrMgAl samples. Ce addition to NiMgAl reduced metal particles dimension while the presence of lanthanum increased the surface Ni content and the number of basic sites; in both cases, a reduced carbon formation rate was measured. Similarly, the benefits of supporting $LaNiO_3$ catalysts on $CeSiO_2$ were reported (Marinho et al., 2016): SiO_2 presence avoided the sintering of ceria particles and the very low carbon formation rate recorded during ESR at 700°C and H_2O/C_2H_5OH of 3 over the $LaNiO_3/CeSiO_2$ catalyst was ascribed to the metal-support interactions, which contributed to maintain small dimensions for Ni crystallites. The size of metal particles, in fact, affects the nucleation rate of carbon and a critical ensemble size (ensemble of 6-7 atoms) was proposed, below which carbon formation does not occur. For these catalysts, it was also reported that, after an initial deactivation, new stability conditions were reached, despite the presence of carbon on catalyst surface. The initial loss of activity was observed when the rate of formation of CH_x species was higher than their desorption to form CH_4. Such species can be further dehydrogenated to C and H, and the highly reactive carbon species can both encapsulate metallic particles, leading to complete deactivation, or diffuse through the Ni crystallites and nucleate the growth of carbon filaments. In the latter case, the top surface is still in contact with the reacting mixture and the catalyst is able to maintain its activity for the ESR. Dan et al. (Dan et al., 2015) investigated the steam reforming of a fir wood crude bioethanol over Ni/Al_2O_3 catalysts (containing methanol, acetic acid, higher alcohols, esters, aldehydes, organic acids and dimethylfuran) which, however, displayed a rapid deactivation during tests at 350°C due to the deposition of graphitic carbon. A significant improvement in its durability was observed upon addition of rare earth oxides (stable performance for 4 h at 350°C), with La_2O_3 decreasing the alumina surface acidity and CeO_2 promoting water activation for coke deposits gasification.

Likewise, Au incorporation into Ni/SBA-5 catalysts improved the dispersion of the NiO phase to form smaller nickel oxide particles, but also strengthened the interaction between the SBA-15 support and the NiO phase, thus efficiently reducing coke deposition on the active sites (He et al., 2015).

Mondal et al. (Mondal et al., 2015b) described the performance of un-promoted and Rh-promoted Ni/CeO_2-ZrO_2 catalyst for oxidative steam reforming of a crude bioethanol stream (containing ethanol, butanediol, butandioic acid, acetic acid and glycerol). Stability tests were performed at 600°C and $EtOH/H_2O/O_2=1/13/0.35$. Rh addition led to smaller dimensions for Ni crystallites and, despite both amorphous and rod-shaped filamentous carbon nanotubes was recorded over the two spent catalysts, the Rh-Ni/CeO_2-ZrO_2 assured a lessened deposition of encapsulating amorphous coke, thus exhibiting a significantly lower deactivation rate.

In some cases, the addition of promoter did not assure the desired performance improvement: for Ni/CeO_2 catalyst, K addition caused a faster deactivation (Figure II. 7) due to the deposition of a very large amount of only graphitic fibres, longer and thicker than those found in the un-promoted catalyst; such graphitic fibres encapsulated nickel crystallites resulting in an activity loss (Słowik et al., 2018).

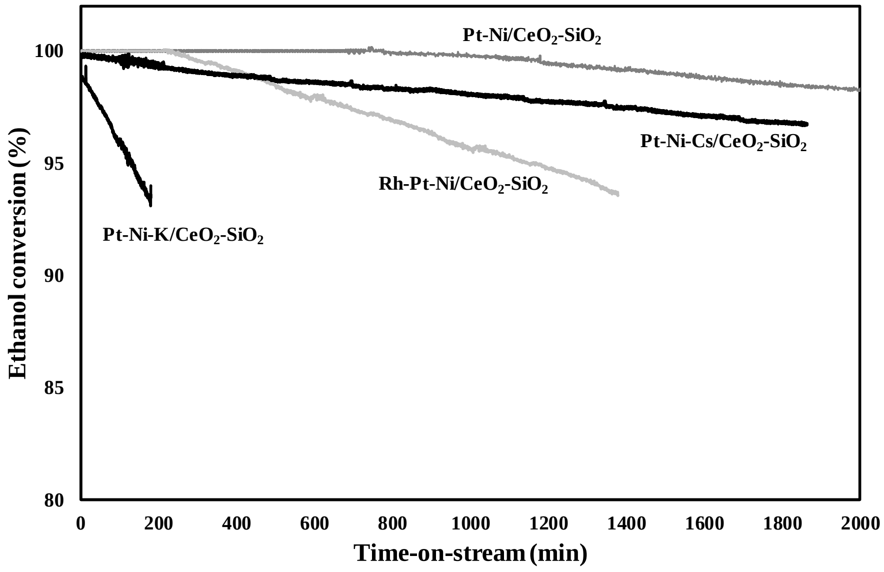

Figure II. 7 *Results of ethanol steam reforming stability tests in the presence of a Pt-Ni/*CeO_2*-*SiO_2 *catalyst doped with Rh, Cs and K;* H_2O/C_2H_5OH *ratio=4, T=450°C, WHSV=4.1* h^{-1} *(Palma et al., 2017c).*

For Pt-Ni catalysts, the addition of a third metal (K, Cs or Rh) as promoter was investigated, finding that caesium and rhodium are able to reduce carbon formation rate during ESR a 450°C and under stoichiometric feeding conditions, while in the presence of potassium, such addition was detrimental for catalyst stability (Palma et al., 2017c).

II.2 Catalysts performance for oxidative steam reforming of ethanol

Table II. 1 summarizes the stability performance of different catalysts proposed for oxidative steam reforming of ethanol. As discussed above, various parameters affect catalyst durability and carbon formation rate, including catalyst composition (active species, support, promoters) and operative conditions (temperature, feeding and space velocity): high ethanol concertation, low contact time and steam to ethanol ratio increase carbon accumulation on catalyst surface. Moreover, noble metals-based catalysts displayed lower coke formation compared to Ni or Co based catalysts and promoters addition assured lessened coke selectivity. Carbon formation rates range between 10^{-2} to 10^{-7}; overall, as described in Par. II.1, during oxidative steam reforming of ethanol, reduced coke selectivities were recorded compared to the steam reforming, due to the enhanced contribution of gasification reactions promoted by O_2.

Table II. 1 *Comparison of the stability performance of various catalysts for oxidative steam reforming of ethanol.*

Catalyst[a]	**Operative conditions**[b]	**WHSV**[c] **(h^{-1})**	**X (%)**	**CFR**[d]	**Ref.**
30Ni/CeO_2-ZrO_2	T=600°C f.r.=9 o.r.=0.35	5.1	95% after 36h	0.92	(Mondal et al., 2015a)
1Rh-30Ni/CeO_2-ZrO_2	T=600°C f.r=9 o.r.=0.35	5.1	85% after 36h	0.45	
$La_{0.6}Sr_{0.4}CoO_{3-\delta}$	T=600°C f.r.=3 o.r.=0.5 Et_{OH}=4.4%	3.6	96% after 5h	2.1	(Morales and Segarra, 2015)
$Mg_2AlNi_3H_zO_y$	T=260°C f.r=3 o.r.=1.6 Et_{OH}=14.4%	81.9	100% after 75h	0.31	(Fang et al., 2016)
NiCo-MgAl (Ni+Co=20 wt%) Traditional synthesis	T=550°C f.r.=3 o.r.=0.5 Et_{OH}=12.8%	47.3	100% after 100h	0.072	(Muñoz et al., 2016)
NiCo-5PrMgAl	T=550°C f.r.=3 o.r.=0.5 Et_{OH}=12.8%	47.3	100% after 100h	0.044	
NiCo-5CeMgAl	T=550°C f.r.=3 o.r.=0.5 Et_{OH}=12.8%	47.3	100% after 100h	0.049	
NiCo-MgAl (Ni+Co=20 wt%) Traditional synthesis	T=550°C f.r.=3 o.r.=0.5 Et_{OH}=12.8%	91.6	100% after 100h	7.7	(Muñoz et al., 2017)

NiCo-MgAl (Ni+Co=20 wt%) Microwave assisted precipitation	T=550°C f.r=3 o.r.=0.5 Et_{OH}=12.8%	91.6	100% after 100h	7	
NiCo-MgAl (Ni+Co=20 wt%) Sonication assisted precipitation	T=550°C f.r.=3 o.r.=0.5 Et_{OH}=12.8%	91.6	100% after 100h	5.4	
1Pt-3Ni/CeO_2-SiO_2 CeO_2/SiO_2 ratio=25	T=500°C f.r.=4 o.r.=0.5 Et_{OH}=10%	4.1	100% after 100h	0.0076	(Palma et al., 2017d)
1Pt-3Ni/CeO_2-SiO_2 CeO_2/SiO_2 ratio=30	T=500°C f.r.=4 o.r.=0.5 Et_{OH}=10%	4.1	100% after 135h	0.0012	
1Pt-3Ni/CeO_2-SiO_2 CeO_2/SiO_2 ratio=40	T=500°C f.r.=4 o.r=0.5 Et_{OH}=10%	4.1	100% after 120h	0.0065	
15Ni/$MgAl_2O_4$	T=500°C f.r.=3 o.r.=0.5 Et_{OH}=2.5%	9.2	80% after 28h	22	(Braga et al., 2018)
4Co11Ni/$MgAl_2O_4$	T=500°C f.r.=3 o.r.=0.5 Et_{OH}=2.5%	9.2	70% after 28h	21	
7.5Co7.5Ni/	T=500°C	9.2	70%	7.1	

$MgAl_2O_4$	f.r.=3 o.r.=0.5 Et_{OH}=2.5%		after 28h		
11Co4Ni/$MgAl_2O_4$	T=500°C f.r.=3 o.r.=0.5 Et_{OH}=2.5%	9.2	60% after 28h	6.7	
15Co/$MgAl_2O_4$	T=500°C f.r.=3 o.r.=0.5 Et_{OH}=2.5%	9.2	60% after 28h	1.9	
4Co4Ni/$MgAl_2O_4$	T=500°C f.r.=3 o.r.=0.5 Et_{OH}=2.5%	9.2	60% after 28h	0.11	
$La_2Ce_{1.8}Ru_{0.2}O_7/La_2Zr_2O_7$	T=400°C f.r.=3 o.r.=0.6 Et_{OH}=14.6%	28.1	100% after 100h	0.0013	(Hsieh et al., 2019b)
$Mg_xLa_{2-x}Ce_{1.8}Ru_{0.2}O_7/La_2Zr_2O_{7-\delta}$	T=400°C f.r.=3 o.r.=0.6 Et_{OH}=14.6%	28.1	100% after 100h	0.00021	
$Ca_xLa_{2-x}Ce_{1.8}Ru_{0.2}O_7/La_2Zr_2O_{7-\delta}$	T=400°C f.r.=3 o.r.=0.6 Et_{OH}=14.6%	28.1	100% after 100h	0.0011	

[a] the metal or oxides loadings are intended for weight of catalyst
[b] all the tests were performed at atmospheric pressure
[c] referred to the ethanol mass flow-rate
[d] carbon formation rate $g_{coke}\cdot g_{catalyst}^{-1}\cdot g_{carbon,fed}^{-1}\cdot h^{-1}$, multiplied for 10^3

In particular, among the investigated catalytic samples, the lowest carbon formation was recorded in the presence of rare earth oxides or magnesium oxides, which appears as promising candidate for improving catalyst stability during oxidative steam reforming of bioethanol.

II.3 Catalysts development: background

According to the results described in the previous paragraphs, the selection of rare earth oxides (i.e. ceria) as catalytic supports as well as the choice of noble metals as active species assure high activity and stability during oxidative steam reforming of ethanol; transition metals (including nickel and cobalt) also displayed a satisfactory performance for the desired reaction. However, ceria nonopowders have a cohesive character and a market tendency to channeling (Group C of Geldard diagram) during fluidization. In this regard, Ni/CeO_2-ZrO_2/SiO_2, NiCo@SiO_2, Ni/SiO_2, Ni/Al_2O_3, Ni/La_2O_3/Al_2O_3 and Ni/Al_2O_3 has been reported as promising formulations for reforming reactions in fluidized beds (Gao et al., 2008, Zhao et al., 2018, Vicente et al., 2014b, Yus et al., 2018). Nonetheless, as described above, alumina, due to the presence of acidic sites, promotes ethanol dehydration, followed by ethylene formation, which is a well-known coke precursor. Thus, SiO_2 was selected to assure the desired fluidization properties to the final formulation. In particular, in the attempt of improving metals dispersion on rare earth oxides (well-known for their oxygen storage and release capacity, but also for their relatively low surface areas), mesoporous silica gel was selected as carrier and a mixed CeO_2-SiO_2 oxide was proposed for metals supporting.

Chapter II

Chapter III

III Thermodynamic analysis

III.1 Thermodynamic aspects of ethanol reforming

Ethanol steal reforming is a highly endothermic reaction and a great amount of heat is required to sustain the process. The necessary heat can be supplied either externally by burning a fuel or internally by co-feeding oxygen and burning a part of the ethanol (Graschinsky et al., 2012).

Under a thermodynamic point of view, at very low temperatures, no reaction occurs between ethanol and water while only ethanol decomposition can be observed; conversely, ethanol steam reforming is a feasible reaction above 227°C, with methane, hydrogen and carbon oxides being the major products (García and Laborde, 1991). In fact, ethanol reacts at very low temperatures, with hydrogen formation instead of methane being favoured by increasing temperatures. Other species, such as ethylene, acetone and acetaldehyde, may coexist in the reacting system.

Coke formation is reported for steam to ethanol ratios lower than the stoichiometric value of 3. In this regard, oxygen co-feeding has been proposed as a viable route to mitigate the deposition of carbonaceous deposits. In addition, by adding oxygen/air to the reacting mixture, it is also possible to provide the energy required for the endothermic reaction (Rabenstein and Hacker, 2008). In particular, by properly adjusting the feeding ratio (C_2H_5OH:H_2O:O_2), a thermally neutral or slightly exothermic process can be achieved.

By changing the temperature, the oxygen/ethanol as well as water/ethanol ratio, different auto-thermal points can be reached. For example, Liu et al. found that, at 627 °C, the enthalpy of the oxidative steam reforming reaction reaches the zero value for H_2O/C_2H_5OH ratio of 1,2,3, 4 and 7 with corresponding O_2/C_2H_5OH ratio of 0.64, 0.75, 0.82, 0.88 and 1.03 (Liu et al., 2008). It was also reported that, for steam to ethanol ratio in the interval 0-10 and oxygen to ethanol ratio ranging from 0 to 3, the auto-thermal point moves to higher temperatures by increasing the O_2/C_2H_5OH ratio while higher water contents in the reforming mixture move the auto-thermal point towards lower temperatures (Sun et al., 2012).

Most of the thermodynamic studies focused on oxidative steam reforming of ethanol also involves nitrogen co-feeding, as air is economically preferred rather than oxygen.

III.2 Method for the calculation of the equilibrium composition

In order to calculate the products distribution under equilibrium conditions, the implement of the method based on the equilibrium constants is very complex for reacting systems (like the current one) involving numerous simultaneous reactions. Thus, in the present thesis, the thermodynamic aspects of ethanol reforming have been investigated by using the software GasEq (Simson et al., 2009), which allows calculating the chemical equilibrium for perfect gases mixtures. The thermodynamic analysis by means of the GasEq software is based on the Gibbs free energy minimization method, which can be easily applied to multicomponent systems in the presence of a great number of reactions.

The total Gibbs free energy of the system (*G*, eq. (III. 1)) is related to the initial moles *n* of every species *s*, to the Gibbs free energy of the i-species under normal conditions (NTP) of temperature and pressure (G_i°) and to the Gibbs free energy of the same species under the operative conditions (G_i). The difference between the two latter values of free energies depends on the fugacity of the i-species at NTP (f_i°) and its fugacity under the selected operative conditions f_i (eq. ((III. 2)), where R_g is the state constant of the gases).

$$G = \sum_{i=1}^{s} n_i \cdot G_i = \sum_{i=1}^{s} n_i \cdot \left[\left(G_i - G_{i^\circ} \right) + G_i^\circ \right] \qquad \text{(III. 1)}$$

$$\left(G_i - G_i^\circ \right) = R_g \cdot T \cdot \ln\left(\frac{f_i}{f_i^\circ} \right) \qquad \text{(III. 2)}$$

All the species in the system are intended as gases and the ratio between the fugacities can be expressed as shown in eq. (III. 3), where *P* is the total pressure of the system, *n* are the total moles of the gaseous system (including those of the unreacted species), y_i is the molar fraction of the i-species and γ_i its fugacity.

$$\frac{f_i}{fi^\circ} = y_i \cdot \gamma_i \cdot P = \frac{n_i}{n} \cdot \gamma_i \cdot P \qquad \text{(III. 3)}$$

Under the hypothesis of perfect gas mixture, the fugacity of all the species is equal to 1 and eq. (III. 1) becomes:

$$G = \sum_{i=1}^{s} n_i \cdot R_g \cdot T \cdot \left[\frac{G_i^\circ}{R_g \cdot T} + \ln\left(\frac{n_i}{n}\right) + \ln P \right] \qquad \text{(III. 4)}$$

The product of temperature and the gas constant is not dependent on the composition; thus, the final expression of G is reported in eq. (III. 5).

$$\frac{G}{R_g \cdot T} = \sum_{i=1}^{s} n_i \left[\frac{G_i^\circ}{R_g \cdot T} + \ln\left(\frac{n_i}{n}\right) + \ln P \right] \qquad \text{(III. 5)}$$

The software can calculate the n_i values minimizing the objective function (eq. (III. 5)) under the constraints fixed by the mass elementary balance (eq. (III. 6)).

$$\sum_{j=1}^{m} a_{ji} = b_j \qquad \text{(III. 6)}$$

In eq. (III. 6), *aji* is the number of gram atoms of the j^{th} atomic element in a mole of i^{th} species, *m* is the number of elements present in the reaction mixture, b_j is the total number of gram atoms of j^{th} in the reaction mixture and *s* is the number of species present in the reaction mixture.

The general reaction used for the thermodynamic analysis is reported in eq. (*III. 7*).

$$\begin{aligned} &xC_2H_5OH + yH_2O + zO_2 \leftrightarrow aC_2H_5OH + \\ &bH_2O + cO_2 + dH_2 + eCH_4 + fCO + gCO_2 + \\ &hC_2H_4O + iC_3H_6O + lC_{(s)} \end{aligned} \qquad \text{(III. 7)}$$

Together with the gaseous species present in the reacting system, one species in solid phase is also taken into account (carbon in graphite form). Moreover, acetone, acetaldehyde and ethylene have been included in the thermodynamic study, as their formation during oxidative steam reforming of ethanol has been reported (Cai et al., 2008, Hung et al., 2012). In order to analyse coke formation for a thermodynamic point of view, it is assumed that carbon formed is elemental and in the graphitic form; thus, free energy of carbon formation is zero and vapour pressure is zero in the range of temperature analysed. As a consequence, the total Gibbs free energy can be considered to be independent of carbon. However, the amount of carbon can be included in the elemental mass balance.

The results of the thermodynamic analysis are reported in terms of ethanol conversion, selectivity to products and hydrogen yield, as shown in eq. (III. 8)-(III. 17).

$$X_{C2H5OH}(\%) = \frac{mol_{C2H5OH,in} - mol_{C2H5OH,out}}{mol_{C2H5OH,in}} \cdot 100 \qquad \text{(III. 8)}$$

$$Y_{H2}(\%) = \frac{mol_{H2}}{6 \cdot mol_{C2H5OH,in}} \cdot 100 \qquad \text{(III. 9)}$$

$$S_{H2}(\%) = \frac{mol_{H2}}{6 \cdot (mol_{C2H5OH,in} - mol_{C2H5OH,out})} \cdot 100 \qquad \text{(III. 10)}$$

$$S_{CH4}(\%) = \frac{mol_{CH4}}{2 \cdot (mol_{C2H5OH,in} - mol_{C2H5OH,out})} \cdot 100 \qquad \text{(III. 11)}$$

$$S_{C2H4}(\%) = \frac{mol_{C2H4}}{mol_{C2H5OH,in} - mol_{C2H5OH,out}} \cdot 100 \qquad \text{(III. 12)}$$

$$S_{C2H4O}(\%) = \frac{mol_{C2H4O}}{mol_{C2H5OH,in} - mol_{C2H5OH,out}} \cdot 100 \qquad \text{(III. 13)}$$

$$S_{C3H6O}(\%) = \frac{3 \cdot mol_{C3H6O}}{2 \cdot (mol_{C2H5OH,in} - mol_{C2H5OH,out})} \cdot 100 \qquad \text{(III. 14)}$$

$$S_{CO}(\%) = \frac{mol_{CO}}{2 \cdot (mol_{C2H5OH,in} - mol_{C2H5OH,out})} \cdot 100 \qquad \text{(III. 15)}$$

$$S_{CO2}(\%) = \frac{mol_{CO2}}{2 \cdot (mol_{C2H5OH,in} - mol_{C2H5OH,out})} \cdot 100 \qquad \text{(III. 16)}$$

$$S_{C(s)}(\%) = \frac{mol_{C(s)}}{2 \cdot (mol_{C2H5OH,in} - mol_{C2H5OH,out})} \cdot 100 \qquad \text{(III. 17)}$$

The equilibrium calculations were performed at ambient pressure, from 100 to 1000°C by changing the steam to ethanol ratio (f.r.) from 1 to 8 and the oxygen to ethanol ratio (o.r.) from 0 to 1.

Under all the investigated operative conditions, ethanol was completely converted; thus, products selectivity and yield were the same. Moreover, ethylene, acetaldehyde and acetone were absent at the equilibrium.

III.3 Effect of the steam to ethanol ratio

A preliminary thermodynamic analysis was performed by fixing the oxygen to ethanol ratio to zero; under these conditions, the effect of the steam to ethanol ratio on products yield was investigated as a function of the reaction temperature. Hydrogen yield increases for a growth in the reaction temperature above 200°C: due to the endothermicity of steam reforming reaction, an improvement in H_2 production rate is predicted at high temperatures (Figure III. 1). However, this results are true only below 600°C: by increasing the temperature in the interval 600-1000°C, a slight decrease in the H_2 yields profiles was observed for feeding ratios above 3, due to the contribution of the exothermic water gas shift reaction. For example, at feeding ratios slightly higher than the stoichiometric value (f.r = 4), the maximum H_2 yield is recorded between 600 and 700°C, with values of almost 80%.

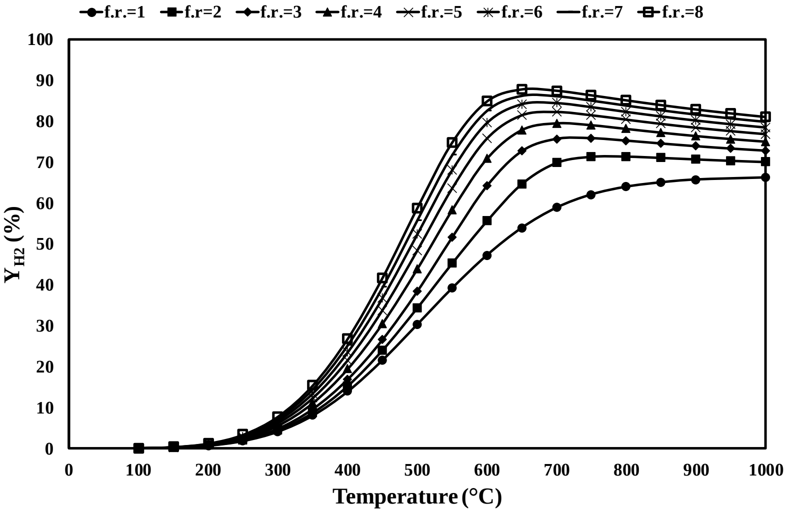

Figure III. 1 *Hydrogen yield as a function of the reaction temperature and steam to ethanol ratio; P=1 atm without oxygen.*

A growth in the steam to ethanol ratio is beneficial in terms of hydrogen selectivity as a consequence of the more promoted reforming reactions. CO selectivity (Figure III. 2) is unaffected by temperature and steam to ethanol ratio changes below 350°C: CO formation is not predicted at low temperatures due to the contribution of the exothermic water gas shift reaction. Following thermodynamic predictions, at high temperatures it is possible to reduce carbon monoxide yield by increasing the steam to ethanol ratio: for example, at 750°C, a change in the f.r. from 1 to 8 resulted in a CO reduction of almost 1 half. Carbon dioxide selectivity profile (Figure III. 3) displays a maximum between 400 and 600°C, whatever the selected steam to ethanol ratio: in fact, at low temperatures, the exothermic water gas shift is promoted while, at temperatures above 600°C, the contribution of the reverse water gas shift is more pronounced.

Methane conversion is promoted at high temperatures and high steam to ethanol ratios, due to the contribution of the endothermic steam reforming: for f.r. higher than 2, methane yield is negligible above 700°C (Figure III. 4). Coke yield reaches considerable values for low feeding ratios in the whole temperature interval, while for f.r. at least equal to the stoichiometric value of 3, coke selectivity is equal to zero above 250°C (Figure III. 5).

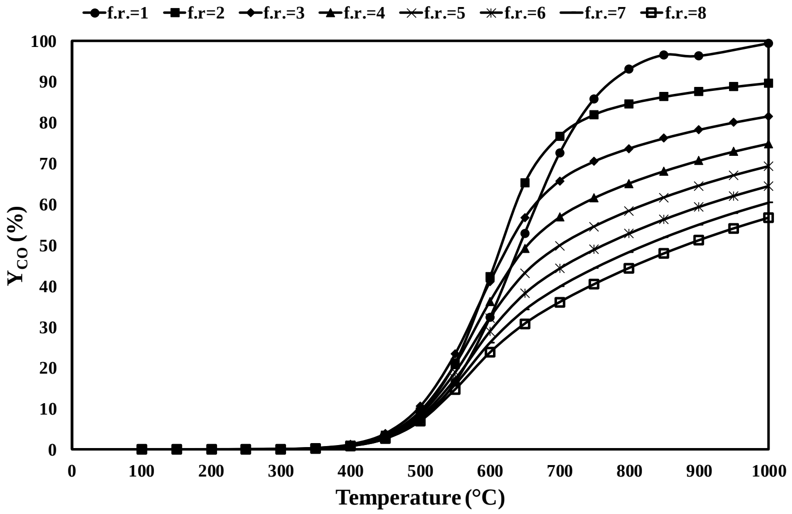

Figure III. 2 *Carbon Monoxide selectivity as a function of the reaction temperature and steam to ethanol ratio; P=1 atm without oxygen.*

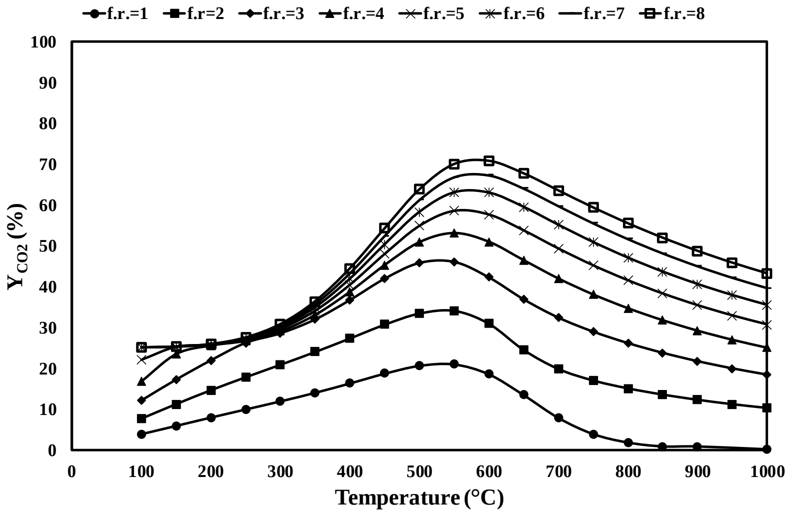

Figure III. 3 *Carbon Dioxide selectivity as a function of the reaction temperature and steam to ethanol ratio; P=1 atm without oxygen.*

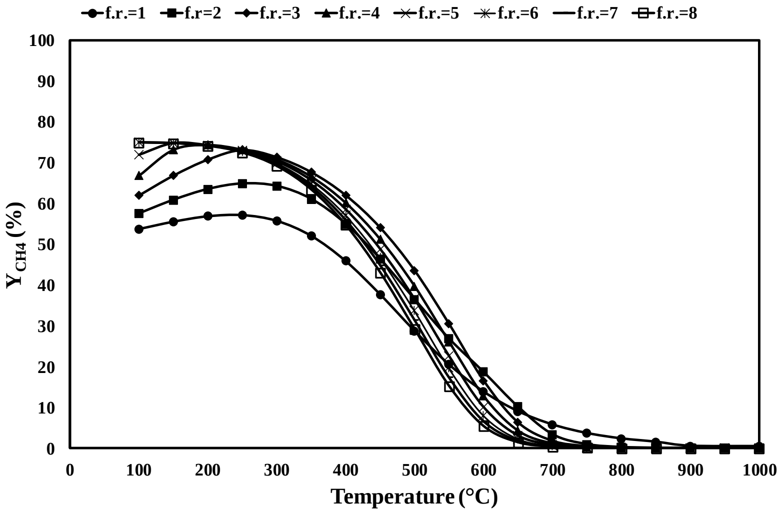

Figure III. 4 *Methane yield as a function of the reaction temperature and steam to ethanol ratio; P=1 atm without oxygen.*

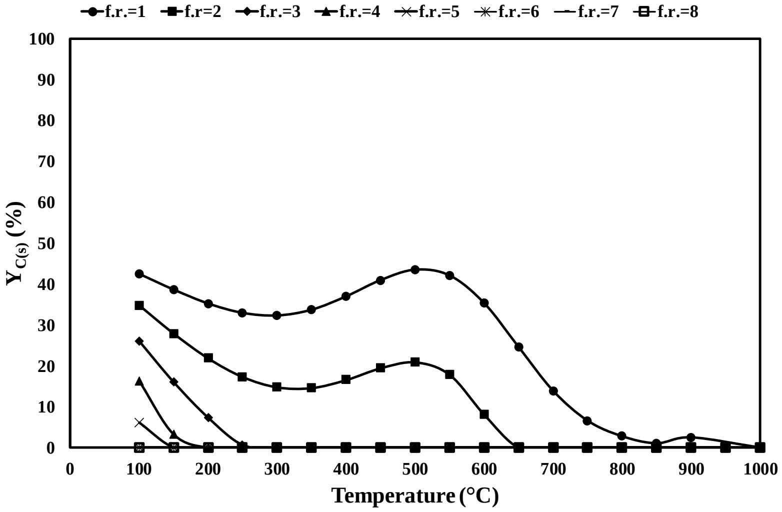

Figure III. 5 *Coke selectivity as a function of the reaction temperature and steam to ethanol ratio; P=1 atm without oxygen.*

The results of thermodynamic analysis reveal that high temperatures and high steam to ethanol ratios are required to increase H_2 yield. However, as discussed above (Par. I.5.1), considerable water contents are prohibitive in terms of vaporization costs. On the other hand, steam to ethanol ratios slightly higher than the stoichiometric value (f.r. of 3) are sufficient to assure satisfactory H_2 yields, allowing, at the same time, low CO levels (a critical issue especially when the produced H_2 is fed to fuel cells) for reaction temperatures below 600°C. Therefore, the effect of oxygen to ethanol ratio was investigated for a feeding ratio of 4.

III.4 Effect of the oxygen to ethanol ratio

As depicted in Figure III. 6, the increase of the o.r. ratio below 500°C has a negligible impact on hydrogen yield while, at higher temperatures, a growth in the oxygen to ethanol ratio from 0 to 1 resulted in a reduction of the hydrogen production rate of more than 30% at 800°C.

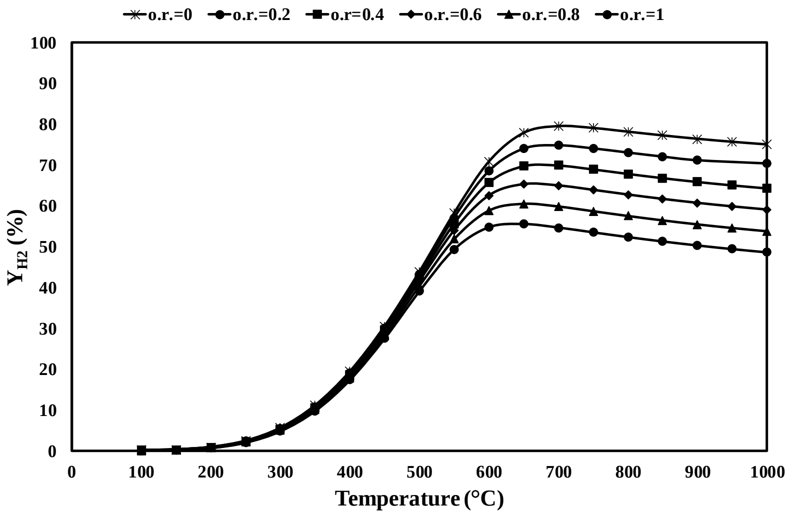

Figure III. 6 *Hydrogen yield as a function of the reaction temperature and oxygen to ethanol ratio; P=1 atm and steam to ethanol ratio of 4.*

Higher oxygen contents also promote CO conversion (Figure III. 7), especially at temperatures higher than 500°C, with a consequent growth in CO_2 selectivity (Figure III. 8).

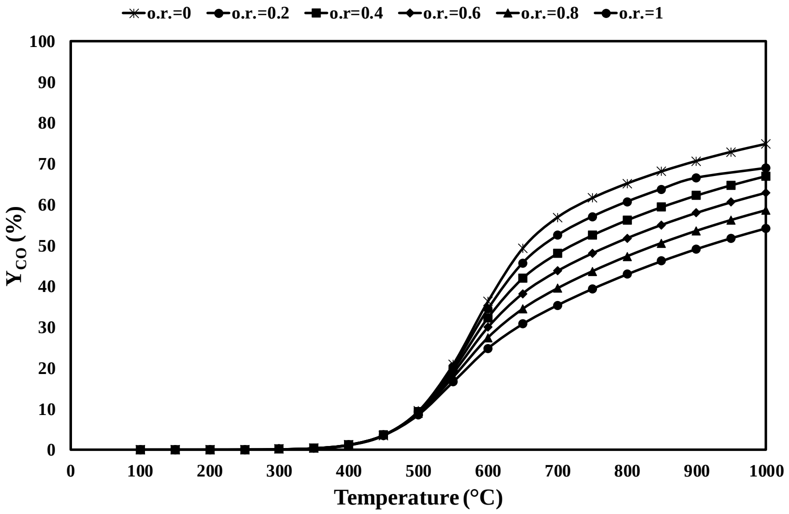

Figure III. 7 *Carbon monoxide selectivity as a function of reaction temperature and oxygen to ethanol ratio; P=1 atm and steam to ethanol ratio of 4.*

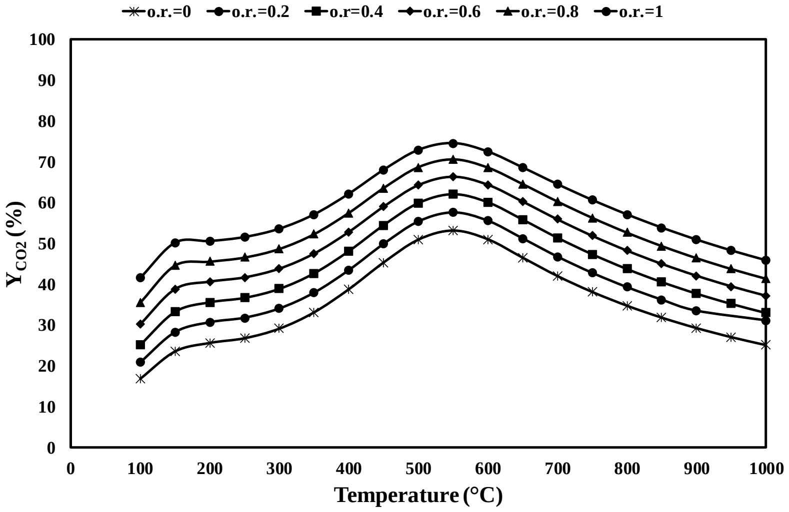

Figure III. 8 *Carbon monoxide selectivity as a function of reaction temperature and oxygen to ethanol ratio; P=1 atm and steam to ethanol ratio of 4.*

CH_4 production rate is affected by o.r. below 700°C and methane yield decreases from 71 to 46% at 300°C, due to the contribution of oxidation reactions (Figure III. 9). Coke yield is practically unaffected by the oxygen to ethanol ratio and a negligible formation of carbonaceous species is observed above 200°C (Figure III. 10).

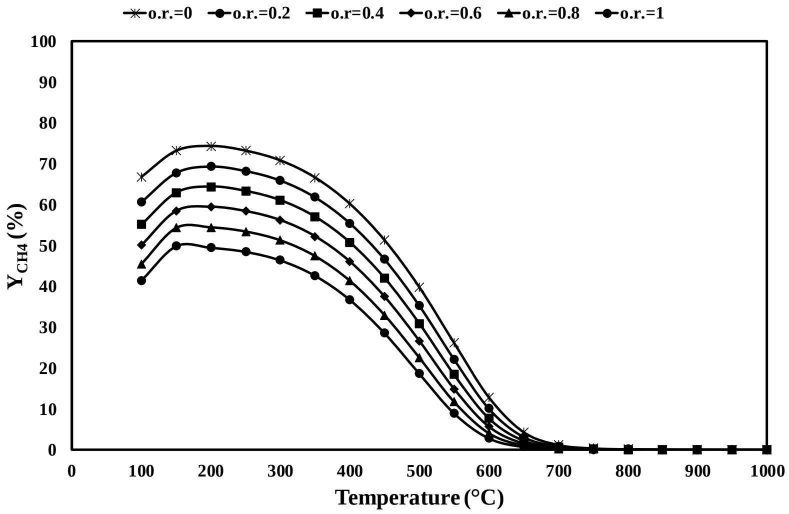

Figure III. 9 *Methane selectivity as a function of reaction temperature and oxygen to ethanol ratio; P=1 atm and steam to ethanol ratio of 4.*

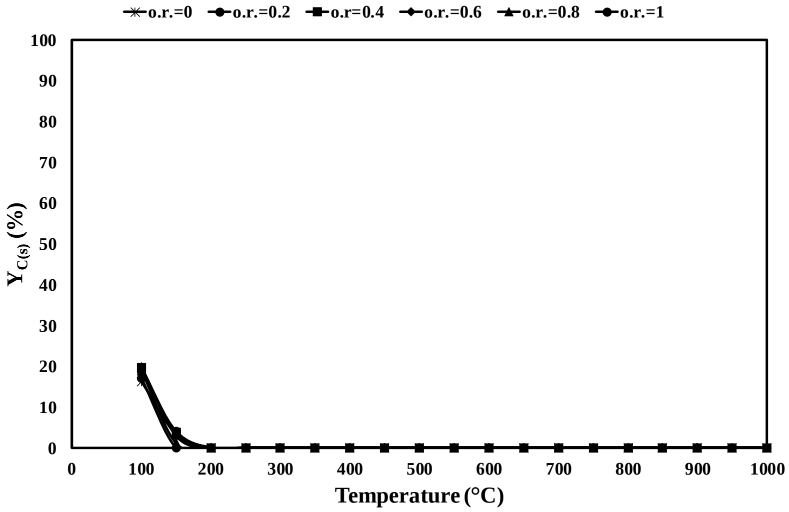

Figure III. 10 *Coke selectivity as a function of reaction temperature and oxygen to ethanol ratio; P=1 atm and steam to ethanol ratio of 4.*

The choice of adding oxygen to the reaction system is dictated by the necessity of reducing external thermal duties by exploiting the exothermic contribution of oxidation reactions. In this regard, the effect of oxygen to ethanol ratio on the reaction enthalpy was also investigated as a function of the reaction temperature: such analysis will help to shed light on the temperature at which the system reaches autothermal conditions for a datum oxygen to ethanol ratio (Figure III. 11). On the basis of the above results, an intermediate value in the investigated o.r. interval was selected for preliminary tests under oxidative conditions which, following the thermodynamic predictions, is expected to still assure satisfactory H_2 yield at intermediate temperatures.

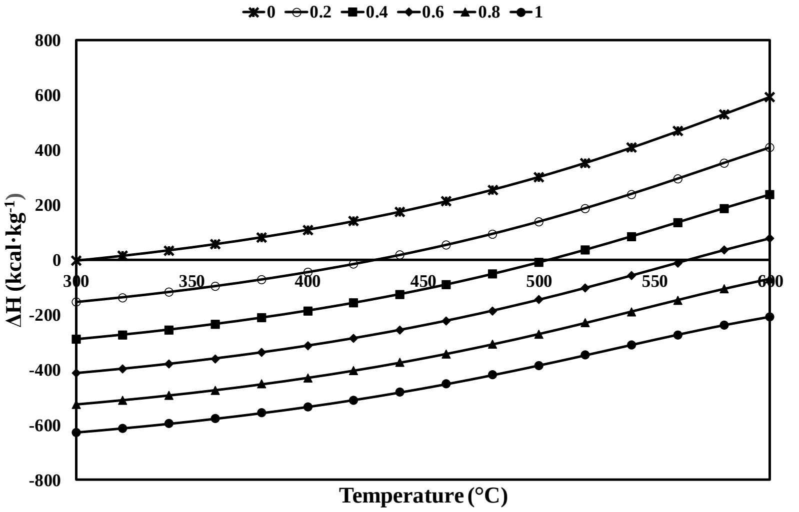

Figure III. 11 *Specific enthalpy per unit of fed mixture as a function of temperature and oxygen to ethanol ratio for a steam to ethanol molar ratio of 4.*

III.5 Choice of the operative conditions

The results of thermodynamic analysis reveal that high temperatures and water contents in the reforming mixture promote hydrogen production via reforming. However, the choice of proper reactor configurations (i.e. membrane reactors) can allow reaching the desired hydrogen productivity by working at lower temperatures (below 600°C), with a considerable reduction of the plant fixed costs. Moreover, thermodynamics predicts that, in the low temperature interval, where carbon formation may be significant during ESR, coke selectivity can be considerably reduced by adding oxygen (as highlighted by the comparison of Figure III. 5 and Figure III. 10). Thus, it can be sufficient to select water/ethanol ratio slightly higher than the stoichiometric value to avoid coke deposition.

As described above, the addition of oxygen to the reacting mixture is beneficial under both the point of view of catalyst stability (reduced carbon formation) and lessened operative costs (low or zero thermal duty for the reformer). However, it is expected to reduce hydrogen production rate, due to the combustion of a portion of the H_2 to steam.

In this regard, for the thermodynamic analysis, the water to ethanol ratio was fixed to 4 and the oxygen to ethanol ratio to 0.5 and a comparison was made between the hydrogen yield during steam reforming and oxidative steam reforming. The results are shown in Figure III. 12. It is very interesting noting that, below 500°C, the two profiles are very close and the effect of oxygen addition on hydrogen selectivity is negligible.

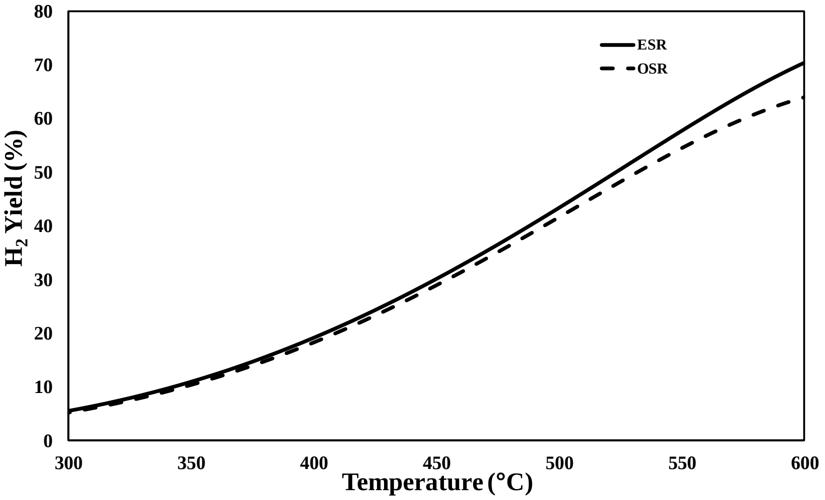

Figure III. 12 *Comparison between hydrogen yield during ethanol steam and oxidative reforming; f.r.=4 and o.r.=0.5.*

Thus, according to the results of thermodynamic analysis, it is possible to work under oxidative conditions with a negligible effect on hydrogen selectivity. These theoretical results were also confirmed by experimental tests over bimetallic catalysts supported on CeO_2/SiO_2 (Palma et al., 2017a).

Based on the above discussion, the operative conditions for preliminary activity and stability tests were fixed as follows: f.r=4, o.r.=0.5 and T ranging from 300 to 600°C.

Chapter IV

IV Experimental

IV.1 Catalysts preparation

Bimetallic catalysts supported on a mixed oxide CeO_2-SiO_2 were prepared by the wet impregnation method.

Three different cerium salt precursors were selected for catalysts preparation: cerium nitrate hexahydrate (99.0%, Strem Chemicals), cerium ammonium nitrate hexahydrate (99.0%, Strem Chemicals) and cerium acetyl acetonate hydrate (99.9%, Alfa-Aesar). The nitrates were easily dissolved in distilled water while, for the organic salt, a mixture composed by 40% of glacial acetic acid (Pure, Carlo Erba Reagents) in methanol (≥ 99.8, Sigma-Aldrich) and heated at 50°C was used. The samples prepared from cerium nitrate hexahydrate, cerium ammonium nitrate hexahydrate and cerium acetyl acetonate hydrate were denoted respectively as NH, ANH and AAH.

In the first part of the work, cerium nitrate hexahydrate was employed as cerium precursor; thereafter, the effect of CeO_2 salt precursor on the catalyst performance was investigated and the most suitable salt was selected, which was used henceforth. Independently from the selected cerium precursor, the ceria/silica ratio was fixed to 30 wt%.

The catalyst preparation procedure was developed starting from the measurement of the blank solution adsorption (aqueous or organic) at 80 °C for 2 h by a certain amount of calcined silica (the treatment of calcination was performed in air from ambient temperature to 600°C with a heating rate of $10°C\cdot min^{-1}$ and the final temperature was held for 3 hours). After impregnation, the solid was separated through a vacuum system by means of a Buckner filter (porosity II). Based on the solution volume adsorbed by silica during the above measurements, the cerium salt amount to be added in order to reach the desired loading can be calculated. The same approach was followed for metals deposition.

Table IV. 1 *List of the investigated catalysts.*

Catalyst	**CeO_2 precursor (%)**	**Metals loading**
Pt-Ni/CeO_2-SiO_2	NH	10 wt% Ni 3 wt% Pt
Pt-Ni/CeO_2-SiO_2	ANH	10 wt% Ni 3 wt% Pt
Pt-Ni/CeO_2-SiO_2	AAH	10 wt% Ni 3 wt% Pt
Pt-Co/CeO_2-SiO_2	NH	10 wt% Co 3 wt% Pt
K-Pt-Co/CeO_2-SiO_2	NH	10 wt% Co 3 wt% Pt 0.5 wt% K
Ni-Co/CeO_2-SiO_2	NH	10 wt% Co 10 wt% Ni
Ni/CeO_2-SiO_2	AAH	10 wt% Ni
0.5Ag-Ni/CeO_2-SiO_2	AAH	10 wt% Ni 0.5 wt% Ag
1Ag-Ni/CeO_2-SiO_2	AAH	10 wt% Ni 1 wt% Ag
2Ag-Ni/CeO_2-SiO_2	AAH	10 wt% Ni 2 wt% Ag
3Ag-Ni/CeO_2-SiO_2	AAH	10 wt% Ni 3 wt% Ag
0.5Ru-Ni/CeO_2-SiO_2	AAH	10 wt% Ni 0.5 wt% Ru
1Ru-Ni/CeO_2-SiO_2	AAH	10 wt% Ni 1 wt% Ru
2Ru-Ni/CeO_2-SiO_2	AAH	10 wt% Ni 2 wt% Ru
3Ru-Ni/CeO_2-SiO_2	AAH	10 wt% Ni 3 wt% Ru
0.5Pt-Ni/CeO_2-SiO_2	AAH	10 wt% Ni 0.5 wt% Ru
1Pt-Ni/CeO_2-SiO_2	AAH	10 wt% Ni 1 wt% Ru
2Pt-Ni/CeO_2-SiO_2	AAH	10 wt% Ni 2 wt% Ru

The first step of catalyst preparation involved CeO_2 deposition on silica gel (pore size 60 Å, supplied by Sigma-Aldrich).

In the case of cerium nitrate, the salt was dissolved in deionized water at ambient temperature (concentration of 1.5 M); afterwards, calcined SiO_2 was added to the solution and impregnation was carried out at 80 °C for 2 hours. The resulting suspension was filtered and the solid dried overnight and calcined at 600 °C for 3h (heating rate of 10 °C min^{-1}). The above procedure involves an impregnation-precipitation method: during impregnation, the inclusion of cerium nitrate solution in silica meso-pores occurred while, during catalyst drying, salt precipitation on catalyst surface was assured.

Different catalysts, reported in Table IV. 1, were prepared. The tested catalysts contained a non-noble metal (Nickel or Cobalt) and a noble metal (Platinum, Silver or Ruthenium). A Ni/CeO_2-SiO_2 catalyst was also prepared for comparison. For the bimetallic formulations, the noble metal was impregnated after the Ni (or Co) deposition.

For Ni (or Co) and Pt impregnation, a known amount of nickel nitrate hexaydrate supplied by Strem Chemicals (or cobalt nitrate hexahydrate, Sigma Aldrich) and platinum chloride (Strem Chemicals) was dissolved in deionized water, with a concentration of 0.7 M for Ni (or 0.6 M in the case of cobalt) and 0.06 M for Pt. After impregnation, the same procedure reported above was followed. Non-noble and noble metal content was fixed to 10 wt% and 3 wt%, respectively, on the basis of ceria mass. The impregnation order (Ni or Co earlier than Pt), as well as ceria loadings were previously optimized (Palma et al., 2017d, Palma et al., 2014). For the K-Pt-Ni based sample, potassium was deposited on the Pt-Ni/CeO_2/SiO_2 catalyst starting from an aqueous solution of KOH (Sigma-Aldrich) having a concentration of 0.02 M and the alkali metal loading was 0.5 wt% with respect to ceria mass.

The effect of noble metal loading on the performance of the bimetallic catalyst was also investigated and the noble metal content (Pt, Ag or Ru) was varied from 0.5 to 3 wt%; $PtCl_4$ (Strem Chemicals), $AgNO_3$ (SigmaAldrich) and $RuCl_3 \cdot xH_2O$ (SigmaAldrich) were selected as salt precursors.

IV.2 Catalysts characterization

Different techniques were used for the characterization of the fresh and spent catalysts, aiming to correlate their physiochemical properties with samples activity and stability. In the following paragraphs, the different techniques, including X-ray diffraction (XRD), Thermogravimetric analysis (TGA), Temperature programmed reduction (TPR), Zero point charge (ZPC) and surface area (BET) measurements, will be briefly described.

IV.2.1 X-ray Fluorescence (XRF)

The chemical composition of the samples was determined by X-ray fluorescence (XRF) spectrometry in a ThermoFischer QUANT'X EDXRF spectrometer equipped with a rhodium standard tube as the source of radiation; a compressed tablet of the powder was analysed by the Fundamental Parameters method.

IV.2.2 X-ray Diffraction (XRD)

X-ray power diffraction (XRD) patterns were recorded under a CuKα radiation (λ=1.5406 Å) using a D-8 Advance Bruker WAXRD instrument and Scherer formula was employed to evaluate crystallites dimensions; the samples were scanned over a 2Θ range of 10–80° with a step of 0.05°.

IV.2.3 Specific surface area measurements (BET)

The specific surface areas of all the samples were estimated from the nitrogen isotherms using the BET (Branauer-Emmet-Teller) method: after degassing at 150 °C for 2 hours, adsorption-desorption measurements were performed at -196 °C in a Micromeritics ASAP 2020.

IV.2.4 Temperature Programmed Reduction (TPR)

The reduction behaviour of the fresh catalysts was investigated in situ in the laboratory apparatus described below (Par.IV.3): temperature programmed reduction (TPR) measurements were performed by using a 500 $Ncm^3\ min^{-1}$ flow of a hydrogen/argon stream at a volumetric H_2 content of 5%, while temperature was increased up to 800 °C with an heating rate of 10 °C min^{-1}. The final temperature was held for 1 hour.

IV.2.5 Temperature Programmed Oxidation (TPO)

The oxidation profile of the spent catalysts was investigated in situ in the laboratory apparatus described below (Par.IV.3): temperature programmed reduction (TPO) measurements were performed by using a 500 $Ncm^3\ min^{-1}$ flow of an oxygen/argon stream at a volumetric O_2 content of 5%, while temperature was increased up to 800 °C with an heating rate of 10 °C min^{-1}.

IV.2.6 Thermogravimetric Analysis (TGA)

Thermogravimetric analysis (TGA) is a technique which allows measuring the weight change in a material as a function of temperature and time, in a controlled environment. The extent of carbon deposition on the catalysts used in the experiments was investigated by thermogravimetric analysis (TGA) in the TA Instrument Q600. This instrument is coupled with a PFEIFFER Quadrupole Mass Spectrometer (MS) in order to analyse the gaseous products leaving the solid material.

IV.2.7 Zero Point Charge measurements (ZPC)

Mass titration method was used to estimate the point of zero charge (PZC) of all samples. ZPC was measured using the mass titration method proposed by Noh and Schwarz (Noh and Schwarz, 1989). The solid material was suspended in a mixed aqueous solution and the pH of the system was monitored by means of a device for the pH measurements provided by Labwaretools (model PC 62 DHS). During the analysis, for high mass fractions, a constant pH was reached and this limiting value assures a reasonable estimation for the point of zero charge of the solid.

IV.2.8 MicroRaman Spectroscopy

The Raman spectra were produced in a Dispersive MicroRaman (Invia, Renishaw), equipped with 785 nm diode-laser, in the range 200-2000 cm^{-1} Raman shift.

IV.3 Laboratory apparatus and procedure

The plant employed for activity and stability tests in the oxidative steam reforming of ethanol has the classical configuration of a laboratory apparatus with a feed, reaction and analysis section. The schematic representation of the laboratory apparatus is shown in Figure IV. 1. A system of 2 four-way heated valves (provided by Swagelok) allows switching from the bypass to the reaction configuration: the two valves are placed in an heated block (the temperature control is done through a K thermocouple, connected to a PID temperature programmer-controller).

In the bypass configuration, the feeding stream is sent to the analysis while washing argon can be fed to the reactor and finally to the vent. In the reaction configuration, the stream exiting the boiler reaches the reactor, flows in the analysis block and, after the separation of condensable species, the stream is ultimately sent to the vent.

IV.3.1 Feed Section

The feed section is made up of different mass flow-controllers (MFC) for gases and liquid admission.

The MFC consists of a thermal mass flow sensor (thermal mass flow instruments make use of a bypass i.e. capillary bypass or bypass sensor) and a precise control valve.

One block of MFC is devoted to the calibration of the analysis system and includes two mass flow controllers provided by Brooks (for methane and carbon monoxide feeding) and one mass flow controller provided by Alicat for CO_2 admission. For these MFC, an analogic control panel is provided. All the other controllers, for hydrogen, argon, water and water/ethanol (or water/bioethanol) mixture feeding, are provided by Bronkhorst High-Tech and are digitally controlled through the PC.

During activity and stability tests, a premixed H_2O/C_2H_5OH solution was fed from a tank pressurized at 5 bar by means of nitrogen to a vaporizer (T=200 °C) through a proper mass flow controller. In the boiler, the desired flow of argon, acting as diluent, was mixed with the reacting stream.

Before every test, a mixture of 5%H_2 in N_2 can be sent to the reactor in order to assure the conversion of the metal oxides deposited on the catalyst in a metallic form (catalyst reduction).

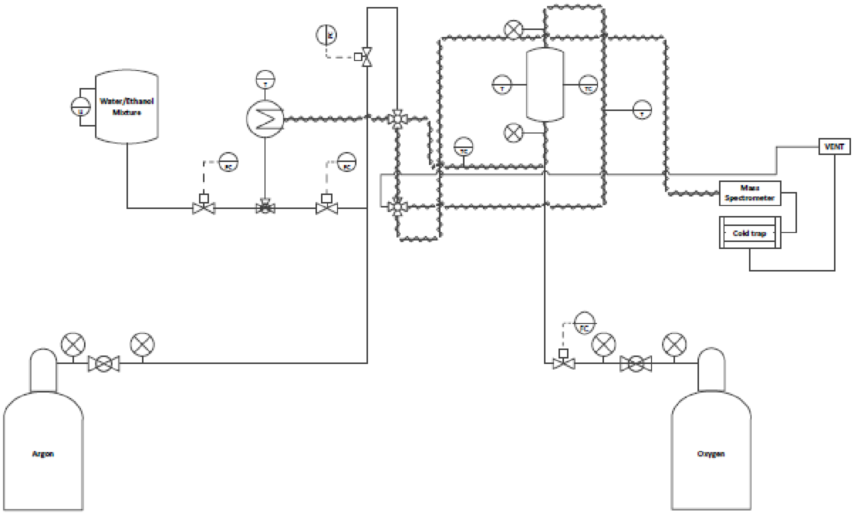

Figure IV. 1 *Scheme of the laboratory apparatus.*

All the lines after the boiler are heated at 170°C to avoid condensation and the temperature control is done through a K thermocouple, connected to a PID temperature programmer-controller (mod. TLK 43).

IV.3.2 Reaction Section: First configuration

The reaction section is composed of an electrical oven, whose temperature control is done through a K thermocouple, connected to a PID temperature programmer-controller (mod. TLK 43). Oxidative steam reforming tests were carried out in a tubular quartz reactor placed in the electrical oven and operating in a continuous mode under atmospheric pressure.

Preliminarily, an empty stainless steel (AISI-310) tubular reactor equipped with a mobile K-thermocouple was placed in the oven; an argon flow-rate of 600 $Ncm^3 \cdot min^{-1}$ was fed to the reactor and the oven controller was fixed to 500°C. By changing the thermocouple position in the empty reactor, it was possible to evaluate the thermal profile of the oven, depicted in Figure IV. 2.

As shown in Figure IV. 3 and Figure IV. 4, the reactor had an annular configuration (i.d.=2.5 cm, e.d. 4.5 cm) and contained a porous plate to block the catalytic bed in the isothermal zone of the oven (Figure IV. 2, 27-31 cm from the bottom of the oven). The reactor ends with an expansion (a kind of bubble), designed with the aim of reducing catalysts entrainment. In this regard, in order to assure a more uniform heating of the top of the reactor, an homemade heating system (visible on the top of the oven in Figure IV. 3 and shown in Figure IV. 5), was developed: also in the latter case, the temperature control is done through a K thermocouple, connected to a PID temperature programmer-controller (mod. TLK 43).

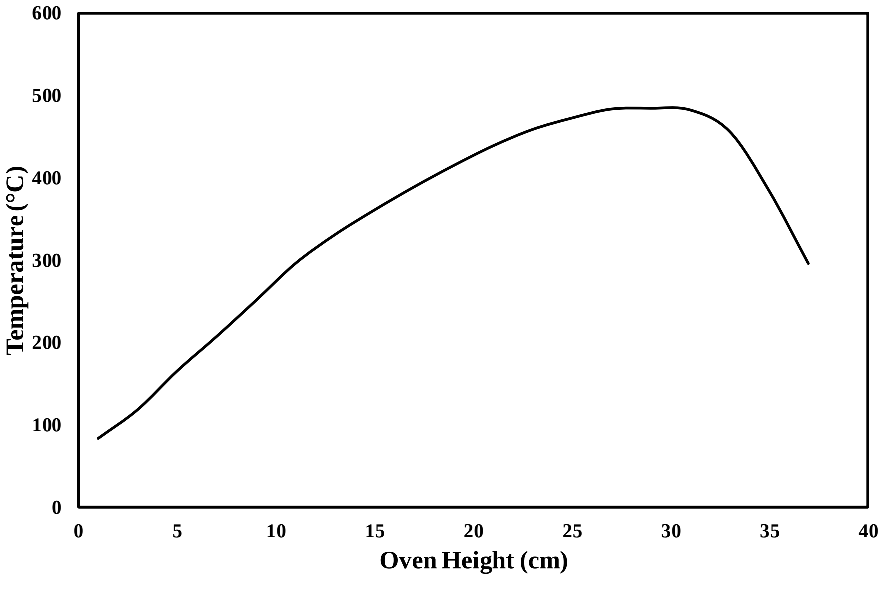

Figure IV. 2 *Thermal profile of the electrical oven.*

During catalytic tests, it was possible to measure the temperature at the catalyst end section by means of a thermocouple placed in a proper thermocouple sheet while a differential monometer allowed evaluating the pressure drops through the catalytic bed.

For oxidative steam reforming tests, oxygen was sent directly into the reactor in correspondence of the catalytic bed through an independent line, in order to limit the contribution of homogeneous reactions.

In a typical test, the catalyst (usually 7 g, 90–115 μm) diluted with the bare CeO_2-SiO_2 (90–115 μm, the volumetric ratio being 4:1) is placed into the reactor.

The choice of diluting the catalyst with the bare support is related to the potential use of the catalytic samples in the presence of membrane. Typically, in membrane reactors, the catalyst is diluted to assure the necessary contact time to the membrane for its normal operation. Such choice also allows to obtain a homogeneous and uniform fluidized bed and to exploit the available surface membrane area without requiring an increase of the catalytic mass (Roses et al., 2013).

For the development of the kinetic model, the quartz reactor was operated in a fixed bed mode and the catalyst alone, crushed and sieved to reach a particle size distribution between 180 and 355 μm, was sandwiched between two quartz flakes.

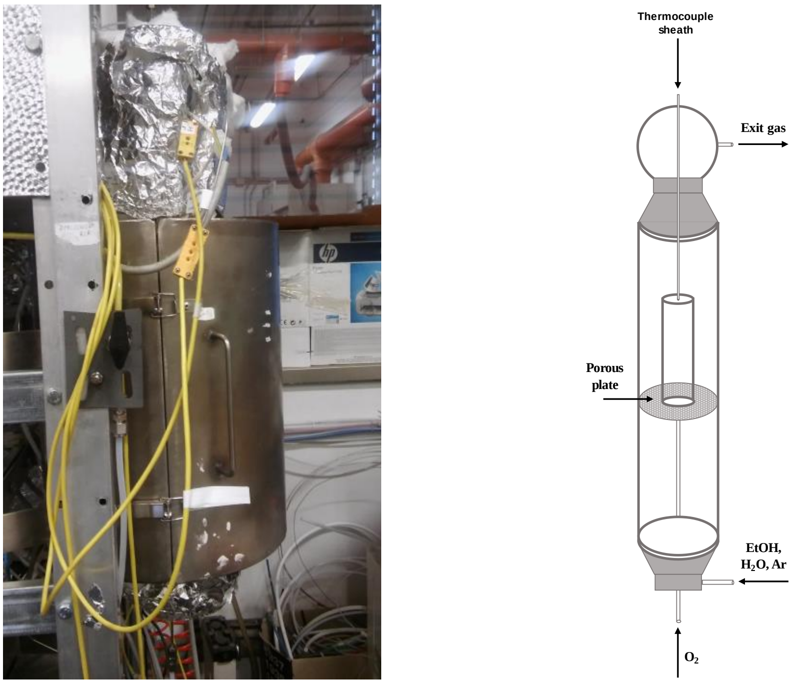

Figure IV. 3 *Picture of the electrical oven (right) and scheme of the quartz reactor (left).*

In fact, previous studies revealed that, by selecting a particle size distribution in the above range, internal and external diffusion did not play any role on reactants conversion during reforming (Ciambelli et al., 2010, Theron et al., 1997). Such phenomena are obviously avoided in the fluidized bed reactor.

In order to select the proper operative conditions of the reactor, the minimum fluidization velocity of the Pt-Ni/CeO_2-SiO_2 catalyst was investigated and it was also observed that, in the presence of different active species, the behaviour of the sample under fluidization was almost the same.

Figure IV. 6 reports the experimental results of pressure drops (ΔP) through the catalytic bed as a function of the flow-rate at 500°C.

For low flow-rates, the pressure drops increase linearly with the flow-rate while, above 120 $Ncm^3 \cdot min^{-1}$, a change of the slope was observed and a minimum fluidization velocity of 0.0018 $m \cdot s^{-1}$ was calculated, which correspond to a flow-rate of 118 $Ncm^3 \cdot min^{-1}$ (Figure IV. 6).

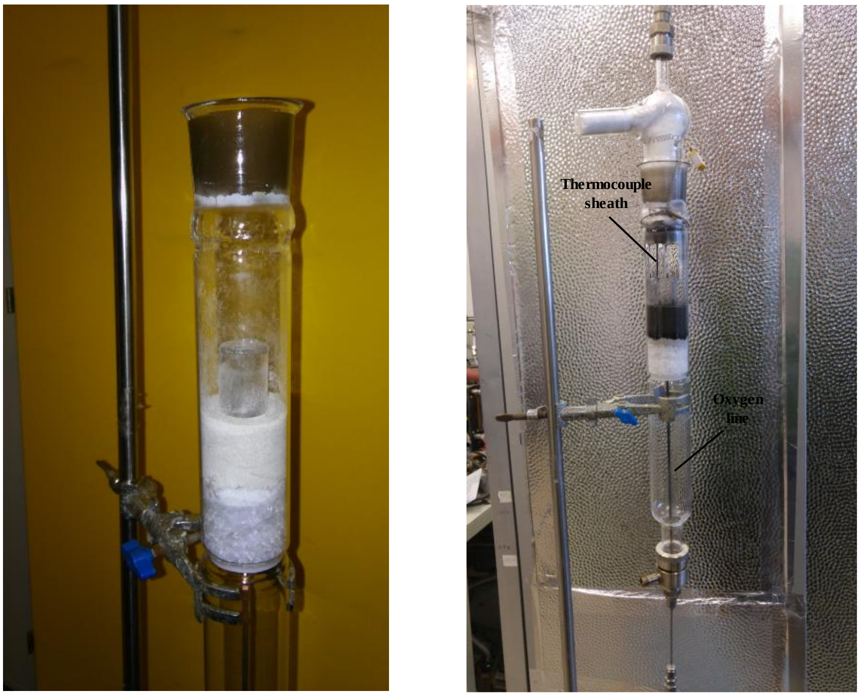

Figure IV. 4 *Picture of the quartz reactor loaded with the fresh sample (right) and with the same sample after a stability test (left).*

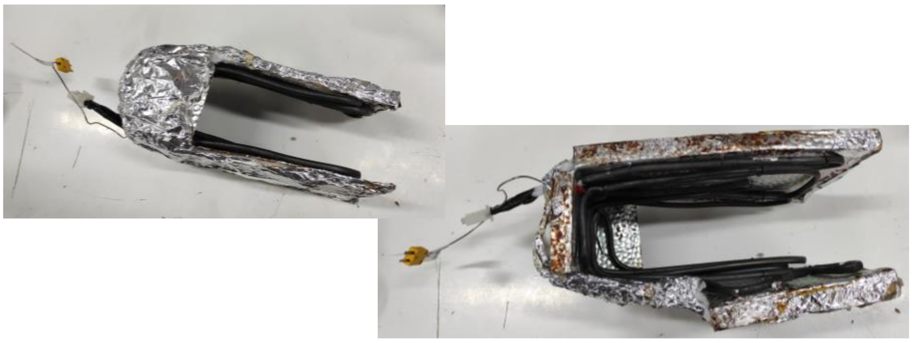

Figure IV. 5 *Homemade system developed for the heating of the upper part of the reactor.*

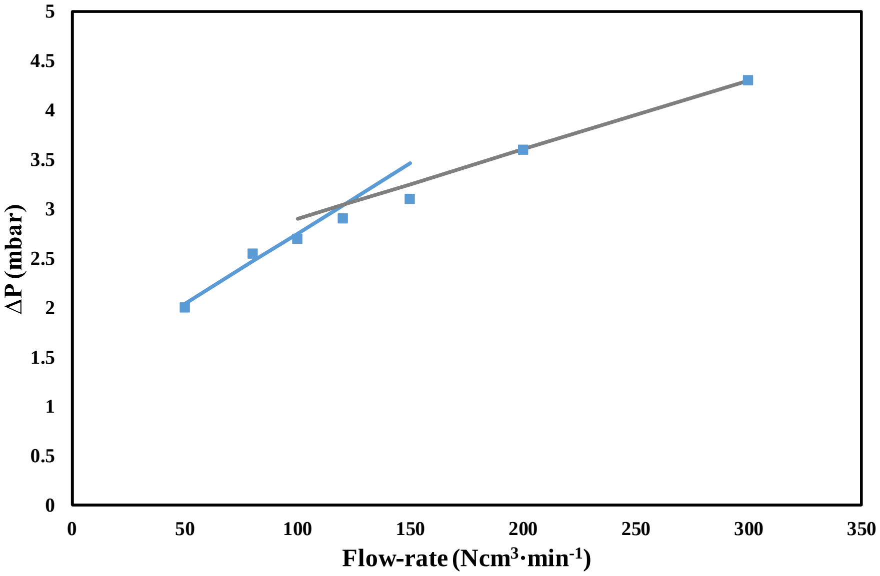

Figure IV. 6 *Measurements of the minimum fluidization velocity at 500°C.*

Table IV. 1 reports the variation of the minimum fluidization velocity as a function of the reactor temperature.

Table IV. 2 *Minimum fluidization velocity as a function of the reactor temperature.*

Temperature (°C)	**Minimum fluidization velocity ($m \cdot s^{-1}$)**
25°C	0.0040
300°C	0.0024
450°C	0.0020
500°C	0.0018
600°C	0.0017

IV.3.3 Reaction Section: final configuration

In order to perform the activity and stability tests under fuel-grade bioethanol, the reaction configuration was further optimized in terms of fluidization conditions. In this regard, the porous plate was substituted by a stainless-steel grid and the annular configuration was substituted by a narrower tubular reactor. The reactor head was also optimized in order to limit particles entrainment. The scheme of the new stainless steel reactor configuration is reported in Figure IV. 7.

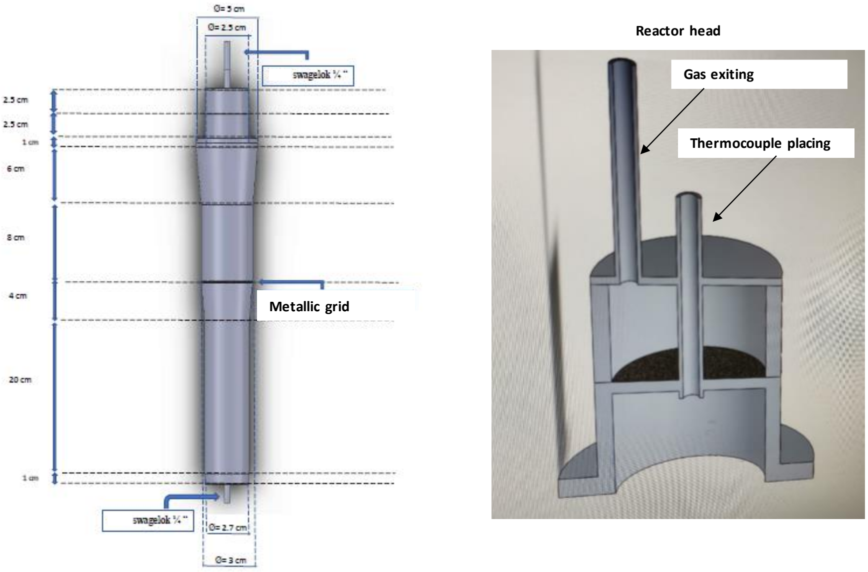

Figure IV. 7 *New reactor configuration employed for tests under fuel-grade bioethanol.*

IV.3.4 Analysis Section

The analysis of the stream exiting the reactor was performed by means of a Quadrupole Mass Spectrometer (mod. QGA) provided by Hiden Analytical.
MS works on the principles of gas ionization and fragmentation (typically through the bombardment by electrons), the physical separation of the charged fragments and their detection.
The schematic representation of a mass spectrometer is reported in Figure IV. 8.
Concerning the mass spectrometer operation, firstly the flowing gaseous stream is evaporated. The vapour is leaking into the ionization chamber where the pressure is maintained of about 10^{-6}-10^{-7} mbar. The vapour molecules are now ionized by an electron-beam. A heated cathode (the filament) produces this beam. Ionization is achieved by inductive effects

rather than strict collision. By loss of valence electrons, mainly positive ions are produced. The positive ions are forced out of the ionization chamber by a small positive charge applied to the repeller opposing the exit-slit (A). After the ions have left the ionization chamber, they are accelerated by an electrostatic field (A>B) of several hundreds to thousands of volts before they enter the analyser. The separation of ions takes place in the analyser (in this example a magnetic sector) at a pressure of about 10^{-8} mbar. A strong magnetic field is applied perpendicular to the motional direction of the ions. The fast moving ions then will follow a circular trajectory, due to the Lorentz acceleration, whose radius is determined by the mass/charge ratio of the ion and the strength of the magnetic field. Ions with different mass/charge ratios are forced through the exit-slit by variation of the accelerating voltage (A>B) or by changing the magnetic-field force. After the ions have passed the exit-slit, they collide on a collector-electrode. The resulting current is amplified and registered as a function of the magnetic-field force or the accelerating voltage.

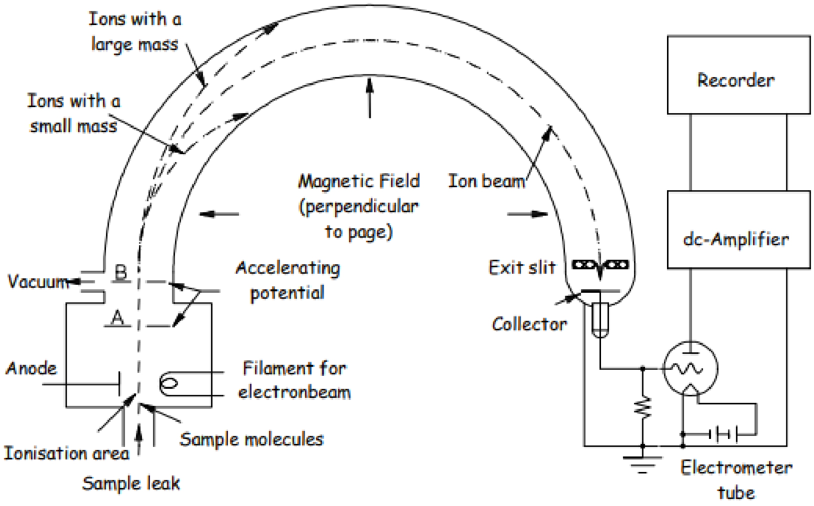

Figure IV. 8 *Schematic representation of a mass spectrometer.*

There are several ways to separate ions with different mass/charge ratios, including the employment of quadrupole mass filters.

A quadrupole mass spectrometer (depicted in Figure IV. 9) consists of an ionizer (bombardment by electrons from a hot filament), an ion accelerator and a mass filter consisting of four parallel metal rods. Two opposite rods have an applied potential of $(U+V\cos(\omega t))$ and the other two rods have a potential of $-(U+V\cos(\omega t))$, where U is a dc (continuous current) voltage and $V\cos(\omega t)$ is an ac (alrernate current) voltage. The applied voltages affect the trajectory of ions traveling down the flight path centred between the four rods. For given dc and ac voltages, only ions of a certain mass-to-charge ratio pass through the quadrupole filter and all other ions are thrown out of their original path.

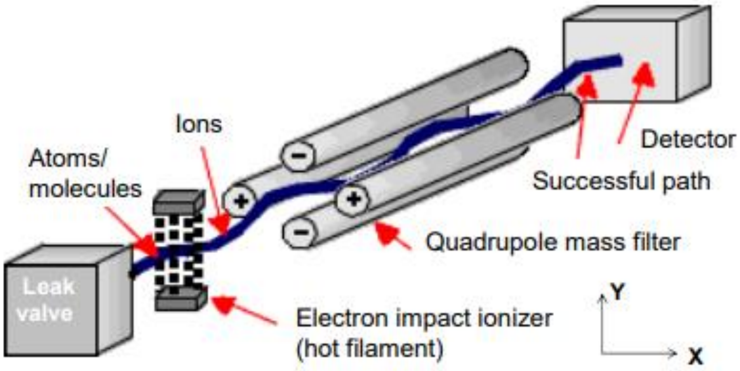

Figure IV. 9 *Schematic representation of a quadrupole mass filter.*

A mass spectrum is obtained by monitoring the ions passing through the quadrupole filter as the voltages on the rods are varied. There are two methods: varying ω and holding U and V constant, or varying U and V with (U/V) fixed for a constant angular frequency, ω. The general principle of operation of the mass filter can be visualized qualitatively as follows: light ions (low mass to charge ratio) are able to follow the alternating component of the field. For the X-direction, those ions will stay in phase with the RF drive, gain energy from the field and oscillate with increasingly large amplitude until they encounter one of the rods and are discharged. Therefore, the X-direction is a high-pass mass filter: only high masses will be transmitted to the other end of the quadrupole without striking the X-electrodes. On the other hand, in the Y-direction, heavy ions will be unstable because of the defocusing effect of the DC component, but some lighter ions will be stabilized by the AC component if its magnitude is such as to correct the trajectory whenever its amplitude tends to increase. Thus, the Y-direction is a low-pass mass filter: only low masses will be transmitted to the other end of the quadrupole without striking the Y electrodes. By a suitable choice of the RF/DC ratio, the two directions together give a mass filter which is capable of resolving individual atomic masses.

The Hiden QGA quantitative gas analysis system is for continuous analysis of multiple gases and vapours at pressures near atmospheric. The QGA system has a mass range of 200 amu (300 amu option) and a detection capability from 100% to less than 100 parts per billion).

The instrument (shown in Figure IV. 10) assures multiple gas and vapour analysis (until 200 amu mass range) and is characterized by a 2 meter continuous sampling heated capillary inlet, gas sample flow rate of 16 atm $\cdot cc \cdot min^{-1}$ standard. 1 atm. $cc \cdot min^{-1}$ option, high sensitivity (detection to 100 ppb), <300 ms response time to changes in gas concentration, fast data acquisition (up to 650 measurements per second), integrated CO analyser option for the analysis of low level CO in the presence of N_2 and CO_2, soft ionisation for reduced spectral fragmentation and simplified data interpretation, broad range of sampling accessories.

Figure IV. 10 *Bench-top gas analysis system.*

As depicted in Figure IV. 1, part of the flow coming from the reaction section reaches the mass spectrometer, which is then followed by a cold trap for the condensation of water, unreacted ethanol and other condensable species eventually formed; the gaseous stream finally is sent to the vent.

The instrument is equipped with a specific software package for quantitative gas and vapour analysis providing real time continuous analysis of up to 32 species with concentrations measured in the range 0.1PPM to 100%. Moreover, the software assures automatic subtraction of spectral overlaps and automated calibration routines; it is also characterized by a mass spectral library with intelligent scan feature.

The software interface is shown in Figure IV. 11. After the connection to the instrument (which automatically establishes the filament switch), it is possible to select the desired species through the function “*Setup Analysis*”. The software is equipped with a specific library, which reports the intensity of every fragment for the selected species. A LED key (see Figure IV. 12) indicates wheatear the overlapping is resolvable or not (dark green: peak is not used; light green: unique peak; orange: a resolvable overlap; red: unable to resolve overlap). For the analysis of the products stream during oxidative steam reforming of ethanol; in order to avoid overlapping, the customized fragments spectra of some species (i.e. acetone, acetaldehyde and ethylene) was properly modified through the function “*Engineering Settings*” (Figure

IV. 11 and Figure IV. 12) , which forces the instrument to read a component on a specified fragment.

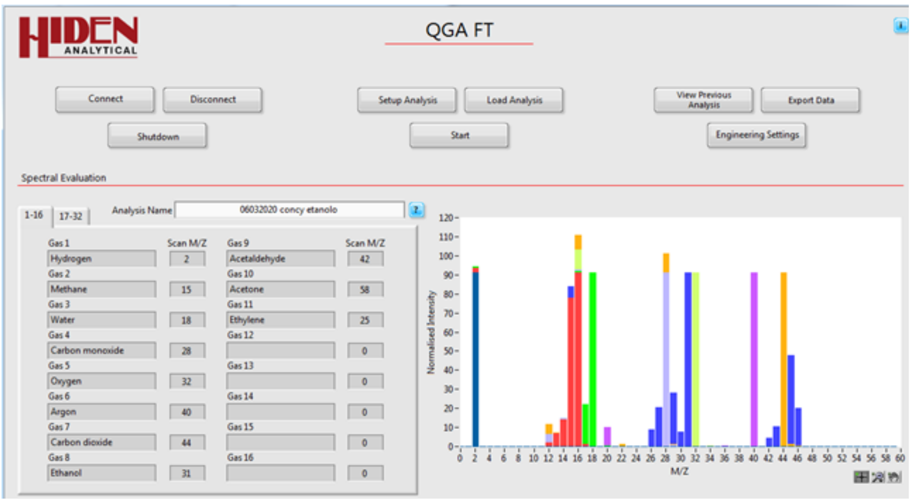

Analysis Name: 06032020 concy etanolo

	Scan M/Z		Scan M/Z
Gas 1: Hydrogen	2	Gas 9: Acetaldehyde	42
Gas 2: Methane	15	Gas 10: Acetone	58
Gas 3: Water	18	Gas 11: Ethylene	25
Gas 4: Carbon monoxide	28	Gas 12:	0
Gas 5: Oxygen	32	Gas 13:	0
Gas 6: Argon	40	Gas 14:	0
Gas 7: Carbon dioxide	44	Gas 15:	0
Gas 8: Ethanol	31	Gas 16:	0

Figure IV. 11 *Interface of the QGA software for the analysis through the mass spectrometer.*

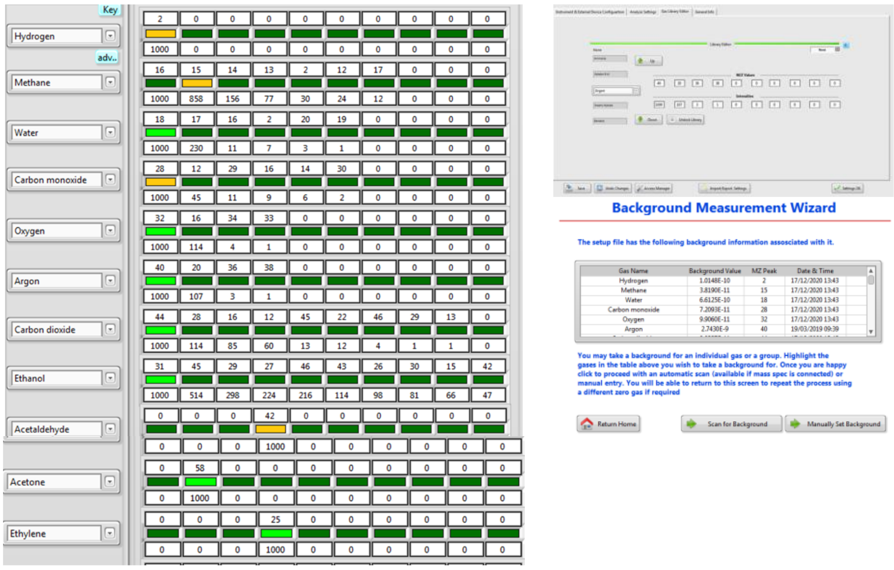

Hydrogen	2	0	0	0	0	0	0	0	0	0
	🟨									
	1000	0	0	0	0	0	0	0	0	0
Methane	16	15	14	13	2	12	17	0	0	0
		🟨								
	1000	858	156	77	30	24	12	0	0	0
Water	18	17	16	2	20	19	0	0	0	0
	🟩									
	1000	230	11	7	3	1	0	0	0	0
Carbon monoxide	28	12	29	16	14	30	0	0	0	0
	🟨									
	1000	45	11	9	6	2	0	0	0	0
Oxygen	32	16	34	33	0	0	0	0	0	0
	🟩									
	1000	114	4	1	0	0	0	0	0	0
Argon	40	20	36	38	0	0	0	0	0	0
	🟩									
	1000	107	3	1	0	0	0	0	0	0
Carbon dioxide	44	28	16	12	45	22	46	29	13	0
	🟩									
	1000	114	85	60	13	12	4	1	1	0
Ethanol	31	45	29	27	46	43	26	30	15	42
	🟩									
	1000	514	298	224	216	114	98	81	66	47
Acetaldehyde	0	0	0	42	0	0	0	0	0	0
				🟨						
	0	0	0	1000	0	0	0	0	0	0
Acetone	0	58	0	0	0	0	0	0	0	0
		🟩								
	0	1000	0	0	0	0	0	0	0	0
Ethylene	0	0	0	25	0	0	0	0	0	0
				🟩						
	0	0	0	1000	0	0	0	0	0	0

Background Measurement Wizard

The setup file has the following background information associated with it.

Gas Name	Background Value	MZ Peak	Date & Time
Hydrogen	1.0148E-10	2	17/12/2020 13:43
Methane	3.8190E-11	15	17/12/2020 13:43
Water	6.6125E-10	18	17/12/2020 13:43
Carbon monoxide	7.2093E-11	28	17/12/2020 13:43
Oxygen	9.9060E-11	32	17/12/2020 13:43
Argon	2.7430E-9	40	19/03/2019 09:39

You may take a background for an individual gas or a group. Highlight the gases in the table above you wish to take a background for. Once you are happy click to proceed with an automatic scan (available if mass spec is connected) or manual entry. You will be able to return to this screen to repeat the process using a different zero gas if required

Figure IV. 12 *Interface of the QGA software for species settings and background.*

In the menu “*Setup Analysis*”, it is possible to launch the background procedure (Figure IV. 12), in which it is necessary to select all the desired species except the molecule used for the background (i.e. argon).

Concerning the calibration procedure, launched again through the “Setup Analysis” screen, based on the number of gas streams which is desired to analyse (one or more), it is possible to select the function “*Single Cylinder*” or “*Multiple Cylinder*” calibration. Figure IV. 13 reports the screens for the streams calibration. It is necessary to select the common gas as well as the components present in the feeding streams. When the MS response is constant with scanning (maximum 100 scans are available), through the “*Abort*” button it is possible to stop the acquisition and add the desired data to calculate the calibration factor.

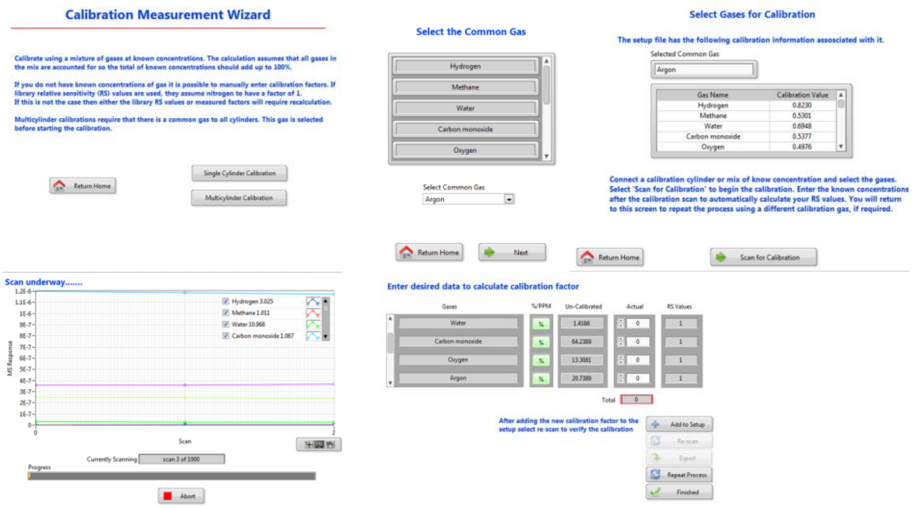

Calibration Measurement Wizard

Calibrate using a mixture of gases at known concentrations. The calculation assumes that all gases in the mix are accounted for so the total of known concentrations should add up to 100%.

If you do not have known concentrations of gas it is possible to manually enter calibration factors. If library relative sensitivity (RS) values are used, they assume nitrogen to have a factor of 1.
If this is not the case then either the library RS values or measured factors will require recalculation.

Multicylinder calibrations require that there is a common gas to all cylinders. This gas is selected before starting the calibration.

Select the Common Gas

Select Common Gas: Argon

Select Gases for Calibration

The setup file has the following calibration information associated with it.

Selected Common Gas: Argon

Gas Name	Calibration Value
Hydrogen	0.8230
Methane	0.5301
Water	0.6948
Carbon monoxide	0.5377
Oxygen	0.4976

Connect a calibration cylinder or mix of know concentration and select the gases. Select 'Scan for Calibration' to begin the calibration. Enter the known concentrations after the calibration scan to automatically calculate your RS values. You will return to this screen to repeat the process using a different calibration gas, if required.

Scan underway.......

Currently Scanning: scan 3 of 1000

Enter desired data to calculate calibration factor

Gases	%/PPM	Un-Calibrated	Actual	RS Values
Water	%	1.4166	0	1
Carbon monoxide	%	64.2389	0	1
Oxygen	%	13.3081	0	1
Argon	%	20.7389	0	1

Total: 0

After adding the new calibration factor to the setup select re-scan to verify the calibration

Figure IV. 13 *Interface of the QGA software for calibration.*

IV.4 Operative conditions of OSR tests

The activity and stability tests of the different catalytic formulations was investigated in the fluidized bed reactor at atmospheric pressure.

Typically, for the experiments performed by using the simulated bioethanol feeding (i.e. water and pure ethanol), the steam to ethanol ratio was fixed to 4, the oxygen to ethanol ratio to 0.5, the reaction temperature to 500°C and the weight hourly space velocity (WHSV), defined as shown in eq.(IV. 1), where the ethanol mass flow-rate (W_{C2H5OH}, in $g \cdot h^{-1}$) is normalized by the catalytic mass ($m_{catalyst}$, in g), was fixed to 4.1 h^{-1}.

$$WHSV = \frac{W_{C2H5OH}}{m_{catalyst}} \qquad \text{(IV. 1)}$$

7 g of catalysts, diluted with 22 g of CeO_2-SiO_2, were loaded into the reactor and a total flow rate of 770 $Ncm^3 \cdot min^{-1}$ (which assured a linear velocity almost 6 times the minimum fluidization value) was selected. The feeding

flow rate had the following composition (on volumetric basis): 10% C_2H_5OH, 40%H_2O, 5%O_2 and 45%Ar.

The performance of the bimetallic catalysts were also tested under different steam to ethanol ratios (3,4 and 6), oxygen to ethanol ratios (0.25, 0.5 and 0.75), temperatures (400, 500 and 600°C) and WHSV values (4.1, 12.3 h^{-1}, 61.7 h^{-1}). In order to change the contact time, the total flow-rate and the catalytic mass were modified accordingly.

The above tests, devoted to the identification of the most suitable formulation for the oxidative steam reforming, along with the experimental analysis focused on the development of the kinetic model, were performed by feeding a mixture of pure ethanol and distilled water.

Once selected the most stable catalysts, its performance was also studied under a fuel-grade ethanol stream, described in Par. IV.5.

IV.5 Properties of the bioethanol

The fuel-grade ethanol was provided by the *Eldor Corporation S.p.a*. The composition of this liquid is described in Figure IV. 14.

Besides ethanol, methanol and higher saturated mono-alchols alcohols (C3-C5) were contained in the bioethanol, with a maximum content of 1 and 2 % (on mass basis), respectively. Phosphorus, copper sulphide, and inorganic chloride were also detected in the liquid; trace of water (maximum 0.3 %) were found in the bioethanol. The properties of the liquid described in Figure IV. 14 are in line with the EN 15376:2014, which regulates the composition of the ethanol as a blending component for the petrol.

In order to evaluate the stability of the bimetallic catalysts, a steam to fuel grade bioethanol ratio equal to 4 was fixed.

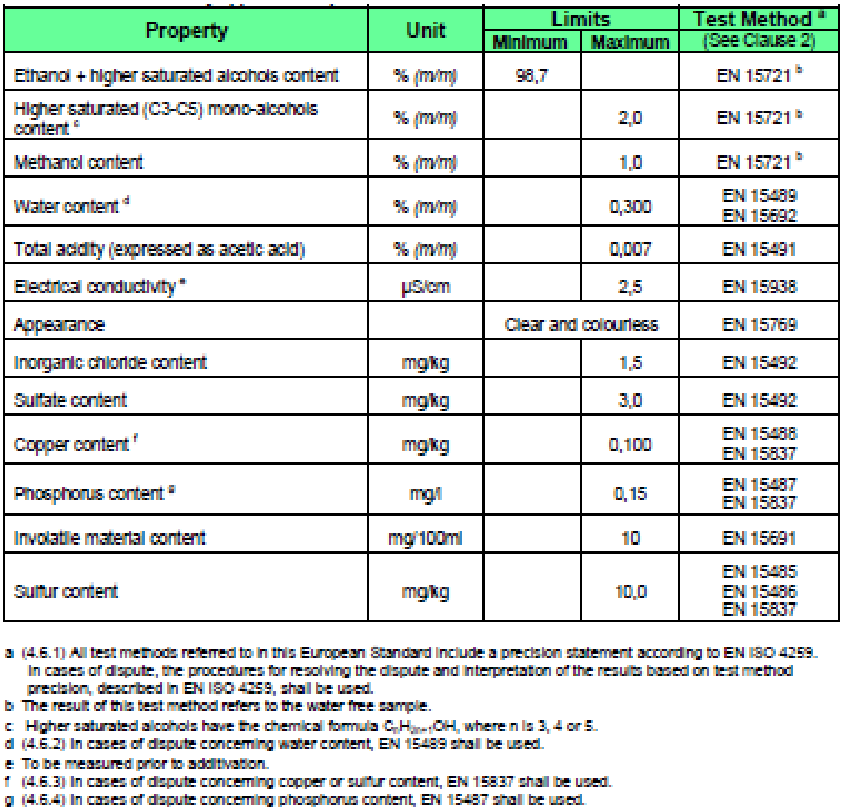

Property	Unit	Limits		Test Method [a]
		Minimum	Maximum	(See Clause 2)
Ethanol + higher saturated alcohols content	% (m/m)	98,7		EN 15721 [b]
Higher saturated (C3-C5) mono-alcohols content [c]	% (m/m)		2,0	EN 15721 [b]
Methanol content	% (m/m)		1,0	EN 15721 [b]
Water content [d]	% (m/m)		0,300	EN 15489 EN 15692
Total acidity (expressed as acetic acid)	% (m/m)		0,007	EN 15491
Electrical conductivity [e]	µS/cm		2,5	EN 15938
Appearance		Clear and colourless		EN 15769
Inorganic chloride content	mg/kg		1,5	EN 15492
Sulfate content	mg/kg		3,0	EN 15492
Copper content [f]	mg/kg		0,100	EN 15488 EN 15837
Phosphorus content [g]	mg/l		0,15	EN 15487 EN 15837
Involatile material content	mg/100ml		10	EN 15691
Sulfur content	mg/kg		10,0	EN 15485 EN 15486 EN 15837

a (4.6.1) All test methods referred to in this European Standard include a precision statement according to EN ISO 4259. In cases of dispute, the procedures for resolving the dispute and interpretation of the results based on test method precision, described in EN ISO 4259, shall be used.

b The result of this test method refers to the water free sample.

c Higher saturated alcohols have the chemical formula $C_nH_{2n+1}OH$, where n is 3, 4 or 5.

d (4.6.2) In cases of dispute concerning water content, EN 15489 shall be used.

e To be measured prior to additivation.

f (4.6.3) In cases of dispute concerning copper or sulfur content, EN 15837 shall be used.

g (4.6.4) In cases of dispute concerning phosphorus content, EN 15487 shall be used.

Figure IV. 14. *Composition of the fuel grade ethanol provided by Eldor Corporation S.p.a.*

Chapter V

V Results and discussion

V.1Results of catalysts characterization

In the following paragraphs, the results of various analyses, including XRF, surface area measurements, XRD, TPR and ZPC, performed to highlight the physical and chemical properties of the fresh catalysts, are described and discussed. Such measurements will help to shed light on the different activity and stability of the catalytic formulations tested for oxidative steam reforming of ethanol.

V.1.1 Results of XRF, BET and XRD analysis

In this paragraph, the data obtained for the catalysts prepared from the cerium nitrate hexahydrate precursor (Pt-Ni, K-Pt-Ni and Pt-Co supported on CeO_2-SiO_2) will be discussed at first. Then, the measurements on the samples prepared form the different precursors will be commented. Finally, some details on the characterization of the samples prepared at different Pt, Ru and Ag loadings were also added.

The chemical composition of the sample was investigated via XRF analysis to verify that the preparation procedure allowed the deposition of the desired CeO_2 as well as active phases loading (Table V. 1).

The ceria content in all the samples was close to the nominal value. A fairly good agreement was also observed for Ni/Co and platinum loading (the expected values of 10 wt % and 3 wt %, respectively, refers to ceria mass).

Table V. 1 *Results of catalysts characterization for the Pt-Ni, K-Pt-Ni and Pt-Co samples supported on CeO_2-SiO_2.*

Sample	**SiO_2 (wt%)**	**CeO_2 (wt%)**	**Ni/Co (wt%)***	**Pt (wt%)***
CeO_2-SiO_2	69.8	31.1	-	-
Pt-Ni/CeO_2-SiO_2	65.3	30.3	10.3	2.9
K-Pt-Ni/CeO_2-SiO_2	65.3	30.2	10.2	2.9
Pt-Co/CeO_2-SiO_2	65.2	30.4	10.4	3.2

* the metals content refers to the M-Ni/CeO_2 catalyst (without SiO_2)

Table V. 2 reports the specific surface area (S_{BET}) and the average crystallite sizes of CeO_2 as well as Ni or Co oxides (d_{CeO2} and $d_{NiO}/_{Co3O4}$, respectively), determined by means of the Scherrer formula from XRD patterns. For the purpose of comparison, the S_{BET} of the bare support before active species deposition is also shown. All the samples displayed large specific surface areas due to the meso-porosity of SiO_2. In particular, the BET surface area was the highest one for the Pt-Ni/CeO_2-SiO_2 catalyst (217 m^2 g^{-1}) and decreased in the order of Pt-Ni > Pt-Co > K-Pt-Ni.

In Figure V. 1, all the patterns exhibited XRD peaks that correspond to the (111), (200), (220), (311), (222), (400), and (331) planes for the cubic fluorite structure of CeO_2 (Iulianelli et al., 2016b, Jeong et al., 2015). The broad peak around 22° can be assigned to amorphous silica (Mao and Ye, 2010). Moreover, NiO crystals are clearly notable in Ni impregnated catalysts at 2Θ values of 43.8° (Dave and Pant, 2011). In addition, one peak related to Co_3O_4 at 36.8° was observed in the XRD pattern of the Pt-Co/CeO_2-SiO_2 catalyst (Wang et al., 2013). No diffraction lines pertaining to Pt oxides were visible in the spectra, probably due to the oxide presence in highly amorphous or well-dispersed state, that is beyond the detection limit of the instrument.

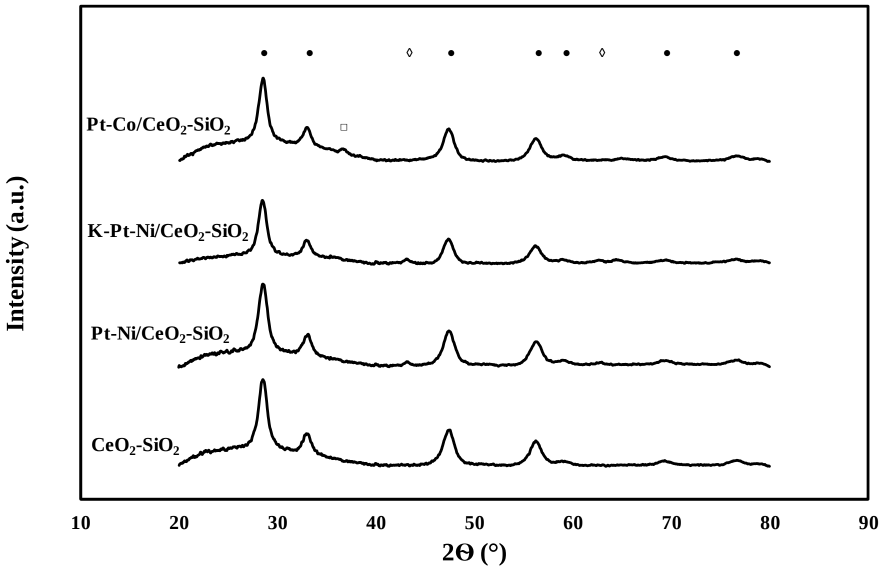

Figure V. 1 *XRD patterns of the catalysts prepared from cerium nitrate hexahydrate and the bare support (CeO_2 circle, Co_3O_4 square, NiO diamond).*

The results of particles dimension measurements (Table V. 2) highlighted that the use of silica as support helps to obtain high CeO_2 dispersion: the average size of ceria particles is around 7-8 nm for all the samples. Very low dimensions (9-11 nm) were also recorded for NiO and Co_3O_4 crystallites, proving again the positive effect of catalyst deposition on SiO_2. However, K addition slightly increased NiO particle sizes with respect to the potassium-free catalyst.

Table V. 2 *Results of catalysts characterization for the Pt-Ni, K-Pt-Ni and Pt-Co samples supported on CeO_2-SiO_2.*

Sample	**S_{BET} ($m^2 \cdot g^{-1}$)**	**d_{CeO2} (nm)**	**$d_{NiO}/_{Co3O4}$**
SiO_2	400	-	-
CeO_2-SiO_2	258	70	-
Pt-Ni/CeO_2-SiO_2	217	76	98
K-Pt-Ni/CeO_2-SiO_2	183	76	110
Pt-Co/CeO_2-SiO_2	202	76	88

The results of N_2 adsorption measurements and XRD analysis (reported in terms of average crystallite sizes for CeO_2 and NiO particles) obtained for the supports (S-NH, S-ANH, S-AAH) and catalysts prepared from different salt precursors are summarized in Table V. 3. For the final catalysts, the surface area follows the order AAH > ANH > NH. However, very close values were recorded over the three samples and S_{BET} was only decreased slightly (almost 11%) after the incorporation of the active species, due to Ni and Pt entering into the pores of the CeO_2-SiO_2 support (Kim et al., 2003).

The XRD patterns of the support and the Pt-Ni/CeO_2-SiO_2 catalysts prepared by using different cerium salt precursors are displayed in Figure V. 2. The identified phases are the same discussed for Figure V. 1. Moreover, ceria peaks for the samples S-AAH and AAH are broader and less high than those observed on the other two samples, which proves that the employment of acetyl acetonate as precursor can assure a better ceria dispersion (an average particle size of 6 nm was recorded while the dimension of ceria particles was almost 8 nm for the catalysts NH and ANH). Finally, as shown in Table V. 3, the average crystallite sizes of NiO for the final catalysts ranged between 9 and 11 nm.

The effect of the type (Ag, Ru and Pt) as well as loading (0.5-3 wt%) of the second metal (M) was investigated after having selected cerium acetyl acetonate as precursor.

Table V. 4 summarizes the results of specific surface area measurements and XRD analysis of Ag-, Ru- and Pt-based catalysts, in comparison with the Ni/CeO_2-SiO_2 sample. The surface area of the 10Ni catalyst (230 m^2 g^{-1}) was found slightly higher than the bimetallic formulations and a mild decrease in S_{BET} values upon Ag, Ru and Pt loading growth was observed for all the series, which might be due to the occupying of the CeO_2-SiO_2 pores by the active species. In addition, the change of the second metal loading, especially in the case of the Pt and Ru series, had a very low effect on the final specific surface area of the catalysts. A fairly good agreement between measured and expected metals loading was shown by XRF results; however, for M contents lower than 2 wt% (which corresponds to 0.65 wt% calculated on the basis of the SiO_2-free sample), it was not possible to detect the noble metal loading with sufficient precision.

Table V. 3 *BET surface area (S_{BET}) and average particle sizes (d) for the supports and the final catalysts prepared from the different CeO_2 precursors.*

Sample	**S_{BET} ($m^2 \cdot g^{-1}$)**	**d_{CeO2} (Å)**	**d_{NiO} (Å)**
S-NH	258	71	-
S-ANH	277	75	-
S-AAH	268	59	-
NH	217	76	98
ANH	223	77	107
AAH	227	60	92

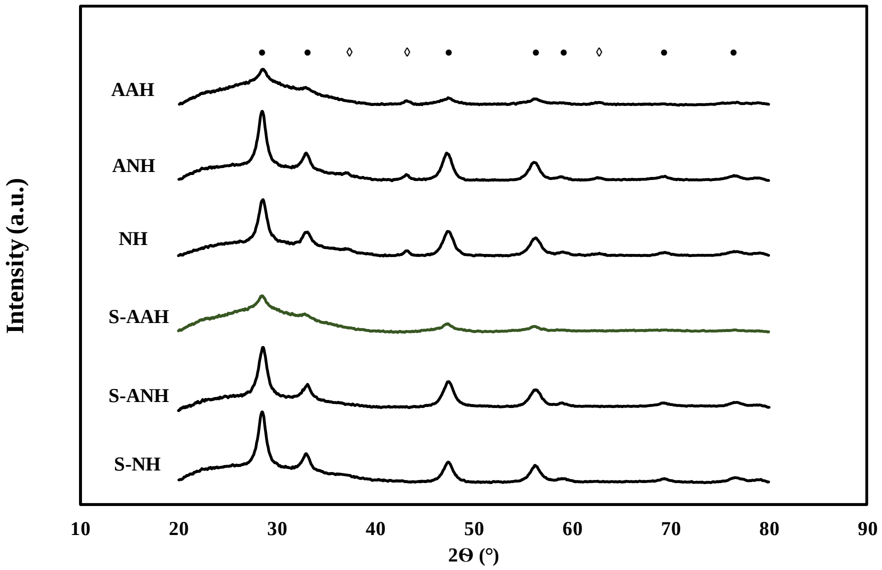

Figure V. 2 *XRD patterns for the samples prepared from different cerium salt precursors (CeO_2 circle and NiO diamond).*

Table V. 4 *Results of the BET measurements and XRF analysis for the catalysts prepared at different loadings of the second metal.*

Sample	**S_{BET} ($m^2 \cdot g^{-1}$)**	**Ni content (wt %*)**	**M content (wt %*)**
10Ni	230	10.5	-
0.5Ag10Ni	205	10.3	-
1Ag10Ni	213	10.4	-
2Ag10Ni	216	10.5	1.8
3Ag10Ni	220	10.2	3.2
0.5Ru10Ni	212	10.3	-
1Ru10Ni	208	10.2	-
2Ru10Ni	210	10.1	2.2
3Ru10Ni	218	9.9	3.1
0.5Pt10Ni	213	-	-
1Pt10Ni	214	10.3	-
2Pt10Ni	226	10.3	1.9
3Pt10Ni	227	10.1	3.2

* the metals content refers to the M-Ni/CeO_2 catalyst (without SiO_2)

V.1.2 Results of TPR analysis

The reducibility of the catalysts was investigated by TPR analysis and the consumption profiles of the support and the final catalysts prepared from cerium nitrate hexahydrate as precursor, after baseline subtraction, are presented in Figure V. 3.

The hydrogen consumption was evaluated via the deconvolution of consumptions peak, carried out by a least-squares fitting to Gaussian-Lorentzian functions using the software Microcal Origin. All the samples (Pt-Ni, K-Pt-Ni and Pt-Co/CeO_2-SiO_2) exhibited a hydrogen consumption at low temperatures, that is widely associated to the reduction of surface PtO_x species (Vita et al., 2016, Dufour et al., 2011). However, the reduction of Ce-PtO_x species which possess an intimate interaction between Pt and CeO_2 as well as Pt-Ni/Pt-Co species cannot be excluded (Abdelouahab-Reddam et al., 2015). The bare support (CeO_2-SiO_2) showed a weak and broad reduction peak above 350 °C and centred at 509 °C with a negligible consumption at 300 °C, corresponding to the removal of surface-capping oxygen of ceria (Deeprasertkul et al., 2014). On the other hand, for all the tested catalysts, as reported in Table V. 5, the low-temperature consumption is larger than the theoretical consumption of PtO_2 (308 $\mu mol_{H2}\cdot g_{catalyst}^{-1}$). This feature proposes that the intimate contact between noble and non-noble metals may result in a leftward shift in NiO/Co_3O_4 reduction peaks (Xie et al., 2015) and that the surface reduction of CeO_2 can be enhanced by the presence of Pt (Zhang et al., 2016).

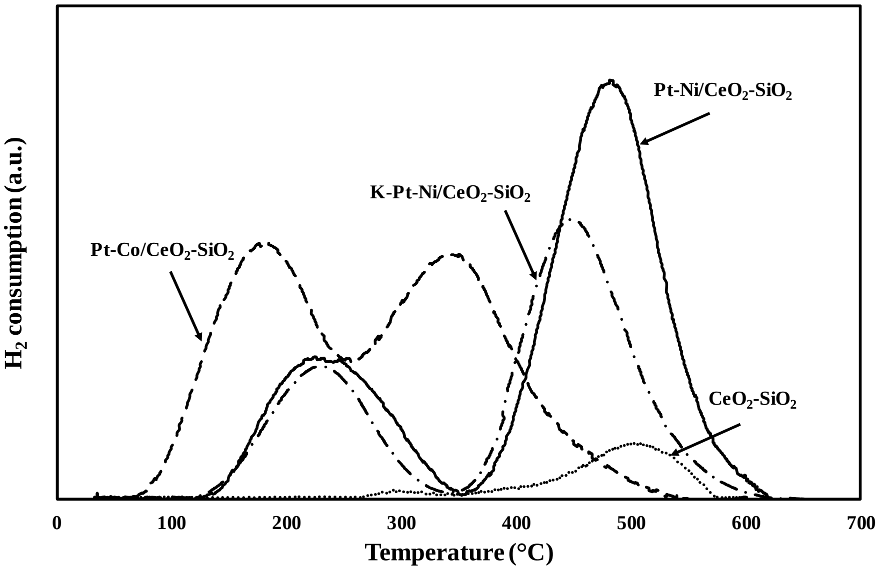

Figure V. 3 *TPR profiles of the support and the catalysts prepared by using the cerium nitrate hexahydrate precursor.*

In fact, the above results suggest that the presence of Pt increases the surface concentration of adsorbed hydrogen, thus leading to an enhancement of Ni (or Co)/CeO_2 reduction influenced by the hydrogen spillover from the metallic platinum particles to the surface. For the Pt-Ni/CeO_2-SiO_2 catalyst, the hydrogen consumption of 2024 $\mu mol_{H2}\cdot g_{catalyst}^{-1}$, centred at 480 °C and ascribable to NiO reduction (Adamu et al., 2017), was again higher than expected one (1707 $\mu mol_{H2}\cdot g_{catalyst}^{-1}$). This behaviour can be linked to both Ni spillover as well as the increased oxygen capacity of the support due to the CeO_2-SiO_2 interactions (Mamontov et al., 2016, Ay and Üner, 2015). Potassium deposition on the Pt-Ni/CeO_2-SiO_2 catalyst modified the hydrogen consumption profile, leading to a lower H_2 consumption (1923 vs 2780 $\mu mol_{H2}\cdot g_{catalyst}^{-1}$). This result suggests that K-addition partially hindered catalyst reduction. In the case of the Pt-Co/CeO_2-SiO_2 catalyst, the area under the peak centred at 339 °C (1633 $\mu mol_{H2}\cdot g_{catalyst}^{-1}$) was very close to the expected one (1697 $mmol_{H2}/g_{catalyst}$) and it can be attributed to the progressive of the pathway Co_3O_4/CoO/Co (Konsolakis et al., 2017). However, for the latter catalyst, the low temperature hydrogen consumption (1143 $\mu mol_{H2}\cdot g_{catalyst}^{-1}$) is the highest among the tested samples, suggesting that Co_3O_4 reduction could also start at temperatures lower than 339 °C and/or that hydrogen spillover occurred, thus promoting a beforehand ceria reduction.

Table V. 5 *Hydrogen uptake calculate by deconvolutiong the TPR peaks of Figure V. 3.*

Sample	**Peak temperature (°C)**	**Experimental consumption ($\mu mol_{H2}\cdot g_{catalyst}^{-1}$)**
CeO_2-SiO_2	300 448 509	13 94 191
Pt-Ni	235 480	756 2024
K-Pt-Ni	212 259 453	389 209 1325
Pt-Co	135 187 339	243 900 1633

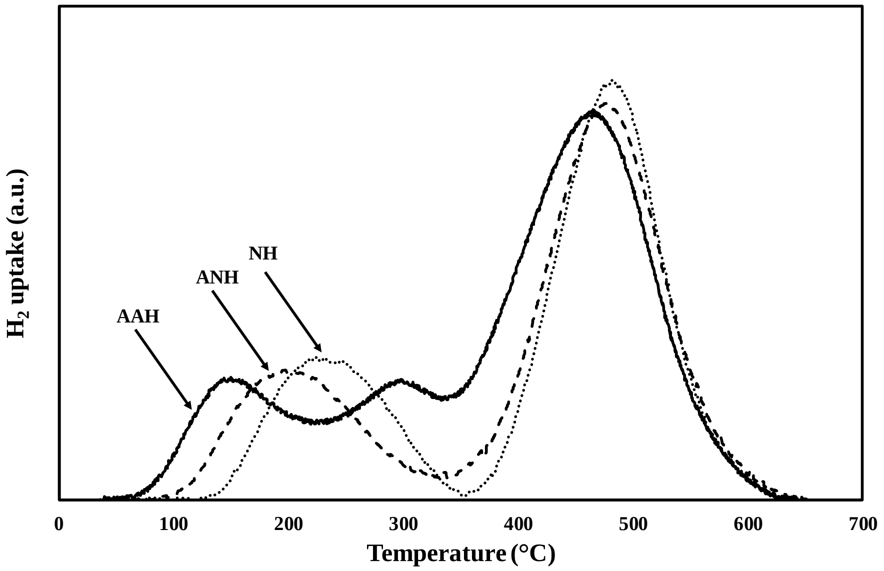

Figure V. 4 *TPR profiles of Pt-Ni/CeO_2-SiO_2 catalysts prepared from the different cerium precursors.*

Figure V. 4 presents the hydrogen consumption profiles recorded over the catalysts NH, ANH and AAH during TPR experiments. For the three catalysts, the reduction takes place into two steps (at temperatures below 350°C and between 350 and 600°C), according to the easier reduction of noble metals oxides with respect to non-noble species, widely reported in the literature (Jeon et al., 2017, Ocsachoque et al., 2011, Palma et al., 2015b). However, the cerium salt precursor choice affected the peak position and the experimental uptake, reported in Table V. 6. For the catalytic samples prepared from cerium nitrate hexhydrate and cerium ammonium nitrate hexahydrate a broad peak was observed at low temperature (centred at 235 and 207°C, respectively), which is corresponded to the reduction of PtO_x species (He et al., 2012). The sample AAH displayed the lowest reduction temperatures, with PtO_x reduction starting below 100°C. In fact, the employment of acetyl acetonate hydrate as cerium salt precursor helps to form smaller Pt particles with a better dispersion of the noble metals, which is expected to be beneficial for catalyst activity (Santos et al., 2005, Dong et al., 2002). This result also suggests that the strength of interaction between PtO_x and CeO_2-SiO_2 support is weakened in the order NH > ANH > AAH.

Table V. 6 *Hydrogen uptake calculated by deconvolutiong the TPR peaks of Figure V. 4.*

Sample	**Peak temperature (°C)**	**Experimental uptake ($\mu mol_{H2} \cdot g_{cat}^{-1}$)**
NH	235 480	756 2024
ANH	207 458	765 2162
AAH	149 288 462	466 327 2329

The TPR analysis was also performed for the catalytic samples prepared from cerium acetyl acetonate and containing Ag, Ru or Pt with loadings in the interval 0.5-3 wt%; the results are shown in Figure V. 5, Figure V. 6 and Figure V. 7 in comparison with the reduction profile of the 10Ni/CeO_2-SiO_2 catalyst. Table V. 7 reports the experimental uptake in comparison with the theoretical consumption for all the above samples.

The monometallic catalyst underwent hydrogen consumption above 200°C, with two reduction zones, ascribable to NiO reduction (below 500°C) (Sepehri et al., 2018) and surface oxygen Ce^{4+}-O-Ce^{4+} as well as bulk ceria reduction (observed at higher temperatures) (Xue et al., 2018). The deposition of a noble metal on the Ni/CeO_2-SiO_2 catalyst resulted in the development of reduction peaks at lower temperatures (below 200°C), which finds wide confirmation in the literature (Bizkarra et al., 2018, Fiorenza et al., 2016, Stanley et al., 2019, Mauriello et al., 2019). Thus, silver, ruthenium and platinum addition to the Ni/CeO_2-SiO_2 sample resulted in a leftward shift of Ni reduction peaks. This result suggests that the addition of a second metal decreases the NiO-CeO_2 interactions (Zangouei et al., 2010), thus observing an anticipated NiO reduction promoted by the MO_x phases.

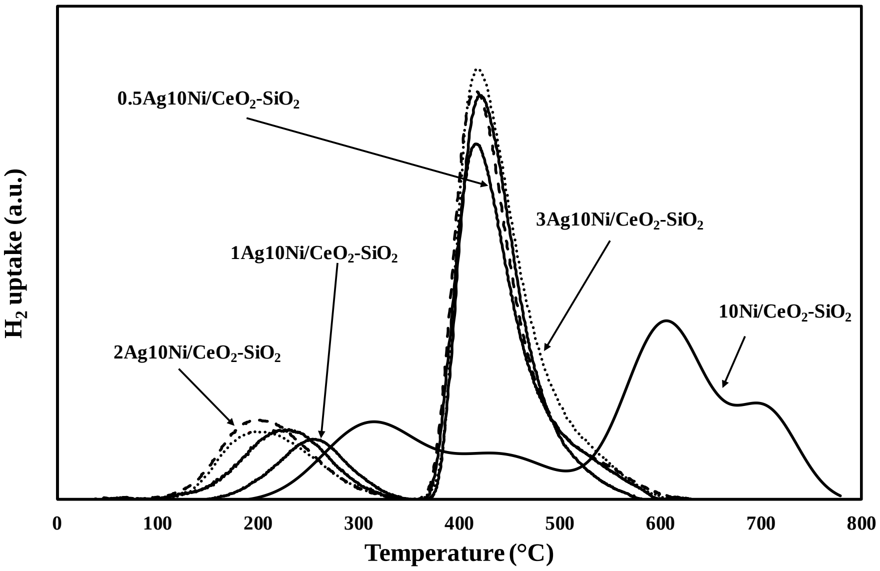

Figure V. 5 *TPR profiles of the Ag-based catalysts in comparison with the Ni/CeO_2-SiO_2 sample.*

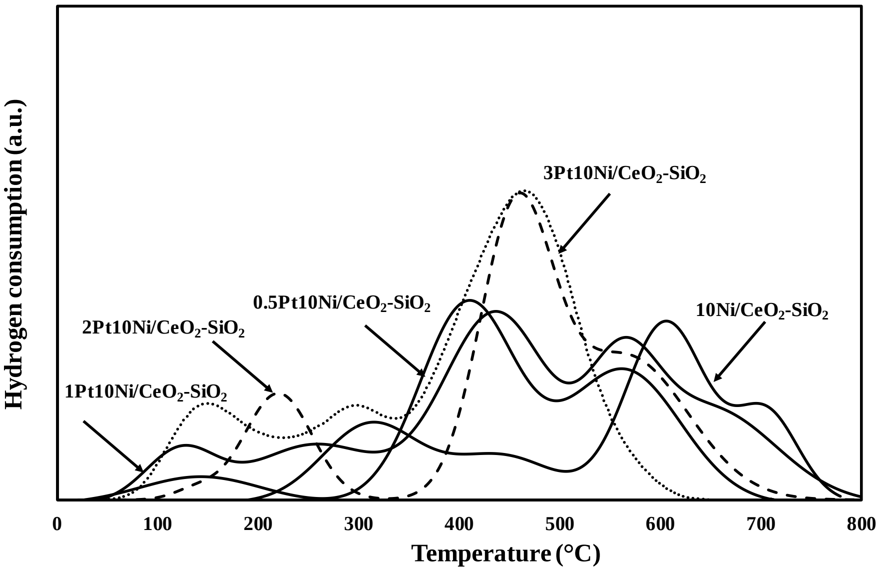

Figure V. 6 *TPR profiles of the Pt-based catalysts in comparison with the Ni/CeO_2-SiO_2 sample.*

The low-temperature peaks in Figure V. 5 can be related to the reduction of silver oxide: due to the Ag-Ni interactions, NiO reduction is also promoted by spillover and the low-temperature H_2 uptake is slightly higher than the expected one, especially for increased Ag contents (Hohmeyer et al., 2010). In fact, the total H_2 consumption increased in the order 0.5Ag > 1Ag > 2Ag > 3Ag, according to the growth in silver content and the higher contribution of spillover phenomena; hydrogen consumption increased from the value of 1799 of the 0.5 wt% laoded sample to 2401 $\mu mol_{H2} \cdot g_{cat}^{-1}$ of the $3Ag10Ni/CeO_2-SiO_2$ catalyst. The same trend was also observed in the presence of Ru and Pt; however, the hydrogen consumption over the Pt and Ru-based catalyst is higher compared to the values observed for the silver-containing samples and the lower reducibility of the latter catalysts is expected to affect their activity and stability for oxidative steam reforming of ethanol.

In particular, concerning the other two series of catalysts, Pt^{4+} and Pt^{2+} species reduction to Pt^0 is reported to occur between 150 and 220°C and a very similar interval is also described for the reduction of Ru^{4+} species to Ru^0 (Pérez-Bustos et al., 2019). Pt and Ru has a higher reducibility compared to Ni; thus, hydrogen dissociates directly over the noble metals sites and its spillover towards the surrounding particles is expected to enhance the reducibility of both NiO and CeO_2. As a consequence of the above observations, the incorporation of the noble metals in the monometallic catalyst has increased the H_2 uptake, which reaches 3122 and 3095 $\mu mol_{H2} \cdot g_{cat}^{-1}$ for the 3Pt10Ni and 3Ru10Ni catalysts, respectively (Table V. 7).

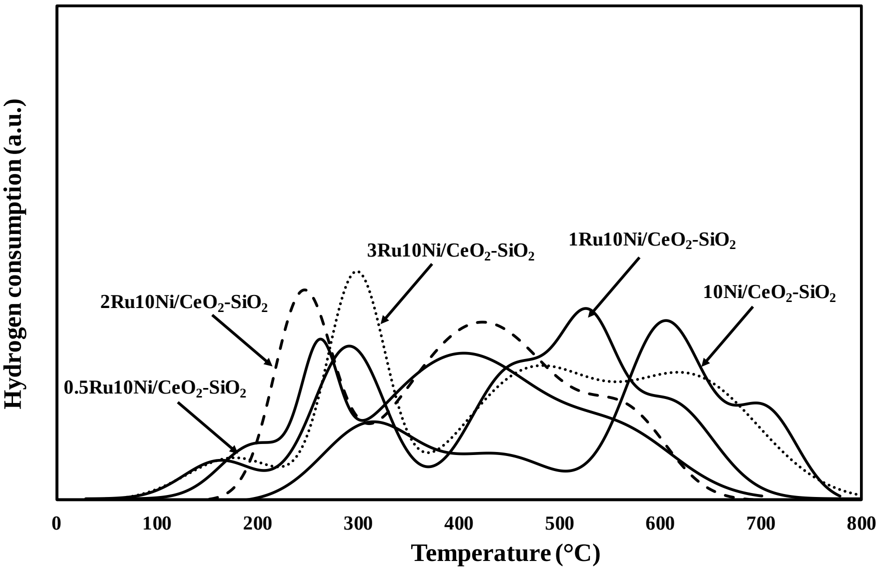

Figure V. 7 *TPR profiles of the Ru-based catalysts in comparison with the Ni/CeO_2-SiO_2 sample.*

Table V. 7 *Comparison between experimental and estimated hydrogen uptake related to Figure V. 5, Figure V. 6 and Figure V. 7.*

Sample	**Theoretical H_2 uptake ($\mu mol \cdot g_{cat}^{-1}$)**	**Experimental H_2 uptake ($\mu mol \cdot g_{cat}^{-1}$)**
10Ni	1704	2035
0.5Ag10Ni	1796	1799
1Ag10Ni	1889	1912
2Ag10Ni	2074	2214
3Ag10Ni	2260	2401
0.5Pt10Ni	1755	2345
1Pt10Ni	1806	2777
2Pt10Ni	1909	2756
3Pt10Ni	2011	3122
0.5Ru10Ni	1803	2341
1Ru10Ni	1902	2586
2Ru10Ni	2099	2714
3Ru10Ni	2297	3095

V.1.3 Results of ZPC measurements

In order to investigate the acidic character of the bare support CeO_2-SiO_2 and the bimetallic catalyst (Pt-Ni/CeO_2-SiO_2), ZPC measurements were performed on the fresh samples. The results are summarized in Table V. 8. These data clearly highlight that active species addition can modulate the surface acidity, by changing the pH from 4.4 to 5.1. In this regard, it is noteworthy that, during ethanol reforming, the acid sites of the catalyst may promote the side reactions (ethanol dehydration) leading to coke formation and sample deactivation (Zhurka et al., 2018).

Table V. 8 *Results of ZPC measurements.*

Sample	**ZPC (pH unit)**
CeO_2-SiO_2	4.4
2Pt-10Ni/CeO_2-SiO_2	5.1

V.2 Results of activity and stability tests for OSR under simulated bioethanol

In the following paragraphs, the performance of the prepared and characterized catalysts during oxidative steam reforming of ethanol in the fluidized bed reactor will be described.

A preliminary study is devoted to the evaluation of the effect of Ni substitution by Co as well as K addition as promoter. The latter analysis have been carried out by choosing cerium nitrate hexahydrate as CeO_2 salt precursor. Thereafter, the effect of ceria salt precursor (nitrate, ammonium nitrate, acetyl acetonate) on the activity and stability of the Pt-Ni/CeO_2-SiO_2 catalyst, which displayed the most stable behaviour during the preliminary tests, will be discussed. In order to select the optimal operative conditions for OSR tests, the effect of temperature and feeding conditions on the catalyst activity and stability was also studied.

The influence of the second metal type M (Pt, Ag and Ru) as well as its loading (0-3 wt%) on the performance of the M-Ni/CeO_2-SiO_2 catalysts prepared by selecting acetyl acetonate as precursor was also investigated. A kinetic model was to predict the variation of product gas distribution as a function of the reaction temperature and the most stable catalyst was identified during durability measurements at 500°C.

Once selected the formulation displaying the highest resistance towards deactivation during the oxidative reforming of a simulated distilled water/pure ethanol stream, further analyses were performed under a commercial fuel grade bioethanol mixture provided by *Eldor Corporation S.p. a*.

Finally, preliminary activity measurements of the developed formulation were performed in a fluidized bed membrane reactor.

V.2.1 OSR activity and stability of Pt-Ni, Pt-Co, and K-Pt-Ni/CeO_2-SiO_2 catalysts

The catalytic behaviour of the Pt-Ni/CeO_2-SiO_2 was compared with Pt-Co/CeO_2-SiO_2 and K-Pt-Ni/CeO_2-SiO_2 samples in the fluidized bed reactor at 500°C, water/ethanol ratio of 4 and oxygen/ethanol ratio of 0.5 and the results are reported in terms of ethanol conversion and hydrogen yield in Figure V. 8 and Figure V. 9, respectively. The catalytic performance was evaluated for at least 100 h of TOS. The K-Pt-Ni/CeO_2-SiO_2 sample displayed a stable behaviour (with a total ethanol conversion) only for 10 h. However, the H_2 yields recorded at the beginning of the test exceeded equilibrium predictions and this result requires an explanation. The reaction mechanism is very complex and, at intermediate temperatures, an H_2 yield deviation from thermodynamic is observed because the system kinetically is not capable to reach equilibrium values. The results reported in Table V.9 summarizes the initial products yields (mean values calculated during the first 10 h, 50 and 100 h of test and corresponding to total ethanol conversion for the K-Pt-Ni, Pt-Co and Pt-Ni catalysts, respectively) in comparison with the values predicted by thermodynamics. For example, in the case of the K-Pt-Ni catalyst, the experimental points suggest that the reaction rate of CO methanation reaction is quite low (Y_{CO}=13.8%), which resulted in a methane yield smaller than that predicted by thermodynamics (21.3 against 28.7%). As a consequence, for H_2 yield exceeding thermodynamic predictions, other species (i.e. methane) displayed yields lower than equilibrium values. With the increase of TOS, a partial catalyst deactivation was observed. However, after almost 60 h, a plateau condition was reached with no more variation in products distribution. In particular, ethanol conversion and hydrogen yield were attested, respectively, to 70 and 35%. The comparison between data reported in Table V. 9 (where the products yield at plateau conditions are also shown) revealed an evident decrease in the yield of carbon-containing species with TOS due, on one hand, to the reduction of ethanol conversion and, on the other hand, to the increase of by-products yield (i.e. acetaldehyde). In addition, reaction pathways involving coke formation, such as methane decomposition and Boudouard reaction, cannot be excluded. A considerable improvement in activity was observed for the Pt-Co/CeO_2-SiO_2 sample, which assured total ethanol conversion and a stable product gas distribution for almost 50 h. Moreover, the initial hydrogen yield well agreed with the equilibrium value (41.5 %).

In addition, looking at the data reported in Table V. 9, which refer to conditions of total ethanol conversion, no acetaldehyde was detected among the reaction products at the beginning of the test. However, for TOS higher than 50 h, product gas distribution over the Pt-Co/CeO_2-SiO_2 catalyst began to move away from equilibrium (a decrease in ethanol conversion was observed in Figure V. 8) and a partial activity decay was recorded.

Nevertheless, the system was attested to a stationary condition, with ethanol conversion and hydrogen yield of almost 60% and 24%, respectively. Also in this case, the change of products yield suggests that deactivation mainly occurred as a consequence of carbon formation on catalyst surface and acetaldehyde yield was not negligible (Y_{C2H4O}=12.9%).

However, the sample containing Co was tested for 220 h and the catalyst ability to hold the stationary conditions was verified for further 20 h. Nevertheless, the best behaviour in terms of activity and stability was recorded over the Pt-Ni/CeO_2-SiO_2 sample, which assured total conversion for more than 150 h and only a partial catalyst deactivation with time-on-stream. In fact, the impact of activity decay was less pronounced in this case and a lower extent of deactivation was observed. Methane yield remained quite high (Y_{CH4}=19.4%) and acetaldehyde formation was not observed; the higher yield to carbon containing species, observed in Table V.9 suggests a less pronounced occurrence of coking reactions over the Pt-Ni/CeO_2-SiO_2. In addition, the plateau behaviour was verified for almost 100 h without observing variation in products gas distribution.

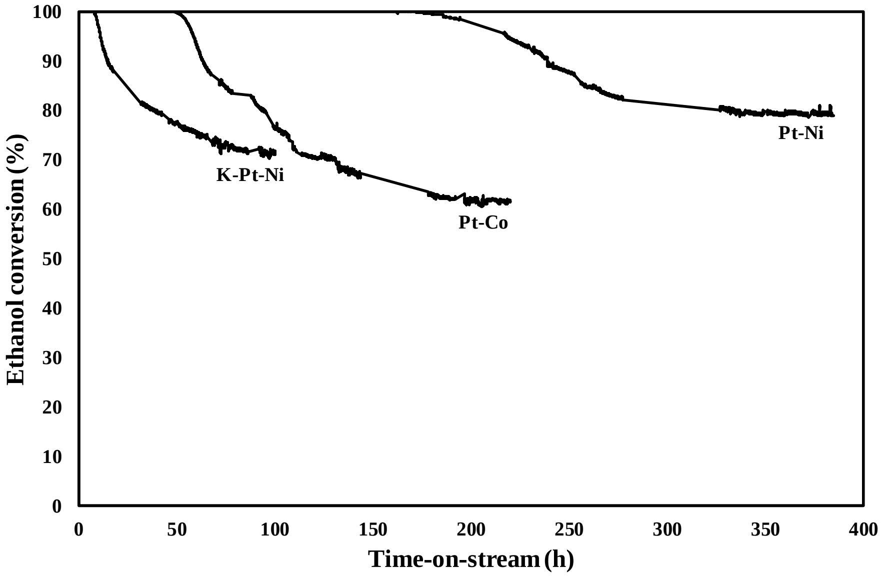

Figure V. 8 *Ethanol conversion as a function of TOS during OSR over catalysts prepared with cerium nitrate as precursor; T=500°C, f.r=4, o.r.=0.5, WHSV=4.1* h^{-1}.

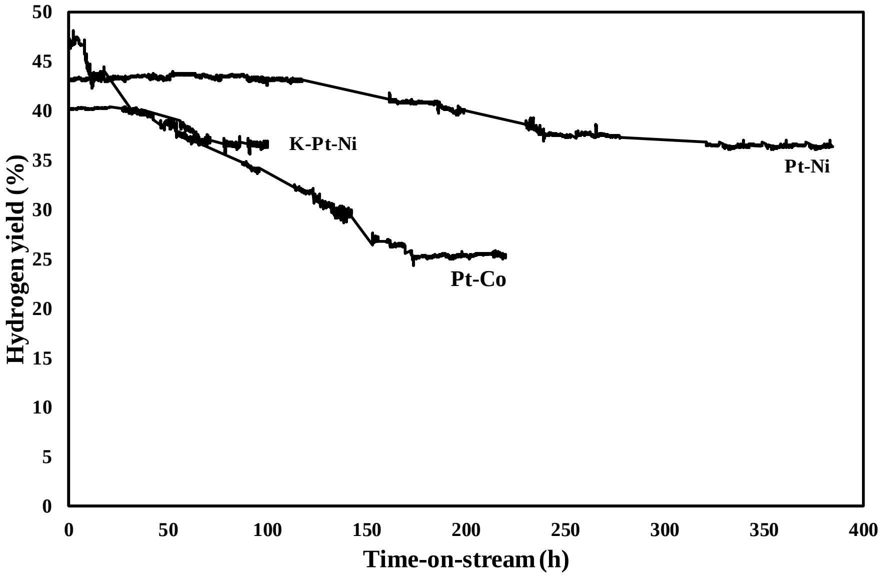

Figure V. 9 *Hydrogen yield as a function of TOS during OSR over catalysts prepared with cerium nitrate as precursor; T=500°C, f.r=4, o.r.=0.5, WHSV=4.1* h^{-1}.

Table V. 9 *Mean conversion and products yield recorded at the beginning of the experiment and under plateau conditions during the tests shown in Figure V. 8; 500°C, f.r.=4 and o.r=0.5; WHSV=4.1 h^{-1}.*

Sample	X (%)	Y_{H2} (%)	Y_{CH4} (%)	Y_{CO} (%)	Y_{CO2} (%)	Y_{C2H4O} (%)
	Products yield at the beginning of the test (mean values in the first 10 h)					
Pt-Ni	100	43.9	27.2	6.8	63.7	-
K-Pt-Ni	100	47.1	21.3	13.8	58.7	-
Pt-Co	100	41.2	33.4	10.9	53.3	-
	Products yield at the end of the test (mean values in the last 8 hours)					
Pt-Ni	80	36.1	19.4	10.6	46.5	-
K-Pt-Ni	71	35.2	12.8	11.3	42.4	5.4
Pt-Co	60	24.3	5.3	4.2	44.4	12.9
	Products yield predicted by thermodynamic analysis					
	100	41.5	28.7	9.2	62.1	-

The fact that, after a partial deactivation, the bimetallic catalysts reached a new stationary condition can be explained considering that coke deposited during the test is responsible for the blockage of the most reactive catalytic sites, involved in both reforming reaction as well as solid carbon formation pathways. Therefore, the partial deactivation of the latter sites gradually reduced carbon formation rate and, under stationary conditions, the net rate of carbon formation (i.e. the difference between coke formation and gasification) becomes equal to zero. Thus, no more activity loss is observed. This hypothesis will be better investigated in ParV.4.2.

Based on the above discussion, the experimental results shown in Figure V. 8 and Figure V. 9 demonstrate that K addition to Pt-Ni catalyst has a detrimental effect on both activity and stability while Ni substitution by Co is not able to improve catalyst resistance towards deactivation. In fact, compared to Pt-Ni/CeO_2-SiO_2 catalyst, the sample containing potassium displayed similar hydrogen yield but a lesser amount of methane was detected in the product stream. However, this result was probably not linked to the contribution of methane steam reforming reaction: CO_2 and CO yield are quite the same in the two cases (Table V.9). Therefore, it is possible to conclude that K addition increased the contribution of methane decomposition reactions, which led to hydrogen and coke formation (Grewal and Roy, 2016). Moreover, an average acetaldehyde yield of 5.4 % was recorded for the potassium-containing sample. For Ni/CeO_2 catalysts employed during ethanol reforming reactions, also other authors found that the addition of K as promoter did not protect the catalyst against formation of carbonaceous deposits, and did not improve its stability during the reaction (Słowik et al., 2018). This result was probably due to the smaller nickel oxide crystallites in Pt-Ni/CeO_2-SiO_2 catalyst (Table V. 2) and a partial sintering of these particles for the K-containing sample, as a consequence of the further calcination step. The strong dependence of catalyst deactivation on NiO particles dimension was previously reported (Palma et al., 2017d).

In the case of Co-based sample, the lowest hydrogen yield (24.3 %) at the end of the test was recorded. Moreover, a very low methane production was observed due, on one hand, to the previously discussed CH_4 decomposition pathways and/or, on the other hand, to the quite low rate of acetaldehyde decomposition reaction. The study of reaction mechanism for ethanol reforming on bimetallic CeO_2-based catalysts, in fact, highlighted that the latter pathway, together with acetaldehyde steam reforming, is crucial to assure high hydrogen yield (Palma et al., 2013). However, at plateau conditions, the Pt-Co/CeO_2-SiO_2 catalyst is not capable to promote complete C_2H_4O conversion. Conversely, the production of only CO, CO_2, CH_4 and H_2 was observed over the bimetallic catalyst containing Ni, which resulted the most stable among the tested catalysts.

Based on the above results, further studies were focused on the Pt-Ni/CeO_2-SiO_2 formulation.

V.2.2 OSR activity and stability of Pt-Ni/CeO_2-SiO_2 catalysts: effect of cerium salt precursor

Figure V. 10 and Figure V. 11 show the results obtained in the fluidized bed reactor for 100 h of test with the three catalysts prepared from different cerium salt precursors and compared in terms of ethanol conversion and hydrogen yield evolution with time-on-stream.

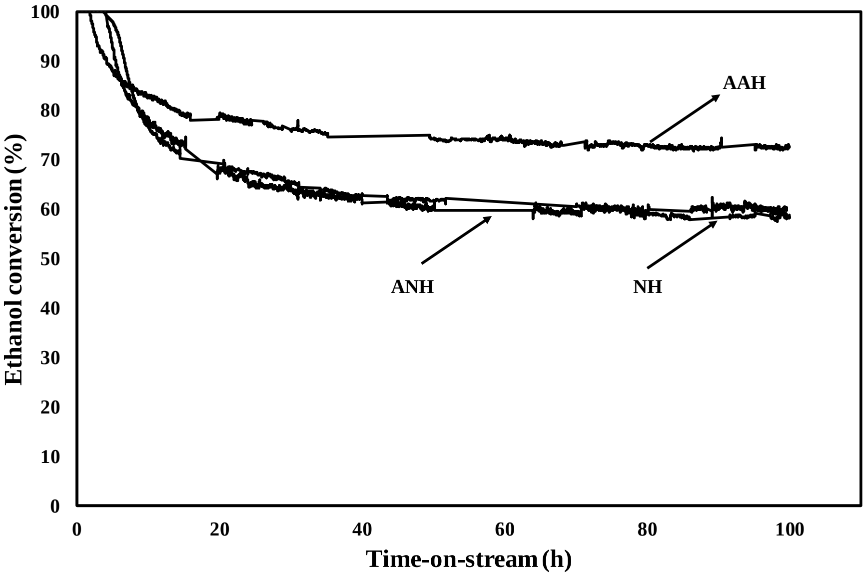

Figure V. 10 *Ethanol conversion as a function of TOS during OSR over catalysts prepared with different cerium precursors; T=500°C, f.r=4, o.r.=0.5, WHSV=12.3 h^{-1}.*

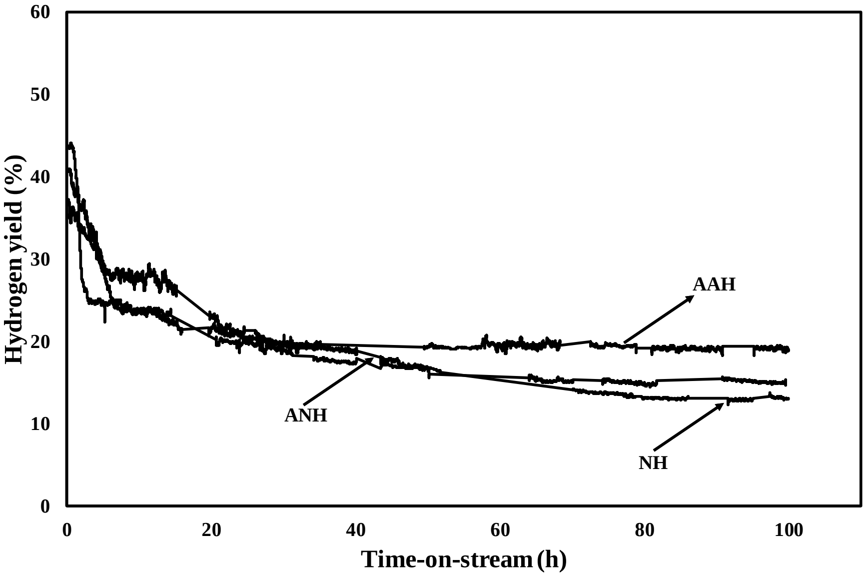

Figure V. 11 *Hydrogen yield as a function of TOS during OSR over catalysts prepared with different cerium precursors; T=500°C, f.r=4, o.r.=0.5, WHSV=12.3 h^{-1}.*

The performance was evaluated at 500°C, H_2O/C_2H_5OH ratio of 4, O_2/C_2H_5OH ratio of 0.5 (denoted, respectively, as f.r. and o.r. respectively) and WHSV of 12.3 h^{-1}.

A quite high space velocity was selected in order to evaluate catalyst behaviour under more stressful operative conditions. The three catalysts suffered for a partial deactivation with TOS and total ethanol conversion was recorded only at the beginning of the test. Similarly, hydrogen yield approached the value predicted by thermodynamic equilibrium (41.5 %) only for the first minutes of test. However, despite the partial activity loss recorded in the three cases, after almost 80 h of test, conversion and yield profile were attested to new stationary values. This phenomenon has been described in the previous paragraph. Very close conversion and yield profiles were observed for the catalysts prepared by impregnating cerium nitrate hexahydrate and cerium ammonium nitrate hexahydrate on the silica support. Ethanol conversion decreased from 100% to 60% within 100 h of test over the samples NH and ANH, while hydrogen yields were almost 15% (with slightly lower values for the catalyst prepared from cerium nitrate hexahydrate). A clear improvement in the performance of the Pt-Ni/CeO_2-SiO_2 catalyst was reached by selecting acetyl acetonate as precursor. The ethanol conversion measured after 100 h of test was of almost 74% and an increase of 20% in hydrogen yield with respect to the samples NH and ANH was also observed. In order to understand better the effect of cerium salt precursor choice on the catalyst performance, the products yield recorded under total conversion conditions and after 100 h of tests are compared with thermodynamic predictions and discussed for the catalysts NH, ANH and AAH (Table V. 10).

Within the first 2 hours of the test, both ethanol and acetaldehyde were not detected in the stream exiting the fluidized bed reactor and the mean product selectivity was negligibly affected by the salt precursor choice. However, hydrogen yield was lower than the value predicted by thermodynamic analysis over all the samples. In fact, the results of Y_{CH4}, Y_{CO} and Y_{CO2} suggest that the activity towards methane steam reforming reaction is lessened compared to equilibrium conditions. The quite high space velocity could inhibit the above pathway, as previously reported for the Pt-Ni catalyst (Palma et al., 2016). For example, in the case of the NH sample, methane yield was equal to 33.1%, against a thermodynamic value of 28.7%. However, as time-on-stream went on, a decrease in methane production was observed over the three catalysts. This result can be attributed to methane decomposition reactions (Sharma et al., 2017), responsible for carbon deposition on catalyst surface. Independently from the selected cerium salt precursor, after 100 h of test, acetaldehyde was observed in the reforming mixture, demonstrating that the partial deactivation involves the catalytic sites devoted in promoting C_2H_4O decomposition to methane and carbon monoxide (Vaidya and Rodrigues, 2006).

Table V. 10 *Mean conversion and products yield recorded at the beginning of the experiment and under plateau conditions during the tests shown in* Figure V. 10*; 500°C, f.r.=4 and o.r=0.5; WHSV=12.3 h^{-1}.*

Sample	X (%)	Y_{H2} (%)	Y_{CH4} (%)	Y_{CO} (%)	Y_{CO2} (%)	Y_{C2H4O} (%)
	Products yield at the beginning of the test (mean values in the first 2 hours)					
NH	100	34.2	33.1	12.3	50.9	-
ANH	100	34.4	32.7	11.9	51.7	-
AAH	100	35.3	31.2	12.6	53.1	-
	Products yield at the end of the test (mean values in the last 20 hours)					
NH	59.3	13.1	10.9	25.6	5.6	18.9
ANH	60.1	15.4	5.5	31.5	4.5	18.1
AAH	73.3	19.4	12.2	30.1	19.1	11.1
	Products yield predicted by thermodynamic analysis					
-	100	41.5	28.7	9.2	62.1	-

Acetaldehyde yield was above 18% over the samples prepared from cerium nitrates while a reduction of almost 40% was observed over the sample AAH: the less promoted formation of C_2H_4O resulted in an improved H_2 yield, which was attested to 19.4% after 100 h of time-on-stream.

The more interesting results (in terms of activity, selectivity and stability) for OESR reaction recorded over the sample AAH are obviously related to the salt chemical structure. In the case of acetyl acetonate, the organic group of the salt probably assures a templating effect, which protects ceria molecules, improving their dispersion (as demonstrated by XRD results, Table V. 3 and Figure V. 2). Therefore, the catalyst is much more reactive towards both reforming and coke gasification reactions. The above phenomenon was also reported by other authors (Faria et al., 2008). Song et al. (Song et al., 2010) observed a significantly better catalytic performance for ethanol steam reforming over Co/CeO_2 samples prepared by using Co acetyl acetonate, which might facilitate Co dispersion on the surface of the ceria support. Bensalem et al. (Bensalem et al., 1995) prepared CeO_2-SiO_2 supports either through anchoring cerium acetyl acetonate in organic medium or by aqueous impregnation of cerium nitrate, observing that the classical latter procedure led to larger ceria particles.

V.2.3 Effect of operative conditions on the activity and stability of the AAH sample

The stability performance of the 3Pt-10Ni/CeO_2-SiO_2 sample prepared by using cerium acetylacetonate as salt precursor was preliminary investigated at different temperatures (400, 500, 600°C), oxygen to ethanol ratios (0.25, 0.5, 0.75) and steam to ethanol ratio (3,4, 6) in the fluidized bed reactor.

The results reported in Figure V. 12 and Figure V. 13 describe the impact of the reaction temperature on catalyst stability, in terms of ethanol conversion and hydrogen yield. At 600°C, total ethanol conversion was recorded in the whole investigated interval. The mean hydrogen yield of 52.3% recorded at the beginning of the test (Table V. 11) was lower than the value predicted by thermodynamics, due to the reduced activity of the catalyst towards methane steam reforming reaction with respect to the expected one, attested by a methane selectivity of 10.6% against the equilibrium value of 6.6%. However, the increase of the reaction temperature led to a decrease in the H_2/CO molar ratio, due to the progressive growth in the CO amount, based on the contribution of the endothermic reverse water gas shift reaction (Vita et al., 2014). An expected worsening in the catalyst performance was observed as the reaction temperature decreases, with the initial mean hydrogen yield lowering from a value of 52.3% recorded at 600°C to 21.8%, measured during the test carried out at 400°C. Moreover, the behaviour of the catalyst tested at 400°C was unstable even at the beginning of the test, while a stationary trend for at least the first 2 hours was observed at 500 and 600°C. In particular, when reaction temperature was fixed to 400°C, total ethanol conversion was recorded only at the early moments of the test, and the decreasing trend in catalytic performance resulted in a mean value of X in the first 2 hours of test of 97.5%. For the Pt-Ni/CeO_2-SiO_2 sample tested at different temperatures, a decreasing trend of hydrogen yield with time-on-stream was observed, even at 600°C under conditions of total ethanol conversion. In fact, the formation of carbonaceous deposits on catalyst surface could partially inhibit methane reforming, thus leading to a reduction in the mean hydrogen yield of almost 22%. However, it is interesting to observed that the contribution of acetaldehyde decomposition/reforming reactions is unaffected by time-on-stream at 600°C, thus resulting in the absence of C_2H_4O in the products stream; in addition, acetone formation was not observed during these tests. Conversely, reduced temperatures resulted in an increase of acetaldehyde yield after 100 hours of test, with mean values of 11.1% at 500°C and of 15.5% at 400°C. Despite the worsening of the catalytic performance with time-on-stream observed in Table V. 12, the Pt-Ni/CeO_2-SiO_2 sample, tested under different temperatures, approached a new stationary condition after a certain number of hours (almost 80 hours at 500°C as well as 600°C).

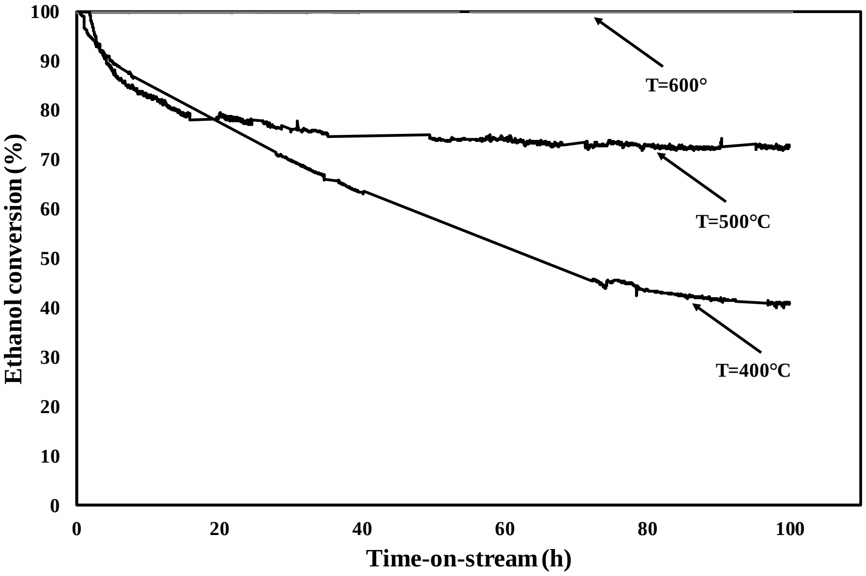

Figure V. 12 *Ethanol conversion as a function of TOS during OSR over the AAH sample; f.r=4, o.r.=0.5, WHSV=12.3 h*$^{-1}$.

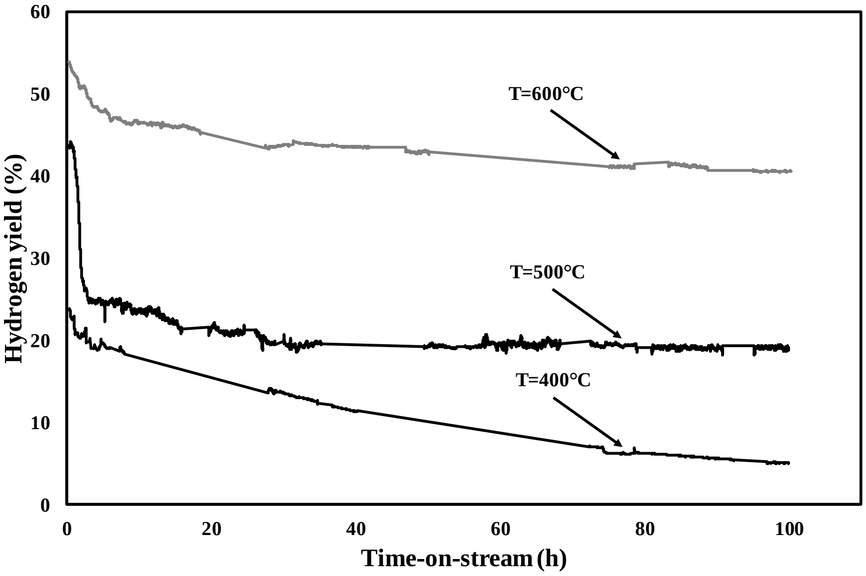

Figure V. 13 *Hydrogen yield as a function of TOS during OSR over the AAH sample; f.r=4, o.r.=0.5, WHSV=12.3 h*$^{-1}$.

On the other hand, the above phenomenon was less pronounced during the test performed at 400°C: the system displayed a stable behaviour only after

96 hours of time-on-stream. Reduced temperatures are also expected to lead to higher methane yield, due to disadvantaged reforming pathways. However, an inverse trend can be observed in Table V. 11 with reference to the results recorded at the end of test. In fact, the decomposition of methane formed during ethanol reforming is one of the main cause of coke formation on catalyst surface (Ni et al., 2007).

Table V. 11 *Mean conversion and products yield recorded at the beginning of the experiment and under plateau conditions during the tests shown in* Figure V. 12*; 500°C, f.r.= 4, o.r.= 0.5; WHSV=12.3 h*$^{-1}$.

T	**X (%)**	**Y_{H2} (%)**	**Y_{CH4} (%)**	**Y_{CO} (%)**	**Y_{CO2} (%)**	**Y_{C2H4O} (%)**
	Products yield at the beginning of the test (mean values in the first 2 hours)					
400	97.5	21.8	34.6	8.3	50.5	-
500	100	35.3	31.2	12.6	53.1	-
600	100	52.3	10.6	29.2	57.5	-
	Products yield at the end of the test (mean values in the last 8 hours)					
400	41.7	5.5	1.1	5.7	20.1	15.5
500	73.3	19.4	12.2	30.1	19.1	11.1
600	100	40.8	19.1	31.8	44.1	-
	Products yield predicted by thermodynamic analysis					
400	100	18.4	48.3	1.2	50.5	**-**
500	100	41.5	28.7	9.2	62.1	**-**
600	100	64.2	6.6	31.1	62.3	**-**

The effect of oxygen content increase in the reacting mixture is summarized in Figure V. 14 and Figure V. 15, in terms of ethanol conversion and hydrogen yield as a function of time-on-stream, respectively. Total ethanol conversion was recorded during the first 2 hours of the test, whatever the selected O_2/C_2H_5OH ratio. The mean product yields recorded under the condition of total conversion are summarized in Table V. 12, in comparison with equilibrium values. Hydrogen yields higher than 40% for r.o. in the interval 0.25-0.75, with a decrease in CH_4 formation and a corresponding growth in CO_2 yield by increasing the oxygen content were predicted by thermodynamics.

The highest initial H_2 yield (41.1%) was recorded under an o.r. of 0.25; on the other hand, by increasing the oxygen concentration in the reacting mixture form 5 to 7.5%, no significant changes in initial hydrogen yields were observed. However, a more pronounced decrease in CH_4 yield (from 31.2 to 20.5%) was observed, proving the higher extent of oxidation reactions, thus leading to an enhancement in CO_2 formation (Srisiriwat et al., 2009). The 3Pt-10Ni/CeO_2-SiO_2 sample, tested at r.o.=0.25 and 0.75, reached a stationary condition after more than 90 hours of time-on-stream, and the mean product selectivity was evaluated in the last 8 hours of test.

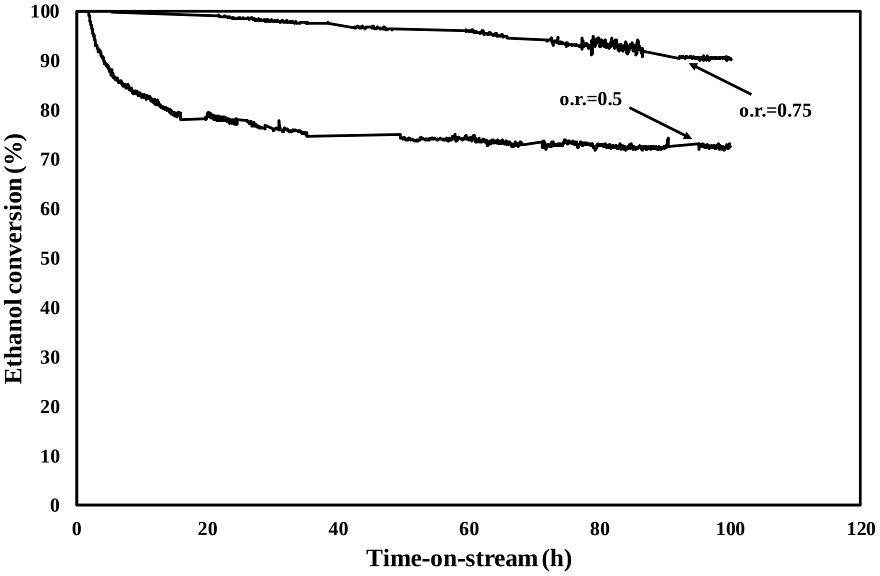

Figure V. 14 *Ethanol conversion as a function of TOS during OSR over the AAH sample; T=500°C, f.r=4, WHSV=12.3* h^{-1}.

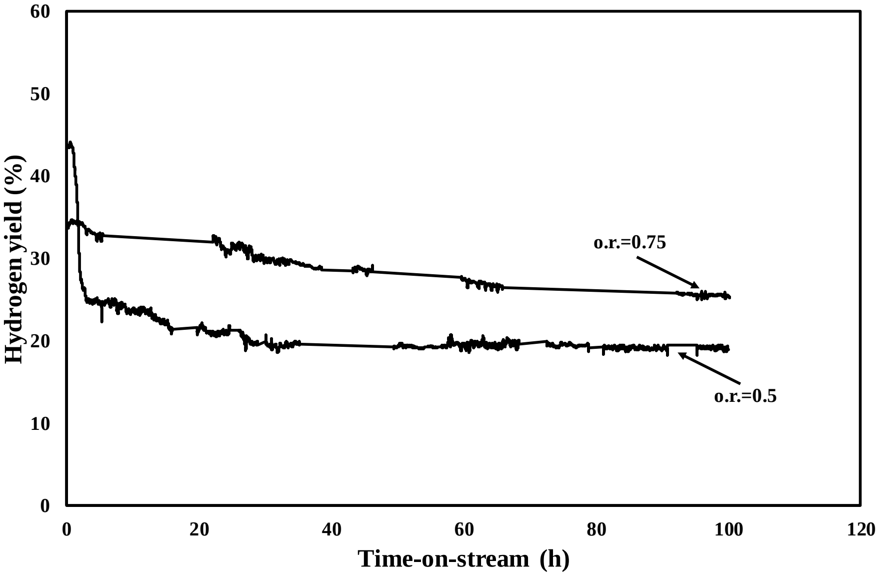

Figure V. 15 *Hydrogen yield as a function of TOS during OSR over the AAH sample;T=500°C, f.r=4, WHSV=12.3* h^{-1}.

Table V. 12 *Mean conversion and products yield recorded at the beginning of the experiment and under plateau conditions during the tests shown in* Figure V. 12*; 500°C, T=500°C, f.r.= 4, WHSV=12.3* h^{-1}*.*

o.r.	X (%)	Y_{H2} (%)	Y_{CH4} (%)	Y_{CO} (%)	Y_{CO2} (%)	Y_{C2H4O} (%)
	Products yield at the beginning of the test (mean values in the first 2 hours)					
0.25	100	41.1	29.5	11.4	54.2	-
0.5	100	35.3	31.2	12.6	53.1	-
0.75	100	34.3	20.5	9.9	66.9	-
	Products yield at the end of the test (mean values in the last 8 hours)					
0.25	65.9	21.5	14.9	11.8	25.1	14.9
0.5	73.3	19.4	12.2	30.1	19.1	11.1
0.75	90.5	25.1	15.4	18.5	46.7	5.1
	Products yield predicted by thermodynamic analysis					
0.25	100	43.1	34.2	9.3	56.5	
0.5	100	41.5	28.7	9.2	62.1	-
0.75	100	40.7	23.5	8.9	67.6	

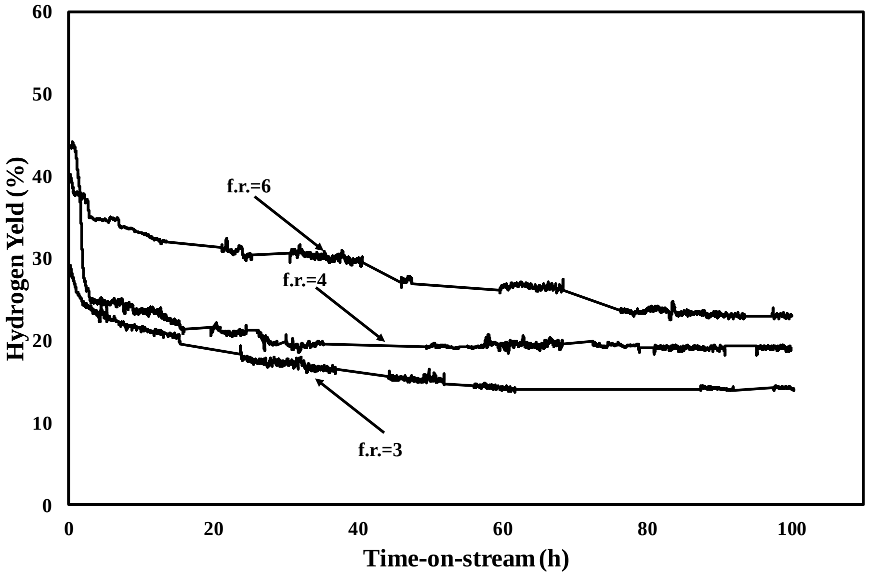

Figure V. 16 *Ethanol conversion as a function of TOS during OSR over the AAH sample; T=500°C, o.r.=0.5, WHSV=12.3* h^{-1}*.*

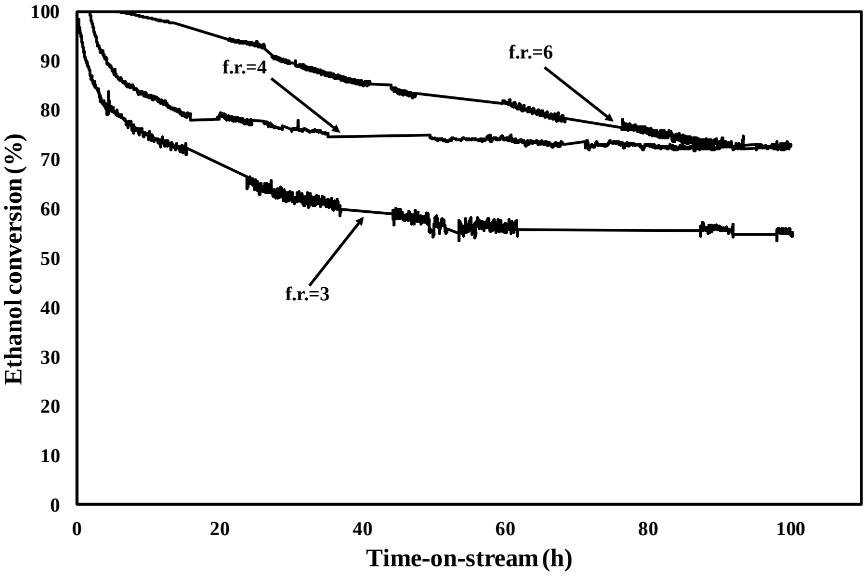

Figure V. 17 *Hydrogen yield as a function of TOS during OSR over the AAH sample; T=500°C, o.r.=0.5, WHSV=12.3 h^{-1}.*

The addition of more oxygen in the reacting mixture should led to a reduction on the final hydrogen yield; however, by increasing O_2/C_2H_5OH ratio in the range 0.5-0.75, an inversion in this trend was observed. In particular, the hydrogen yield profile recorded during the test at r.o.=0.75 was higher than that measured for an O_2/C_2H_5OH ratio of 0.5 and an ethanol conversion of 90.5 % was observed at plateau conditions. This interesting result can be explained considering that high oxygen contents in the presence of catalytic supports with remarkable ionic conductivity (Sun et al., 2008) encourages the oxidation of carbon-containing species, but not at the expense of hydrogen. As a result, the growth of oxygen content in the interval 0.25-0.75 led to a lower by-products formation: acetaldehyde yield measured at plateau conditions decreased from 14.1% at r.o.=0.25 to 5.1% at r.o.=0.75 (Table V. 12), due to easier oxidation of C-containing species. The above results show that, by fixing the oxygen to ethanol ratio to 0.75, it is possible to obtain an improvement in the catalytic performance, with high conversions and hydrogen yields.

The effect of the steam to ethanol ratio on C_2H_5OH conversion and H_2 yield is shown in Figure V. 16 and Figure V. 17. Total ethanol conversion was recorded for the first 4 hours of test when the steam to ethanol ratio was fixed to 6; moreover, hydrogen yield profile was higher than that recorded in the other two operative conditions in the whole investigated temperature interval. In fact, according to thermodynamic predictions (Table V. 13), higher water content in the reacting mixture can increase hydrogen production, due to the promotion of reforming reaction.

Table V. 13 *Mean conversion and products yield recorded at the beginning of the experiment and under plateau conditions during the tests shown in* Figure V. 16*; 500°C, T=500°C, f.r.= 4, WHSV=12.3 h^{-1}.*

f.r.	X (%)	Y_{H2} (%)	Y_{CH4} (%)	Y_{CO} (%)	Y_{CO2} (%)	Y_{C2H4O} (%)
	Products yield at the beginning of the test (mean values in the first 2 hours)					
3	91.6	26.3	25.5	13.9	43.1	12.1
4	100	35.3	31.2	12.6	53.1	-
6	100	38.2	32.7	7.7	64.4	-
	Products yield at the end of the test (mean values in the last 8 hours)					
3	54.3	13.7	5.1	8.1	27.7	17.1
4	73.3	19.4	12.2	30.1	19.1	11.1
6	73.5	23.1	14.7	11.7	42.4	-
	Products yield predicted by thermodynamic analysis					
3	100	37.6	31.8	10.3	57.9	**-**
4	100	41.5	28.7	9.2	62.1	**-**
6	100	48.9	23.9	7.7	68.4	**-**

The experimental data reflected this trend; however, when the f.r. was fixed to 6, the mean H_2 yield at the beginning of the test was equal to 38.2 %, more than 20% lower than the predicted value. The latter result was coherent with the mean methane yield, which was also higher than the equilibrium datum. However, by increasing the steam to ethanol ratio, methane yield is also enhanced (Table V. 13), due to the lower selectivity towards acetaldehyde (which diminished from 17.1% at r.a.=3 to almost 0 at r.a.=6). The mean H_2 yield recorded at the end of the test is slightly affected by an increase in f.r. above the stoichiometric value; similar results were obtained by other authors in the temperature range 500-550°C (Carrera Cerritos et al., 2011), which were ascribed to the lower extent of ethanol decomposition reactions. However, a growth in the added steam can facilitate the water gas shift reaction, leading to a slightly increase in the H_2/CO ratio. The by-products (i.e. acetaldehyde) yield decreased with an increase in the steam to ethanol ratio and, at the beginning of the test, C_2H_4O was not detected for f.r.=4 and 6. On the other hand, for a steam to ethanol ratio equal to the stoichiometric value, acetaldehyde formation was observed even at low time-on-stream values while, for f.r.=6, the reforming of C_2H_4O eventually formed was promoted, thus leading to the absence of the latter by-product in the whole investigated time interval. The increase of the steam content in the reforming mixture was beneficial in terms of reduced by-products selectivity (acetaldehyde and coke) resulting, however, in a less positive effect (in terms of hydrogen yield) compared to o.r. growth from 0.5 to 0.75.

In summary, the effect of operative conditions (temperature, steam to ethanol as well as oxygen to ethanol ratio) on the performance of the most stable catalyst was investigated, finding that the increase of temperature can effectively reduce the extent of catalyst deactivation. By feeding mixtures with higher oxygen to ethanol ratio, it was also possible to reduce activity losses and, improving, at the same time, hydrogen production. When f.r. was increased from 4 to 6, at the end of the test, acetaldehyde disappeared in the products stream and H_2 yield increased to 23.1%, with a very low extent of deactivation. Therefore, aiming at improving H_2 yield and catalyst resistance towards deactivation, it can be convenient to fix 600°C, o.r. of 0.75 and f.r. of 6. However, high reaction temperatures negatively affects fixed as well operative costs and a f.r. of 6 implies to manage high water quantities, which can undermine the normal plant operations. In addition, oxygen can have a negative impact during operation in the presence of membranes. In this regard, it was reported that carbon deposited during reforming reactions in the presence of oxygen can form pinholes, which is a fatal reason for poor stability, especially in the case of ultra-thin Pd membranes. Oxygen, in fact, helps to roughen the surface which, despite improves H_2 adsorption/desorption, favours the formation of open pin hols, thus negatively affecting membrane perm-selectivity (Ismail et al., 2018). Based on these observation, intermediate feeding conditions and temperatures were selected for the following experiments.

V.2.4 Influence of the type (Ag, Pt, Ru) and the loading of the second metal (M) on the activity of M-Ni/CeO_2-SiO_2

The results shown in the previous paragraphs highlighted the promising behaviour of the Pt-Ni/CeO_2-SiO_2 catalysts for oxidative steam reforming of ethanol. However, Pt is a quite expensive metal having a not negligible impact on the final cost of the catalyst. In this regard, the effect of Pt substitution by cheaper metals (Ag and Ru (Hou et al., 2015b, Ramos et al., 2012)) on catalyst activity for OSR of ethanol between 300 and 600°C was investigated. The loading of the second metal (Pt, Ag, Ru) was optimized in the interval 0-3 wt% and a kinetic study on the most promising samples was carried out to develop a model able to predict the product gas distribution as a function of the reaction temperature.

The performance of the Ag-Ni, Ru-Ni and Pt-Ni/CeO_2-SiO_2 catalysts for oxidative reforming of ethanol were preliminary compared in terms of ethanol conversion and H_2 yield. The results display the positive effect of temperature growth on C_2H_5OH conversion (Figure V. 18, Figure V. 20 and Figure V. 22) and hydrogen yield (Figure V. 19, Figure V. 21 and Figure V. 23), as a consequence of the favoured thermodynamics and beneficial impact of temperature on reaction kinetics (Karakaya et al., 2013), with a clear improvement in the performance of all the tested samples.

Moreover, Ag deposition did not allow an evident enhancement of the monometallic catalyst activity (Figure V. 18 and Figure V. 19): above 400°C, a nonlinear dependence of ethanol conversion on silver content was observed and the worst performance was recorded over the 1 and 2 wt% Ag catalysts. Conversely, total conversion was measured at 600°C over the monometallic sample and the bimetallic catalysts containing Pt and Ru (Figure V. 20 and Figure V. 22); moreover, the deposition of both platinum and ruthenium on the Ni/CeO_2-SiO_2 catalyst assured higher conversions, whatever the selected reaction temperature.

Concerning the influence of the second metal content, the highest ethanol conversion was observed for the 3Ag10Ni sample, while for the Pt series, the 2Pt10Ni catalyst displayed the best results in terms of ethanol conversion (Figure V. 22).

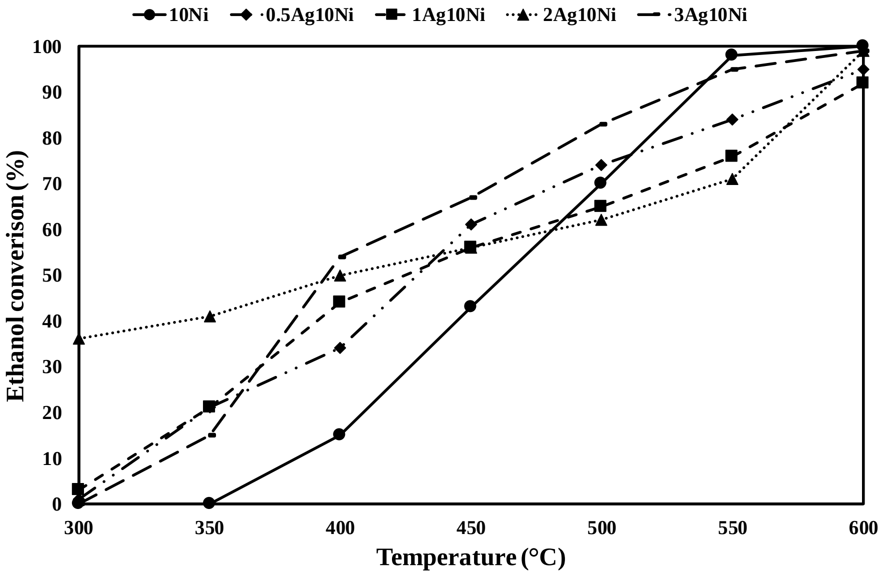

Figure V. 18 *Ethanol conversion as a function of reaction temperature during OSR over the Ag-Ni samples in comparison with the Ni/CeO_2-SiO_2 catalyst; f.r=4, o.r.=0.5, WHSV=61.7* h^{-1}.

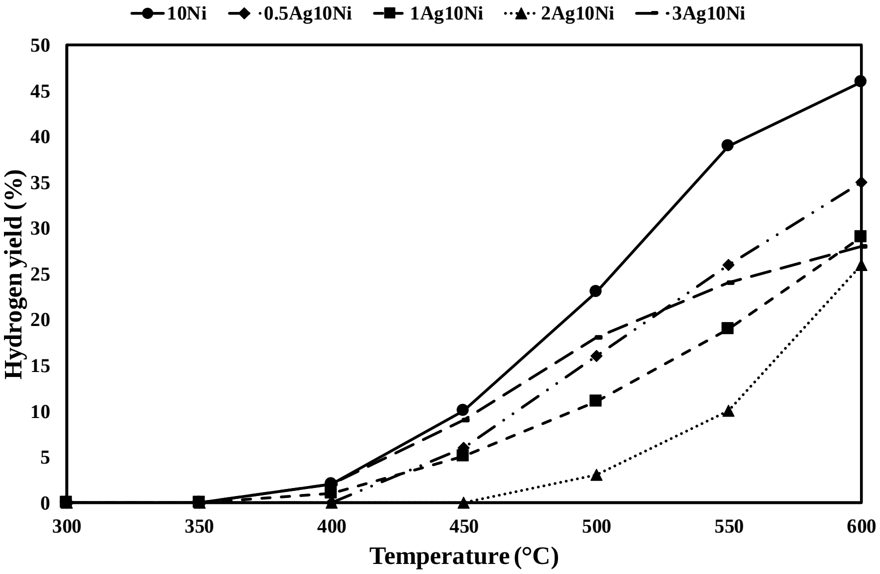

Figure V. 19 *Hydrogen yield as a function of reaction temperature during OSR over the Ag-Ni samples in comparison with the Ni/CeO₂-SiO₂ catalyst; f.r=4,, o.r.=0.5, WHSV=61.7 h⁻¹.*

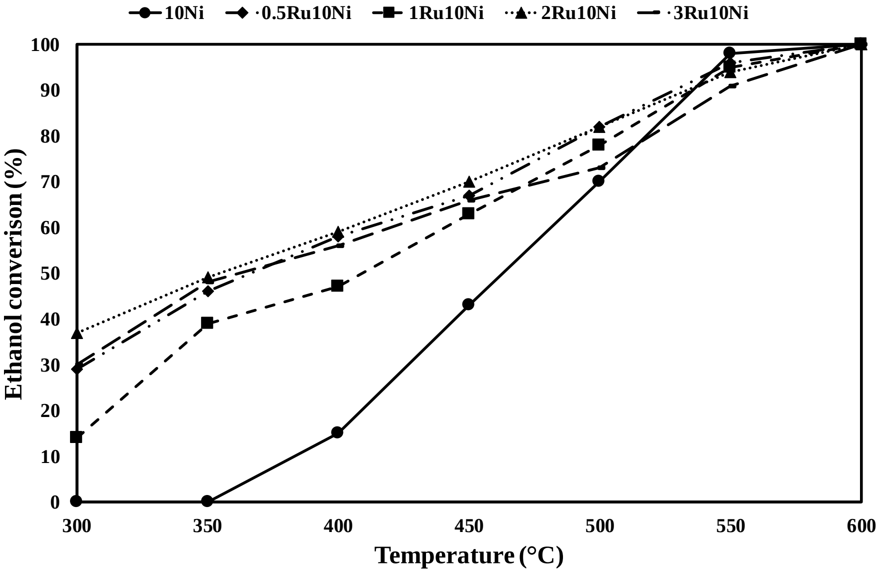

Figure V. 20 *Ethanol conversion as a function of reaction temperature during OSR over the Ru-Ni samples in comparison with the Ni/CeO₂-SiO₂ catalyst; f.r=4, o.r.=0.5, WHSV=61.7 h⁻¹.*

In the case of Ru-based catalysts, a less pronounced effect of metal loading on catalyst activity was observed and only a slightly improvement in conversion was measured for the 2Ru-10Ni/CeO_2-SiO_2 sample (Figure V. 20). Despite the stressful operative conditions selected (the contact time is very low compared to the typical reforming conditions), high ethanol conversions were recorded over all the catalysts, especially above 400°C. However, the complex reaction mechanism resulted in different products selectivities and Figure V. 19, Figure V. 21 and Figure V. 23 compare the hydrogen yield profiles recorded over the monometallic and bimetallic samples. All the catalysts containing Ag, independently from the metal loading, displayed lower H_2 production compared to the monometallic Ni/CeO_2-SiO_2 sample. Once again, the worst performance was recorded over the 1 and 2wt% Ag-based samples and the results shown in Figure V. 19 also proved that it is not necessary to increase the metal loading up to 3wt%, as comparable results in terms of hydrogen yield were measured for the 0.5Ag10Ni and 3Ag10Ni samples.

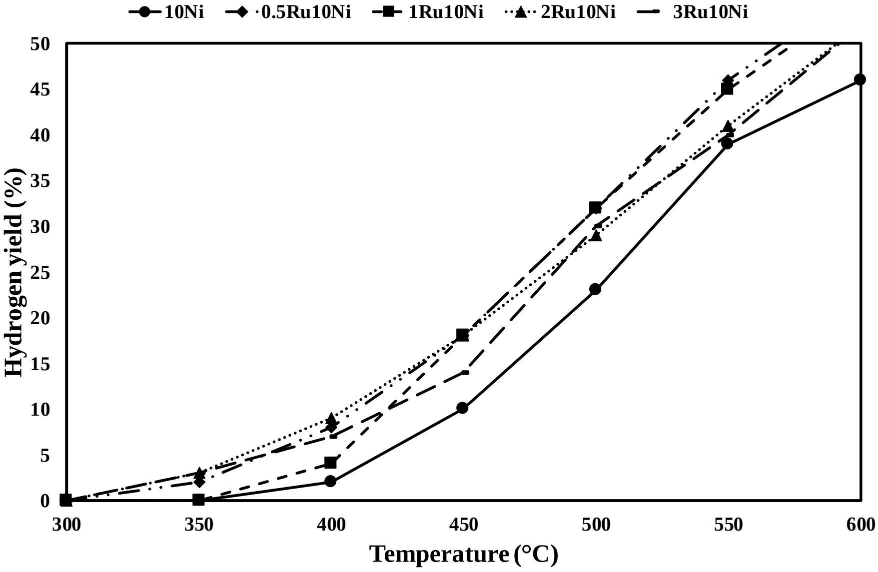

Figure V. 21 *Hydrogen yield as a function of reaction temperature during OSR over the Ru-Ni samples in comparison with the Ni/CeO_2-SiO_2 catalyst; f.r=4, o.r.=0.5, WHSV=61.7 h^{-1}.*

The best results in terms of H_2 yield were recorded over the Pt- and Ru-based catalysts at 600°C, which assured values higher than 50%, due to the positive effect of temperature increase on the contribution of reforming reactions (Yentekakis et al., 2015). Very similar results were recorded over the platinum and ruthenium samples prepared at the same metal loading; moreover, for the Ru-based catalysts, the effect of ruthenium loading increase in the interval 0.5-2 wt% was less pronounced with respect to the Pt-containing samples, with very close H_2 yield profiles: for example, at 450°C (Figure V. 21), hydrogen yield was attested to 18% for the 0.5Ru10Ni, 1Ru10Ni and 2Ru10Ni samples. The worst performance in terms of hydrogen production were recorded over the 3wt% samples for both the Ru and Pt series; however, the 3Ru10Ni catalyst displayed better H_2 production than the Pt-sample in the whole investigate temperature interval. By reducing the metal loading, in fact, higher H_2 yields were recorded (Figure V. 21 and Figure V. 23), proving that low noble metal contents are sufficient to assure promising activity for oxidative steam reforming of ethanol.

In order to better understand the reactivity of the different employed samples, a comparison was also performed in terms of reaction products yield (Figure V. 24). As an example, CH_4, CO and CO_2 yield recorded at 500°C over all the catalyst are provided.

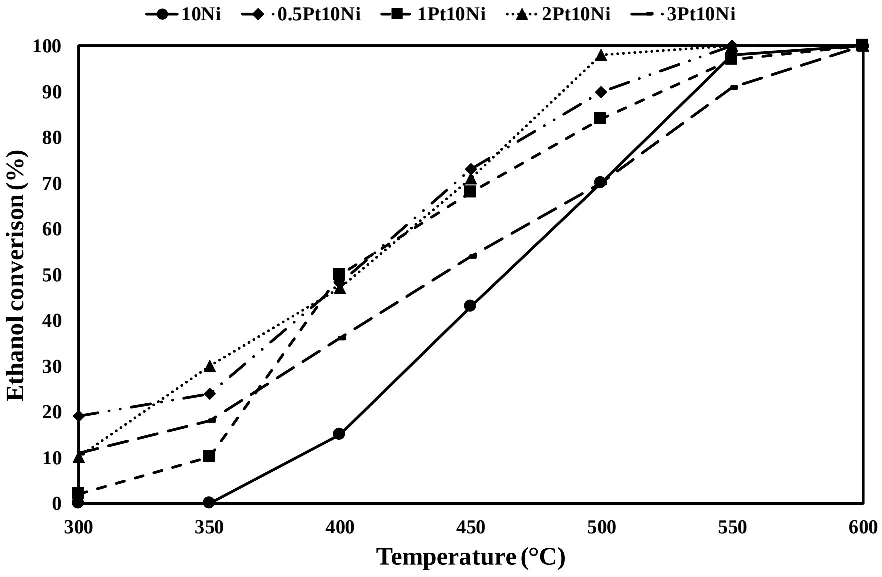

Figure V. 22 *Ethanol conversion as a function of reaction temperature during OSR over the Pt-Ni samples in comparison with the Ni/CeO_2-SiO_2 catalyst; f.r=4, o.r.=0.5, WHSV=61.7 h^{-1}.*

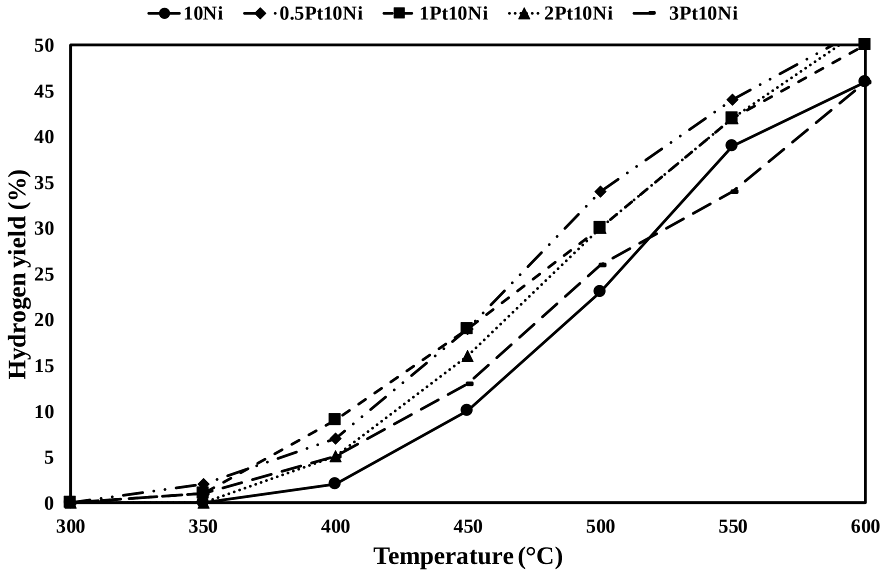

Figure V. 23 *Hydrogen yield as a function of reaction temperature during OSR over the Pt-Ni samples in comparison with the Ni/CeO_2-SiO_2 catalyst; f.r=4, o.r.=0.5, WHSV=61.7 h^{-1}.*

Under the selected operative conditions, only the formation of H_2, CH_4, CO and CO_2 was observed over the investigated catalysts while other by-products (i.e. ethylene or acetaldehyde) were not detected. At 500°C, the Ag-based catalysts displayed the highest methane selectivity, which demonstrates, together with the results shown in Figure V. 19, the quite low methane steam reforming activity of these samples. Conversely, the Pt and Ru-containing samples assured lessened CH_4 yields compared to the Ag-Ni/CeO_2-SiO_2 series and improved hydrogen production rates.

In addition, the relative weight of CO/CO_2 ratios was determined by the contribution of both reforming and water gas shift reactions. In particular, it is worthwhile noting that silver addition to the Ni catalyst, whatever the metal content, increases carbon monoxide formation compared both to the monometallic sample and the Pt-Ni/CeO_2-SiO_2 as well as Ru-Ni/CeO_2-SiO_2 catalyst. This result confirms the low applicability of Ag-Ni samples for ethanol reforming, especially in view of reactor coupling with fuel cells devices: high CO levels, in fact, are responsible for fuel cells anode poisoning (Lu et al., 2008).

Based on the above results, it is clear that, despite the growth of M loading assures better catalyst reducibility (Figure V. 5, Figure V. 6 and Figure V. 7), which is envisaged to improve catalyst performance, low-loaded noble metals are also expected to increase active species dispersion. Previous studies on the bimetallic Pt-Ni/CeO_2 catalysts (Castaldo et al., 2015) revealed the better performance of the 3wt% loaded sample with respect to the 1 and 2 wt% during ethanol steam reforming. However, the more interesting results obtained over the catalysts with lower noble metals content may be ascribed to presence of SiO_2, which assures high surface areas to the final catalyst and better active species dispersion (Palma et al., 2018a).

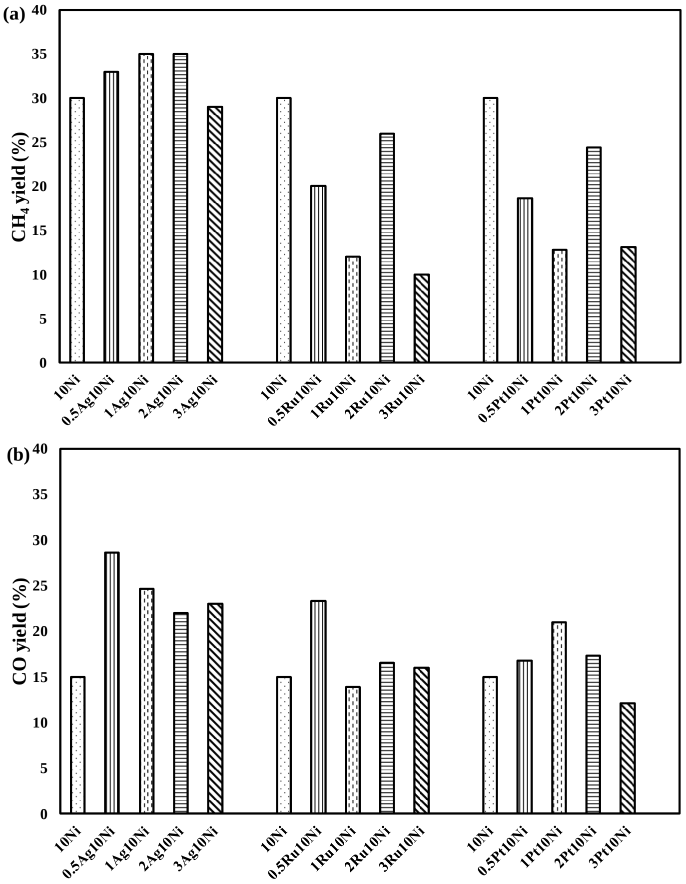

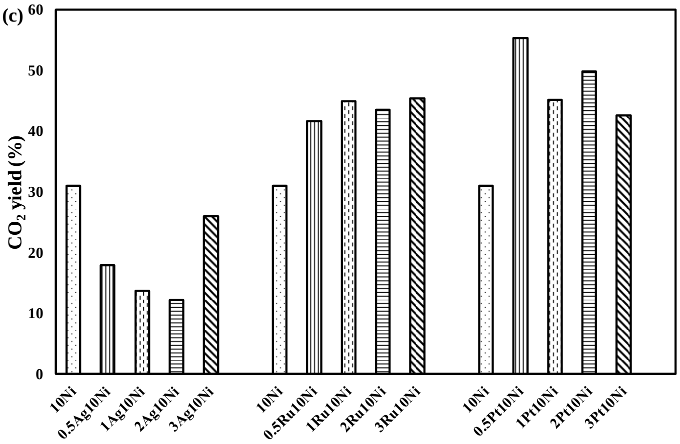

Figure V. 24 *Effect of M loading on CH_4 (a), CO (b) and CO_2 (c) yield during OSR tests at 500°C, f.r=4, o.r.=0.5 and WHSV=61.7 h^{-1}.*

According to the above experimental results, the 0.5 wt% is the most promising formulation for every series; in the following paragraph (Par. V.2.5), a kinetic study for these latter samples is proposed and discussed in comparison with the monometallic Ni/CeO_2-SiO_2 catalyst. Moreover, as the Pt as well as Ru series displayed the highest activity for oxidative steam reforming of ethanol, durability measurements were also performed (Par. 0).

V.2.5 Kinetic model for OSR over the M-Ni/CeO_2-SiO_2 catalysts

The products gas distribution obtained over 10Ni, 0.5Ag-10Ni, 0.5Ru-10Ni, 0.5Pt-10Ni/CeO_2-SiO_2 catalysts under the experimental conditions used for this work suggests the reaction network reported in eq. (V. 1)-(V. 4), previously used for bimetallic catalysts supported on the same mixed oxide (Ruocco et al., 2018). The first step of ethanol reforming is C_2H_5OH adsorption on catalyst surface (Santos et al., 2005), which can easily decompose via the reaction shown in eq. (V. 1). The produced methane can be oxidized through the instantaneous and irreversible reaction reported in eq. (V. 2). Eq. (V. 1) was described by a power-low reaction rate (Ciambelli et al., 2010) while for eq. (V. 3) and eq. ((V. 4) the model proposed by Xu and Froment (Xu and Froment, 1989) was taken into account. Euler's method was used to integrate the mass balance equations over the length of an isothermal catalytic bed and the results were compared in terms of the molar rates F_i of the species present in the reforming mixture, estimated as the ratio between the molar flow-rate of the i-species and the rate of the feeding ethanol.

In particular, the mathematical model was based on the hypothesis of a isothermal tubular plug flow reactor (PFR), with a fixed bed of catalyst. The model equations was implemented in the software Microsoft Excel, Office 2010.

$$r_1\ C2H_5OH \rightarrow H_2 + CH_4 + CO\ \Delta H^{\circ}_{298K} = 49.9 kJ \cdot mol^{-1} \qquad \text{(V. 1)}$$

$$r_2\ CH_4 + 2O_2 \rightarrow 2H_2O + CO_2\ \Delta H^{\circ}_{298K} = -802.6 kJ \cdot mol^{-1} \qquad \text{(V. 2)}$$

$$r3\ CH_4 + H_2O \leftrightarrow 3H_2 + CO\ \Delta H^{\circ}_{298K} = 206 kJ \cdot mol^{-1} \qquad \text{(V. 3)}$$

$$r4\ CO + H_2O \leftrightarrow H_2 + CO_2\ \Delta H^{\circ}_{298K} = -41 kJ \cdot mol^{-1} \qquad \text{(V. 4)}$$

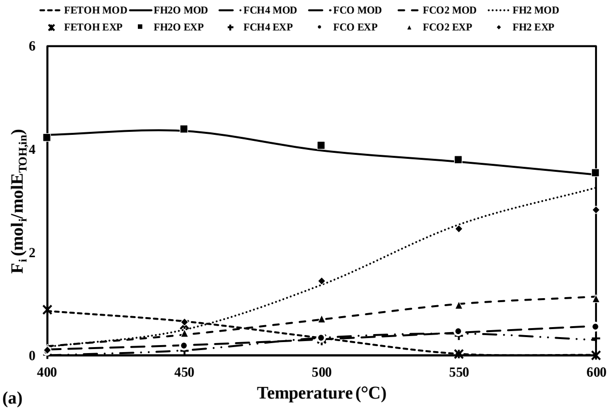

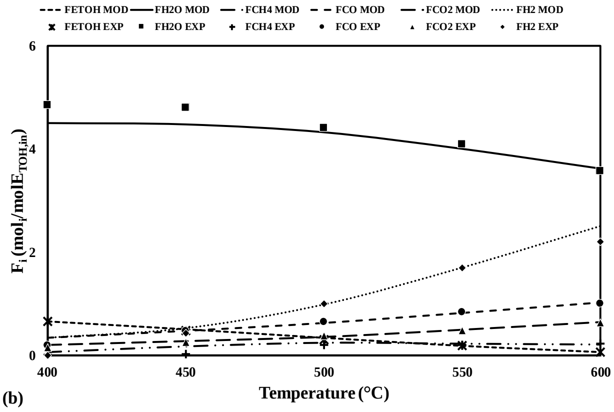

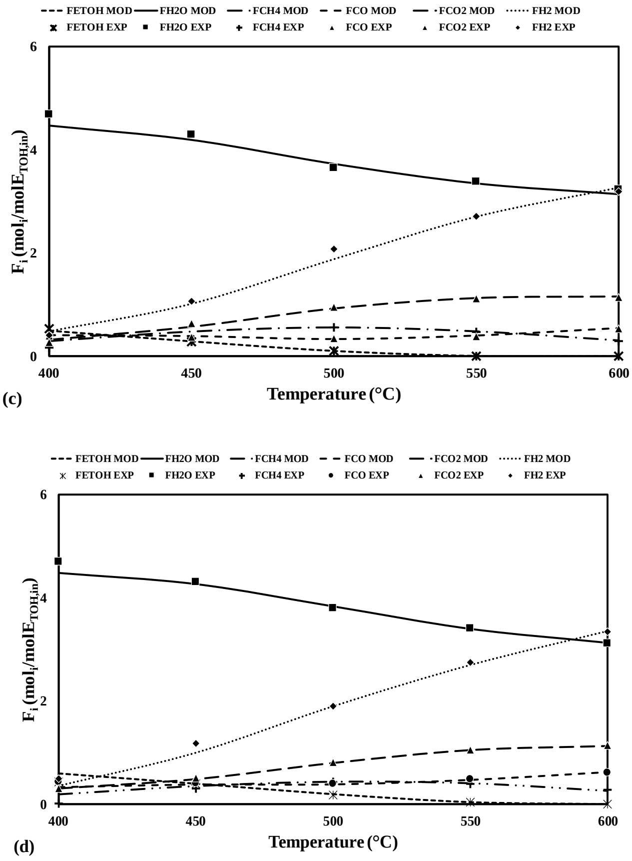

Figure V. 25 *Comparison between experimental and calculated molar rates (f.r.=4, o.r.=0.5, WHSV=61.7* h^{-1}*) for the (a) 10Ni, (b) 0.5Ag-10Ni, (c) 0.5Ru-10Ni, (d) 0.5Pt-10Ni/*CeO_2*-*SiO_2 *catalysts.*

A total gas flow rate of 990 $Ncm^3 \cdot min^{-1}$ at atmospheric pressure is sent to the tubular reactor, with 10 vol.% of ethanol, 40 vol.% of steam, 5 vol.% of oxygen in argon.

The system was solved through *n* mass balance to the PFR, where n is the components number, *a* is an index of the component, *j* an index of the reaction and *q* the total number of the hypothesized reactions (eq, (V.5)). To solve the six differential equations (one for each component, expect argon that is inert), the Euler method was used to integrate the system (eq. (V.6)).

$$\frac{dF_a}{dW} = -\sum_{j=1}^{q} \nu_{aj} \cdot r_j \qquad \text{(V. 5)}$$

$$Fa_{i+1} = Fa_i - \sum_{j=1}^{q} \left(\nu_{aj} \cdot r_j\right)_i \cdot \Delta W \qquad (V.\ 6)$$

$$f = \sum_{i=1}^{n} \sum_{j=1}^{m} \left(Fa_{ij}^{\mathrm{mod}} - Fa_{ij}^{\mathrm{exp}}\right)^2 \qquad (V.\ 7)$$

ΔW was fixed to 0.002013 and, after the solution of the mass balance, the results of the model were compared with the experimental values, through an objective function defined in eq. (V.7), where *n* is the components number, *m* the overall number of temperatures used in the integration procedures, Fa_{ij} the molar flow-rate of the ith component at the jth temperature values. This function should be maximized to obtain a minimum difference between experimental and model values, using the kinetic constants as the variable terms.

A fairly good agreement between the experimental values and the model curves was observed for the monometallic and 0.5 wt% M-loaded bimetallic catalysts above 450°C (Figure V. 25). For lower temperatures, a lessen predictivity of the model was observed, which can be ascribed to the change of catalyst selectivity towards coke formation: methane molar rate is lower compared to the model curve, which suggests that CH_4 decomposition is the main route responsible for carbon deposition below 450°C.

Table V. 14 reports the pre-exponential coefficients and the activation energy for the reactions reported in eq. (V. 1), (V. 3) and (V. 4), estimated for the different CeO_2-SiO_2 based catalysts.

Table V. 14 *Pre-exponential factor (ko) and activation energy (Ea) for OSR of ethanol over monometallic and bimetallic catalysts supported on CeO_2-SiO_2.*

	10Ni		**0.5Ag10Ni**		**0.5Ru10Ni**		**0.5Pt10Ni**	
	$\mathbf{k_o}^1$	$\mathbf{E_a}^2$	$\mathbf{k_o}^1$	$\mathbf{E_a}^2$	$\mathbf{k_o}^1$	$\mathbf{E_a}^2$	$\mathbf{k_o}^1$	$\mathbf{E_a}^2$
$\mathbf{r_1}$	$4.7 \cdot 10^{-1}$	76	$7.2 \cdot 10^{-4}$	35	$2.2 \cdot 10^{-3}$	40	$1.9 \cdot 10^{-3}$	38
$\mathbf{r_3}$	$3.7 \cdot 10^{3}$	70	$3.1 \cdot 10^{9}$	164	$1.6 \cdot 10^{3}$	60	$1.3 \cdot 10^{3}$	61
$\mathbf{r_4}$	$2.5 \cdot 10^{-5}$	30	$4.1 \cdot 10^{-6}$	35	$9.3 \cdot 10^{-6}$	23	$2.3 \cdot 10^{-5}$	26
$\boldsymbol{\sigma}^3$	0.18		0.17		0.15		0.15	

[1] $mol \cdot Pa^n \cdot s^{-1} \cdot g_{cat}^{-1}$ [2] $kJ \cdot mol^{-1}$ [3] sum of the square roots

The results proves that Ag addition to the Ni/CeO_2-SiO_2 sample increase the catalyst activity towards ethanol decomposition reaction; however, slower reaction rates for both methane steam reforming and water gas shift reactions were estimated (E_a referred to r_3 was more than twice upon silver deposition), which resulted in a reduced H_2 production rate. Conversely, the addition of platinum and ruthenium assured lower activation energies for all the investigated reactions, especially in the case of ethanol decomposition (40 and 38 $kJ \cdot mol^{-1}$ for Ru and Pt-based samples, respectively, against 76 $kJ \cdot mol^{-1}$ estimated for the Ni/CeO_2-SiO_2 catalysts).

The model accuracy was evaluated in terms of the sum of the square roots. In this regard, it is interesting noting that, above 450°C, the standard deviation is strongly reduced above the Pt and Ru-based catalysts, decreasing below 0.005. This result is ascribable to the enhanced model predictivity observed at high temperatures and described above. The kinetic evaluations also confirmed that 0.5Ru10Ni and 0.5Pt10Ni catalysts assure a similar performance for oxidative steam reforming of ethanol, showing improved activity compared to a Pt-based bimetallic catalyst prepared with an higher Pt loading and previously investigated (Palma et al., 2018b), demonstrating, on one hand, that it is possible to reduce Pt loading and, on the other hand, that the less expensive ruthenium can be employed instead of platinum to effectively reduce the catalyst price.

The experimental tests described above led to focus further attention on the Pt-Ni and Ru-Ni catalysts, which were employed for durability measurements described in the Par. V.2.6.

V.2.6 OSR stability tests over the M-Ni/CeO_2-SiO_2 catalysts

The time-on-stream behaviour of the Pt- as well as Ru-based catalyst was studied for 25 hours at 500°C, under a water/ethanol molar ratio of 4 and oxygen/ethanol molar ratio of 0.5; very stressful conditions were selected in terms of contact time (50 ms), which was considerably lower than the values commonly selected for ethanol reforming (Xiao et al., 2019, Li et al., 2019). This quite high space velocity allowed observing eventual activity losses in the investigated time interval. The catalytic performance of the prepared catalysts were reported in terms of ethanol conversion and hydrogen yield, as shown in Figure V. 26 and Figure V. 27, respectively.

Due to the quite severe operative conditions, complete conversion was only recorded on few samples at the beginning of the test. All the catalysts underwent deactivation with time-on-stream and a decreasing trend in ethanol conversion was observed. The highest activity was recorded over the 2Pt10Ni sample, which reached 95% of ethanol conversion after 25 hours of time-on-stream. Interestingly, the monometallic catalyst containing only nickel performed better than the other bimetallic samples, with measured X_{C2H5OH} values higher than 90% at the end of the test. Concerning the Pt-series, the catalyst loaded with 1 wt% of noble metal was more active than the 3Pt10Ni sample while the highest conversion among the Ru-containing samples was measured over the 2Ru10Ni catalyst, which displayed X_{C2H5OH} values higher than 85% after 25 hours of time-on-stream. The worst results in terms of ethanol conversion were recorded over the low-loaded samples: despite the 0.5Ru10Ni and 0.5Pt10Ni catalysts assured high activity in the interval 300-600°C, as described in the Par. V.2.5, the small noble metal content resulted in poor stability and in not eligible catalyst for ethanol reforming under the selected operative conditions.

The investigated catalysts also displayed a different selectivity with time-on-stream. The catalyst showing the highest conversion also assured the most promising hydrogen yield, with values slightly below 30% after 25 hours of test. All the samples containing Pt, except for the 0.5Pt10Ni, displayed considerable H_2 production rates compared to the Ru-series.

The monometallic Ni catalyst, despite the high conversion, only reached 15% of hydrogen yield at the end of the test, suggesting the formation of other by-products. The less interesting results, also in terms of hydrogen yield, were measured over the 0.5Pt10Ni and 0.5Ru10Ni catalysts. In order to understand better the behaviour of the different catalysts, their performance were also compared in terms of products yield.

Figure V. 28 and Figure V. 29 report the H_2, CH_4, CO, CO_2 and C_2H_4O yield measured over the various catalysts at the end of the test.

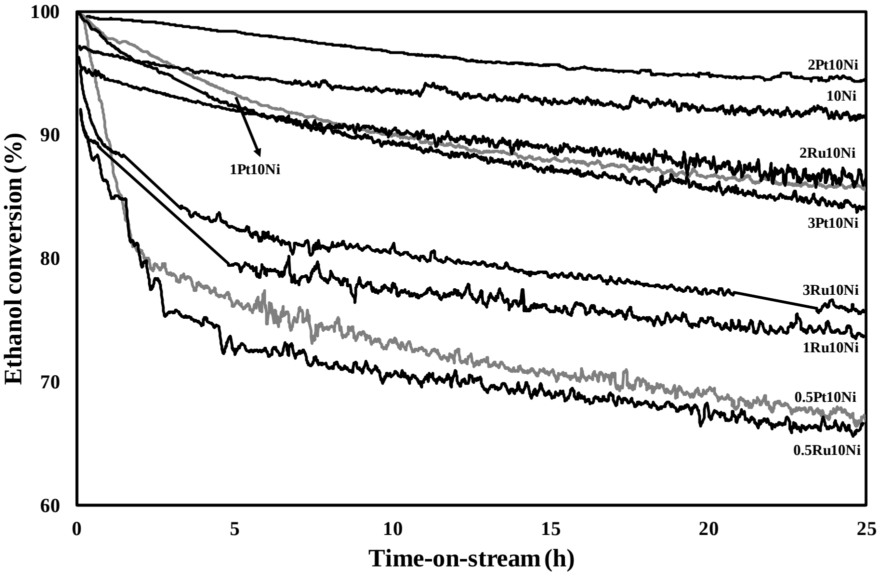

Figure V. 26 *Ethanol conversion as a function of TOS during OSR over the Pt-Ni and Ru-Ni samples in comparison with the Ni/CeO$_2$-SiO$_2$ catalyst; 1 atm, 500°C, f.r.= 4, o.r.= 0.5, WHSV=61.7 h^{-1}.*

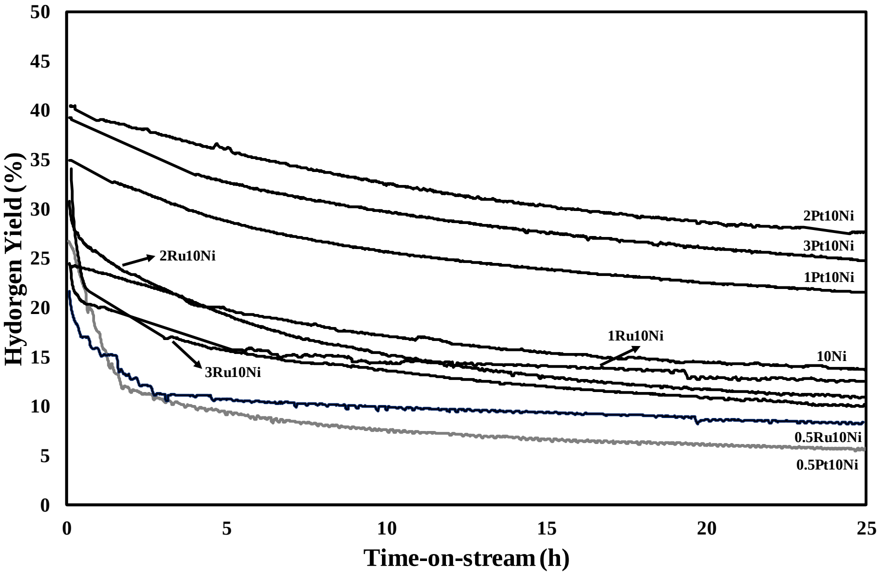

Figure V. 27 *Hydrogen yield as a function of TOS during OSR over the Pt-Ni and Ru-Ni samples in comparison with the Ni/CeO$_2$-SiO$_2$ catalyst; 1 atm, 500°C, f.r.= 4, o.r.= 0.5, WHSV=61.7 h^{-1}.*

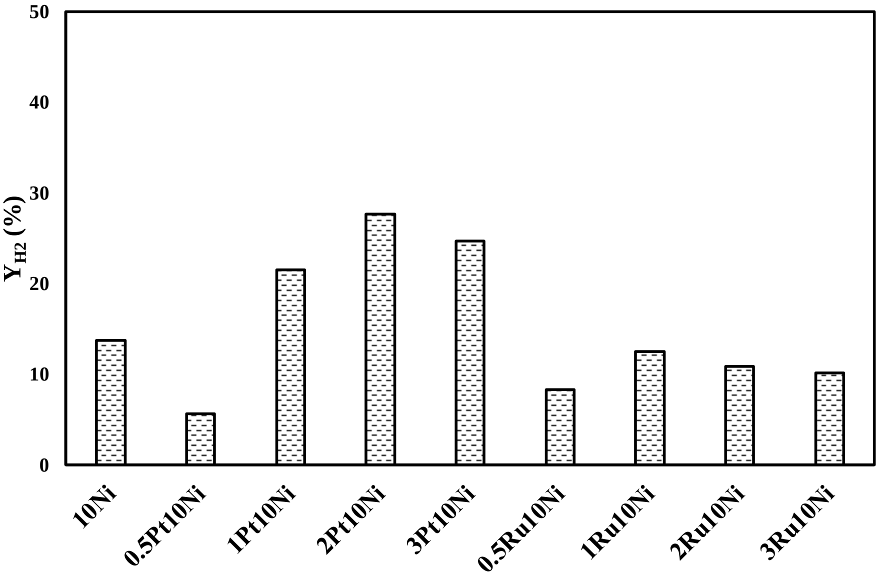

Figure V. 28 *Comparison between hydrogen yield recorded at the end of the stability tests over the Pt-Ni and Ru-Ni catalysts; 1 atm, 500°C, f.r.=4, o.r.= 0.5, 61.7* h^{-1}.

The three samples (i.e. 1Pt10Ni, 2Pt10Ni, 3Pt10Ni) assuring the highest H_2 production rate also allowed a very low acetaldehyde formation (equal or smaller than 10%). Conversely, CH_4 and CO_2 yield (Figure V. 29 (a) and (c), respectively) together with Y_{H2} are the highest ones among the tested catalysts, demonstrating that platinum is a more appropriate active species, compared to ruthenium, in promoting ethanol steam reforming and ethanol decomposition to CH_4, CO and H_2. Anyway, the best results in terms of hydrogen yield were recorded over the 2Pt10Ni catalyst.

The monometallic 10Ni/CeO_2-SiO_2, despite displaying a quite high ethanol conversion, showed a final hydrogen yield below 15%, due to the not negligible contribution of ethanol dehydrogenation to C_2H_4O (Llera et al., 2012) (Figure V. 29 (d)). As previously reported (Dantas et al., 2016), under oxidative conditions, it is easier for Ni to be re-oxidized to NiO, which favours the dehydrogenation of C_2H_5OH to C_2H_4O. Conversely, the addition of Pt to the Ni/CeO_2-SiO_2 sample prevented this phenomenon.

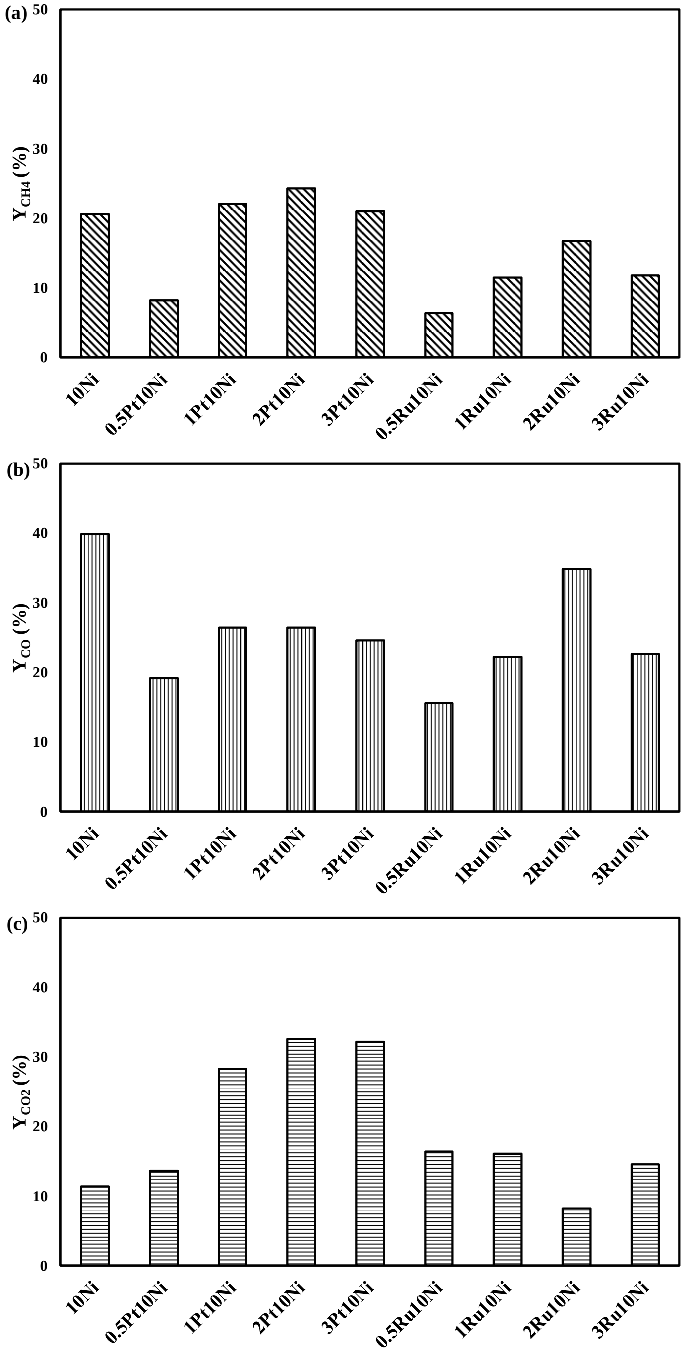
(a)
Y_{CH4} (%)
0
10
20
30
40
50
10Ni
0.5Pt10Ni
1Pt10Ni
2Pt10Ni
3Pt10Ni
0.5Ru10Ni
1Ru10Ni
2Ru10Ni
3Ru10Ni
(b)
Y_{CO} (%)
0
10
20
30
40
50
10Ni
0.5Pt10Ni
1Pt10Ni
2Pt10Ni
3Pt10Ni
0.5Ru10Ni
1Ru10Ni
2Ru10Ni
3Ru10Ni
(c)
Y_{CO2} (%)
0
10
20
30
40
50
10Ni
0.5Pt10Ni
1Pt10Ni
2Pt10Ni
3Pt10Ni
0.5Ru10Ni
1Ru10Ni
2Ru10Ni
3Ru10Ni

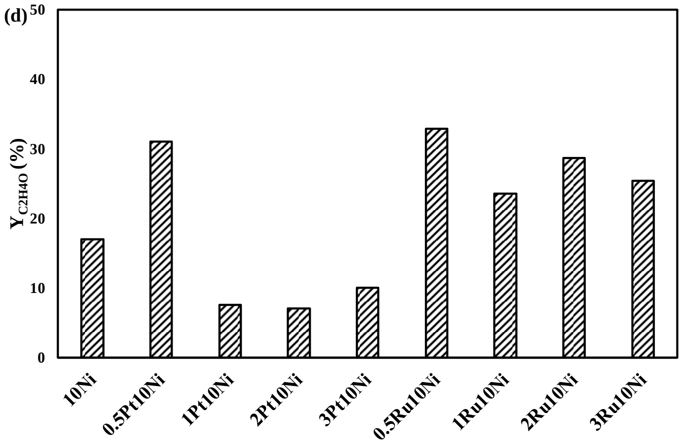

Figure V. 29 *Comparison between methane (a), carbon monoxide (b), car bon dioxide (c) and acetaldehyde (d) yields recorded at the end of the stability tests over the Pt-Ni and Ru-Ni catalysts; 1 atm, 500°C, f.r.=4, o.r.= 0.5, 61.7* h^{-1}.

On the other hand, the catalysts of the Ru series together with the 0.5Pt10Ni sample, besides reaching Y_{C2H4O} values higher than 25% (with values exceeding 30% over the 0.5wt% catalysts), also displayed quite low methane formation, which suggests that methane decomposition (Özkan et al., 2019), responsible for carbonaceous deposits formation on catalyst surface, may also occur.

Based on the above results, the 2Pt-10Ni/CeO_2-SiO_2 catalyst appeared the most promising one and was selected for further tests in the presence of commercial fuel grade bioethanol.

V.3Results of activity and stability tests for OSR under commercial fuel grade bioethanol

The catalytic tests under commercial fuel grade bioethanol have been performed in the optimized reactor configuration shown in Figure IV. 7. Following the experimental procedure of all the tests described in the previous paragraphs, a preliminary investigation was performed over the 2Pt-10Ni/CeO_2-SiO_2 mixed with the CeO_2-SiO_2 support. Thereafter, in order to highlight the role of the ceria-silica filler on the activity and stability, a further test was also performed only in the presence of the catalyst.

V.3.1 Catalytic performance of the 2Pt-10Ni/CeO_2-SiO_2 catalyst under fuel grade bioethanol: diluent effect

The influence of the CeO_2-SiO_2 addition to the 2Pt-10Ni/CeO_2-SiO_2 catalyst during oxidative steam reforming of the fuel grade ethanol described in

Figure IV. 14 is shown in terms of ethanol conversion and hydrogen yield (Figure V. 30 and Figure V. 31, respectively).

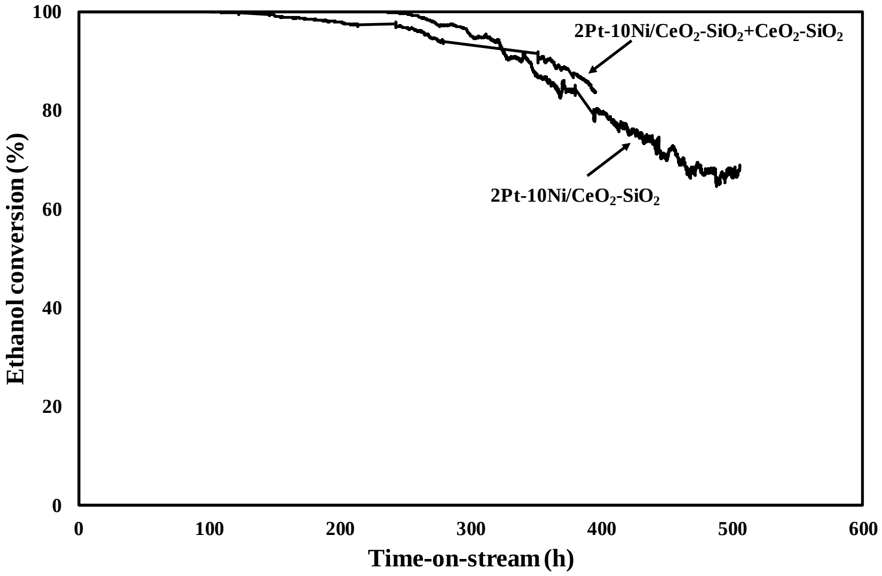

Figure V. 30 *Ethanol conversion as a function of TOS during OSR over the 2Pt-10Ni with and without the* CeO_2*-*SiO_2 *(diluent); 1 atm, 500°C, f.r.=4, o.r.= 0.5, 4.1* h^{-1}*, feeding of fuel grade bioethanol.*

Both the tests were performed for several hours (at least 400). In the presence of the diluent, ethanol vas completely converted for more than 100 hours with a corresponding hydrogen yield above 50%. For higher time-on-stream values, a slow and gradual deactivation was observed that did not stop and lead to a very low hydrogen production after 400 hours of test. Conversely, when the 2Pt10Ni catalyst was tested in the absence of the diluent, despite a slightly lower initial hydrogen conversion, a stable behaviour with complete ethanol conversion was recorded for almost 220 hours. During the same time, a negligible variation of hydrogen yield around 45% was observed. It is also interesting to note that, compared to the results reported in Par. V.2.1, the hydrogen yield recorded under fuel grade bioethanol was higher: in fact, as previously reported, the contribution of impurities (mainly higher alcohols) reforming pathways cannot be negligible ((Palma et al., 2016).

When time-on-stream increased above 220 hours, a gradual activity loss was observed. However, it is very interesting pointing out that, after almost 450 h, a new stationary condition was reached, corresponding to a mean ethanol conversion and hydrogen yield of 68% and 14%, respectively. It was also verified that the catalyst was able to hold this condition for further 50 hours.

In order to better highlight the differences observed in Figure V. 30 and Figure V. 31, the products yield recorded at the beginning of the test under stationary conditions (first 50 hours for the test performed with the diluent and first 220 hours for the test carried out without the diluent) were compared and the results are shown in Figure V. 32.

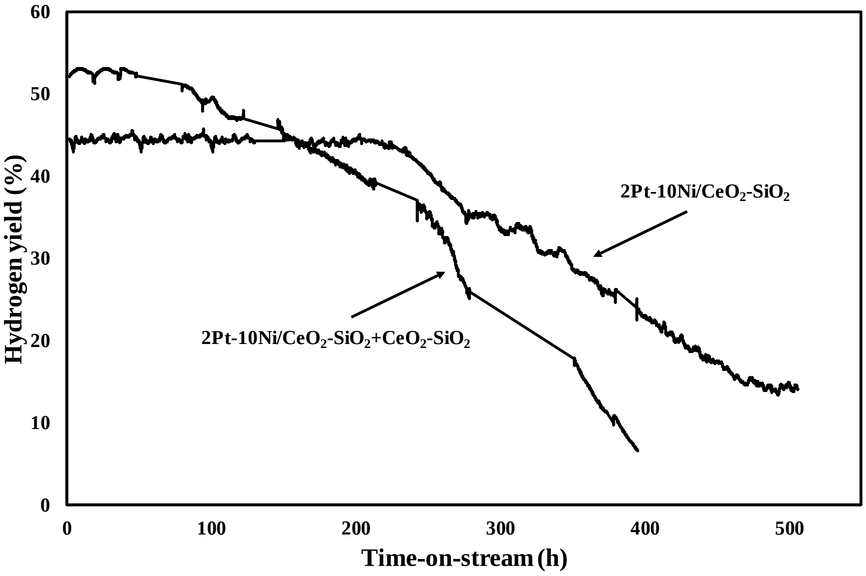

Figure V. 31 *Hydrogen yield as a function of TOS during OSR over the 2Pt-10Ni with and without the* CeO_2*-*SiO_2 *(diluent); 1 atm, 500°C, f.r.=4, o.r.= 0.5, 4.1* h^-*, feeding of fuel grade bioethanol.*

For both the samples, at the beginning of the test, only the formation of hydrogen, carbon monoxide, methane and carbon dioxide was observed, while acetone, ethylene and acetaldehyde were absent in the exiting mixture. Moreover, the carbon balance was closed with a maximum error of 3 %. The comparison between the products yield in the two cases revealed that CeO_2-SiO_2 presence promote hydrogen formation, with a mean yield of 53% against the value of 45% recorded without the diluent. Such high hydrogen production was coupled to a methane yield of 24%, lower than the 33% measured over the 2Pt-10Ni catalyst alone. The increased CO yield recorded when the catalyst is mixed with the support also indicates that water gas shift was less promoted. However, CO_2 yield (61.7%) was still reduced in the presence of the diluent, which suggest that the CeO_2-SiO_2 was not able to enhance the rate of methane steam reforming reaction. Instead, the faster activity loss observed during the test performed in the presence of the diluent suggests that methane decomposition to hydrogen and coke is also occurring. In this regard, it has been widely reported that the presence of acid sites enhances coke deposition on catalyst surface and that the rate of carbon formation via methane decomposition is proportional to the concentration of acid sites (Lercher et al., 1996, Nichele et al., 2014). Based on the above observation and considering the results of ZPC measurements (shown in Par.V.1.3), the worst performance recorded in the presence of the CeO_2-SiO_2 support can be ascribed to its higher acidity compared to the sample obtained upon Ni and Pt deposition.

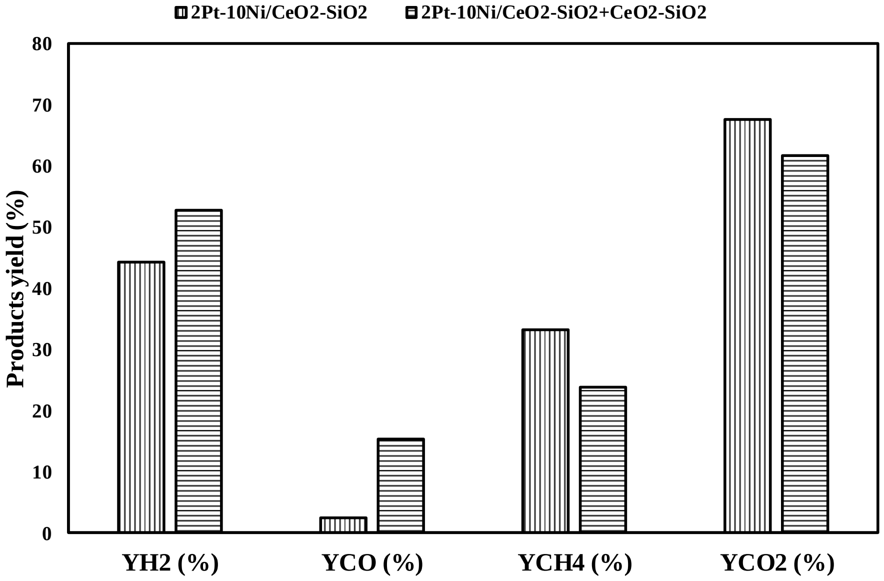

Figure V. 32 *Comparison between the products yield recorded at the beginning of the tests (under stationary conditions) shown in Figure V. 30.*

It is also interesting to compare the product distribution obtained at the end of the tests. The presence of contaminants in the fuel grade bioethanol affected the type of formed by-products and acetone as well as ethylene were found in the reforming mixture along with acetaldehyde (the only by-product observed during the tests performed in the presence of simulated ethanol, Par. V.2.1 and V.2.2). Figure V. 33 reports the final products yield recorded after 400 hours in the presence of the diluent as well as the mean products yield during the last 50 hours of the durability tests described in Figure V. 30 and Figure V. 31. For the test performed over the only 2Pt-10Ni/CeO_2-SiO_2 catalyst, an increase in the CO yield was observed with respect to the initial values (2.4 vs 8.1%), which demonstrate that the partial activity loss caused a decreased activity towards WGS reaction. Moreover, CH_4 and CO_2 selectivity decrease, with a subsequent growth on the contribution of methane decomposition reaction. Moreover, acetaldehyde along with acetone traces were observed in the mixture during the last 50 hours ($YC_2H_4O=2.3\%$ and $YC_3H_6O=0.2\%$), ascribable to the reduced capability of the catalyst to convert such species formed during the reaction, due to the establishing of different pathways, including ethanol dehydrogenation to acetaldehyde, which can be involved in aldol condensation, thus leading to acetone formation ((Nishiguchi et al., 2005). Anyway, during the last hours of the test, the closure of carbon balances was still assured with a maximum error of 4%.

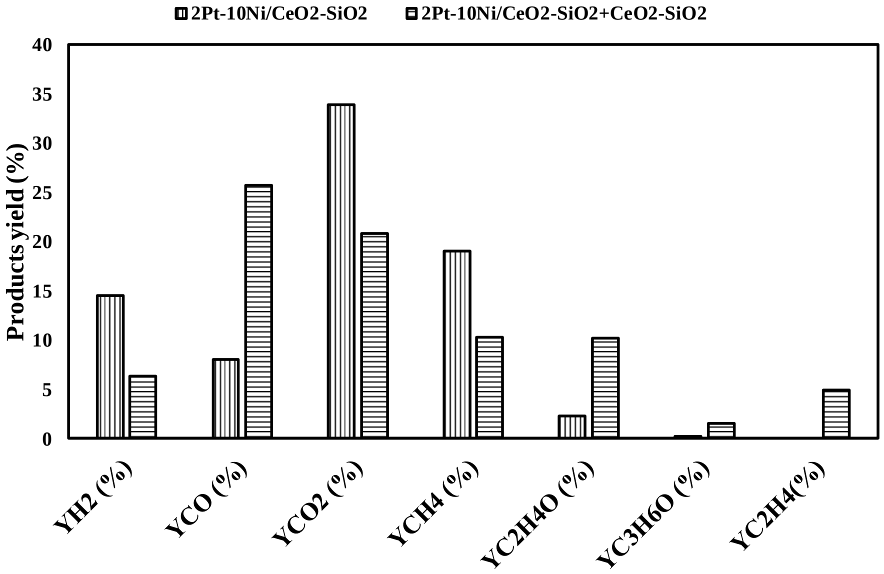

Figure V. 33 *Comparison between the products yield recorded at the end of the tests (after 400 h on the presence of the diluent and under stationary conditions after 450 h in the absence of CeO_2-SiO_2) shown in Figure V. 30.*

For oxidative steam reforming of commercial fuel grade bioethanol in the presence of the CeO_2-SiO_2 support, the final CO yield was higher than 25% and CO_2 as well as CH_4 yield decreased to 21 and 10%, respectively. Moreover, due to the higher extent of deactivation, the by-production reached 10.2, 1.5 and 4.9%, for acetaldehyde, acetone and ethylene, respectively. In the latter case, in fact, the contribution of ethanol dehydration reactions, also responsible for carbon formation, became not negligible. As a consequence, the error on carbon balance is significant (around 10%).

Based on the above results, it is possible to conclude that the 2Pt-10Ni/CeO_2-SiO_2 catalyst (tested without the diluent), is a suitable formulation for oxidative steam reforming of fuel grade bioethanol: under the selected operative conditions (500°C, f.r.=4, o.r=5, WHSV=4.1 h^{-1}), complete conversion and a stable behaviour was assured for more than 200 hours and, after a partial activity loss, a new stationary condition was reached, with no more deactivation and a not negligible hydrogen yield (around 15%).

V.4Spent catalysts characterization

V.4.1 Characterization of the Pt-Ni, K-Pt-Ni and Pt-Co/CeO_2-SiO_2 catalysts after stability tests

The physiochemical properties of the reduced samples were investigated via XRD analysis (Figure V. 34) and the average sizes of CeO_2 and Ni/Co crystallites for fresh (reduced) and spent catalysts were compared. Moreover, BET measurements were also carried out on the catalysts after stability tests. As shown in Table V. 15, the average particle size of CeO_2 and Ni/Co was unaffected by time-on-stream tests at 4.1 h^{-1}: the good metals dispersion and the small dimensions of CeO_2 crystallites provide high resistance toward sintering. As a consequence, the specific surface area reduction was not ascribable to structure collapsing. Hence, it is possible to ascribe catalysts deactivation to pore blockage/narrowing via carbon deposition (Parlett et al., 2017), consisting with the oxidation profiles, displayed in Figure V. 35, which allowed the evaluation of carbon formation rate (Table V. 15). The oxygen consumption profiles, deconvoluted after background subtraction by a least-squares fitting to Gaussian–Lorentzian functions using the software Microcal Origin, are displayed in Figure V. 35.

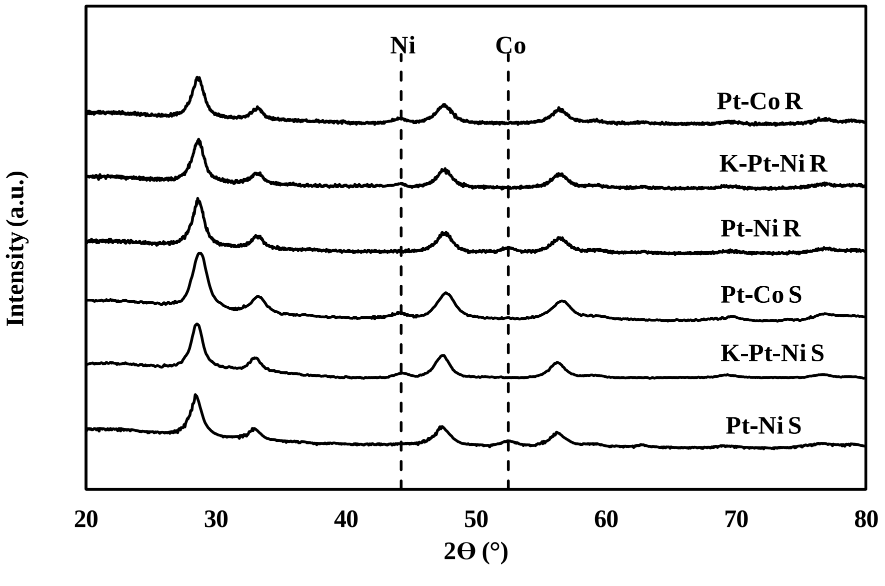

Figure V. 34 *XRD patterns of the reduced catalysts and the samples after stability tests of Figure V. 8.*

The origin of the deactivation by coke of the catalysts in ethanol reforming is ascribable to the following pathways: polymerization of ethylene formed by ethanol dehydration, Boudouard reaction and methane decomposition (Song et al., 2017, Palma et al., 2017e). For reforming reactions, it is generally accepted (Vicente et al., 2014b, Horváth et al., 2011, Djinović et al., 2012) that the main cause of deactivation is the metallic sites blockage by encapsulating coke, which has an amorphous nature and is identified by means of peaks at low temperatures (450 °C); this route of carbon formation is generally associated to ethylene polymerization.

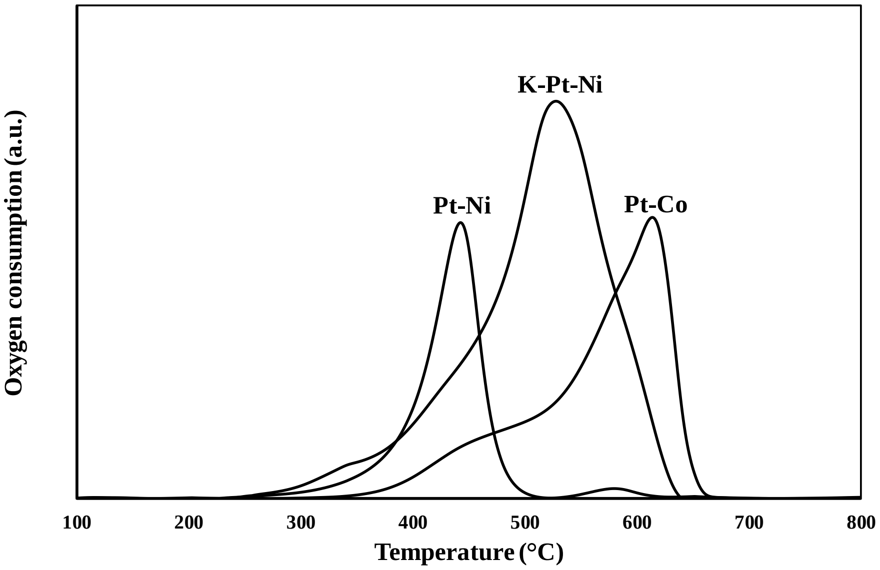

Figure V. 35 *Oxygen consumption profile recorded during oxidation measurements carried out on the three catalysts after stability tests of* Figure V. 8.

Table V. 15 *Physiochemical properties of the reduced (R) spent (S) catalysts and carbon formation rate over the spent samples after the tests of Figure V. 8.*

Sample	**d_{CeO2} R (Å)**	**$d_{Ni/Co}$ R (Å)**	**d_{CeO2} S (Å)**	**$d_{Ni/Co}$ S (Å)**	**S_{BET} ($m^2 \cdot g^{-1}$)**	**CFR***
Pt-Ni	70	80	72	79	249	3.2
K-Pt-Ni	74	103	75	105	152	63
Pt-Co	75	93	75	95	203	17

$^*g_{coke} \cdot g_{catalyst}^{-1} \cdot g_{carbon,fed}^{-1} \cdot h^{-1}$ multiplied for 10^7

Conversely, filamentous coke hinders the access of ethanol and water to the catalyst active sites only when its structure growth is very high and is identified through peaks at temperatures higher than 550°C; its formation is related to methane decomposition and Boudouard reaction (Choong et al., 2011, Vicente et al., 2014a). The oxidation temperature of more ordered carbon (graphitic) is shifted towards higher temperatures (above 750°C), depending on the degree of graphitization of the deposits (Arslan et al., 2014, Erdogan et al., 2018). The oxidation measurements performed on the spent catalysts after tests at 4.1 h^{-1} (Figure V. 35) revealed the main formation of encapsulated carbon on the Pt-Ni catalyst, which was oxidized at temperatures lower than 500°C; the very small peak observed at 580 °C attested a negligible formation of filamentous coke. For the latter sample, carbon accumulated on the catalyst surface is expected to encapsulate the active sites, reducing the active surface accessible for the reactants and resulting in a partial catalyst deactivation .Conversely, for the other two samples tested at 4.1 h^{-1}, the growth of filamentous coke is the main reason of activity loss. In fact, the XRD analysis of the catalysts after ethanol reforming tests shows no peak related to graphitic type carbon (Figure V. 34).

From the TPO measurements, it was possible to evaluate the carbon formation rate, which increases over the K-promoted catalyst and Co-based samples and justifies the considerably higher stability observed over the Pt-Ni/CeO_2-SiO_2 catalyst.

V.4.2 Characterization of the catalysts prepared from different cerium precursors after stability tests

After the stability tests on the samples prepared from the different cerium salt precursors, the catalysts were characterized by means of specific surface area measurements and thermogravimetric analysis. The results are reported in Table V. 16.

Table V. 16 *Characterization of the spent catalysts after the tests shown in Figure V. 10.*

Spent sample	S_{BET} ($m^2 \cdot g^{-1}$)	CFR*
NH	169	$3 \cdot 10^{-6}$
ANH	175	$2.9 \cdot 10^{-6}$
AAH	206	$1.4 \cdot 10^{-6}$

$^{*}g_{coke} \cdot g_{catalyst}^{-1} \cdot g_{carbon,fed}^{-1} \cdot h^{-1}$

The S_{BET} of the spent NH and ANH catalysts decreased of more than 20% after reaction while a variation lower than 10% was observed for the sample C. This results verify the formation of carbonaceous species and their deposition on catalyst surface, thus closing the smallest pores of the CeO_2-SiO_2 support. The amount of coke formation over the spent catalysts changes in the following sequence: NH ≈ ANH > AAH, thus confirming that the catalysts prepared from cerium nitrates are more susceptible to deactivation with respect to the sample AAH, which displayed a carbon formation rate of almost one half compared to the other two samples.

The results shown in Par. V.2.1, V.2.2 and V.2.3 suggest that carbon formation does not follow a constant trend during the test; conversely, it is supposed that coke deposited during test progressively deactivated the most reactive catalytic sites, involved in both reforming and by-products formation pathways. As a result, catalyst activity remain unchanged with no further increase in catalyst deactivation. In order to verify the above assumption, a further test was performed over the Pt-Ni/CeO_2-SiO_2 catalyst prepared from cerium nitrate: concerning the measurements shown in Figure V. 10, at regular intervals, the test was stopped and a sample was withdrawn and characterized by TGA to study the variation of the carbon formation rate with time-on-stream (Figure V. 36).

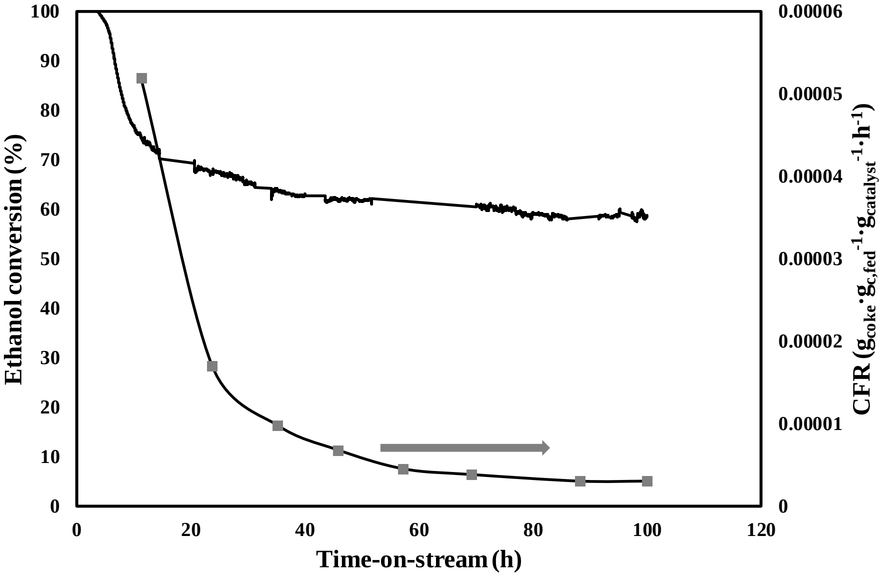

Figure V. 36 *Trend of ethanol conversion and CFR as a function of TOS during OSR over the NH sample; T=500°C, f.r=4, o.r.=0.5, WHSV=12.3* h^{-1}.

At WHSV = 12.3 h^{-1}, the system reached a stationary condition after almost 80 hours; CFR was quite high at the beginning of the test and displayed a decreasing trend with time-on-stream. In particular, the carbon formation rates after 80 and 100 hours were almost the same, proving that the net rate of carbon formation (i.e. the difference between carbon formation and carbon gasification rate) was equal to zero.

Also other authors studied the evolution of coke during reforming reaction in fluidized bed reactors over Ni-based catalysts (Vicente et al., 2014b, Montero et al., 2015). However, a markedly different behaviour was observed during operation: an almost steady performance was followed by a severe drop in ethanol conversion and finally a slow decrease in ethanol conversion until total deactivation of the catalyst.

Concerning the effect of operative conditions on carbon formation rate, the post-reaction characterization measurements, summarized in Table V. 17, display the detrimental impact of temperature reduction on coke selectivity. A temperature lowering from 500 to 400°C was accompanied by an increase in CFR of almost 4 times. However, the specific surface area of the spent sample was unaffected by the temperature variation in the above interval. This result can be explained considering that the excess of carbon formed during the test at 400 °C is mainly present as external coke (Zhou et al., 2017) (i.e. coke deposited on the external surface), which is expected to be less effective at blocking catalyst pores. Moreover, when the stability test was performed at 600°C, a negligible variation in specific surface area was observed with respect to the fresh catalyst, which is in agreement with the lower carbon formation rate ($6.9 \cdot 10^{-7}$ $g_{coke,oxidized} \cdot g_{catalyst}^{-1} \cdot g_{carbon,fed}^{-1} \cdot h^{-1}$) compared with the samples tested at 400 and 500°C. In fact, as previously reported (Palma et al., 2017c), the contribution of carbon formation pathways is more significant than that of gasification reactions at low reaction temperatures.

Carbon formation rates (Table V. 17), recorded after stability tests at o.r.=0.5 and 0.75, are very close one to each other, proving that the addition of more oxygen is not directly involved in carbonaceous deposit removal. But, instead, it is able to promote the oxidation of carbon-based intermediates formed during ethanol reforming. In addition, the specific surface area of the spent catalyst after 100 h of test was slightly affected by oxygen to ethanol ratio increase from 0.5 and 0.75. For o.r.=0.25, the carbon formation rate ($4.9 \cdot 10^{-6}$ $g_{coke,oxidized} \cdot g_{catalyst}^{-1} \cdot g_{carbon,fed}^{-1} \cdot h^{-1}$) was slightly lower than the value measured during the test carried out at 400°C; nevertheless, the specific surface area was reduced of almost 15% with respect to the above case. This result can be explained considering that, during the test performed at 500°C, f.r.=4 and o.r.=0.25, coke is mainly deposited in the catalyst pores, causing their partial blocking.

Table V. 17 *Characterization of the spent catalysts after the tests shown in Figure V. 12, Figure V. 14 and Figure V. 16.*

Spent sample	**S_{BET} ($m^2 \cdot g^{-1}$)**	**CFR***
Test at 400°C, f.r.=4, o.r.=0.5	209	$5.7 \cdot 10^{-6}$
Test at 500°C, f.r.=4, o.r.=0.5	206	$1.4 \cdot 10^{-6}$
Test at 600°C, f.r.=4, o.r.=0.5	223	$6.9 \cdot 10^{-7}$
Test at 500°C, f.r.=4, o.r.=0.25	179	$4.9 \cdot 10^{-6}$
Test at 500°C, f.r.=4, o.r.=0.75	219	$1.6 \cdot 10^{-6}$
Test at 500°C, f.r.=3, o.r.=0.5	161	$7.9 \cdot 10^{-6}$
Test at 500°C, f.r.=6, o.r.=0.5	220	$1.1 \cdot 10^{-6}$

$^* g_{coke} \cdot g_{catalyst}^{-1} \cdot g_{carbon,fed}^{-1} \cdot h^{-1}$

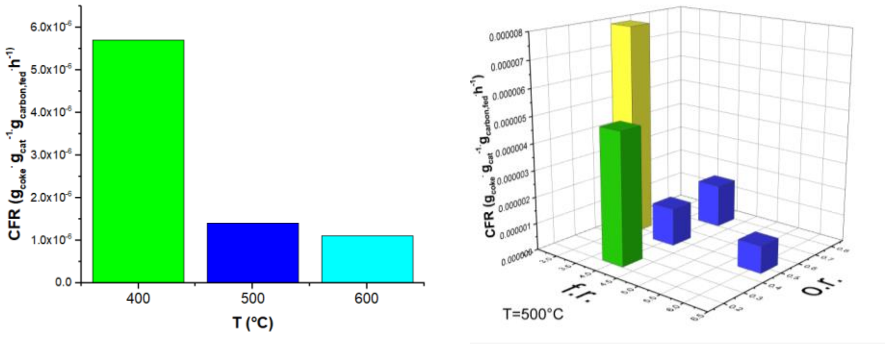

Figure V. 37 *Dependence of carbon formation rate on temperature and feeding conditions.*

Very close specific surface areas and carbon formation rates were recorded on the spent catalysts tested at f.r.=4 and f.r:=6; conversely, the lowest S_{BET} value (161 $m^2 \cdot g^{-1}$) was determined for the exhaust sample tested at stoichiometric feeding conditions, which also displayed the highest carbon formation rate ($7.9 \cdot 10^{-6}$ $g_{coke} \cdot g_{catalyst}^{-1} \cdot g_{carbon,fed}^{-1} \cdot h^{-1}$) among the investigated operative conditions.

The influence of T, f.r. and o.r. on carbon formation rate are summarized in Figure V. 37.

V.4.3 Characterization of the M-Ni/CeO_2-SiO_2 catalysts after stability tests

The Pt-Ni/CeO_2-SiO_2 and Ru-Ni/CeO_2-SiO_2 catalysts after the durability tests shown in Figure V. 26 were characterized by BET measurements and TGA analysis; the same measurements were also performed over the 10Ni/CeO_2-SiO_2 sample and the results are shown in Table V. 18.

The results of BET characterization revealed that all the catalysts suffered for an SSA variation as a consequence of time-on-stream tests. As expected, the highest extent of surface area reduction was measured for the Ru-series and the 0.5Pt10Ni catalyst. Conversely, the 1Pt10Ni, 2Pt10Ni and 3Pt10Ni samples underwent an SSA variation lower than 20%. During thermogravimetric analysis, a weight loss occurred for all the samples, which was assigned to the combustion of coke and demonstrated that the surface area reduction is due to carbon accumulation during stability tests (Laosiripojana and Assabumrungrat, 2006). The formation of carbonaceous deposits on the catalyst surface was estimated in terms of carbon formation rate (Table V. 18). The results confirmed that Pt addition to the Ni/CeO_2-SiO_2 catalyst can effectively reduce the deposited carbon on catalyst surface, improving the catalyst stability since the active sites was not covered by carbon. Ru addition has a different effect, with higher carbon formation rates (equal, for example, to $6.3 \cdot 10^{-6}$ $g_{coke} \cdot g_{catalyst}^{-1} \cdot g_{carbon,fed}^{-1} \cdot h^{-1}$ for the 3Ru10Ni catalyst), which justify the worst performance recorded over the Ru series under the selected operative conditions.

Table V. 18 *Characterization of the spent catalysts after the tests shown in Figure V. 26.*

Sample	S_{BET} ($m^2 \cdot g^{-1}$)	CFR*
10Ni	182	$3.9 \cdot 10^{-6}$
0.5Pt10Ni	145	$8.4 \cdot 10^{-6}$
1Pt10Ni	179	$2.4 \cdot 10^{-6}$
2Pt10Ni	191	$1.5 \cdot 10^{-6}$
3Pt10Ni	186	$2 \cdot 10^{-6}$
0.5Ru10Ni	142	$7.9 \cdot 10^{-6}$
1Ru10Ni	143	$5.1 \cdot 10^{-6}$
2Ru10Ni	145	$5.8 \cdot 10^{-6}$
3Ru10Ni	149	$6.3 \cdot 10^{-6}$

$^{*}g_{coke} \cdot g_{catalyst}^{-1} \cdot g_{carbon,fed}^{-1} \cdot h^{-1}$

V.4.4 Characterization of the catalysts tested under commercial fuel grade bioethanol

The samples employed for the tests reported in Figure V. 30 were characterized by means of BET measurements and thermogravimetric analysis devoted to the calculation of the carbon formation rate. For comparison, the characterization of the fresh (after calcination) and reduced catalysts have also been added.

Table V. 19 *Characterization of the fresh and reduced samples as well as the spent catalysts after the tests shown in Figure V. 30.*

Sample	S_{BET} ($m^2 \cdot g^{-1}$)	CFR*
2Pt-10Ni/CeO_2-SiO_2 fresh	226	-
2Pt-10Ni/CeO_2-SiO_2 reduced	219	-
2Pt-10Ni/CeO_2-SiO_2 spent	91	$3.1 \cdot 10^{-7}$
2Pt-10Ni/CeO_2-SiO_2+CeO_2-SiO_2 fresh	291	-
2Pt-10Ni/CeO_2-SiO_2+CeO_2-SiO_2 reduced	286	-
2Pt-10Ni/CeO_2-SiO_2+CeO_2-SiO_2 spent	164	$1.3 \cdot 10^{-6}$

$^{*}g_{coke} \cdot g_{catalyst}^{-1} \cdot g_{carbon,fed}^{-1} \cdot h^{-1}$

Both the catalysts displayed a negligible area reduction upon TPR treatment. When the catalyst was tested together with the diluent, a surface area variation of more than 40% was recorded, ascribable to the carbon deposition, as demonstrated by the quite high CFR. The 2Pt-10Ni/CeO_2-SiO_2 underwent a more significant area reduction (of almost 60%) upon the time-on-stream test; however, due to the contribution of the CeO_2-SiO_2, which is characterized by an increased surface area compared to the final catalyst, the diluted sample had an initially higher S_{BET} value. Anyway, the carbon formation rate averaged for the 500 hours of test is 1 order of magnitude lower than the value recorded for the sample tested in the presence of the diluent ($3\ 10^{-7}$ vs $1\cdot10^{-6}$ $g_{coke}\cdot g_{catalyst}^{-1}\cdot g_{carbon,fed}^{-1}\cdot h^{-1}$): such result can be ascribed to the reduction of surface acidity upon active species deposition.

In order to better investigate the partial activity loss observed for the 2Pt-10Ni/CeO_2-SiO_2 catalyst tested in the presence and absence of the diluent, further analyses were performed, including XRD and Raman.

Figure V. 38 reports the X-ray diffraction patterns of the 2Pt-10Ni/CeO_2-SiO_2 before (after reduction) and after the stability test of 500 hours; for comparison, the spectrum of the fresh (calcined) catalyst is also reported. The identification of the various phases was discussed in the previous paragraphs and, in the present figure, only the peaks selected for the calculation of average crystallite sizes have been highlighted.

As shown in Table V. 20, both the fresh samples displayed a size of ceria crystallites of almost 6 nm. During reduction, a slight increase of ceria crystallite sizes to 7 nm was observed. This phenomenon can be explained considering that H_2-TPR treatments involve the partial reduction of Ce^{4+} to Ce^{3+} and that the creation of oxygen vacancies as well as Ce^{3+} species may determine a lattice expansion and a consequent growth of CeO_2 particles (da Silva et al., 2017). In fact, the ionic radius of Ce^{3+} is higher compared to that of Ce^{4+}. Moreover, the average crystallite size of Ni particles was unaffected by 500 hours of time-on-stream for the 2Pt-10Ni/CeO_2-SiO_2 catalyst which, together with the low variation observed in terms of CeO_2 crystallite sizes, leads concluding that sintering phenomena was not the main cause of catalyst activity loss. It would also be possible that, when ceria particles slightly grow, they can encapsulate active phases, thus being responsible of a partial activity reduction. On the other hand, based on TGA as well as Raman analyses (described below), catalyst deactivation can mainly be ascribed to the deposition of carbonaceous species on the catalyst surface.

In this regard, the diffraction patterns of both the 2Pt-10Ni/CeO_2-SiO_2 and 2Pt-10Ni/CeO_2-SiO_2+CeO_2-SiO_2 spent samples (Figure V. 39) did not show any peak ascribable to graphitic carbon (normally displaying intense peaks at 26.5, 42.3 and 54.6°) (Sayah et al., 2018), demonstrating that its content is too low to be detected.

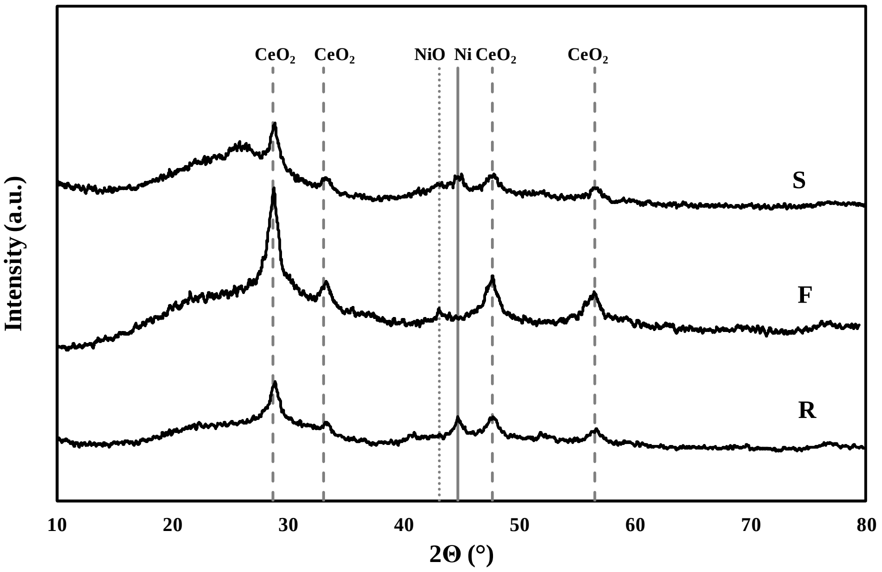

Figure V. 38 *Comparison between the XRD patterns of the fresh (calcined, F), reduced (R) and spent (S) 2Pt-10Ni/CeO_2-SiO_2 catalyst after the test shown in Figure V. 30.*

In addition, it is worthwhile noting the absence of a net peak ascribable to the nickel phase in the spent catalyst containing also the diluent. This result can be explained considering, on one hand, the presence of more CeO_2-SiO_2 which may disturb the 2Pt-10Ni/CeO_2-SiO_2 XRD pattern and, on the other hand, the probable very low dimensions of nickel particles. In fact, no phases other than ceria were detected in the XRD pattern of the sample tested for 400 hours.

Table V. 20 *Results of XRD measurements over the fresh, reduced and spent catalysts after the test shown in Figure V. 30.*

Sample	d_{CeO2} (Å)	d_{NiO} (Å)	d_{Ni} (Å)
2Pt-10Ni/CeO_2-SiO_2 fresh	64	88	
2Pt-10Ni/CeO_2-SiO_2 reduced	74		110
2Pt-10Ni/CeO_2-SiO_2 spent	87		106
2Pt-10Ni/CeO_2-SiO_2+CeO_2-SiO_2 fresh	62	-	
2Pt-10Ni/CeO_2-SiO_2+CeO_2-SiO_2 reduced	74		-
2Pt-10Ni/CeO_2-SiO_2+CeO_2-SiO_2 spent	82		-

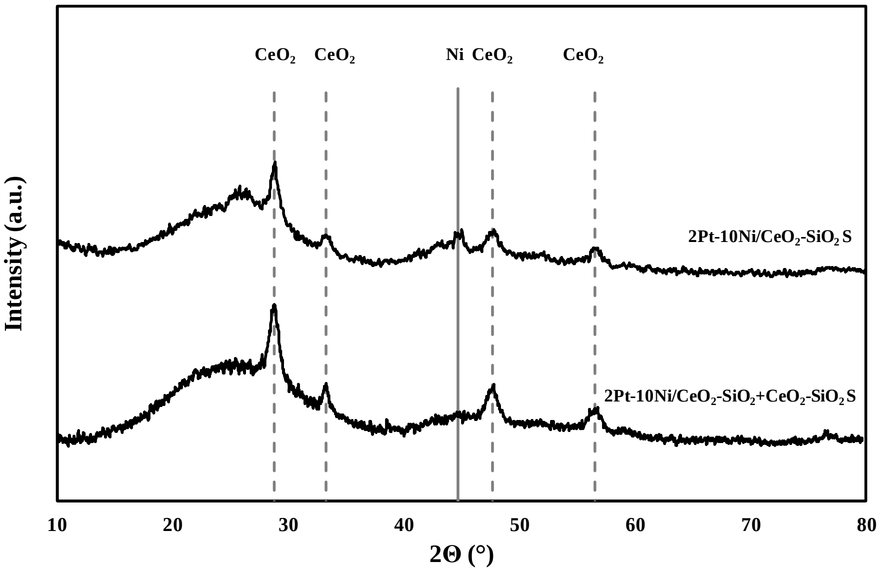

Figure V. 39 *Comparison between the XRD patterns of the spent (S) samples after the test shown in Figure V. 30.*

In Figure V. 40, Raman spectroscopy results are presented for the fresh (calcined), reduced and spent 2Pt-10Ni/CeO_2-SiO_2 catalyst after the test shown in Figure V. 30. The fresh catalyst displayed a main band located at 460 cm^{-1}, ascribed to the symmetric vibrational mode of the ceria phase; in addition, the defect induced vibrational mode is normally observed at 588 cm^{-1}. Bulk NiO exhibits a longitudinal optical mode around 560 cm^{-1} in Raman spectra and the overlapping of NiO and CeO_2 modes generating a wide band between 500 and 730 cm^{-1}(Vivek et al., 2016). Moreover, the presence of the vibrational mode of the Ce-Ni-O bond, typically observed at 588 cm^{-1}, cannot be excluded (Du et al., 2012), together with the bands at 550 and 690 cm^{-1}, indicative of Pt-O-Ce bonds (Palma et al., 2017b).

The reduced catalyst only displayed the most intense CeO_2 peak at 460 cm^{-1}; the small peak observed around 800 cm^{-1} can be linked to the metallic nickel phase (Neale et al., 2014).

In the Raman spectra of the spent catalyst, tested for almost 500 hours, two major bands at around 1343 cm^{-1} (D band) and 1572 cm^{-1}(G band) and the intensity of the G band (0.95) was stronger than that of the D band (0.68). The D band (disorder-induced) band refers to the typical structural imperfections of defective, polycrystalline graphite and other carbonaceous materials; conversely, the G band is attributed to graphitic carbon (Odedairo et al., 2013). These results demonstrates that two types of carbonaceous species were deposited on the catalyst.

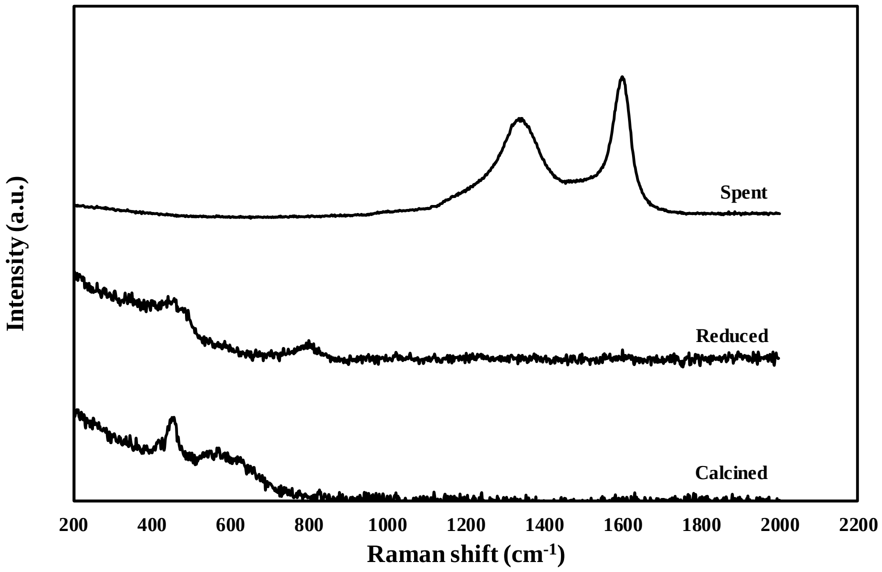

Figure V. 40 *Raman spectra for the fresh (calcined), reduced and spent 2Pt-10Ni/*CeO_2*-*SiO_2*.*

The same two peaks were also observed in the Raman spectrum of the catalyst tested along with the CeO_2-SiO_2 support (Figure V. 41). The ratio I_D/I_G for the latter sample was 0.55, lower than the value recorded for the catalyst alone (0.72), demonstrating again that the support acidity is deleterious under the point of view of catalyst stability, due to the promoted formation of more structured carbon: in fact, a lower degree of graphitization is reported to be observed when the catalyst acidity is reduced (Zhang et al., 2017). In this regard, it has been reported that the anti-coking ability of a catalyst is related not only to the carbon formation rate, but also to the types of coke, particularly: graphitic carbon with an ordered and compact structure is more stable than amorphous carbon, thus being more difficult to be removed (Sun et al., 2020). When the 2Pt-10Ni/CeO_2-SiO_2 catalyst is tested without the support, the amorphous carbon content is higher compared to the ordered one, demonstrating that its anti-coking capability is enhanced with respect to the results obtained in the presence of CeO_2-SiO_2.

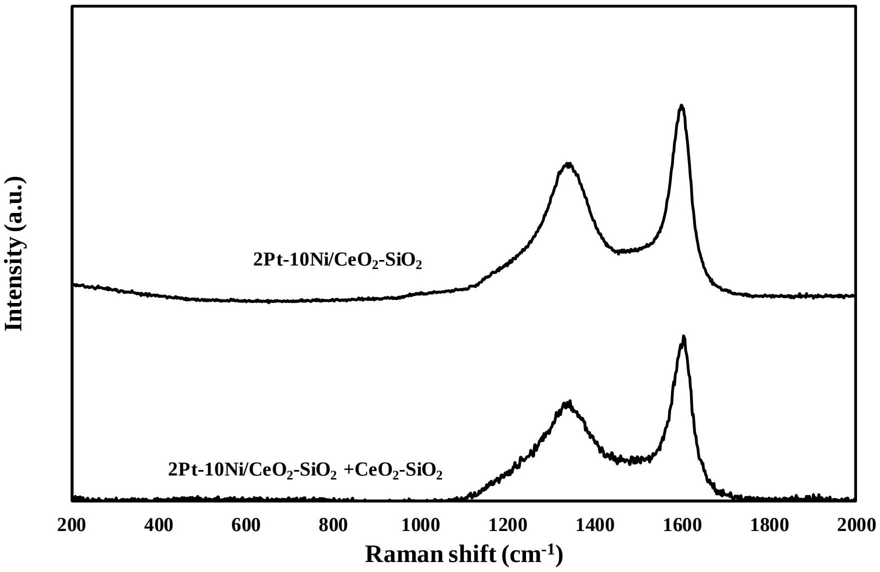

Figure V. 41 *Raman spectra of the spent samples after the tests shown in Figure V. 30.*

V.5 Stability performance of the 2Pt-10Ni/CeO$_2$-SiO$_2$ catalyst: a literature comparison

The stability performance of the 2Pt-10Ni/CeO$_2$-SiO$_2$ catalyst was compared with recent tests found in the literature referring to bioethanol reforming. First of all, it is interesting to highlight that some authors tested CeO$_2$-based catalysts under simulated mixtures containing only certain of the typical bioethanol impurities. For example, Sanchez et al.(Sanchez et al., 2019) employed a RhPt/CeO$_2$-SiO$_2$ catalyst for steam reforming of a stream containing 0.5 mol% of 3-Methyl-1-butanol at 700°C under a f.r.=3: the test was performed for 10 hours and complete conversion was recorded. Also other authors investigated the single effect of various contaminants (including methanol, propanol, acetaldehyde and even amines or H_2S and H_2SO_4); however, stability tests were not carried out for more than 100 hours (Sanchez et al., 2020).

Moreover, different “real” bioethanol sources (including corn and wood bioethanol, sugar beet and fermentation broth) have been employed for hydrogen generation via reforming and Table V. 21 summarizes and compares the performance of different catalysts tested during reforming; since the 2Pt-10Ni/CeO$_2$-SiO$_2$ catalyst was employed for almost 500 hours, only the most long tests (in terms of time-on-stream) available in the recent literature have been taken into account.

Table V. 21 *Ethanol reforming under "real bioethanol": literature comparison.*

Catalyst[a]	**Operative conditions**[b]	**WHSV**[c] **(h^{-1})**	**X e Y_{H2} (%)**	**CFR**[d]	**Ref.**
0.4Rh-0.4Pt/CeO_2-SiO_2 monolith	Sugarcane bioethanol T=700°C f.r.=3 Et_{OH}=8.3%	10.2	X=100 Y=68 after 120 hours	0.096	(Cifuentes et al., 2021)
10Ni-9CaO/ZrO_2	Commercial bioethanol (Biochemtex) T=500°C f.r.=3 Et_{OH}=0.5%	1	X=100 Y=43 after 100 h	n.a. $C_{balance}$= 4-8%	(Tripodi et al., 2018)
Co/Mg/Al hydrotalcite with 1%K monolith	Commercial bioethanol (Deulep) T=550°C f.r.=4 Et_{OH}=- 200 h (ethanol feed) + 100 h (bioethanol feed)	14.4	X=100 Y=38 after 300 h	0.021	(Espinal et al., 2012)
0.5Rh-0.5Pd/CeZrO_2-Al_2O_3 monolith	Commercial bioethanol (Deulep) T=610°C f.r.=6 Et_{OH}=--	50	X=100 Y=56 after 200 h	n.a.	(Casanovas et al., 2017)
0.7Pt-3Ni/CeO_2-SiO_2[e]	Commerical bioethanol (Eldor) T=500°C f.r.=4 o.r.=0.5 Et_{OH}=10%	4.1	X=100 Y=45 after 220 h	0.00031	This thesis

[a] the metal or oxides loadings are intended for weight of catalyst

[b] all the tests were performed at atmospheric pressure

[c] referred to the ethanol mass flow-rate

[d] carbon formation rate $g_{coke} \cdot g_{catalyst}^{-1} \cdot g_{carbon,fed}^{-1} \cdot h^{-1}$, multiplied for 10^3

n.a. not available

[e] the Pt and Ni loading are referred to the total mass

The reported studies are focused on steam reforming performed at higher temperatures (with consequently higher H_2 yields compared to those found over the 2Pt10Ni/CeO_2-SiO_2 catalyst) with respect to the values selected in the present thesis.

Moreover, the catalyst were tested under the bioethanol stream only for 100 hours. Anyway, the carbon formation rate recorded in this work is one order of magnitude lower than the values reported in Table V. 21.

However, to the best of our knowledge, the effect of bioethanol impurities have been rarely investigated under oxidative conditions. Only Mondal et al. (Mondal et al., 2015b) tested a Rh-Ni/CeO_2-SiO_2 catalyst at 600°C under a crude bioethanol stream (f.r.=13, o.r.=0.35) and, after 50 hours of test, ethanol conversion was around 90%. Moreover, we are not aware of other papers available in the literature on catalytic tests under oxidative steam reforming of "real bioethanol" in fluidized bed reactor.

From the above discussion, it is clear that, during this research activity, a promising catalyst was developed, able to assure a stable performance for more than 200 hours (such a long test has never been reported) in a fluidized bed under oxidative reforming of fuel grade bioethanol.

V.6Preliminary catalytic tests in a fluidized bed membrane reactor

The catalyst selected in the present thesis was employed for preliminary tests in a fluidized bed membrane reactor under a simulated bioethanol stream. The prepared catalyst was sent to Eindhoven University for the test. The membrane selected for this preliminary activity test, provided by Tue University of Eindhoven, is a thin film (~4 μm) Pd-Ag membrane prepared by direct simultaneous Pd and Ag electroless plating; such technique assures membrane stability under the fluidization regime (Fernandez et al., 2016). The Pd-Ag layer is deposited onto alumina porous tubes with a thicker wall (10/4 mm o.d./i.d) to improve the mechanical properties compared to the 10/7 mm o.d./i.d. supports. The prepared membranes are characterized by very high H_2 permeance ($8\cdot10^{6}$ mol m^{2} s^{1} Pa^{1}) at 400°C. The test were performed in a single tube membrane reactor where a 50 cm membrane having an external diameter of 10 mm can be placed. The heating of the reactor is performed through an electrically heated oven. The reactor is equipped with three thermocouples and two pressure sensors distributed over the length of the reactor. A vacuum pump is located at the permeate side, in order to separate H_2 at up to 30 mbar. Ethanol and water lines are connected to a controlled evaporated mixer before reaching the reaction section. A Fourier Transform Infrared Spectrometer and a Sick analyser were used to evaluate the composition of the retentate side; a Sick analyser was also used to evaluate the H_2 concentration in the permeate side. The permeate side can be connected to a Horiba film flow meter able to accurately measure the flow-rate of the produced hydrogen.

The measurements were performed under a f.r.=4, a o.r.=0.5 at 500°C and WHSV=4.1 h^{-1} while the operating pressure varied from 2 to 4 bar (a).

Figure V. 42 and Figure V. 43 report the retentate dry composition as well as the flow rate of the produced hydrogen as a function of the operative pressure. Under the selected operative conditions, ethanol and oxygen were completely converted.

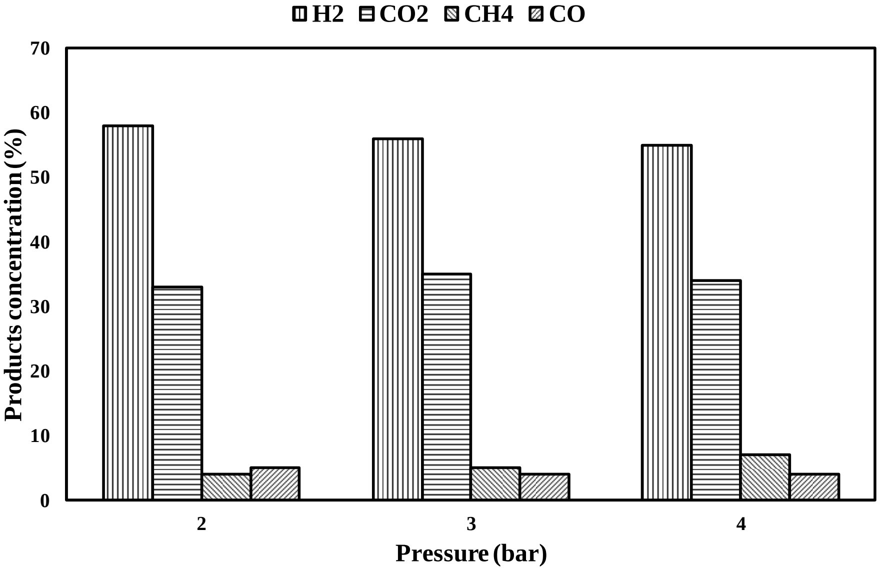

Figure V. 42 *Retentate composition (dry basis) as a function of the operative pressure during fluidized bed membrane tests at 500°C, f.r.=4 and o.r.=0.5.*

These results highlighted that ethanol reforming reaction was negatively affected (even if this effect is slightly visible) by the pressure growth, with a reduction in H_2 concentration in the retentate from 58 to 55% for a pressure increase in the interval 2-4 bar. This phenomenon can be explained considering that ethanol reforming proceeds with an increasing moles number and is disfavoured by a pressures rise. However, the rate of hydrogen production (Figure V. 43) strongly increases with the pressure, reaching 400 $Ncm^3 \cdot min^{-1}$ at 4 bar. In fact, in membrane reactors, it is necessary to take into account two properties: a transport property (hydrogen separation) and a thermodynamic quantity (hydrogen production) which have opposing pressure dependencies (Lee et al., 2004). Anyway, the above results demonstrate that, under the selected operative conditions, the negative effect of pressure on the thermodynamics of the system can be neglected.

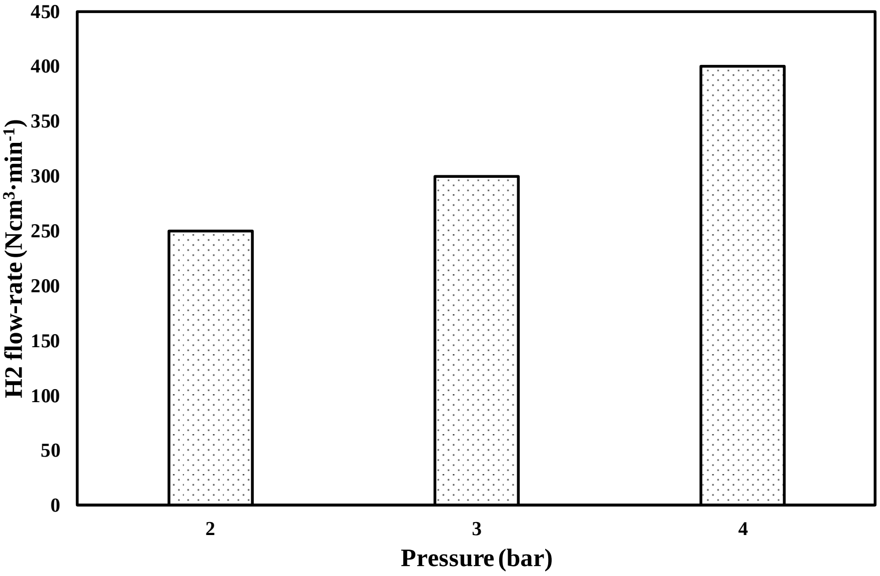

Figure V. 43 *Hydrogen flow-rate as a function of operating pressure during fluidized bed membrane reactor tests at 500°C, f.r.=4 and o.r.=0.5.*

The Hydrogen Recovery factor (HRF), defined as the ratio between the flow-rate of produced hydrogen and the flowrate of fed ethanol, was also estimated finding a value of 35% at 500°C and 4 bar. However, by increasing the temperature to 550°C, the HRF rises to 47%. This values are similar or higher than those found from other authors working for ethanol reforming at pressure differences of about 400 kPa (Seelam et al., 2012, Tosti et al., 2011).

Chapter VI

VI Conclusions

In this work, oxidative steam reforming has been investigated in a fluidized bed reactor with the aiming of developing very stable catalytic formulations for tests in the presence of commercial bioethanol fuel grade.

A preliminary thermodynamic analysis revealed that, by fixing a f.r=4, o.r.=0.5, in the low-temperature range (300-500°C), hydrogen yield is practically unaffected by oxygen addition which, on the contrary, is expected to assure several benefits in terms of catalyst stability and reduced heat requirements to sustain the reaction.

An in-depth literature survey revealed that a 3Pt-10Ni/CeO_2-SiO_2 catalyst (prepared by sequential wet impregnation), previously developed in the Proceed labs of UNISA and tested in the fixed bed mode, can assure carbon formation rates among the lowest available. However, in view of the latter catalyst employment in the presence of unclean fuel grade bioethanol, different strategies were followed to further improve its stability in a fluidized bed reactor. The results of stability tests demonstrated that potassium addition as well as nickel substitution by cobalt had a detrimental effect on catalyst performance. Conversely, the substitution of cerium nitrate hexaydrate (previously selected for the preparation of the CeO_2-SiO_2) by an organic salt (cerium acetylacetonate hydrate) lead to a significant improvement of catalyst durability, due to a better dispersion of ceria crystallite on the silica support, as attested by XRD measurements.

The 3Pt-10Ni/CeO_2-SiO_2 catalyst prepared from the above organic salt was tested at different temperature and feeding compositions in order to highlight the best operative conditions for minimizing coke selectivity: 500°C, f.r.=4 and o.r.=0.5 were selected as the optimal conditions for further tests.

In order to reduce the cost of the developed catalyst, the opportunity of substituting platinum by cheaper metals (i.e. silver or ruthenium) as well as the route of reducing the second metal loading were investigated. However, the performance of the Ag-based catalyst was very unsatisfactory while Pt and Ru-based catalysts displayed comparable activities. The most active catalysts (containing 0.5 wt% of Pt and Ru) were studied to develop a kinetic model able to predict the products gas distribution as a function of reaction temperature. The kinetic model assuring a fairly good agreement with experimental data included ethanol decomposition, methane oxidation, methane steam reforming and water gas shift reactions.

However, looking at the stability results, the lowest carbon formation rates (for every series) were measured for a Pt as well as Ru loadings of 2 wt% . Moreover, the 2Pt-10Ni/CeO_2-SiO_2 catalyst assured the highest ethanol conversion and hydrogen yield with time-on-stream and was, therefore, selected for the investigations in the presence of fuel grade bioethanol.

The stability tests were performed at 500°C, under a steam to bioethanol ratio of 4 and oxygen to bioethanol ratio of 0.5 while the contact time was fixed to 250 ms. The catalyst was tested both alone and in the presence of the bare support (volumetric ratio of 1:4). The undiluted catalyst displayed the best performance, with a total ethanol conversion recorded for more than 200 hours and a corresponding hydrogen yield of 45 %. For higher time-on-stream values, a gradual catalyst deactivation was observed; however, after almost 450 hours, a new stationary condition was reached with no further activity loss. Conversely, the faster deactivation observed in the presence of the diluent was attributed to the higher acidity of the bare support with respect to the activated one, as attested by the enhanced carbon formation rate recorded in the latter case. The 2Pt-10Ni/CeO_2-SiO_2 catalyst assured a CFR of $3 \cdot 10^{-7}$ $g_{coke} \cdot g_{catalyst}^{-1} \cdot g_{carbon,fed}^{-1} \cdot h^{-1}$, which is considerably lower than the values typically found in the recent literature. Moreover, to the best of our knowledge, stability tests under raw bioethanol have not been performed yet for more than 200 hours. Thus, the 2Pt-10Ni/CeO_2-SiO_2 catalyst is a promising candidate for reforming of raw bioethanol.

Finally, some preliminary tests with the catalyst developed in this work were performed in a fluidized bed membrane reactor, in collaboration with Tue University of Eindhoven: the HRF at 500°C and 4 bar was around 35%, close or higher than the values found by other authors under similar pressure differences between the retentate and the permeate side.

Finally, the work here reported paves the way for an in-depth investigation of raw bioethanol reforming in a fluidized bed catalytic membrane reactor, in order to study the performance of the integrated reactor, which has not been studied until now.

References

Abdalla, A. M., Hossain, S., Nisfindy, O. B., Azad, A. T., Dawood, M.andAzad, A. K. (2018). Hydrogen production, storage, transportation and key challenges with applications: A review. *Energy Convers Manage*. **165,** 602-627.

Abdelouahab-Reddam, Z., Mail, R. E., Coloma, F.andSepúlveda-Escribano, A. (2015). Platinum supported on highly-dispersed ceria on activated carbon for the total oxidation of VOCs. *Applied Catalysis A: General*. **494,** 87-94.

Adamu, S., Binous, H., Razzak, S. A.andHossain, M. M. (2017). Enhancement of glucose gasification by Ni/La2O3-Al2O3 towards the thermodynamic extremum at supercritical water conditions. *Renewable Energy*. **111,** 399-409.

Adris, A. M., Lim, C. J.andGrace, J. R. (1994). The fluidized bed membrane reactor system: a pilot scale experimental study. *Chem Eng Sci*. **49,** 5833-5843.

Anzelmo, B., Liguori, S., Mardilovich, I., Iulianelli, A., Ma, Y. H., Wilcox, J.andBasile, A. (2018). Fabrication & performance study of a palladium on alumina supported membrane reactor: Natural gas steam reforming, a case study. *Int J Hydrogen Energy*. **43,** 7713-7721.

Argyle, M.andBartholomew, C. (2015). Heterogeneous Catalyst Deactivation and Regeneration: A Review. *Catalysts*. **5,** 145.

Arratibel, A., Medrano, J. A., Melendez, J., Pacheco Tanaka, D. A., Van Sint Annaland, M.andGallucci, F. (2018). Attrition-resistant membranes for fluidized-bed membrane reactors: Double-skin membranes. *Journal of Membrane Science*. **563,** 419-426.

Arslan, A., Gunduz, S.andDogu, T. (2014). Steam reforming of ethanol with zirconia incorporated mesoporous silicate supported catalysts. *Int J Hydrogen Energy*. **39,** 18264-18272.

Arvelakis, S.andKoukios, E. G. (2002). Physicochemical upgrading of agroresidues as feedstocks for energy production via thermochemical conversion methods. *Biomass Bioenergy*. **22,** 331-348.

Asumadu-Sarkodie, S.andOwusu, P. A. (2016). Carbon dioxide emissions, GDP, energy use, and population growth: a multivariate and causality analysis for Ghana, 1971–2013. *Environmental Science and Pollution Research*. **23,** 13508-13520.

Ay, H.andÜner, D. (2015). Dry reforming of methane over CeO2 supported Ni, Co and Ni–Co catalysts. *Applied Catalysis B: Environmental*. **179,** 128-138.

Badwal, S. P. S., Giddey, S. S., Munnings, C., Bhatt, A. I.andHollenkamp, A. F. (2014). Emerging electrochemical energy conversion and storage technologies. *Frontiers in Chemistry*. **2**.

Barbarias, I., Lopez, G., Alvarez, J., Artetxe, M., Arregi, A., Bilbao, J.andOlazar, M. (2016). A sequential process for hydrogen production based on continuous HDPE fast pyrolysis and in-line steam reforming. *Chem Eng J*. **296,** 191-198.

Baruah, R., Dixit, M., Parejiya, A., Basarkar, P., Bhargav, A.andSharma, S. (2017). Oxidative steam reforming of ethanol on rhodium catalyst – I: Spatially resolved steady-state experiments and microkinetic modeling. *Int J Hydrogen Energy*. **42,** 10184-10198.

Basile, A. (2008). Hydrogen Production Using Pd-based Membrane Reactors for Fuel Cells. *Top Catal*. **51,** 107.

Basile, A., Iulianelli, A., Longo, T., Liguori, S.andDe Falco, M. (2011). Pd-based selective membrane state-of-the-art. *Membrane reactors for hydrogen production processes.* Springer.

Baykara, S. Z. (2018). Hydrogen: A brief overview on its sources, production and environmental impact. *Int J Hydrogen Energy*. **43,** 10605-10614.

Bensalem, A., Bozon-Verduraz, F., Delamar, M.andBugli, G. (1995). Preparation and characterization of highly dispersed silica-supported ceria. *Applied Catalysis A: General*. **121,** 81-93.

Bilal, M.andJackson, S. D. (2017). Ethanol steam reforming over Pt/Al2O3 and Rh/Al2O3 catalysts: The effect of impurities on selectivity and catalyst deactivation. *Applied Catalysis A: General*. **529,** 98-107.

Bizkarra, K., Bermudez, J. M., Arcelus-Arrillaga, P., Barrio, V. L., Cambra, J. F.andMillan, M. (2018). Nickel based monometallic and bimetallic catalysts for synthetic and real bio-oil steam reforming. *Int J Hydrogen Energy*. **43,** 11706-11718.

Braga, A. H., Ribeiro, M. C., Noronha, F. B., Galante, D., Bueno, J. M. C.andSantos, J. B. O. (2018). Effects of Co Addition to Supported Ni Catalysts on Hydrogen Production from Oxidative Steam Reforming of Ethanol. *Energy & Fuels*. **32,** 12814-12825.

Cai, W., Wang, F., Zhan, E., Van Veen, A. C., Mirodatos, C.andShen, W. (2008). Hydrogen production from ethanol over Ir/CeO2 catalysts: A comparative study of steam reforming, partial oxidation and oxidative steam reforming. *J Catal*. **257,** 96-107.

Campos, C. H., Pecchi, G., Fierro, J. L. G.andOsorio-Vargas, P. (2019). Enhanced bimetallic Rh-Ni supported catalysts on alumina doped with mixed lanthanum-cerium oxides for ethanol steam reforming. *Molecular Catalysis*. **469,** 87-97.

Carrera Cerritos, R., Fuentes Ramírez, R., Aguilera Alvarado, A. F., Martínez Rosales, J. M., Viveros García, T.andGalindo Esquivel, I. R. (2011). Steam Reforming of Ethanol over Ni/Al2O3−La2O3

Catalysts Synthesized by Sol−Gel. *Industrial & Engineering Chemistry Research*. **50,** 2576-2584.

Carrero, A., Calles, J. A.andVizcaíno, A. J. (2010). Effect of Mg and Ca addition on coke deposition over Cu–Ni/SiO2 catalysts for ethanol steam reforming. *Chem Eng J*. **163,** 395-402.

Carrette, L., Friedrich, K.andStimming, U. (2001). Fuel cells-fundamentals and applications. *Fuel cells*. **1,** 5-39.

Carvalho, F. L. S., Asencios, Y. J. O., Bellido, J. D. A.andAssaf, E. M. (2016). Bio-ethanol steam reforming for hydrogen production over Co3O4/CeO2 catalysts synthesized by one-step polymerization method. *Fuel Process Technol*. **142,** 182-191.

Casanovas, A., Divins, N. J., Rejas, A., Bosch, R.andLlorca, J. (2017). Finding a suitable catalyst for on-board ethanol reforming using exhaust heat from an internal combustion engine. *Int J Hydrogen Energy*. **42,** 13681-13690.

Castaldo, F., Palma, V., Ruocco, C., Ciambelli, P.andIaquaniello, G. (2015). Low temperature-ethanol steam reforming over Ni-based catalysts supported on CeO2. *Journal of Power Technologies*. **95,** 54-66.

Cerdá-Moreno, C., Da Costa-Serra, J. F.andChica, A. (2019). Co and La supported on Zn-Hydrotalcite-derived material as efficient catalyst for ethanol steam reforming. *Int J Hydrogen Energy*. **44,** 12685-12692.

Chai, R., Li, Y., Zhang, Q., Zhao, G., Liu, Y.andLu, Y. (2015). Monolithic Ni–MOx/Ni-foam (M=Al, Zr or Y) catalysts with enhanced heat/mass transfer for energy-efficient catalytic oxy-methane reforming. *Catal Commun*. **70,** 1-5.

Chen, L., Choong, C. K. S., Zhong, Z., Huang, L., Ang, T. P., Hong, L.andLin, J. (2010). Carbon monoxide-free hydrogen production via low-temperature steam reforming of ethanol over iron-promoted Rh catalyst. *J Catal*. **276,** 197-200.

Chen, L. C., Cheng, H., Chiang, C. W.andLin, S. D. (2015). Sustainable hydrogen production by ethanol steam reforming using a partially reduced copper–nickel oxide catalyst. *ChemSusChem*. **8,** 1787-1793.

Chen, M., Wang, C., Wang, Y., Tang, Z., Yang, Z., Zhang, H.andWang, J. (2019). Hydrogen production from ethanol steam reforming: Effect of Ce content on catalytic performance of Co/Sepiolite catalyst. *Fuel*. **247,** 344-355.

Choong, C. K. S., Zhong, Z., Huang, L., Wang, Z., Ang, T. P., Borgna, A., Lin, J., Hong, L.andChen, L. (2011). Effect of calcium addition on catalytic ethanol steam reforming of Ni/Al2O3: I. Catalytic stability, electronic properties and coking mechanism. *Applied Catalysis A: General*. **407,** 145-154.

Ciambelli, P., Palma, V.andRuggiero, A. (2010). Low temperature catalytic steam reforming of ethanol. 2. Preliminary kinetic investigation of

Pt/CeO2 catalysts. *Applied Catalysis B: Environmental*. **96,** 190-197.

Cifuentes, B., Gómez, J., Sánchez, N., Proaño, L., Bustamante, F.andCobo, M. (2021). Bioethanol steam reforming over monoliths washcoated with RhPt/CeO2–SiO2: The use of residual biomass to stably produce syngas. *Int J Hydrogen Energy*. **46,** 4007-4018.

Cifuentes, B., Valero, M., Conesa, J.andCobo, M. (2015). Hydrogen Production by Steam Reforming of Ethanol on Rh-Pt Catalysts: Influence of CeO2, ZrO2, and La2O3 as Supports. *Catalysts*. **5,** 1872.

Cih-Ying, S.andJeng-Han, W. (2013). Mechanistic Study of the Oxidative Steam Reforming of EtOH on Rh(111): The Importance of the Oxygen Effect. *ChemCatChem*. **5,** 3164-3174.

Coll, R., Salvadó, J., Farriol, X.andMontané, D. (2001). Steam reforming model compounds of biomass gasification tars: conversion at different operating conditions and tendency towards coke formation. *Fuel Process Technol*. **74,** 19-31.

Colpan, C. O., Nalbant, Y.andErcelik, M. (2018). 4.28 Fundamentals of Fuel Cell Technologies. *In:* DINCER, I. (ed.) *Comprehensive Energy Systems.* Oxford: Elsevier.

Comas, J., Mariño, F., Laborde, M.andAmadeo, N. (2004). Bio-ethanol steam reforming on Ni/Al2O3 catalyst. *Chem Eng J*. **98,** 61-68.

Contreras, J. L., Salmones, J., Colín-Luna, J. A., Nuño, L., Quintana, B., Córdova, I., Zeifert, B., Tapia, C.andFuentes, G. A. (2014). Catalysts for H2 production using the ethanol steam reforming (a review). *Int J Hydrogen Energy*. **39,** 18835-18853.

Da Costa-Serra, J. F.andChica, A. (2018). Catalysts based on Co-Birnessite and Co-Todorokite for the efficient production of hydrogen by ethanol steam reforming. *Int J Hydrogen Energy*. **43,** 16859-16865.

Da Silva, A. a. A., Bion, N., Epron, F., Baraka, S., Fonseca, F. C., Rabelo-Neto, R. C., Mattos, L. V.andNoronha, F. B. (2017). Effect of the type of ceria dopant on the performance of Ni/CeO2 SOFC anode for ethanol internal reforming. *Applied Catalysis B: Environmental*. **206,** 626-641.

Dan, M., Senila, L., Roman, M., Mihet, M.andLazar, M. D. (2015). From wood wastes to hydrogen – Preparation and catalytic steam reforming of crude bio-ethanol obtained from fir wood. *Renewable Energy*. **74,** 27-36.

Dantas, S. C., Resende, K. A., Ávila-Neto, C. N., Noronha, F. B., Bueno, J. M. C.andHori, C. E. (2016). Nickel supported catalysts for hydrogen production by reforming of ethanol as addressed by in situ temperature and spatial resolved XANES analysis. *Int J Hydrogen Energy*. **41,** 3399-3413.

Dave, C. D.andPant, K. K. (2011). Renewable hydrogen generation by steam reforming of glycerol over zirconia promoted ceria supported catalyst. *Renewable Energy*. **36,** 3195-3202.

De Lima, A. F. F., Colman, R. C., Zotin, F. M. Z.andAppel, L. G. (2010). Acetaldehyde behavior over platinum based catalyst in hydrogen stream generated by ethanol reforming. *Int J Hydrogen Energy*. **35,** 13200-13205.

De Lima, S. M., Da Cruz, I. O., Jacobs, G., Davis, B. H., Mattos, L. V.andNoronha, F. B. (2008). Steam reforming, partial oxidation, and oxidative steam reforming of ethanol over Pt/CeZrO2 catalyst. *J Catal*. **257,** 356-368.

De Nooijer, N., Gallucci, F., Pellizzari, E., Melendez, J., Pacheco Tanaka, D. A., Manzolini, G.andVan Sint Annaland, M. (2018). On concentration polarisation in a fluidized bed membrane reactor for biogas steam reforming: Modelling and experimental validation. *Chem Eng J*. **348,** 232-243.

De Vasconcelos, P. D. S.andMesquita, A. L. A. (2011). Minimum and Full Fluidization Velocity for Alumina Used in the Aluminum Smelter. *International Journal of Engineering Business Management*. **3,** 23.

Deeprasertkul, C., Longloilert, R., Chaisuwan, T.andWongkasemjit, S. (2014). Impressive low reduction temperature of synthesized mesoporous ceria via nanocasting. *Mater Lett*. **130,** 218-222.

Dehkordi, T. K., Hormozi, F.andJahangiri, M. (2016). Using conical reactor to improve efficiency of ethanol steam reforming. *Int J Hydrogen Energy*. **41,** 17084-17092.

Demirbaş, A. (2001). Biomass resource facilities and biomass conversion processing for fuels and chemicals. *Energy Convers Manage*. **42,** 1357-1378.

Demirbaş, A. (2002). Hydrogen Production from Biomass by the Gasification Process. *Energy Sources*. **24,** 59-68.

Deshmukh, S. a. R. K., Van Sint Annaland, M.andKuipers, J. a. M. (2007). Gas back-mixing studies in membrane assisted bubbling fluidized beds. *Chem Eng Sci*. **62,** 4095-4111.

Di Michele, A., Dell'angelo, A., Tripodi, A., Bahadori, E., Sànchez, F., Motta, D., Dimitratos, N., Rossetti, I.andRamis, G. (2019). Steam reforming of ethanol over Ni/MgAl2O4 catalysts. *Int J Hydrogen Energy*. **44,** 952-964.

Djinović, P., Osojnik Črnivec, I. G., Erjavec, B.andPintar, A. (2012). Influence of active metal loading and oxygen mobility on coke-free dry reforming of Ni–Co bimetallic catalysts. *Applied Catalysis B: Environmental*. **125,** 259-270.

Dolan, M. D., Dave, N. C., Ilyushechkin, A. Y., Morpeth, L. D.andMclennan, K. G. (2006). Composition and operation of hydrogen-selective amorphous alloy membranes. *Journal of Membrane Science*. **285,** 30-55.

Dong, W.-S., Jun, K.-W., Roh, H.-S., Liu, Z.-W.andPark, S.-E. (2002). Comparative Study on Partial Oxidation of Methane over Ni/ZrO2, Ni/CeO2 and Ni/Ce–ZrO2 Catalysts. *Catal Lett*. **78,** 215-222.

Du, X., Zhang, D., Shi, L., Gao, R.andZhang, J. (2012). Morphology Dependence of Catalytic Properties of Ni/CeO2 Nanostructures for Carbon Dioxide Reforming of Methane. *The Journal of Physical Chemistry C*. **116,** 10009-10016.

Du, Y.-L., Wu, X., Cheng, Q., Huang, Y.-L.andHuang, W. (2017). Development of Ni-based catalysts derived from hydrotalcite-like compounds precursors for synthesis gas production via methane or ethanol reforming. *Catalysts*. **7,** 70.

Dufour, J., Serrano, D. P., Gálvez, J. L., Moreno, J.andGonzález, A. (2011). Hydrogen production from fossil fuels: life cycle assessment of technologies with low greenhouse gas emissions. *Energy & Fuels*. **25,** 2194-2202.

Ejikeme, P. M., Makgopa, K.andOzoemena, K. I. (2016). Effects of Catalyst-Support Materials on the Performance of Fuel Cells. *In:* OZOEMENA, K. I. & CHEN, S. (eds.) *Nanomaterials for Fuel Cell Catalysis.* Cham: Springer International Publishing.

Erdogan, B., Arbag, H.andYasyerli, N. (2018). SBA-15 supported mesoporous Ni and Co catalysts with high coke resistance for dry reforming of methane. *Int J Hydrogen Energy*. **43,** 1396-1405.

Espinal, R., Taboada, E., Molins, E., Chimentao, R. J., Medina, F.andLlorca, J. (2012). Cobalt hydrotalcites as catalysts for bioethanol steam reforming. The promoting effect of potassium on catalyst activity and long-term stability. *Applied Catalysis B: Environmental*. **127,** 59-67.

Fang, W., Pirez, C., Paul, S., Jiménez-Ruiz, M., Jobic, H., Dumeignil, F.andJalowiecki-Duhamel, L. (2016). Advanced functionalized Mg2AlNiXHZOY nano-oxyhydrides ex-hydrotalcites for hydrogen production from oxidative steam reforming of ethanol. *Int J Hydrogen Energy*. **41,** 15443-15452.

Faria, W. L. S., Dieguez, L. C.andSchmal, M. (2008). Autothermal reforming of propane for hydrogen production over Pd/CeO2/Al2O3 catalysts. *Applied Catalysis B: Environmental*. **85,** 77-85.

Fatsikostas, A. N., Kondarides, D. I.andVerykios, X. E. (2002). Production of hydrogen for fuel cells by reformation of biomass-derived ethanol. *Catal Today*. **75,** 145-155.

Fatsikostas, A. N.andVerykios, X. E. (2004). Reaction network of steam reforming of ethanol over Ni-based catalysts. *J Catal*. **225,** 439-452.

Fernandez, E., Sanchez-Garcia, J. A., Melendez, J., Spallina, V., Van Sint Annaland, M., Gallucci, F., Pacheco Tanaka, D. A.andPrema, R.

(2016). Development of highly permeable ultra-thin Pd-based supported membranes. *Chem Eng J*. **305,** 149-155.

Fierro, V., Akdim, O., Provendier, H.andMirodatos, C. (2005). Ethanol oxidative steam reforming over Ni-based catalysts. *J Power Sources*. **145,** 659-666.

Fiorenza, R., Crisafulli, C.andScirè, S. (2016). H2 purification through preferential oxidation of CO over ceria supported bimetallic Au-based catalysts. *Int J Hydrogen Energy*. **41,** 19390-19398.

Fishtik, I., Alexander, A., Datta, R.andGeana, D. (2000). A thermodynamic analysis of hydrogen production by steam reforming of ethanol via response reactions. *Int J Hydrogen Energy*. **25,** 31-45.

Freni, S., Cavallaro, S., Mondello, N., Spadaro, L.andFrusteri, F. (2003). Production of hydrogen for MC fuel cell by steam reforming of ethanol over MgO supported Ni and Co catalysts. *Catal Commun*. **4,** 259-268.

Gac, W., Greluk, M., Słowik, G.andTurczyniak-Surdacka, S. (2018). Structural and surface changes of cobalt modified manganese oxide during activation and ethanol steam reforming reaction. *Appl Surf Sci*. **440,** 1047-1062.

Gallucci, F., Fernandez, E., Corengia, P.andVan Sint Annaland, M. (2013). Recent advances on membranes and membrane reactors for hydrogen production. *Chem Eng Sci*. **92,** 40-66.

Gao, J., Guo, J., Liang, D., Hou, Z., Fei, J.andZheng, X. (2008). Production of syngas via autothermal reforming of methane in a fluidized-bed reactor over the combined CeO2–ZrO2/SiO2 supported Ni catalysts. *Int J Hydrogen Energy*. **33,** 5493-5500.

Gao, Y., Jiang, J., Meng, Y., Yan, F.andAihemaiti, A. (2018). A review of recent developments in hydrogen production via biogas dry reforming. *Energy Convers Manage*. **171,** 133-155.

García-Lario, A. L., Aznar, M., Martinez, I., Grasa, G. S.andMurillo, R. (2015). Experimental study of the application of a NiO/NiAl2O4 catalyst and a CaO-based synthetic sorbent on the Sorption Enhanced Reforming process. *Int J Hydrogen Energy*. **40,** 219-232.

García, E. Y.andLaborde, M. A. (1991). Hydrogen production by the steam reforming of ethanol: Thermodynamic analysis. *Int J Hydrogen Energy*. **16,** 307-312.

Gaudillere, C., González, J. J., Chica, A.andSerra, J. M. (2017). YSZ monoliths promoted with Co as catalysts for the production of H2 by steam reforming of ethanol. *Applied Catalysis A: General*. **538,** 165-173.

Geldart, D. (1973). Types of gas fluidization. *Powder Technol*. **7,** 285-292.

Gonçalves, A. a. S., Faustino, P. B., Assaf, J. M.andJaroniec, M. (2017). One-Pot Synthesis of Mesoporous Ni–Ti–Al Ternary Oxides: Highly

Active and Selective Catalysts for Steam Reforming of Ethanol. *ACS Applied Materials & Interfaces*. **9,** 6079-6092.

Gong, Z., Laura, B., Stefano, A., D., S. S., Jaime, E., Anna, K., Michael, E., C., H. J., Arturo, M.-A., Marcos, F.-G.andA., R. J. (2010). High Activity of Ce1−xNixO2−y for H2 Production through Ethanol Steam Reforming: Tuning Catalytic Performance through Metal–Oxide Interactions. *Angew Chem Int Ed*. **49,** 9680-9684.

Graschinsky, C., Giunta, P., Amadeo, N.andLaborde, M. (2012). Thermodynamic analysis of hydrogen production by autothermal reforming of ethanol. *Int J Hydrogen Energy*. **37,** 10118-10124.

Greluk, M., Rotko, M.andTurczyniak-Surdacka, S. (2020). Enhanced catalytic performance of La2O3 promoted Co/CeO2 and Ni/CeO2 catalysts for effective hydrogen production by ethanol steam reforming. *Renewable Energy*. **155,** 378-395.

Greluk, M., Rybak, P., Słowik, G., Rotko, M.andMachocki, A. (2015). Comparative study on steam and oxidative steam reforming of ethanol over 2KCo/ZrO2 catalyst. *Catal Today*. **242,** 50-59.

Greluk, M., Słowik, G., Rotko, M.andMachocki, A. (2016a). Steam reforming and oxidative steam reforming of ethanol over PtKCo/CeO2 catalyst. *Fuel*. **183,** 518-530.

Greluk, M., Słowik, G., Rotko, M.andMachocki, A. (2016b). Steam reforming and oxidative steam reforming of ethanol over PtKCo/CeO2 catalyst. *Fuel*. **183,** 518-530.

Grewal, T. P. K.andRoy, S. (2016). Modeling the effect of coke deposition in a heat integrated ethanol reformer. *Int J Hydrogen Energy*. **41,** 19863-19880.

Guandalini, G., Campanari, S.andValenti, G. (2016). Comparative assessment and safety issues in state-of-the-art hydrogen production technologies. *Int J Hydrogen Energy*. **41,** 18901-18920.

Habe, H., Shinbo, T., Yamamoto, T., Sato, S., Shimada, H.andSakaki, K. (2013). Chemical Analysis of Impurities in Diverse Bioethanol Samples. *Journal of the Japan Petroleum Institute*. **56,** 414-422.

Han, S. J., Song, J. H., Bang, Y., Yoo, J., Park, S., Kang, K. H.andSong, I. K. (2016). Hydrogen production by steam reforming of ethanol over mesoporous Cu–Ni–Al2O3–ZrO2 xerogel catalysts. *Int J Hydrogen Energy*. **41,** 2554-2563.

He, S., He, S., Zhang, L., Li, X., Wang, J., He, D., Lu, J.andLuo, Y. (2015). Hydrogen production by ethanol steam reforming over Ni/SBA-15 mesoporous catalysts: Effect of Au addition. *Catal Today*. **258,** 162-168.

He, S., Mei, Z., Liu, N., Zhang, L., Lu, J., Li, X., Wang, J., He, D.andLuo, Y. (2017). Ni/SBA-15 catalysts for hydrogen production by ethanol steam reforming: Effect of nickel precursor. *Int J Hydrogen Energy*. **42,** 14429-14438.

He, Z., Wang, X., Pu, Y.andQian, Z. (2012). Fundamental understanding of the role of potassium on the activity of Pt/CeO2 for the hydrogen production from ethanol. *Int J Hydrogen Energy*. **37,** 11132-11140.

Hohmeyer, J., Kondratenko, E. V., Bron, M., Kröhnert, J., Jentoft, F. C., Schlögl, R.andClaus, P. (2010). Activation of dihydrogen on supported and unsupported silver catalysts. *J Catal*. **269,** 5-14.

Horváth, A., Stefler, G., Geszti, O., Kienneman, A., Pietraszek, A.andGuczi, L. (2011). Methane dry reforming with CO2 on CeZr-oxide supported Ni, NiRh and NiCo catalysts prepared by sol–gel technique: Relationship between activity and coke formation. *Catalysis Today*. **169,** 102-111.

Hou, T., Yu, B., Zhang, S., Xu, T., Wang, D.andCai, W. (2015a). Hydrogen production from ethanol steam reforming over Rh/CeO2 catalyst. *Catal Commun*. **58,** 137-140.

Hou, T., Zhang, S., Chen, Y., Wang, D.andCai, W. (2015b). Hydrogen production from ethanol reforming: Catalysts and reaction mechanism. *Renewable and Sustainable Energy Reviews*. **44,** 132-148.

Hsieh, H.-C., Chang, Y.-C., Tsai, P.-W., Lin, Y.-Y., Chuang, Y.-C., Sheu, H.-S.andLee, C.-S. (2019a). Metal substituted pyrochlore phase Li x La 2− x Ce 1.8 Ru 0.2 O 7− δ (x= 0.0–0.6) as an effective catalyst for oxidative and auto-thermal steam reforming of ethanol. *Catalysis Science & Technology*. **9,** 1406-1419.

Hsieh, H.-C., Tsai, P.-W., Chang, Y.-C., Weng, S.-F., Sheu, H.-S., Chuang, Y.-C.andLee, C.-S. (2019b). Oxidative steam reforming of ethanol over MxLa2−xCe1.8Ru0.2O7−δ (M = Mg, Ca) catalysts: effect of alkaline earth metal substitution and support on stability and activity. *RSC Advances*. **9,** 39932-39944.

Hung, C.-C., Chen, S.-L., Liao, Y.-K., Chen, C.-H.andWang, J.-H. (2012). Oxidative steam reforming of ethanol for hydrogen production on M/Al2O3. *Int J Hydrogen Energy*. **37,** 4955-4966.

Ibrahim, N., Kamarudin, S. K.andMinggu, L. J. (2014). Biofuel from biomass via photo-electrochemical reactions: An overview. *J Power Sources*. **259,** 33-42.

Ismail, A. F., Rahman, M. A., Othman, M. H. D.andMatsuura, T. (2018). *Membrane Separation Principles and Applications: From Material Selection to Mechanisms and Industrial Uses*, Elsevier.

Iulianelli, A., Liguori, S., Vita, A., Italiano, C., Fabiano, C., Huang, Y.andBasile, A. (2016a). The oncoming energy vector: Hydrogen produced in Pd-composite membrane reactor via bioethanol reforming over Ni/CeO2 catalyst. *Catal Today*. **259,** 368-375.

Iulianelli, A., Liguori, S., Vita, A., Italiano, C., Fabiano, C., Huang, Y.andBasile, A. (2016b). The oncoming energy vector: Hydrogen produced in Pd-composite membrane reactor via bioethanol reforming over Ni/CeO2 catalyst. *Catal Today*. **259,** 368-375.

Iulianelli, A., Palma, V., Bagnato, G., Ruocco, C., Huang, Y., Veziroğlu, N. T.andBasile, A. (2018). From bioethanol exploitation to high grade hydrogen generation: Steam reforming promoted by a Co-Pt catalyst in a Pd-based membrane reactor. *Renewable Energy*. **119,** 834-843.

Jeon, S., Park, Y. M., Saravanan, K., Han, G. Y., Kim, B.-W., Lee, J.-B.andBae, J. W. (2017). Aqueous phase reforming of ethylene glycol over bimetallic platinum-cobalt on ceria–zirconia mixed oxide. *Int J Hydrogen Energy*. **42,** 9892-9902.

Jeong, D.-W., Jang, W.-J., Shim, J.-O., Han, W.-B., Kim, H.-M., Lee, Y.-L., Bae, J. W.andRoh, H.-S. (2015). Optimization of a highly active nano-sized Pt/CeO2 catalyst via Ce(OH)CO3 for the water-gas shift reaction. *Renewable Energy*. **79,** 78-84.

Jha, S. K., Bilalovic, J., Jha, A., Patel, N.andZhang, H. (2017). Renewable energy: Present research and future scope of Artificial Intelligence. *Renewable and Sustainable Energy Reviews*. **77,** 297-317.

Jian, Q., Zhao, Y.andWang, H. (2015). An experimental study of the dynamic behavior of a 2 kW proton exchange membrane fuel cell stack under various loading conditions. *Energy*. **80,** 740-745.

Jing, Q., Fang, L., Lou, H.andZheng, X. (2009). Fabrication of CeZrO2 on Ni/SiO2 and promoted catalysis for methane autothermal reforming in a fluidized bed reactor. *Journal of Rare Earths*. **27,** 431-436.

Jo, S. W., Kwak, B. S., Kim, K. M., Do, J. Y., Park, N.-K., Lee, T. J., Lee, S.-T.andKang, M. (2016). Reasonable harmony of Ni and Mn in core@shell-structured NiMn@SiO2 catalysts prepared for hydrogen production from ethanol steam reforming. *Chem Eng J*. **288,** 858-868.

Karakaya, M., Ilsen Onsan, Z.andAvci, A. K. (2013). Microchannel Autothermal Reforming of Methane to Synthesis Gas. *Top Catal*. **56,** 1716-1723.

Khetkorn, W., Rastogi, R. P., Incharoensakdi, A., Lindblad, P., Madamwar, D., Pandey, A.andLarroche, C. (2017). Microalgal hydrogen production – A review. *Bioresour Technol*. **243,** 1194-1206.

Kim, D., Kwak, B. S., Park, N.-K., Han, G. B.andKang, M. (2015). Dynamic hydrogen production from ethanol steam-reforming reaction on NixMoy/SBA-15 catalytic system. *International Journal of Energy Research*. **39,** 279-292.

Kim, P., Kim, Y., Kim, C., Kim, H., Park, Y., Lee, J. H., Song, I. K.andYi, J. (2003). Synthesis and Characterization of Mesoporous Alumina as a Catalyst Support for Hydrodechlorination of 1,2-Dichloropropane: Effect of Catalyst Preparation Method. *Catal Lett*. **89,** 185-192.

Konsolakis, M., Carabineiro, S. a. C., Marnellos, G. E., Asad, M. F., Soares, O. S. G. P., Pereira, M. F. R., Órfão, J. J. M.andFigueiredo, J. L.

(2017). Effect of cobalt loading on the solid state properties and ethyl acetate oxidation performance of cobalt-cerium mixed oxides. *J Colloid Interface Sci*. **496,** 141-149.

Konsolakis, M., Ioakimidis, Z., Kraia, T.andMarnellos, G. (2016). Hydrogen Production by Ethanol Steam Reforming (ESR) over CeO2 Supported Transition Metal (Fe, Co, Ni, Cu) Catalysts: Insight into the Structure-Activity Relationship. *Catalysts*. **6,** 39.

Koros, W. J.andFleming, G. (1993). Membrane-based gas separation. *Journal of membrane science*. **83,** 1-80.

Kugai, J., Subramani, V., Song, C., Engelhard, M. H.andChin, Y.-H. (2006). Effects of nanocrystalline CeO2 supports on the properties and performance of Ni–Rh bimetallic catalyst for oxidative steam reforming of ethanol. *J Catal*. **238,** 430-440.

Kunii, D.andLevenspiel, O. (2013). *Fluidization engineering*, Elsevier.

Kwak, B. S., Lee, G., Park, S.-M.andKang, M. (2015). Effect of MnOx in the catalytic stabilization of Co2MnO4 spinel during the ethanol steam reforming reaction. *Applied Catalysis A: General*. **503,** 165-175.

Laosiripojana, N.andAssabumrungrat, S. (2006). Hydrogen production from steam and autothermal reforming of LPG over high surface area ceria. *J Power Sources*. **158,** 1348-1357.

Lazar, M. D., Senila, L., Dan, M.andMihet, M. (2019). Chapter 10 - Crude Bioethanol Reforming Process: The Advantage of a Biosource Exploitation. *In:* BASILE, A., IULIANELLI, A., DALENA, F. & VEZIROĞLU, T. N. (eds.) *Ethanol.* Elsevier.

Leal, A. L., Soria, M. A.andMadeira, L. M. (2016). Autothermal reforming of impure glycerol for H2 production: Thermodynamic study including in situ CO2 and/or H2 separation. *Int J Hydrogen Energy*. **41,** 2607-2620.

Lee, B., Lee, S.andLim, H. (2016). Numerical modeling studies for a methane dry reforming in a membrane reactor. *Journal of Natural Gas Science and Engineering*. **34,** 1251-1261.

Lee, D., Hacarlioglu, P.andOyama, S. (2004). The Effect of Pressure in Membrane Reactors: Trade-Off in Permeability and Equilibrium Conversion in the Catalytic Reforming of CH4 with CO2 at High Pressure. *Top Catal*. **29,** 45-57.

Lee, J. S., Han, G. B.andKang, M. (2012). Low temperature steam reforming of ethanol for carbon monoxide-free hydrogen production over mesoporous Sn-incorporated SBA-15 catalysts. *Energy*. **44,** 248-256.

Lee, M., Cho, S.andKim, J. (2017). A comprehensive model for design and analysis of bioethanol production and supply strategies from lignocellulosic biomass. *Renewable Energy*. **112,** 247-259.

Lercher, J. A., Bitter, J. H., Hally, W., Niessen, W.andSeshan, K. (1996). Design of stable catalysts for methane-carbon dioxide reforming. *In:* HIGHTOWER, J. W., NICHOLAS DELGASS, W., IGLESIA, E. & BELL, A. T. (eds.) *Stud Surf Sci Catal.* Elsevier.

Levin, D. B., Pitt, L.andLove, M. (2004). Biohydrogen production: prospects and limitations to practical application. *Int J Hydrogen Energy*. **29,** 173-185.

Li, D., Li, X.andGong, J. (2016). Catalytic Reforming of Oxygenates: State of the Art and Future Prospects. *Chem Rev*. **116,** 11529-11653.

Li, D., Zeng, L., Li, X., Wang, X., Ma, H., Assabumrungrat, S.andGong, J. (2015). Ceria-promoted Ni/SBA-15 catalysts for ethanol steam reforming with enhanced activity and resistance to deactivation. *Applied Catalysis B: Environmental*. **176-177,** 532-541.

Li, L., Tang, D., Song, Y., Jiang, B.andZhang, Q. (2018). Hydrogen production from ethanol steam reforming on Ni-Ce/MMT catalysts. *Energy*. **149,** 937-943.

Li, M.-R.andWang, G.-C. (2018). The mechanism of ethanol steam reforming on the Co0 and Co2+ sites: A DFT study. *J Catal*. **365,** 391-404.

Li, N., Pu, J., Chi, B.andLi, J. (2019). Ethanol steam reforming with a Ni–BaZr0.1Ce0.7 Y0.1Yb0.1O3–δ catalyst. *Materials Today Energy*. **12,** 371-378.

Liu, S., Zhang, K., Fang, L.andLi, Y. (2008). Thermodynamic Analysis of Hydrogen Production from Oxidative Steam Reforming of Ethanol. *Energy & Fuels*. **22,** 1365-1370.

Liu, Z., Duchoň, T., Wang, H., Peterson, E. W., Zhou, Y., Luo, S., Zhou, J., Matolín, V., Stacchiola, D. J., Rodriguez, J. A.andSenanayake, S. D. (2015a). Mechanistic Insights of Ethanol Steam Reforming over Ni–CeOx(111): The Importance of Hydroxyl Groups for Suppressing Coke Formation. *The Journal of Physical Chemistry C*. **119,** 18248-18256.

Liu, Z., Xu, W., Yao, S., Johnson-Peck, A. C., Zhao, F., Michorczyk, P., Kubacka, A., Stach, E. A., Fernández-García, M., Senanayake, S. D.andRodriguez, J. A. (2015b). Superior performance of Ni–W–Ce mixed-metal oxide catalysts for ethanol steam reforming: Synergistic effects of W- and Ni-dopants. *J Catal*. **321,** 90-99.

Llera, I., Mas, V., Bergamini, M. L., Laborde, M.andAmadeo, N. (2012). Bio-ethanol steam reforming on Ni based catalyst. Kinetic study. *Chem Eng Sci*. **71,** 356-366.

Llorca, J., Homs, N., Sales, J.andDe La Piscina, P. R. (2002). Efficient production of hydrogen over supported cobalt catalysts from ethanol steam reforming. *J Catal*. **209,** 306-317.

Lu, H., Rihko-Struckmann, L., Hanke-Rauschenbach, R.andSundmacher, K. (2008). Dynamic Behavior of a PEM Fuel Cell During

Electrochemical CO Oxidation on a PtRu Anode. *Top Catal*. **51,** 89-97.

Łukajtis, R., Hołowacz, I., Kucharska, K., Glinka, M., Rybarczyk, P., Przyjazny, A.andKamiński, M. (2018). Hydrogen production from biomass using dark fermentation. *Renewable and Sustainable Energy Reviews*. **91,** 665-694.

Ma, H., Zeng, L., Tian, H., Li, D., Wang, X., Li, X.andGong, J. (2016). Efficient hydrogen production from ethanol steam reforming over La-modified ordered mesoporous Ni-based catalysts. *Applied Catalysis B: Environmental*. **181,** 321-331.

Mamontov, G. V., Grabchenko, M. V., Sobolev, V. I., Zaikovskii, V. I.andVodyankina, O. V. (2016). Ethanol dehydrogenation over Ag-CeO2/SiO2 catalyst: Role of Ag-CeO2 interface. *Applied Catalysis A: General*. **528,** 161-167.

Mao, L.andYe, H. (2010). New development of one-dimensional Si/SiO2 photonic crystals filter for thermophotovoltaic applications. *Renewable Energy*. **35,** 249-256.

Marinho, A. L. A., Rabelo-Neto, R. C., Noronha, F. B.andMattos, L. V. (2016). Steam reforming of ethanol over Ni-based catalysts obtained from LaNiO3 and LaNiO3/CeSiO2 perovskite-type oxides for the production of hydrogen. *Applied Catalysis A: General*. **520,** 53-64.

Mauriello, F., Ariga-Miwa, H., Paone, E., Pietropaolo, R., Takakusagi, S.andAsakura, K. (2019). Transfer hydrogenolysis of aromatic ethers promoted by the bimetallic Pd/Co catalyst. *Catal Today*.

Md Zin, R., Ross, A. B., Jones, J. M.andDupont, V. (2015). Hydrogen from ethanol reforming with aqueous fraction of pine pyrolysis oil with and without chemical looping. *Bioresour Technol*. **176,** 257-266.

Mekhilef, S., Saidur, R.andSafari, A. (2012). Comparative study of different fuel cell technologies. *Renewable and Sustainable Energy Reviews*. **16,** 981-989.

Mhadmhan, S., Natewong, P., Prasongthum, N., Samart, C.andReubroycharoen, P. (2018). Investigation of Ni/SiO2 Fiber Catalysts Prepared by Different Methods on Hydrogen production from Ethanol Steam Reforming. *Catalysts*. **8,** 319.

Mondal, T., Pant, K. K.andDalai, A. K. (2015a). Catalytic oxidative steam reforming of bio-ethanol for hydrogen production over Rh promoted Ni/CeO2–ZrO2 catalyst. *Int J Hydrogen Energy*. **40,** 2529-2544.

Mondal, T., Pant, K. K.andDalai, A. K. (2015b). Oxidative and non-oxidative steam reforming of crude bio-ethanol for hydrogen production over Rh promoted Ni/CeO2-ZrO2 catalyst. *Applied Catalysis A: General*. **499,** 19-31.

Montero, C., Ochoa, A., Castaño, P., Bilbao, J.andGayubo, A. G. (2015). Monitoring Ni0 and coke evolution during the deactivation of a

Ni/La2O3–αAl2O3 catalyst in ethanol steam reforming in a fluidized bed. *J Catal*. **331,** 181-192.

Montero, C., Remiro, A., Benito, P. L., Bilbao, J.andGayubo, A. G. (2018). Optimum operating conditions in ethanol steam reforming over a Ni/La2O3-αAl2O3 catalyst in a fluidized bed reactor. *Fuel Process Technol*. **169,** 207-216.

Montero, C., Remiro, A., Valle, B., Oar-Arteta, L., Bilbao, J.andGayubo, A. G. (2019). Origin and Nature of Coke in Ethanol Steam Reforming and Its Role in Deactivation of Ni/La2O3–αAl2O3 Catalyst. *Industrial & Engineering Chemistry Research*. **58,** 14736-14751.

Moraes, T. S., Borges, L. E. P., Farrauto, R.andNoronha, F. B. (2018). Steam reforming of ethanol on Rh/SiCeO2 washcoated monolith catalyst: Stable catalyst performance. *Int J Hydrogen Energy*. **43,** 115-126.

Moraes, T. S., Neto, R. C. R., Ribeiro, M. C., Mattos, L. V., Kourtelesis, M., Ladas, S., Verykios, X.andBellot Noronha, F. (2015). The study of the performance of PtNi/CeO2–nanocube catalysts for low temperature steam reforming of ethanol. *Catal Today*. **242, Part A,** 35-49.

Moraes, T. S., Rabelo Neto, R. C., Ribeiro, M. C., Mattos, L. V., Kourtelesis, M., Ladas, S., Verykios, X.andNoronha, F. B. (2016). Ethanol conversion at low temperature over CeO2—Supported Ni-based catalysts. Effect of Pt addition to Ni catalyst. *Applied Catalysis B: Environmental*. **181,** 754-768.

Morales, M.andSegarra, M. (2015). Steam reforming and oxidative steam reforming of ethanol over La0.6Sr0.4CoO3−δ perovskite as catalyst precursor for hydrogen production. *Applied Catalysis A: General*. **502,** 305-311.

Mulewa, W., Tahir, M.andAmin, N. a. S. (2017). MMT-supported Ni/TiO2 nanocomposite for low temperature ethanol steam reforming toward hydrogen production. *Chem Eng J*. **326,** 956-969.

Muñoz, M., Moreno, S.andMolina, R. (2016). Promoter effect of Ce and Pr on the catalytic stability of the Ni-Co system for the oxidative steam reforming of ethanol. *Applied Catalysis A: General*. **526,** 84-94.

Muñoz, M., Moreno, S.andMolina, R. (2017). Oxidative steam reforming of ethanol (OSRE) over stable NiCo–MgAl catalysts by microwave or sonication assisted coprecipitation. *Int J Hydrogen Energy*. **42,** 12284-12294.

Murmura, M. A., Patrascu, M., Annesini, M. C., Palma, V., Ruocco, C.andSheintuch, M. (2015). Directing selectivity of ethanol steam reforming in membrane reactors. *Int J Hydrogen Energy*. **40,** 5837-5848.

Muroyama, H., Nakase, R., Matsui, T.andEguchi, K. (2010). Ethanol steam reforming over Ni-based spinel oxide. *Int J Hydrogen Energy*. **35,** 1575-1581.

Neale, A. R., Jin, Y., Ouyang, J., Hughes, S., Hesp, D., Dhanak, V., Dearden, G., Edwardson, S.andHardwick, L. J. (2014). Electrochemical performance of laser micro-structured nickel oxyhydroxide cathodes. *J Power Sources*. **271,** 42-47.

Nejat, T., Jalalinezhad, P., Hormozi, F.andBahrami, Z. (2019). Hydrogen production from steam reforming of ethanol over Ni-Co bimetallic catalysts and MCM-41 as support. *Journal of the Taiwan Institute of Chemical Engineers*. **97,** 216-226.

Ni, M., Leung, D. Y. C.andLeung, M. K. H. (2007). A review on reforming bio-ethanol for hydrogen production. *Int J Hydrogen Energy*. **32,** 3238-3247.

Ni, M., Leung, D. Y. C., Leung, M. K. H.andSumathy, K. (2006). An overview of hydrogen production from biomass. *Fuel Process Technol*. **87,** 461-472.

Nichele, V., Signoretto, M., Pinna, F., Ghedini, E., Compagnoni, M., Rossetti, I., Cruciani, G.andDi Michele, A. (2015). Bimetallic Ni–Cu Catalysts for the Low-Temperature Ethanol Steam Reforming: Importance of Metal–Support Interactions. *Catal Lett*. **145,** 549-558.

Nichele, V., Signoretto, M., Pinna, F., Menegazzo, F., Rossetti, I., Cruciani, G., Cerrato, G.andDi Michele, A. (2014). Ni/ZrO2 catalysts in ethanol steam reforming: Inhibition of coke formation by CaO-doping. *Applied Catalysis B: Environmental*. **150-151,** 12-20.

Nieto-Márquez, A., Sánchez, D., Miranda-Dahdal, A., Dorado, F., De Lucas-Consuegra, A.andValverde, J. L. (2013). Autothermal reforming and water–gas shift double bed reactor for H2 production from ethanol. *Chemical Engineering and Processing: Process Intensification*. **74,** 14-18.

Nishiguchi, T., Matsumoto, T., Kanai, H., Utani, K., Matsumura, Y., Shen, W.-J.andImamura, S. (2005). Catalytic steam reforming of ethanol to produce hydrogen and acetone. *Applied Catalysis A: General*. **279,** 273-277.

Noh, J. S.andSchwarz, J. A. (1989). Estimation of the point of zero charge of simple oxides by mass titration. *J Colloid Interface Sci*. **130,** 157-164.

Ocsachoque, M., Pompeo, F.andGonzalez, G. (2011). Rh–Ni/CeO2–Al2O3 catalysts for methane dry reforming. *Catal Today*. **172,** 226-231.

Odedairo, T., Chen, J.andZhu, Z. (2013). Metal–support interface of a novel Ni–CeO2 catalyst for dry reforming of methane. *Catal Commun*. **31,** 25-31.

Ogo, S.andSekine, Y. (2020). Recent progress in ethanol steam reforming using non-noble transition metal catalysts: A review. *Fuel Process Technol*. **199,** 106238.

Osorio-Vargas, P., Flores-González, N. A., Navarro, R. M., Fierro, J. L. G., Campos, C. H.andReyes, P. (2016). Improved stability of Ni/Al2O3 catalysts by effect of promoters (La2O3, CeO2) for ethanol steam-reforming reaction. *Catal Today*. **259, Part 1,** 27-38.

Özkan, G., Şahbudak, B.andÖzkan, G. (2019). Effect of molar ratio of water / ethanol on hydrogen selectivity in catalytic production of hydrogen using steam reforming of ethanol. *Int J Hydrogen Energy*. **44,** 9823-9829.

Palma, V., Castaldo, F., Ciambelli, P.andIaquaniello, G. (2014). CeO2-supported Pt/Ni catalyst for the renewable and clean H2 production via ethanol steam reforming. *Applied Catalysis B: Environmental*. **145,** 73-84.

Palma, V., Castaldo, F., Ciambelli, P., Iaquaniello, G.andCapitani, G. (2013). On the activity of bimetallic catalysts for ethanol steam reforming. *Int J Hydrogen Energy*. **38,** 6633-6645.

Palma, V., Ruocco, C., Castaldo, F., Ricca, A.andBoettge, D. (2015a). Ethanol steam reforming over bimetallic coated ceramic foams: Effect of reactor configuration and catalytic support. *Int J Hydrogen Energy*. **40,** 12650-12662.

Palma, V., Ruocco, C., Meloni, E., Gallucci, F.andRicca, A. (2017a). Enhancing Pt-Ni/CeO2 performances for ethanol reforming by catalyst supporting on high surface silica. *Catal Today*.

Palma, V., Ruocco, C., Meloni, E., Gallucci, F.andRicca, A. (2018a). Enhancing Pt-Ni/CeO2 performances for ethanol reforming by catalyst supporting on high surface silica. *Catal Today*. **307,** 175-188.

Palma, V., Ruocco, C., Meloni, E.andRicca, A. (2017b). Highly active and stable Pt-Ni/CeO2-SiO2 catalysts for ethanol reforming. *Journal of Cleaner Production*. **166,** 263-272.

Palma, V., Ruocco, C., Meloni, E.andRicca, A. (2017c). Influence of Catalytic Formulation and Operative Conditions on Coke Deposition over CeO2-SiO2 Based Catalysts for Ethanol Reforming. *Energies*. **10,** 1030.

Palma, V., Ruocco, C., Meloni, E.andRicca, A. (2017d). Oxidative steam reforming of ethanol on mesoporous silica supported PtNi/CeO2 catalysts. *Int J Hydrogen Energy*. **42,** 1598-1608.

Palma, V., Ruocco, C., Meloni, E.andRicca, A. (2017e). Renewable Hydrogen from Ethanol Reforming over CeO2-SiO2 Based Catalysts. *Catalysts*. **7,** 226.

Palma, V., Ruocco, C.andRicca, A. (2015b). Bimetallic Pt and Ni based foam catalysts for low-temperature ethanol steam reforming intensification. *Chemical Engineering Transactions*. **43,** 559-564.

Palma, V., Ruocco, C.andRicca, A. (2016). Ceramic foams coated with PtNi/CeO2ZrO2 for bioethanol steam reforming. *Int J Hydrogen Energy*. **41,** 11526-11536.

Palma, V., Ruocco, C.andRicca, A. (2018b). Renewable H2 production via oxidative reforming on Ni catalysts: an experimental and kinetic study. *Chemical Engineering Transactions*. **70,** 1321-1326.

Pandey, A. (2008). *Handbook of plant-based biofuels*, CRC press.

Parlett, C. M. A., Aydin, A., Durndell, L. J., Frattini, L., Isaacs, M. A., Lee, A. F., Liu, X., Olivi, L., Trofimovaite, R., Wilson, K.andWu, C. (2017). Tailored mesoporous silica supports for Ni catalysed hydrogen production from ethanol steam reforming. *Catal Commun*. **91,** 76-79.

Passos, A. R., Martins, L., Pulcinelli, S. H., Santilli, C. V.andBriois, V. (2017). Correlation of Sol–Gel Alumina-Supported Cobalt Catalyst Processing to Cobalt Speciation, Ethanol Steam Reforming Activity, and Stability. *ChemCatChem*. **9,** 3918-3929.

Passos, A. R., Pulcinelli, S. H., Santilli, C. V.andBriois, V. (2019). Operando monitoring of metal sites and coke evolution during non-oxidative and oxidative ethanol steam reforming over Ni and NiCu ex-hydrotalcite catalysts. *Catal Today*. **336,** 122-130.

Peela, N. R.andKunzru, D. (2011). Oxidative steam reforming of ethanol over Rh based catalysts in a micro-channel reactor. *Int J Hydrogen Energy*. **36,** 3384-3396.

Pérez-Bustos, H. F., Lucio-Ortiz, C. J., De La Rosa, J. R., De Haro Del Río, D. A., Sandoval-Rangel, L., Martínez-Vargas, D. X., Maldonado, C. S., Rodriguez-González, V., Garza-Navarro, M. A.andMorales-Leal, F. J. (2019). Synthesis and characterization of bimetallic catalysts Pd-Ru and Pt-Ru supported on γ-alumina and zeolite FAU for the catalytic transformation of HMF. *Fuel*. **239,** 191-201.

Pinton, N., Vidal, M. V., Signoretto, M., Martínez-Arias, A.andCortés Corberán, V. (2017). Ethanol steam reforming on nanostructured catalysts of Ni, Co and CeO2: Influence of synthesis method on activity, deactivation and regenerability. *Catal Today*. **296,** 135-143.

Psara, N., Van Sint Annaland, M.andGallucci, F. (2015). Hydrogen safety risk assessment methodology applied to a fluidized bed membrane reactor for autothermal reforming of natural gas. *Int J Hydrogen Energy*. **40,** 10090-10102.

Rabenstein, G.andHacker, V. (2008). Hydrogen for fuel cells from ethanol by steam-reforming, partial-oxidation and combined auto-thermal reforming: A thermodynamic analysis. *J Power Sources*. **185,** 1293-1304.

Ramos, I. a. C., Montini, T., Lorenzut, B., Troiani, H., Gennari, F. C., Graziani, M.andFornasiero, P. (2012). Hydrogen production from ethanol steam reforming on M/CeO2/YSZ (M=Ru, Pd, Ag) nanocomposites. *Catal Today*. **180,** 96-104.

Rass-Hansen, J., Johansson, R., Møller, M.andChristensen, C. H. (2008). Steam reforming of technical bioethanol for hydrogen production. *Int J Hydrogen Energy*. **33,** 4547-4554.

Riani, P., Garbarino, G., Canepa, F.andBusca, G. (2019). Cobalt nanoparticles mechanically deposited on α-Al2O3: a competitive catalyst for the production of hydrogen through ethanol steam reforming. *Journal of Chemical Technology & Biotechnology*. **94,** 538-546.

Rodrigues, T. S., De Moura, A. B. L., E Silva, F. A., Candido, E. G., Da Silva, A. G. M., De Oliveira, D. C., Quiroz, J., Camargo, P. H. C., Bergamaschi, V. S., Ferreira, J. C., Linardi, M.andFonseca, F. C. (2019). Ni supported Ce0.9Sm0.1O2-δ nanowires: An efficient catalyst for ethanol steam reforming for hydrogen production. *Fuel*. **237,** 1244-1253.

Rodriguez-Gomez, A.andCaballero, A. (2018). Bimetallic Ni-Co/SBA-15 catalysts for reforming of ethanol: How cobalt modifies the nickel metal phase and product distribution. *Molecular Catalysis*. **449,** 122-130.

Roses, L., Gallucci, F., Manzolini, G.andVan Sint Annaland, M. (2013). Experimental study of steam methane reforming in a Pd-based fluidized bed membrane reactor. *Chem Eng J*. **222,** 307-320.

Ruocco, C., Meloni, E., Palma, V., Van Sint Annaland, M., Spallina, V.andGallucci, F. (2016). Pt–Ni based catalyst for ethanol reforming in a fluidized bed membrane reactor. *Int J Hydrogen Energy*. **41,** 20122-20136.

Ruocco, C., Palma, V.andRicca, A. (2018). Experimental and kinetic study of oxidative steam reforming of ethanol over fresh and spent bimetallic catalysts. *Chem Eng J*.

Sahoo, D. R., Vajpai, S., Patel, S.andPant, K. K. (2007). Kinetic modeling of steam reforming of ethanol for the production of hydrogen over Co/Al2O3 catalyst. *Chem Eng J*. **125,** 139-147.

Saidi, M.andJahangiri, A. (2018). Theoretical study of hydrogen production by ethanol steam reforming: Technical evaluation and performance analysis of catalytic membrane reactor. *Int J Hydrogen Energy*.

Sanchez, N., Ruiz, R., Cifuentes, B.andCobo, M. (2019). Controlling sugarcane press-mud fermentation to increase bioethanol steam reforming for hydrogen production. *Waste Manage (Oxford)*. **98,** 1-13.

Sanchez, N., Ruiz, R., Hacker, V.andCobo, M. (2020). Impact of bioethanol impurities on steam reforming for hydrogen production: A review. *Int J Hydrogen Energy*. **45,** 11923-11942.

Sanchez, N., Ruiz, R. Y., Cifuentes, B.andCobo, M. (2016). Hydrogen from glucose: A combined study of glucose fermentation, bioethanol purification, and catalytic steam reforming. *Int J Hydrogen Energy*. **41,** 5640-5651.

Santos, A. C. S. F., Damyanova, S., Teixeira, G. N. R., Mattos, L. V., Noronha, F. B., Passos, F. B.andBueno, J. M. C. (2005). The effect of ceria content on the performance of Pt/CeO2/Al2O3 catalysts in the partial oxidation of methane. *Applied Catalysis A: General*. **290,** 123-132.

Sarkar, N., Ghosh, S. K., Bannerjee, S.andAikat, K. (2012). Bioethanol production from agricultural wastes: An overview. *Renewable Energy*. **37,** 19-27.

Sayah, A., Habelhames, F., Bahloul, A., Nessark, B., Bonnassieux, Y., Tendelier, D.andEl Jouad, M. (2018). Electrochemical synthesis of polyaniline-exfoliated graphene composite films and their capacitance properties. *J Electroanal Chem*. **818,** 26-34.

Schäfer, R., Noack, M., Kölsch, P., Stöhr, M.andCaro, J. (2003). Comparison of different catalysts in the membrane-supported dehydrogenation of propane. *Catal Today*. **82,** 15-23.

Seelam, P. K., Liguori, S., Iulianelli, A., Pinacci, P., Calabrò, V., Huuhtanen, M., Keiski, R., Piemonte, V., Tosti, S., De Falco, M.andBasile, A. (2012). Hydrogen production from bio-ethanol steam reforming reaction in a Pd/PSS membrane reactor. *Catal Today*. **193,** 42-48.

Sepehri, S., Rezaei, M., Wang, Y., Younesi, A.andArandiyan, H. (2018). The evaluation of autothermal methane reforming for hydrogen production over Ni/CeO2 catalysts. *Int J Hydrogen Energy*. **43,** 22340-22346.

Shahed Gharahshiran, V., Yousefpour, M.andAmini, V. (2020). A comparative study of zirconia and yttria promoted mesoporous carbon-nickel-cobalt catalysts in steam reforming of ethanol for hydrogen production. *Molecular Catalysis*. **484,** 110767.

Sharma, Y. C., Kumar, A., Prasad, R.andUpadhyay, S. N. (2017). Ethanol steam reforming for hydrogen production: Latest and effective catalyst modification strategies to minimize carbonaceous deactivation. *Renewable and Sustainable Energy Reviews*. **74,** 89-103.

Shi, Y., Du, X., Yang, L., Sun, Y.andYang, Y. (2013). Experiments on hydrogen production from methanol steam reforming in fluidized bed reactor. *Int J Hydrogen Energy*. **38,** 13974-13981.

Simson, A., Waterman, E., Farrauto, R.andCastaldi, M. (2009). Kinetic and process study for ethanol reforming using a Rh/Pt washcoated monolith catalyst. *Applied Catalysis B: Environmental*. **89,** 58-64.

Słowik, G., Greluk, M., Rotko, M.andMachocki, A. (2018). Evolution of the structure of unpromoted and potassium-promoted ceria-supported nickel catalysts in the steam reforming of ethanol. *Applied Catalysis B: Environmental*. **221,** 490-509.

Sohn, H.andOzkan, U. S. (2016). Cobalt-Based Catalysts for Ethanol Steam Reforming: An Overview. *Energy & Fuels*. **30,** 5309-5322.

Song, H., Mirkelamoglu, B.andOzkan, U. S. (2010). Effect of cobalt precursor on the performance of ceria-supported cobalt catalysts for ethanol steam reforming. *Applied Catalysis A: General*. **382,** 58-64.

Song, H., Zhang, L.andOzkan, U. S. (2012). The Effect of Surface Acidic and Basic Properties on the Performance of Cobalt-Based Catalysts for Ethanol Steam Reforming. *Top Catal*. **55,** 1324-1331.

Song, J. H., Yoo, S., Yoo, J., Park, S., Gim, M. Y., Kim, T. H.andSong, I. K. (2017). Hydrogen production by steam reforming of ethanol over Ni/Al2O3-La2O3 xerogel catalysts. *Molecular Catalysis*. **434,** 123-133.

Srisiriwat, N., Therdthianwong, S.andTherdthianwong, A. (2009). Oxidative steam reforming of ethanol over Ni/Al2O3 catalysts promoted by CeO2, ZrO2 and CeO2–ZrO2. *Int J Hydrogen Energy*. **34,** 2224-2234.

Srivastava, A.andPant, K. K. (2013). Oxidative steam reforming of bioethanol over Rh/CeO<inf>2</inf>-Al<inf>2</inf>O<inf>3</inf> catalyst for hydrogen production. *J Thermodyn Catal*. **4,** 119.

Stanley, J. N. G., García-García, I., Perfrement, T., Lovell, E. C., Schmidt, T. W., Scott, J.andAmal, R. (2019). Plasmonic effects on CO2 reduction over bimetallic Ni-Au catalysts. *Chem Eng Sci*. **194,** 94-104.

Sun, C., Zheng, Z., Wang, S., Li, X., Wu, X., An, X.andXie, X. (2018). Yolk-shell structured Pt-CeO2@Ni-SiO2 as an efficient catalyst for enhanced hydrogen production from ethanol steam reforming. *Ceram Int*. **44,** 1438-1442.

Sun, D., Du, Y., Wang, Z., Zhang, J., Li, Y., Li, J., Kou, L., Li, C., Li, J., Feng, H.andLu, J. (2020). Effects of CaO addition on Ni/CeO2–ZrO2–Al2O3 coated monolith catalysts for steam reforming of N-decane. *Int J Hydrogen Energy*. **45,** 16421-16431.

Sun, G. B., Hidajat, K., Wu, X. S.andKawi, S. (2008). A crucial role of surface oxygen mobility on nanocrystalline Y2O3 support for oxidative steam reforming of ethanol to hydrogen over Ni/Y2O3 catalysts. *Applied Catalysis B: Environmental*. **81,** 303-312.

Sun, S., Yan, W., Sun, P.andChen, J. (2012). Thermodynamic analysis of ethanol reforming for hydrogen production. *Energy*. **44,** 911-924.

Theron, J. N., Dry, M. E., Van Steen, E.andFletcher, J. C. Q. (1997). Internal and external transport effects during the oxidative reforming of methane on a commercial steam reforming catalyst. *In:* DE PONTES, M., ESPINOZA, R. L., NICOLAIDES, C. P., SCHOLTZ, J. H. & SCURRELL, M. S. (eds.) *Stud Surf Sci Catal.* Elsevier.

Tosti, S., Fabbricino, M., Moriani, A., Agatiello, G., Scudieri, C., Borgognoni, F.andSantucci, A. (2011). Pressure effect in ethanol steam reforming via dense Pd-based membranes. *Journal of Membrane Science*. **377,** 65-74.

Trevisanut, C., Mari, M., Millet, J.-M. M.andCavani, F. (2015). Chemical-loop reforming of ethanol over metal ferrites: An analysis of structural features affecting reactivity. *Int J Hydrogen Energy*. **40,** 5264-5271.

Tripodi, A., Compagnoni, M., Bahadori, E., Rossetti, I.andRamis, G. (2018). Process Intensification by Exploiting Diluted 2nd Generation Bio-ethanol in the Low-Temperature Steam Reforming Process. *Top Catal*. **61,** 1832-1841.

Tripodi, A., Compagnoni, M.andRossetti, I. (2016). Kinetic modeling and reactor simulation for ethanol steam reforming. *ChemCatChem*. **8,** 3804-3813.

Turczyniak, S., Greluk, M., Słowik, G., Gac, W., Zafeiratos, S.andMachocki, A. (2017). Surface State and Catalytic Performance of Ceria-Supported Cobalt Catalysts in the Steam Reforming of Ethanol. *ChemCatChem*. **9,** 782-797.

Tuti, S.andPepe, F. (2008). On the Catalytic Activity of Cobalt Oxide for the Steam Reforming of Ethanol. *Catal Lett*. **122,** 196-203.

Vaidya, P. D.andRodrigues, A. E. (2006). Insight into steam reforming of ethanol to produce hydrogen for fuel cells. *Chem Eng J*. **117,** 39-49.

Vicente, J., Ereña, J., Montero, C., Azkoiti, M. J., Bilbao, J.andGayubo, A. G. (2014a). Reaction pathway for ethanol steam reforming on a Ni/SiO2 catalyst including coke formation. *Int J Hydrogen Energy*. **39,** 18820-18834.

Vicente, J., Montero, C., Ereña, J., Azkoiti, M. J., Bilbao, J.andGayubo, A. G. (2014b). Coke deactivation of Ni and Co catalysts in ethanol steam reforming at mild temperatures in a fluidized bed reactor. *International Journal of Hydrogen Energy*. **39,** 12586-12596.

Vita, A., Italiano, C., Fabiano, C., Pino, L., Laganà, M.andRecupero, V. (2016). Hydrogen-rich gas production by steam reforming of n-dodecane. *Applied Catalysis B: Environmental*. **199,** 350-360.

Vita, A., Pino, L., Cipitì, F., Laganà, M.andRecupero, V. (2014). Biogas as renewable raw material for syngas production by tri-reforming process over NiCeO2 catalysts: Optimal operative condition and effect of nickel content. *Fuel Process Technol*. **127,** 47-58.

Vivek, S., Arunkumar, P.andBabu, K. S. (2016). In situ generated nickel on cerium oxide nanoparticle for efficient catalytic reduction of 4-nitrophenol. *RSC advances*. **6,** 45947-45956.

Vohra, M., Manwar, J., Manmode, R., Padgilwar, S.andPatil, S. (2014). Bioethanol production: Feedstock and current technologies. *Journal of Environmental Chemical Engineering*. **2,** 573-584.

Wang, H., Zhang, L., Li, M., Liu, Y.andBai, X. (2013). Co/CeO2 for ethanol steam reforming: effect of ceria morphology. *Journal of Rare Earths*. **31,** 565-571.

Wang, W.andWang, Y. (2010). Steam reforming of ethanol to hydrogen over nickel metal catalysts. *International Journal of Energy Research*. **34,** 1285-1290.

Wei, Y., Cai, W., Deng, S., Li, Z., Yu, H., Zhang, S., Yu, Z., Cui, L.andQu, F. (2020). Efficient syngas production via dry reforming of renewable ethanol over Ni/KIT-6 nanocatalysts. *Renewable Energy*. **145,** 1507-1516.

Weng, S.-F., Hsieh, H.-C.andLee, C.-S. (2017). Hydrogen production from oxidative steam reforming of ethanol on nickel-substituted pyrochlore phase catalysts. *Int J Hydrogen Energy*. **42,** 2849-2860.

Wenju, W.andQ., W. Y. (2008). Thermodynamic analysis of steam reforming of ethanol for hydrogen generation. *International Journal of Energy Research*. **32,** 1432-1443.

Wu, C., Dupont, V., Nahil, M. A., Dou, B., Chen, H.andWilliams, P. T. (2017). Investigation of Ni/SiO2 catalysts prepared at different conditions for hydrogen production from ethanol steam reforming. *Journal of the Energy Institute*. **90,** 276-284.

Wu, C.andWilliams, P. T. (2012). Effect of process conditions on the steam reforming of ethanol with a nano-Ni/SiO2 catalyst. *Environ Technol*. **33,** 631-638.

Wyman, C. E. (2004). Ethanol Fuel. *In:* CLEVELAND, C. J. (ed.) *Encyclopedia of Energy*. New York: Elsevier.

Xiao, Z., Li, Y., Hou, F., Wu, C., Pan, L., Zou, J., Wang, L., Zhang, X., Liu, G.andLi, G. (2019). Engineering oxygen vacancies and nickel dispersion on CeO2 by Pr doping for highly stable ethanol steam reforming. *Applied Catalysis B: Environmental*. 117940.

Xie, J., Sun, X., Barrett, L., Walker, B. R., Karote, D. R., Langemeier, J. M., Leaym, X., Kroh, F., Traylor, W., Feng, J.andHohn, K. L. (2015). Autothermal reforming and partial oxidation of n-hexadecane via Pt/Ni bimetallic catalysts on ceria-based supports. *Int J Hydrogen Energy*. **40,** 8510-8521.

Xu, J.andFroment, G. F. (1989). Methane steam reforming, methanation and water-gas shift: I. Intrinsic kinetics. *AlChE J*. **35,** 88-96.

Xue, Z., Shen, Y., Li, P., Pan, Y., Li, J., Feng, Z., Zhang, Y., Zeng, Y., Liu, Y.andZhu, S. (2018). Promoting effects of lanthanum oxide on the NiO/CeO2 catalyst for hydrogen production by autothermal reforming of ethanol. *Catal Commun*. **108,** 12-16.

Yang, W.-C. (2003). *Handbook of fluidization and fluid-particle systems*, CRC press.

Yang, Y., Ma, J.andWu, F. (2006). Production of hydrogen by steam reforming of ethanol over a Ni/ZnO catalyst. *Int J Hydrogen Energy*. **31,** 877-882.

Yentekakis, I. V., Goula, G., Panagiotopoulou, P., Katsoni, A., Diamadopoulos, E., Mantzavinos, D.andDelimitis, A. (2015). Dry Reforming of Methane: Catalytic Performance and Stability of Ir Catalysts Supported on γ-Al2O3, Zr0.92Y0.08O2−δ (YSZ) or Ce0.9Gd0.1O2−δ (GDC) Supports. *Top Catal*. **58,** 1228-1241.

Yoshida, H., Yamaoka, R.andArai, M. (2015). Stable hydrogen production from ethanol through steam reforming reaction over nickel-containing smectite-derived catalyst. *International journal of molecular sciences*. **16,** 350-362.

Yus, M., Soler, J., Herguido, J.andMenéndez, M. (2018). Glycerol steam reforming with low steam/glycerol ratio in a two-zone fluidized bed reactor. *Catal Today*. **299,** 317-327.

Zabed, H., Sahu, J., Suely, A., Boyce, A.andFaruq, G. (2017). Bioethanol production from renewable sources: Current perspectives and technological progress. *Renewable and Sustainable Energy Reviews*.

Zangouei, M., Moghaddam, A. Z.andArasteh, M. (2010). The influence of nickel loading on reducibility of NiO/Al 2 O 3 catalysts synthesized by sol-gel method. *2010*. **14,** 6.

Zhang, B., Tang, X., Li, Y., Cai, W., Xu, Y.andShen, W. (2006). Steam reforming of bio-ethanol for the production of hydrogen over ceria-supported Co, Ir and Ni catalysts. *Catal Commun*. **7,** 367-372.

Zhang, H., Wang, J., Zhang, Y., Jiao, Y., Ren, C., Gong, M.andChen, Y. (2016). A study on H2-TPR of Pt/Ce0.27Zr0.73O2 and Pt/Ce0.27Zr0.70La0.03Ox for soot oxidation. *Appl Surf Sci*. **377,** 48-55.

Zhang, L., Wang, X., Chen, C., Zou, X., Shang, X., Ding, W.andLu, X. (2017). Investigation of mesoporous NiAl2O4/MOx (M = La, Ce, Ca, Mg)–γ-Al2O3 nanocomposites for dry reforming of methane. *RSC Advances*. **7,** 33143-33154.

Zhao, X.andLu, G. (2016). Modulating and controlling active species dispersion over Ni–Co bimetallic catalysts for enhancement of hydrogen production of ethanol steam reforming. *Int J Hydrogen Energy*. **41,** 3349-3362.

Zhao, Y., Li, H.andLi, H. (2018). NiCo@SiO2 core-shell catalyst with high activity and long lifetime for CO2 conversion through DRM reaction. *Nano Energy*. **45,** 101-108.

Zhou, F., Gao, Y., Wu, G., Ma, F.andLiu, C. (2017). Improved catalytic performance and decreased coke formation in post-treated ZSM-5 zeolites for methanol aromatization. *Microporous Mesoporous Mater*. **240,** 96-107.

Zhurka, M. D., Lemonidou, A. A., Anderson, J. A.andKechagiopoulos, P. N. (2018). Kinetic analysis of the steam reforming of ethanol over Ni/SiO2 for the elucidation of metal-dominated reaction pathways. *Reaction Chemistry & Engineering*. **3,** 883-897.